UNIVERSITÀ DEGLI STUDI DI PAVIA

DOTTORATO IN SCIENZE CHIMICHE E FARMACEUTICHE E INNOVAZIONE INDUSTRIALE
(XXXV Ciclo)

Coordinatore: Chiar.mo Prof. Giorgio Colombo

Development of new colorimetric and electrochemical sensors for analytical applications

Tesi di Dottorato di
Camilla Zanoni

AA 2022/2023

Tutor
Chiar.ma Prof.ssa Raffaela Biesuz

Co-tutor
Prof.ssa Alberti Giancarla

A mio fratello Lorenzo...

Index of contents

Abstract (ENG)

In this thesis, the results obtained during the Ph.D. project titled “Development of new tailored devices for analytical applications” are reported. The aim of the project was the development of optical and electrochemical sensors for environmental and food applications. During these three years, colorimetric sensors were realized, and as examples, two kinds of Paper-based Analytical devices (PADs) for determining the acidity of commercial drinks or Pd^{2+} in natural waters were described. In all cases, chemometric tools were applied for the data treatment.

Furthermore, electrochemical sensors based on screen-printed cells were proposed. Sensors for Glyphosate and Fe^{3+} were developed by modifying the gold working electrode of the screen-printed cells with proper self-assembled monolayers. Sensors for MCPA, Atrazine, Irbesartan and Ascorbic acid were obtained by modifying the surface of the graphite working electrode of the screen-printed cells with molecularly imprinted polymers (acrylic-based or electro-synthesized). Multivariate techniques were applied for data treatment when necessary.

Abstract (ITA)

In questo lavoro di tesi sono riportati per esteso tutti i risultati ottenuti nel progetto di dottorato dal titolo "*Development of new tailored devices for analytical applications"*. Lo scopo del progetto era di sviluppare sensori ottici ed elettrochimici per la determinazione di analiti di interesse ambientale e alimentare. Durante i tre anni di dottorato sono stati sviluppati sensori colorimetrici di vario tipo e, a titolo d'esempio sono stati descritti in questa tesi due dispositivi a base di carta da filtro (Paper-based Analytical devices, PADs) per la determinazione dell'acidità di bibite commerciali e per la determinazione del Pd^{2+} in acque naturali. In tutti i casi per il trattamento dei dati sono state applicate tecniche chemiometriche.

Inoltre sono stati sviluppati dei sensori elettrochimici basati sull'utilizzo di celle elettrochimiche stampate. Sono stati sviluppati due sensori per il Glifosato e il Fe^{3+} modificando la superficie degli elettrodi di lavoro d'oro con opportuni monostrati di tioli (self assembled monolayers, SAM). Sensori per la determinazione di MCPA, Atrazina, Irbesartan e Acido ascorbico sono stati ottenuti modificando la superficie dell'elettrodo di lavoro in grafite con polimeri a stampo molecolare (acrilici o elettropolimerizzati). Quando necessario sono state applicate tecniche multivariate di analisi dati.

1 INTRODUCTION

1.1 Aim of the project

The project aims to develop new, easy-to-handle and low-cost optical and electrochemical sensors for the detection of analytes of environmental and food interest.

The sensors' receptors are designed to interact selectively with the target analytes; in particular, the functionalization of the sensing surface of the optical and electrochemical sensors with dye-based receptors, molecularly imprinted polymers or self-assembled monolayers is proposed.

For all the sensors developed, first, a characterization of the interaction between the receptor and the analyte is performed. Subsequently, the substrate for the optical devices or the kind of working electrode for the electrochemical sensor is selected, optimizing the strategy to fix the receptor to the substrate/electrode surface.

Once realized, the sensors are characterized and applied to the analyte's determination in synthetic standard solutions and real samples. In some cases, the optimal experimental conditions for the analysis are defined by the application of Design of Experiments (DoE).

The validation of the analytical procedures follows the well-defined steps of blank analysis, dynamic range evaluation, accuracy, precision, LOD and LOQ determinations. When the signal obtained is disturbed and not reproducible, the quantitative analysis is performed by multivariate techniques, such as Partial Least Square regression (PLS).

Figure 1 summarizes the optical and electrochemical sensors developed, indicating the substrate, the receptor and the data treatment.

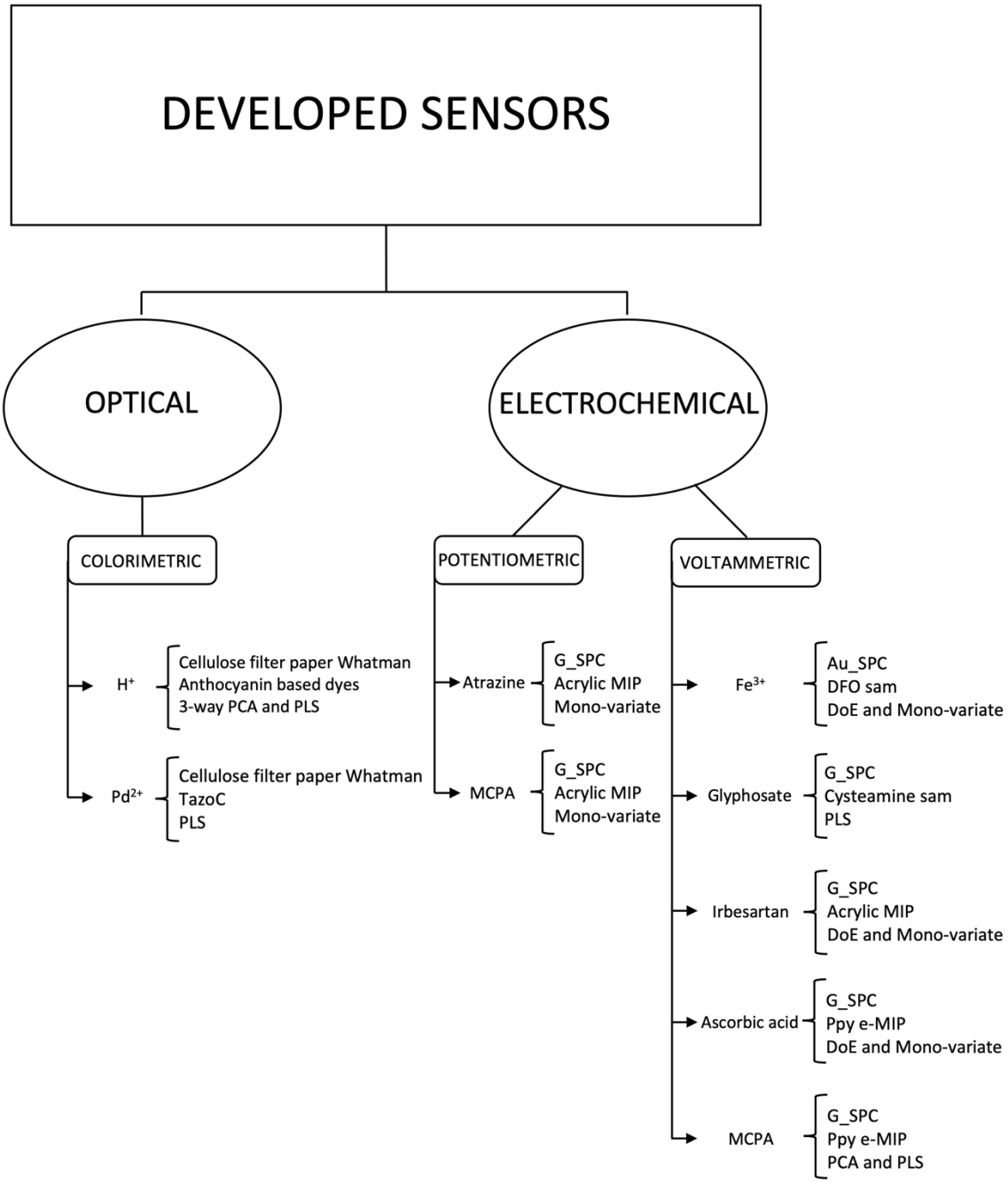

Figure 1.Developed sensors divided on the basis of the detection method and the analyte. The substrate, receptor, and data treatment methods are reported for each sensor.

1.2 Sensors: definition and classification

The research and development activity in the field of sensors has grown in the last decades, and the applications of these devices in everyday life, industry, and research have increased progressively from year to year[1–6].

Nowadays, the most commercialized chemical sensor is the solid-state oxygen one used in catalytic converters, which can continuously and reversibly monitor oxygen levels in

combustion gases. The literature on chemical sensors increased sharply after the 1970s, following the electrochemical sensors' success.

Actually, there is no universally accepted definition of either of the terms sensor, chemical sensor or biosensor; indeed, much confusion and misperceptions of chemo- and biosensor terminology can be attributed[7].

Referring to the IUPAC definition[8], *a chemical sensor is a device that transforms chemical information, ranging from the concentration of a specific sample component to total composition analysis, into an analytically useful signal*.

A sensor contains two units: a receptor and a transducer. The basis of chemosensor and biosensor technology is the interaction between the target analyte and a suitable receptor; this interaction causes the variation of a parameter that produces a signal detected by the transducer, which generates a recordable generally electric signal[9]. A scheme of the operating principle of a sensor is shown in Figure 2.

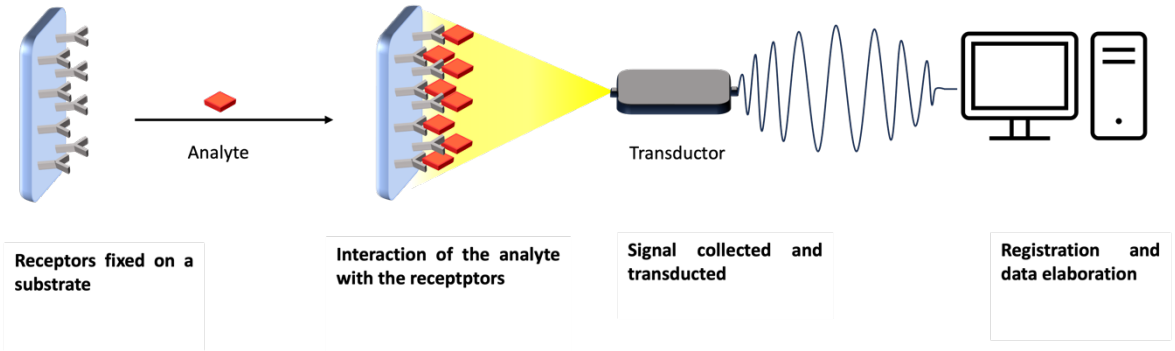

Figure 2. Schematic representation of the sensor's operating principle.

According to the transducer's operating principle, sensors can be classified as optical[10–15], electrochemical[16–19], electrical, mass-sensitive, magnetic, and thermometric[8]. Various sensors may be combined in sets, often called multi-sensors or arrays.

1.3 Aspects of a sensor[20]

1.3.1 Receptors

Receptors are recognition elements and key components of any sensor. They confer selectivity, i.e., the property to respond selectively to a target analyte or class of analytes, avoiding or reducing interferences from other substances in the samples. In chemosensors, the receptors can be supramolecular systems or ligands forming colored or fluorescent

adducts with the target analyte or else Molecularly Imprinted Polymers (MIP), which are biomimetic receptors composed of synthetic materials containing recognition cavities selective for the molecule of interest. In biosensors, the receptors are of biological origins, such as proteins (antibodies, enzymes) and nucleic acids (DNA, RNA, aptamers).

1.3.2 Transducer: the sensor's detector

As for many analytical methods, such as colorimetric and spectroscopic, sensors can have photometric transducers; however, most sensors have been developed using electrochemical transducers due to the ease of construction and low cost. With the rapid development of photon-driven devices based on optical fibers, several optical sensors are developed thanks to greater flexibility and miniaturization. In addition, micro-mass-controlled devices, based mainly on piezo-electric crystals, may become competitive shortly.

1.3.3 Methods of receptor's immobilization

In a sensor, the receptor must be connected to the transducer. Different methods can be exploited, mainly depending on the transductors. For example, the receptors can be sorbed or covalently linked to a suitable substrate for colorimetric sensors. The chemical modification of an electrode surface is the usual approach employed to develop electrochemical sensors.

1.3.4 Figures of merits

The most important characteristic of a sensor is its selectivity, which is the ability to discriminate between the target analyte (or class of analytes) and the other substances in the sample. Such property is principally due to the selectivity of the receptor, although sometimes the transducer can contribute to it.

Additional figures of merit are the sensitivity, usually evaluated through the detection limit (LOD), the limit of quantification (LOQ), and the linear range of concentration that can be investigated. Other important parameters are the method's accuracy, which needs to be lower than ±5%, and the precision, measured through repeatability and reproducibility tests.

There are even aspects depending on the sample characteristics that affect the experimental conditions, such as pH, temperature and ionic strength.

Other parameters to be evaluated concern the sensor's properties, such as the response time and the working lifetime, usually determined by the stability of the receptor or the substrate.

1.4 Data treatment

In Prof Raffaela Biesuz's research group, chemometric data treatment is a routine tool due to the challenges faced in developing differential receptors over the last decade.

Indeed, in addition to the previous classification, sensors are distinguished into specific (or selective) and differential (or generalized) sensors. The first ones, in principle, exhibit a high selectivity towards specific analytes, while the second have different binding properties, none of which are necessarily specific or even selective.

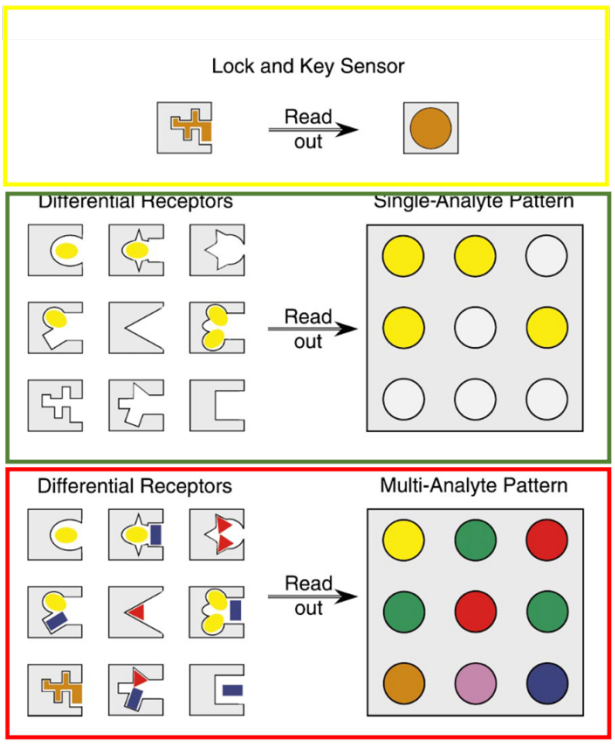

Figure 3. Schematic representation of receptors and transducers binding principles for selective and differential receptors. In the yellow rectangle, a specific binding event manifests a large degree of complementarity between the host and the guest. Below, an array of generalized receptors interacting with one in the green rectangle or multiple analytes in the red rectangle are shown. Adapted by Laving and Anslyn[21].

This difference is well depicted in Figure 3, which can be found in the paper of J. J. Lavigne and E. J. Anslyn[21].

Selective receptors mimic the lock-and-key approach to molecular recognition, typical of several biological systems, as represented in the yellow rectangle of Figure 3. This high-specificity approach, as it will be discussed, is the main feature behind the MIP strategy. As

illustrated below, several case studies will be presented. The main drawback arises when dealing with complex mixtures of analytes. In principle, the design and synthesis of receptors for each component in the mixture is required using a lock-and-key approach. More often, the molecular recognition of molecules with similar structures could become an endless challenge, and the selectivity becomes that of a family of substances instead of that of a specific molecule.

Opposite differential receptors, represented in the green and red rectangles of Figure 3, mimic the binding scenario used in the mammalian senses of taste and smell; they require an array of sensors to be created and a composite signal to be evaluated and interpreted, usually exploiting multivariate tools.

These receptors need neither to be designed nor to be highly specific for any analyte and allow the discrimination of analytes or analyte mixtures that have not been exhaustively characterized.

The arrays of colorimetric sensors developed for following proteinaceous food spoilage are clear examples[22–31]. An array built following this strategy will also be presented below.

As for data processing, for the first class of sensors, for the quantification of the analyte, the univariate approach is the obvious way; in the case of the differential devices, it becomes almost mandatory, even for colorimetric devices, to use multivariate techniques. Becoming more confident using these last techniques, we discovered to be convenient to treat signals that, in principle, can be faced with a dose-response straight line with the multivariate approach. Indeed, it will happen when the baseline, for different reasons, is very disturbed. We will present a case where the solid UV-vis spectra are the analytical signals or cases where an electrochemical signal (E(mV) vs i) varies with the analyte concentration, changes the shape and the redox potential. In such cases, the analytical signal is not the simple absorbance at λ_{max}, or the faradic current measured at the peak potential of the voltammogram, but the entire UV-vis spectra or the voltammogram, avoiding the acquisition of a single signal not rarely burdened by operator bias.

In the following, a brief description of the multivariate tools employed in this research is presented, intending to remind them as a quick reference along the thesis.

The first tool deals with the experimental design. It means strategies of experiments set up to save time and achieve the best results with the lowest effort.

The second tools are common chemometric algorithms: on the one hand, the unsupervised tools such as the PCA (Principal Component Analysis) and the somewhat unfamiliar 3WayPCA, on the other hand, the chemometric supervised technique proper for quantitative multivariate calibration, the PLS, Principal Least Square Regression.

The open-source Chemometric Agile Tool (CAT) program was employed throughout this thesis work[32].

1.4.1 Design of Experiments (DoE)

The DoE is the most accessible tool to employ to optimize any process. Once the variables that influence the process have been selected, through the most suitable DoE, it is possible to perform the lowest number of experiments to achieve the highest quality of the information. It means to quantitatively assess the real contribution of the variables to the process and consider the interactions among them. A deeper description is out of the scope of the work. Here, DoE was used to optimize the experimental parameters of the electrochemical sensors for Fe^{3+}, Irbesartan and Ascorbic acid.

The idea behind this approach, as told above, is that not only the single variables influence the signal (mono-variate approach) but also the interaction between them (multivariate approach). In the present research, we always employed full factorial design, the simplest and most known of DoE for which, to explore correctly the experimental domain, the least number of experiments required to cover the experimental plan is 2^k, where k is the number of variables; for example, if the variables that are selected to optimize the response are three, the least number of experiments to run is $2^3=8$. The experiments must be projected according to the full experimental design rules, assigning a maximum (+1) and a minimum (-1) value for each variable, which defines the experimental domain for each variable, as shown in Table 1, experiments from E_1 to E_8.

Table 1. Experimental design for a full factorial design 2^3.

Experiment	**V_1**	**V_2**	**V_3**
E_1	-1	-1	-1
E_2	+1	-1	-1
E_3	-1	+1	-1
E_4	+1	+1	-1
E_5	-1	-1	+1
E_6	+1	-1	+1
E_7	-1	+1	+1
E_8	+1	+1	+1
V_1	0	0	0
V_2	0	0	0
…	…	…	…

For three variables, it means performing the experiments at each cube vertex. Collecting the eight responses Y, possibly completing the experiments in a random order, the multi-regression function defines the hyperplane, calculating the coefficients of the equation:

$$Y = b_0 + b_1x_1 + b_2x_2 + b_3x_3 + b_{12}x_1x_2 + b_{23}x_2x_3 + b_{13}x_1x_3 \quad (1)$$

Where b_0 is the known term, the b_1 b_2 b_3 are the coefficients associated with each variable: the higher the absolute value, the higher the effect of that variable on the system. The positive sign means that that variable at its high level increases the response, while if negative, it will increase the response only if we want to obtain the minimum response. The b_{12} b_{13} b_{23} are the coefficients that describe the interaction of variables; again, the higher the absolute values, the higher the interaction between the involved variables, while the significance of the sign must be evaluated together with that of each variable and is usually assessed graphically by response surface.

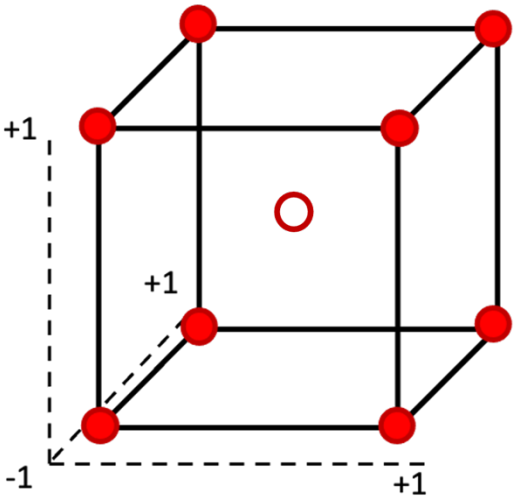

Figure 4. Representation of the 2^3 full factorial design.

Of course, mathematically, all 7 terms are calculated, but only those significantly different from the background noise are considered. The significance of the coefficient is related, in addition to noise, to the degree of freedom, always equal to the number of experiments minus the number of parameters, here equal to one. In this way, the variables' weights and their interaction drive the decision of the best conditions to set up for achieving the best result.

One step is still needed; only validation allows the application of the model for prediction within the entire experimental domain. In the case of continuous variables, this can be easily achieved by performing a series (two or more)of experiments in the codified value 0,0,0, corresponding to the cube's center; see experiments V_1 and V_2 in Table 1. When the calculated value, equal to b_0, falls within the confidence interval, the system is fully validated at a given confidence level.

It must be underlined that, in this thesis, every time DoE was applied, the term “optimization” was used: from a strictly theoretical point of view, this term should be used only when quadratic models are applied, and thus, our use of this term is wrong. Nevertheless, being this thesis for a wider readership, we used the term “optimization” to distinguish from the most common “one variable at a time” approach.

1.4.2 Principal Component Analysis (PCA)

This tool was exploited in Chapters 2.3 Green-PAD array for pH measurements and 3.8 e-MIP-modified screen-printed electrodes for the voltammetric detection of MCPA.

PCA is the most known unsupervised technique that can applied to any bidimensional dataset when a certain number of samples, *m*, called objects, put on rows, are described more than a few variables, *n*, put on columns. Such tables are often encountered in science and, let us say, everywhere. Regularly, it is hard to understand the information behind that table quickly. Assuming that not all the variables bring the same quality of information and the real dimension of the dataset is lower than *n*, the PCA algorithm reduces the dimension of the data set, performing a sort of axes rotation towards none of the original variables but to a first linear combination of all of them able to capture the maximum data variability. The remaining variance is submitted to the same operation so that another dimension, still a linear combination of the original variables, captures most of the residual variance. This operation is repeated as times as the number of variables. The result is the "compression" of the data set's variability, i.e., the information in the first Principal Component (PC), while the noise is left in the last ones. The algorithm follows some rules: variables, most of the time, need autoscaling; some constraints are introduced as the maintenance of the total variance of the system; the orthogonality of all the new dimensions that guarantee the independence of each PCA, that sometimes can be associated to a property of the system. From the geometrical point of view, the principal component analysis, in a limited case of only two variables, performs the axes rotation reported in Figure 5.

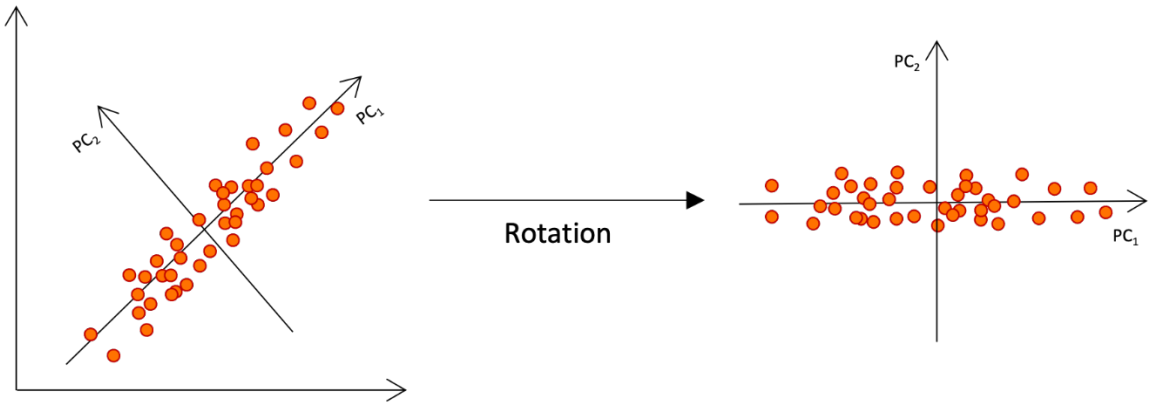

Figure 5. PCA rotation in the direction of maximum explained variance.

In addition to the variance captured by each component that allows the selection of the principal ones, the algorithm outputs are the *loadings* and the *scores* plots. The first gives information about the importance of the variables in each component, discovering variables that bring the same information. The *scores* plot is the projection of the samples into the new space of the PCs. It shows the distribution of samples: similar samples are

allocated together in the new space depending on the importance of the same variables used for their description. For the extreme feasibility of the technique, PCA could be used for first data rationalization, visualization and preliminary pattern recognition. It is not the case to go deeper into the description found in any text of basic chemometrics[33].

As a general rule, valid for any of the chemometric tools employed, the quality of the information extracted and the model are directly related to the goodness of the dataset.

1.4.3 3-Way PCA

This tool was exploited in Chapter 2.3 Green-PAD array for pH measurements.

The 3-Way PCA is still an unsupervised technique that permits obtaining information in all cases where observations on a given number of samples are somehow repeated. In other words, sometimes, the structure of a data set is such that a standard two-way table (objects versus variables) is not enough to describe it. It happens when an environmental investigation on different sites is repeated over time[34], or an analysis on a data set is followed over time, still also for different kinds of samples[22,35], or in a sensory case, the test is repeated on different beverages by different assessors. It could be interesting to separate the contribution to variability given by the selected conditions that produce a tridimensional data set. It must be underlined that while PCA can be applied to every dataset of any dimension, 3-Way PCA can be run only on completely symmetrical matrixes in which the *variables* are acquired for each *object* at each *condition* and vice versa. With CAT software, the 3-way PCA is done using the TUCKER 3 algorithm (decomposition algorithm)[36]. From the geometrical point of view, the dataset can be visualized as a cube where the sides are the components: objects(*i*), variables (*j*) and conditions (*k*), as reported in Figure 6.

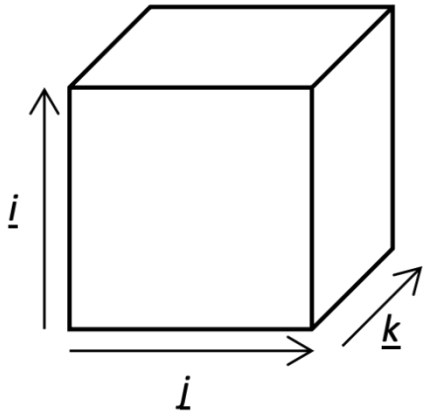

Figure 6.Graphical representation of the 3-Way PCA dataset.

A much easier interpretation of the information contained in the data set is achieved directly considering its three-way structure. Of course, the matrix submitted to the algorithm cannot be a cube, but after the first *i* x *j* matrix referred to the first condition, the others are repeated under it for each remaining *k-1* condition.

The output is given by three sets of loadings together with a core array describing the relationship among them. Setting up a fixed number of components for each way, the core array is a cube. In our application, we always consider two components so that it can be applied to the [2 2 2] T3 model. A comparison between the variance calculated by the Tucker model and that of the single mode after unfolding is usually useful to estimate the loss of information due to the unfolding operation.

Each of the three sets of loadings can be displayed and interpreted in the same way as a score plot of standard PCA, but in the case of a cubic core array, a series of orthogonal rotations can be performed on the three spaces of the objects, variables and conditions, looking for the common orientation for which the core array is as much as possible body-diagonal. Under this condition, i.e., when the core matrix exhibits a superdiagonal condition, the rotated sets of loadings can also be interpreted jointly by overlapping them.

1.4.4 Partial Least Square regression (PLS)

This tool was exploited in the Chapters 2.3 Green-PAD array for pH measurements, 2.4 TazoC-PADs for Pd(II) detection, 3.5 Cysteamine-copper SAM-modified screen-printed gold electrode for glyphosate determination, 3.8 e-MIP-modified screen-printed electrodes for the voltammetric detection of MCPA.

Unlike the unsupervised techniques, the supervised chemometric techniques answer a different question: the possibility of predicting a response from a multivariate dataset. We can deal with data suitable for qualitative or quantitative predictions. Traditionally, the supervised methods refer to classification methods in the first case to multiregression methods in the second. Among these last ones, PLS, or partial least square regression, is the most popular one, applied systematically in many different fields also out of chemistry. The main feature of all the supervised methods is that we must start from reference values for model construction.

PLS algorithm essentially provides a means for regressing the predictor (for example, a spectrum, X) and predicted variables (es concentration, Y)

This technique aims to find the relationship between the dependent and the independent variables[37,38]. The mathematical model that represents this relation is reported in eq.

$$y = \beta_0 + \beta_1 x_1 + \beta_2 x_{2+} + \beta_3 x_3 + \cdots \beta_n x_n + \varepsilon \qquad (2)$$

where β_n are the regression coefficients and ε the error. The PLS algorithm finds the underlying structure present in, for example, spectroscopic/chromatographic/electrochemical data sets and captures maximum variances of both descriptors and predictors, ensuring the maximization of the correlation between them. PLS achieves this using the non-iterative partial least squares (NIPALS) approach.

As discussed above, one of the key points while developing the PLS model is the selection of an optimum number of latent variables, under the general rule that the first latent variable explains the maximum variation followed by the second latent variable, and so on. It is typically achieved using the cross-validation approach, that essentially solves two primary purposes in PLS analysis. It allows the easy assessment of the optimal complexity of the PLS model and provides a measure for evaluating the PLS model performance when applied to a validation data set. The cross-validation step involves the removal of some of the samples (test set) from the calibration set and constructing the PLS model with the remaining samples (model building set). The developed model is subsequently used for predicting the concentration of the analytes of interest in the test set samples.

The same procedure is repeated by varying the latent variables, and a statistical parameter called the root mean square error of cross-validation (RMSECV) is estimated for each of the

developed PLS models. The RMSECV values are plotted against the latent variable index. From the curve, the number of latent variables that minimize the RMSECV value can be used for developing the PLS model.

The risk to be avoided, indeed, is to keep a too low number of latent variables to fall into an underfitting condition, as opposed to keeping too many to fall into overfitting. Both conditions should be avoided, and the best model must be a balance between good description properties and, more importantly, predictive properties. This last performance is evaluated by running the model on an external data set with still-known concentrations. Together with a graphical representation of experimental versus fitting values, the root mean square error of prediction (RMSEP) measures the error in predicting the properties of the samples of the testing set. Deeper insight can be found in any basic chemometric book[33].

1.4.5 Limit of detection (LOD) and limit of quantification (LOQ)

When a univariate method is used for analytical purposes, i.e., when we refer to a dose-response curve and linear regression method, the definition of the limit of detection (LOD) and, consequently, the limit of quantification (LOQ) has a flat and linear form.

With at least 10 replicates of the blank measurements, the limit of detection, for a confidence level of 95%, is given by:

$$LOD = \frac{3.3 \cdot \sigma_B}{b_1} \quad (3)$$

Where σ_B is the standard deviation on the blank measurements, and b_1 is the slope of the calibration straight line. A more exhaustive and correct formula considers the uncertainty on the straight-line parameters, although eq 3 is the most popular version of LOD.

When blank replicates are not available, as is the case of many electrochemical methods, the standard deviation on the regression $s_{y/x}$ can be used as the standard deviation of the blank obtaining the equation 4:

$$LOD = \frac{3.3 \cdot s_{y/x}}{b_1} \quad (4)$$

Where b_1 is the slope of the calibration straight line and $s_{y/x}$ the standard deviation on the regression[39].

The limit of quantification is the first concentration that can be quantified, and it can be calculated as[39]:

$$LOQ = \frac{10 \cdot \sigma_B}{b_1} \quad (5)$$

Or

$$LOQ = \frac{10 \cdot s_{y/x}}{b_1} \quad (6)$$

The computation of LOD and LOQ values from the PLS models is a completely different matter.

Surprisingly, there is currently no defined procedure for multivariate calibration. Defining an estimator for the LOD is more complex since the traditional univariate procedures cannot be applied to the multivariate parameters obtained from the Partial Least Square regression of the calibration measurements.

Different strategies have been proposed, but no unique method has been identified [40–43]. For these reasons, depending on the data set we are dealing with, we explain how we estimate LOD when PLS is used as a calibration method.

2 COLORIMETRIC SENSORS

In this section, two colorimetric sensors are presented. The first paragraph summarizes the general features of colorimetric sensing devices; in the second, the approach to realize and apply these sensors is described. The last two paragraphs present the colorimetric Paper-based Analytical Devices (PADs) developed and applied to real samples.

2.1 General features

Colorimetric sensors provide a naked-eye-observable, quick, low-cost, sensitive and selective response toward various analytes[44].

With the progress in materials science and nanotechnology, various nanomaterials such as nanoparticles (NPs), carbon nanotubes or nanofibers, quantum dots (QDs), graphene, and various 2D-nanomaterials have been exploited for the fabrication of different chemosensors and biosensors. Unluckily, this kind of sensor shows some drawbacks due to the time-consuming preparation and applications, which is not helpful for in-situ analysis.

Otherwise, colorimetric sensors look promising for detecting analytes in different matrixes thanks to their easy preparation, fast detection, naked-eye sensing, and quite good sensitivity[45].

In this perspective, the realization and application of disposable colorimetric sensors are the right direction for quick and on-site detection. These devices are cheap and easy to use; they do not experience memory effects or need pre-treatment before their use or cleaning among measurements. Due to the growing demand for in-situ analysis, the global market for disposable colorimetric sensors is rapidly increasing, particularly for environmental monitoring and medical diagnostics[46].

2.2 Colorimetric sensor's development

In colorimetric sensors, the receptor, linked to a suitable and inert substrate, changes color when in contact with the analyte.

The materials generally used as substrates for colorimetric sensors can be grouped into four categories: cellulose-based materials, textiles and woven non-woven fabrics, synthetic polymeric supports, and sol-gel materials.

The receptor can be fixed on the substrate by exploiting different strategies, such as the simple impregnation of filter papers with an aqueous or hydro-alcoholic solution of a dye or the covalent linkage of the receptor to natural or synthetic polymers. In any case, the interaction receptor/analyte must remain unchanged after the linkage of the receptor to the substrate.

Different detectors can be used for colorimetric sensing, from the latest and low-cost devices, such as scanners or smartphones, to more classical instruments, such as spectrophotometers and spectrofluorimeters.

Scanners provide a fair resolution of the digitalized image, and the image intensity is not affected by the external light. They are usually employed because they can be portable (such as pen scanners) and usable for untrained personnel.

Digital and smartphone cameras can also be employed because they do not require any particular skills.

After digitalization, the resulting images must be analyzed using software or apps to obtain the color indexes in one of the color spaces: RGB, CMYK, grayscale, HSV, or CIE L*a*b*. Depending on the color and tone of the image analyzed, the complete information, or just one channel of the color space, can be used for data treatment.

The last group of detectors comprises simple photometers and homemade devices, such as the one realized during this Ph.D. project: the Arduino-based RGB detector that will be described in the next paragraph[10].

Once the sensor's main components are defined, the data elaboration approach must be selected, depending on the receptor and the final purpose. The most suitable univariate or multivariate data elaboration approach must be identified whether qualitative or quantitative analyses are performed.

2.3 Green-PAD array for pH measurements

2.3.1 Introduction

The first pH definition goes back to 1909 by Sørensen[47] as the negative logarithm of the hydrogen ion concentration expressed in molarity. Generally, the pH measurements are performed electrochemically using glass electrode connected to a potentiostat or, more recently, using solid-state sensors such as ISFET[48]. It can be assessed that the glass electrode is undoubtedly the membrane electrode more widespread and performing than ever, being present in any chemical and biochemical research lab worldwide since its commercialization, dating back to the middle of the last century, allowing precise and accurate pH measurements over an impressive range of H^+ concentrations. As a counterbalance to this success, even after the introduction of its combined version with the reference electrode, pH electrodes are still relatively expensive, fragile, and not suitable for miniaturization, with severe limitations related to the presence of a salt bridge and a filling solution of the reference electrode, resulting in need of frequent calibrations and poisoning. It is because of these drawbacks that the most ancient strategy, employed since the Middle Ages to detect the acidity or basicity of a solution, based on dyes of lichens sorbed on paper, able to change their color as a function of pH, has continued to find significant employment and still does. The litmus test has amended since then, changing and combining different receptors, but it has its place in any laboratory, providing an instantaneous and sufficiently accurate pH value suitable for a wide range of activities. Moreover, we can define it as a colorimetric sensor. Despite that, there is still room for developing new litmus tests. Paper-based analytical devices (PADs) were first proposed by Martinez *et al.*[49] in 2007 and then widely applied for environmental analyses thanks to their simple fabrication, rapid response and environmental sustainability.[50–59] Inspired by Martinez PADs, we developed a green colorimetric sensor for the qualitative and quantitative determination of pH in real samples based on natural pigments present in aqueous extracts of red cabbage (*Brassica oleracea)* and butterfly pea flower *(Clitoria ternatea)*. These two aqueous extracts are rich in anthocyanin, a group of molecules belonging to the family of flavonoids. Anthocyanins (structure reported in Figure 7) are water-soluble pigments that may appear red, purple, blue or black depending on the pH.

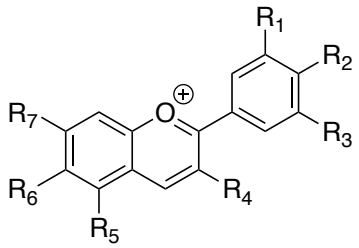

Figure 7. Molecular structure of anthocyanins

These molecules are very well known for their antioxidant properties. As mentioned before, colorimetric naked eye sensors can be used for qualitative determinations only; in this work, the green colorimetric sensors are coupled with chemometric tools to obtain a device for quantitative measurements. The sensor response used for the data analysis was the RGB values obtained from the picture of each sensor.

As for the solid support, filter paper was selected. Together, the paper and the employment of natural dyes make it possible to define the proposed sensor as green without misusing the term.

2.3.2 Material and methods

2.3.2.1 Procedures for the development of PADs modified with natural extracts

Red cabbage extract *(Brassica oleracea, RC)* and butterfly pea flower tea extract (*Clitoria ternatea,* BPF) were prepared using the following procedure. For RC, an appropriate quantity of raw vegetables (corresponding from 1 to 3 g of dry matter, considering its humidity equal to 91.3%), cut in small pieces, was placed in a beaker with 250 mL of distilled water, the suspension was kept in an ultrasonic bath for 60 minutes (keeping the temperature lower than 60°C). After cooling, the suspension was filtered, and 5 mL of concentrated hydrochloric acid was added as a stabilizer, and the total volume was repristinated with distilled water to 250 mL. For BPF, the powder (3 g) was added as received in the 250 mL of water and submitted to the same procedure described for RC. The extracts were stored in a fridge and considered stable for 3 weeks.

The green PADs were obtained by cutting a sheet of filter paper into squares of 2 cm side. Each square was placed on a clean, flat surface and drop-coated with 0.2 mL of each extract or a mix of both and allowed to air dry. The extracts' compositions are 100% RC, 100% BPF,

75% RC-25% BPF, 50% RC-50% BPF and 25%RC-75% BPF. 5 arrays were developed using these five mixtures. In the following, we refer to the different five arrays as Green PADs.

Each PAD of the array was immersed in 5 mL of the extracts at different pH values ranging from 1 to 13 for a few seconds, enough to wet the paper. The PAD was removed from the solutions and left to dry for 5 minutes. Photographs of the PADs (or direct readings of color indexes using the RGB detector) were taken. RGB triplets were collected from the pictures using GIMP software[60]. The pH values of each solution were measured using the pH meter and used as reference values.

2.3.2.2 Chemometric data treatment

Chemometric methods are often used to reduce the data's dimensionality and summarize the information in a simple graphical form, useful for interpretation[61]. As already stated, this is a property of unsupervised techniques. In this work, principal component analysis (PCA) and three-way principal component analysis (3WPCA) were used for this purpose. Conversely, the supervised technique can be employed for qualitative or quantitative detection in cases where the analytical response is not easy to be selected or when a multi-response is available. In this research, the response is the RGB triplets. Instead of reducing them to one parameter[62], partial least square regression, PLS is employed to assess the pH of the unknown solution achieved directly from the RGB reading.

In the present research, the 3WPCA was the first tool employed to understand the structure of a data set. The colors, described by RGB triplets, are considered as variables, while the five different Green PADs are the objects, and the pH values represent the conditions. The results are three loading sets and a core array describing their relationship. Each loading set can be interpreted and displayed similarly to a loading plot of the standard PCA[63]. PCA was applied to the entire data set (15 columns, 3 RGB indexes for 5 PADs, and 39 lines,13 solutions per 3 replicates). From the score plot of PCA, three pH subintervals were highlighted from the 3way analysis: from 1 to 4 (acid solutions), from 5 to 8 (neutral solutions) and from 9 to 13 (alkaline solutions).

Finally, the PLS tool was applied for each subinterval, obtaining a tailored model that correlated the RGB indexes to the pH values of the solutions in the range under investigation. Three PLS models were obtained, one for each subinterval. In this case, a training set must be selected for the subinterval for pH values from 1 to 4 is a matrix of 15

columns (3 RGB for 5 PADs) and 12 lines (4 solutions per 3 replicates); the training set for pH values from 5 to 8 and from 9 to 13 are matrixes of 15 columns per 15 lines (5 solutions per 3 replicates). The test set used for the validation is formed by three replicates of the six real samples listed above and characterized by different pH values: Schweppes tonic water, sprite, white wine vinegar and aloe vera drink as acidic samples, tap water as neutral and ammonia cleaner as alkaline. The matrixes of the samples with pHs between 1 and 4 were formed by 15 columns (3 RGB per 5 PADs) and 12 lines (4 solutions per 3 replicates, the matrix of the samples with pHs between 5 and 8 and between 9 and 13 are composed by 15 columns and 3 lines (1 solution per 3 replicates).

2.3.3 Results and discussion

2.3.3.1 Analysis of Green-PADs

The project aims to produce green, easy-to-use and disposable sensors for determining pH in real samples. To obtain green PADs, natural pigments contained in vegetables were used. Two extracts rich in anthocyanins, which are molecules able to change their color at different pH values, were selected, one from red cabbage (RC) and the other from butterfly pea flower (BPF). The extracts were used pure or mixed in different percentages. Figure 8 reports the UV-vis spectra of the extracts (pure mixtures) at neutral pH in the range of 400-800 nm.

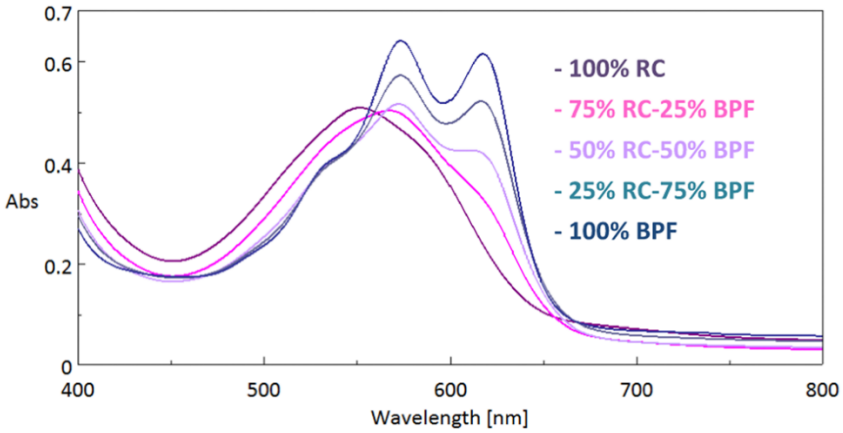

Figure 8.UV-vis spectra of the RC and BPF extracts and their mixtures at pH 7

As can be observed in Figure 8, the UV-vis spectrum of 100% RC is characterized by the broad peak at 550 nm, which is due to the presence of acylated anthocyanins (3-diglucoside-5-glucoside derivatives with various acylated groups linked to the

diglucoside)[64,65]. Increasing the concentration of BPF, a bathochromatic shift and split into two peaks at 570 and 620 nm appears. These peaks are those characteristics of ternatins and polyacylated anthocyanins responsible for the blue color of the butterfly pea flower extract[66].

The PADs modified with the pure extracts (100% RC and 100% BPF) at various pH values were compared with the colors of the aqueous extracts of red cabbage and butterfly pea flower found in literature [64–66]; the results confirmed the correct preparation and preservation of the extracts (3 weeks in the fridge at 4°C, in the dark).

A volume of 0.2mL of extracts was chosen to load the PADs since this volume is enough to cover the whole surface of the sensor. The immersion of the PADs in 5 mL of extract was excluded since the final color was not homogeneous. As a further step, it was necessary to define how to load the sample on the PADs: the drop-coating using 0.2 mL of the sample or plunging the modified PAD in 5mL of the sample per 10 s (the minimum time required to impregnate the paper). Unlike what was found for the dye impregnation step, the second strategy was the one that provided the best color uniformity.

All the steps were conducted at room temperature. Another parameter that must be defined is the time that elapses between the sample loading and the photograph (or the analysis using the RGB detector). It was found that 5 minutes is the time required to obtain homogenous colour on the surface of the PAD, avoiding the drying out of the paper.

Other typologies of paper with similar porosity were used to reduce the waiting time, but no proven advantages was observed.

It is worth underlining again that the green PADs are disposable due to the paper's main constituent and the low stability of the natural extracts. Still, for this reason, PADs must be immediately used after their preparation.

In Figure 9, the overall amazing variation of the Green-PADs arrays is shown. Very distinct colors are developed after immersion in aqueous solutions at different pH values.

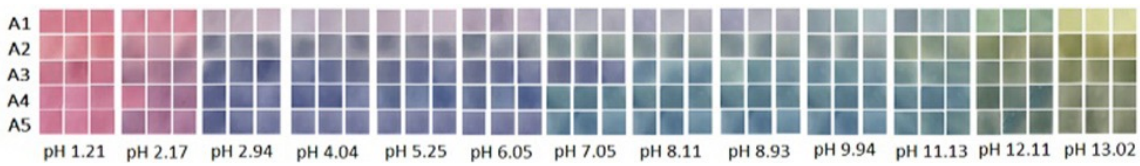

Figure 9.Green-PAD array. A5= 100%RC; A4 = 75%; A3 = 50%RC-50%BPF; A2 = 25%RC-75%BPF; A1 = 100% BPF. Three replicates for each pH.

A first native question arises: which is the best combination? Followed by another: is there a unique best combination for the entire pH range? Rather than choosing in a qualitative and possibly biased way, the multivariate approach is intended to offer an objective way to face the matter.

2.3.3.2 Dataset description and visualization

The RGB model was selected to quantify the color change with the solution's pH. There is room to discuss the pros and cons of other color space descriptors. We found that, among others, RBG is more satisfactory when a color that changes into another is observed, and not different intensity of the same color, where possibly other descriptors resulted more convenient. The golden point to acquiring good data is the strict observation of the reproducible lighting conditions, as we do see above. The open-source program GIMP[60] was used to acquire the RGB triplets for each PAD picture. The values obtained using GIMP are organized in matrixes subjected to multivariate analysis after simpler centering since the RGB indexes are intrinsically scaled from 0 to 255.

As mentioned before, the 3WPCA is the proper tool to describe simultaneously the effect of the different PADs. The objects were the five typologies of PADs, the conditions were the pH of 13 solutions, and the RGB indexes were the variables. In Table 2 the explained variance percentage after the unfolding process is reported.

Table 2. Cumulative % variance explained after unfolding

Mode	Axis 1	Axis 1 & 2
Objects, PADs	47.84	89.10
Variables, RGB	56.71	81.96
Conditions, pHs	50.41	72.47

Comparing the lowest value obtained after the unfolding with the % variance explained by the Tucker3 model (68.09%), no significant loss in information was detected when the overall color evolution was considered. The percentages of explained variance are reasonable, considering the high variability of the data set. Figure 10 shows the triplot in which the loading values of the three modes (object, conditions and variables) are reported. The core matrix and the superdiagonal core matrix are reported in table T 6.2- 1

Appendix II – Green-PAD array for pH measurements (3-Way PCA matrixes, loadings of PCA Dataset description and visualization and ANOVA studies).

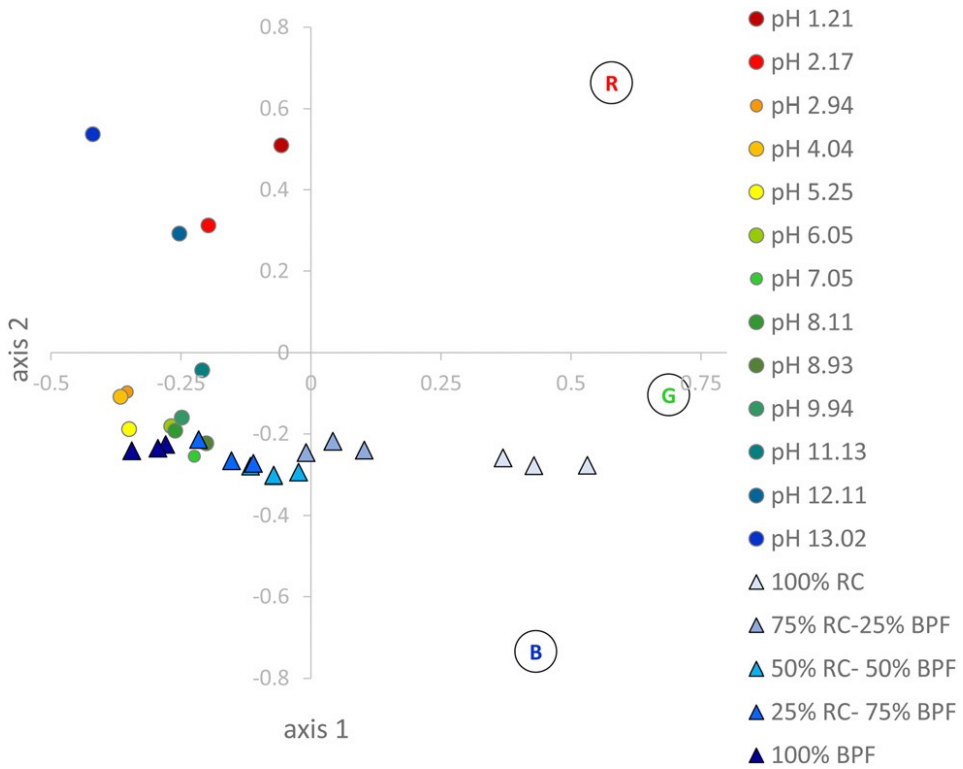

Figure 10.3WPCA applied to the Green-PAD array: triplot of loadings value. A1 = 100%RC; A2 = 75%RC-25%BPF; A3 = 50%-50%BPF; A4 = 25%RC-75%BPF; A5 = 100% BPF. Three replicates for each pH.

The objects, the PADs, show loading values arranged along the horizontal axis (axis 1) explained by the different brightness, which increases with the decrease in the percentage of BPF and the corresponding increase in the % of RC. A confirmation of this behavior is given by the RGB values; in fact, the loadings of the variables are disposed only in the positive section of axis 1, meaning that the higher the values are, the higher the brightness is (light colors are characterized by high RGB values). The loadings of the pH values are described by axis 2, as also the RGB change does.

This assumption is confirmed by the loadings of the variables, i.e., the R, G, and B indexes: they all have a positive value on the axis-1, which indicates that they all increase, moving from the left to the right of the plot, leading to brighter Green-PAD colors when % RC is higher. Conversely, on the axis-2, R has a positive loading value. In contrast, G and B have negative values, suggesting that by the change of the solution pH, the R index increases while the G and B indexes decrease, which corresponds to the numerical effect of the

significant glaring color variations for the PADs immersed in solutions at the extremes of the pH range.

From Figure 10, pH values lower than 4 and higher than 9 are easily recognizable and separated along the axe; conversely, pH values from 5 to 8 are less recognizable as we expected since the similar color of the PADs in this pH range.

As for this first overlook, the BPF high-content PADs seem more promising, answering the first question. For a more detailed description, let us go on with the analysis.

PCA was applied to the whole data set to visualize the color transition and identify the main clusters, knowing that the part of information related to different Green PADs will be compressed.

The model was obtained considering only the first and the second components (81.51% explained variance). In Figure 11 the score plot is reported. (Loadings are reported in Appendix II – Green-PAD array for pH measurements (3-Way PCA matrixes, loadings of PCA Dataset description and visualization.

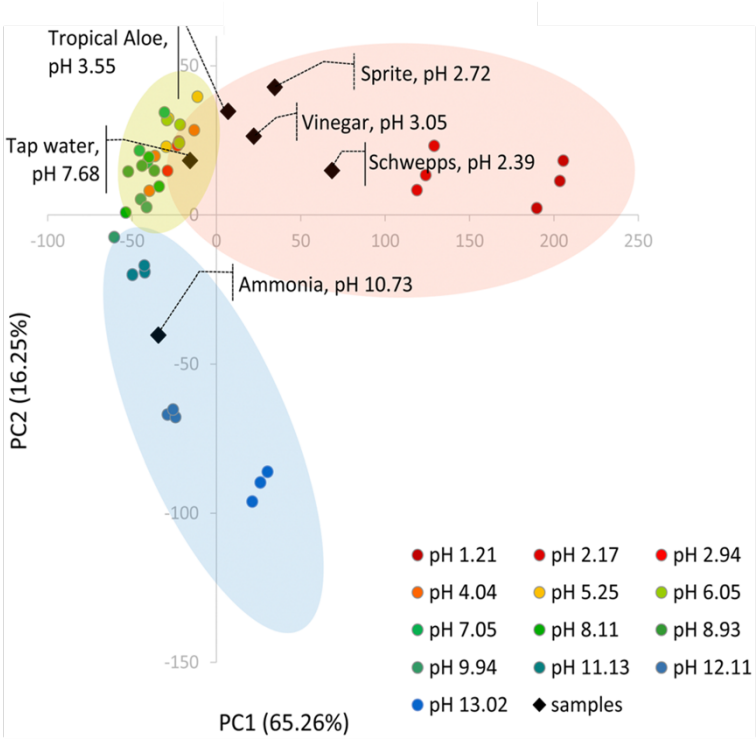

Figure 11.The score plot of the PCA model on the first two principal components, built on the training set. The ellipses are designed only to visualize the pH subintervals better.

In Figure 11 three regions can be observed (delimited by ellipses added by hand as a simplification to highlight the different pH subintervals better) that partially overlap: the first cluster (red ellipsoid) for samples at pH lower than five separated along the PC1 axis;

second cluster (light green ellipsoid) is highlighted for samples at pH between 5 and 8 that are mainly separated along PC2 axis, and the score values decrease with the increasing pH; the third cluster (blue ellipsoid) is for samples at pH between 9 and 13, in this case samples are separated along both PC1 and PC2, with PC1 score values increase while PC2 score values decrease with pH increase.

The RGB triplets of the test set, based on Green-PADs colors registered after contact with the real samples described above, have been projected into this PCA model. Even if PCA is not a classification technique, all the samples collocated in the correct corresponding cluster, as seen by observing the black diamonds of Figure 11b, and we consider it a sort of raw "concept validation", see below.

More interestingly, the scores plot allows us to select the range for a quantitative approach to pH assessment. Indeed, the three clusters area suggests the subintervals for PLS studies, as described below.

2.3.3.3 pH predicted by PLS

Three PLS models are developed, named A for the acid pH range, N for the neutral pH range, and B for the basic pH range.

The RGB triplets make the training set for the five Green-PADs, already submitted to the unsupervised models, each limited within the above pH intervals. They constitute the X matrix of the independent variables or predictors. The pH values, which in PCA analysis were only the labels for the object's identification and not involved in the algorithm calculation, are now the dependent variable (Y). The issue is finding how to describe Y's dependence on X.

The PLS model is built by CAT[32], and the number of latent variables is selected to avoid underfitting and overfitting. The models are subjected to a first validation performed by the PLS tool that divides the samples between a training set and a test set. Table 3 reports the statistics relative to this first step: the number of components used to build the PLS models, the % explained variance in cross-validation (CV) and the root mean square error in CV (RMSECV), model performances are reported in Figure F 6.2- 2 in Appendix II – Green-PAD array for pH measurements (3-Way PCA matrixes, loadings of PCA Dataset description and visualization and ANOVA studies).

Table 3. Number of components, % explained variance in cross-validation (%Exp.Var.CV) and root mean square error in CV (RMSECV) for PLS models.

Model	n. components	%Exp.Var. CV	RMSECV
A	5	90.30	0.3287
N	5	90.81	0.3326
B	4	93.68	0.3674

The lowest RMSECV is obtained with 5 components for models A and N, while for B is obtained with 4. The explained variance is higher than 90% in all cases. Figure 12 shows the plots of experimental vs. fitted values for each model; a pretty good agreement can be observed between the experimental and fitted data for all the models.

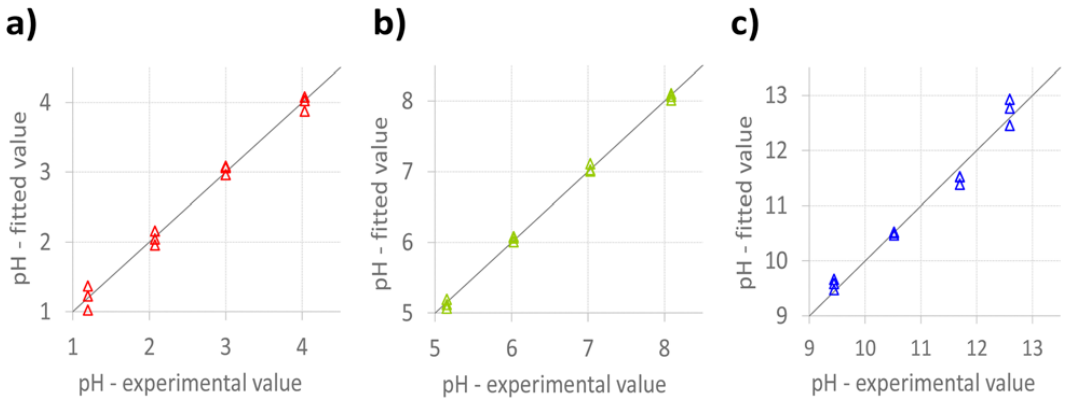

Figure 12. Experimental vs fitted plot for a) model A, b) model N and c) model B . RGB indexes are obtained from the pictures of the sensor using GIMP software.

The models were finally validated by projecting the external data set, employing the RGB obtained by the measurements of the real samples into the most suitable PLS model, previously identified in Figure 11. In Table 4, the pH values of the real samples measured with the glassy carbon (pH_{GE}), Litmus paper (pH_{LP}) and Green-PADs ($pH_{GP(1)}$) are reported. The pH color chart and image of the Litmus paper after immersion in each sample are reported in Figure 13.

Table 4. pH of real samples: comparison between the values measured with the pH meter, with the Litmus paper and with the Green-PAD array PLS models. Data are reported as mean value of three replicate, in brackets are reported the standard deviation on the last digit.

Sample	pH_{GE}	pH_{LP}	$pH_{GP(1)}$	RE%
Schweppes	2.39	2-3	2.4(1)	0.4
Sprite	2.72	3	2.9(3)	6.61
White wine vinegar	3.05	3-4	2.8(2)	8.2
Tropical aloe vera	3.55	4	3.5(4)	1.4
Tap water	7.68	8	7.3(4)	4.2
Ammonia cleaner	10.73	10-11	10.7(1)	0.3

pH_{GE}= value obtained by glass electrode; pH_{LP}= value obtained by the Litmus paper; $pH_{GP(1)}$ value obtained by the Green-PADs. Re% = relative error

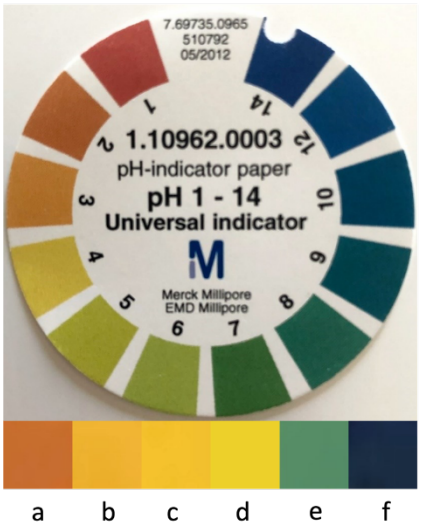

Figure 13. pH color chart of the commercial Litmus paper and color of the Litmus paper after contact with the real samples: a) Schweppes, b) sprite, c) White wine vinegar, d) Tropical aloe vera, e) Tap water, f) ammonia cleaner.

As can be observed from the values reported in Table 4, there is a pretty good agreement among all the pH values despite the wild interval of the litmus test and the limited precision of $pH_{PAD(1)}$ calculated by the models.

The relative high uncertainty of $pH_{PAD(1)}$ can be caused by the RGB acquisition, such as different settings of the photo camera, the focus, and the environmental brightness, despite the efforts put in place to limit these drawbacks. To highlight this aspect, we decided to perform some measurements using an RGB detector prototype developed by Eng. Dario Pistoia. The device comprises a 4-led color sensor, and it is based on an Arduino hardware platform. The same experiments previously described were carried out by

registering the RGB indexes using the above detector to submit the dataset to PLS, producing three models at the three pH subintervals. In Table 5, the statistics, as before referred to the internal test set, are reported. Model performances are reported in F 6.2-3 in Appendix II – Green-PAD array for pH measurements (3-Way PCA matrixes, loadings of PCA Dataset description and visualization and ANOVA studies).

Table 5. Number of components, % explained variance in cross-validation (%Exp.Var.CV), and root mean square error in CV (EMSECV) for PLS models using the RGB detector.

Model	n. components	%Exp.Var.CV	RMSECV
A	3	99.82	0.0537
N	5	92.08	0.2892
B	5	98.65	0.1708

The minimum RMSECV was obtained using 5 principal components for models B and N, while for A, with 3. The explained variance is very high, higher than before, and more than 92% in all three cases. The RMSECV values are lower than those obtained using the RGB of the pictures of the PADs as signals, confirming that the RGB detector is more precise. In Figure 14 are reported the PLS models (pH experimental vs pH fitted) for A, N and B measured using the RGB detector are reported.

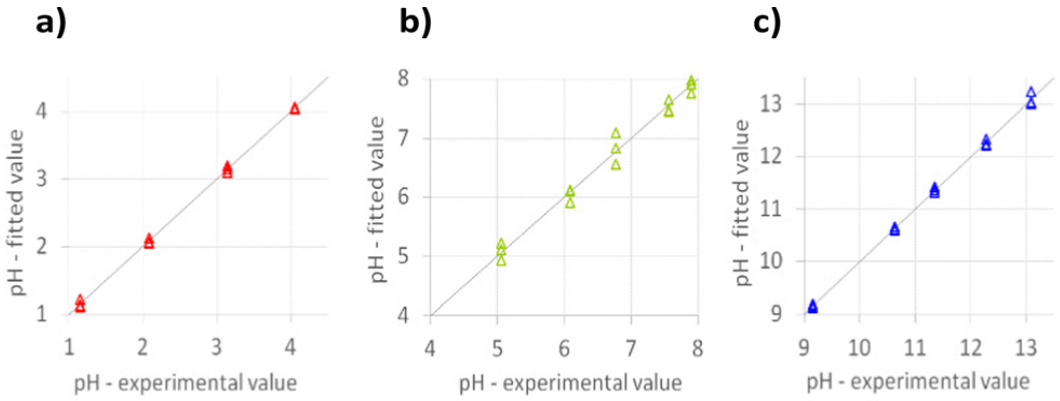

Figure 14.Experimental vs fitted plot for a) model A, b) model N and c) model B. The RGB detector acquires RGB indexes.

The PLS models were validated with the external data set as above. The pH values of the real samples predicted by the PLS models are reported in Table 6. To distinguish the pH obtained by this new measurement strategy, the calculated values are indicated as $pH_{GP(2)}$ while the previous $pH_{GP(1)}$.

Table 6. pH of real samples: comparison between the values measured using a pH meter, estimated by Litmus paper and those calculated by the Green-PAD array-PLS models. RGB indexes are acquired by the RGB detector. Data are reported as the mean value of three replicates; in brackets the standard deviation on the last digit.

Sample	pH_{GE}	pH_{LP}	$pH_{GP(2)}$	RE%
Schweppes	2.39	2-3	2.35(3)	1.7
Sprite	2.72	3	2.84(1)	4.2
White wine vinegar	3.05	3-4	3.03(2)	0.6
Tropical aloe vera	3.55	4	3.51(1)	1.2
Tap water	7.68	8	7.77(6)	1.2
Ammonia cleaner	10.73	10-11	10.80(3)	0.7

pH_{GE}= value obtained by glass electrode; pH_{LP}= value obtained by the Litmus paper; $pH_{GP(2)}$ value obtained by the Green-PADs with . Re% = relative error

The data obtained in GP(2) mode are more precise than those obtained from the RGB data of digital images, GP(1) mode. We can also claim that precision is not so different from that achievable by a glass electrode when a current lab electrode is employed. The above data demonstrate that the RGB detector guarantees measurements free from uncontrollable operating conditions and with low background noise. Thinking of a digital implementation of such a device, GP(2) mode could be the gold choice.

More importantly, applying the "two-way ANOVA without replicates" to the three data sets, pH_{GE}, $pH_{GP(1)}$ and $pH_{GP(2)}$, so comparing true data, pH_{GE}, with calculated ones, the variability among the columns is not significant, meaning that the pH values, within each row, are the same, becoming a further statistical trueness assessment, the results are reported in Appendix II – Green-PAD array for pH measurements (3-Way PCA matrixes, loadings of PCA Dataset description and visualization and ANOVA studies).

2.3.4 Conclusions

In this work, a simple, easy-to-use, low-cost, and completely green paper-based array for pH measurements was proposed. The array was prepared using filter paper as solid support and aqueous extracts of vegetables, allowing rapid and economical preparation. The natural extracts of red cabbage (*Brassica oleracea*) and butterfly pea flower (*Clitoria ternatea*) are sensitive to the pH of the environment, which causes them color change; for this reason, the extracts were used as dyes to modify the paper surface.

Multi-technique chemometric models were developed for calculating pH values, starting from the RGB triplet of each sensing PAD. The RGB indexes were acquired by photographing the PADs or using a RGB detector. Unsupervised techniques (3WPCA and PCA) were first applied to visualize the overall data set. This approach allowed the identification of three pH subintervals, thus developing tailored PLS models. Three PLS models (A for pHs between 1 and 4, N for pHs between 5 and 8and B for pHs from 9 to 13) were developed and validated using real samples at different pH values as a test set. The results obtained with the Green-PAD array-PLS were compared to those obtained with the pHmeter and with the Litmus paper, showing a pretty good agreement. As expected, better data were obtained employing the RGB detector since the measurements are more reproducible. In the case of unknown samples, RGB indexes were projected in the PCA model to identify the most suitable PLS model to calculate the pH values.

2.4 TazoC-PADs for Pd(II) detection

2.4.1 Introduction

The heavy metal ions content in the environment, especially in natural waters, has been growing with the increase of human and industry activities such as the plating and electroplating manufacturing, mining, tanning, textile and rayon industries, batteries, bioreactors, metal smelting, petrochemicals and paper manufacturing[67]. Heavy metals are non-biodegradable; some can bioaccumulate in living organisms and affect various microorganisms because of their biomagnification[67–69]. Platinum-group metals (palladium, platinum, rhodium, ruthenium, osmium and iridium) are naturally found in the Earth's crust[70] but are also used in industrial processes because of their peculiar physical-chemical properties[70]. Despite the advantages of using platinum-group metals in technologies, the significant increase in the concentration of these metals in the environment may affect human health[70]. The World Health Organization (WHO) has provided little information about the impact of these metals on the environment, and these studies concern only platinum and palladium[71–73].

The most employed analytical methods for palladium determination are atomic absorption spectrometry (AAS), inductively coupled plasma-mass spectrometry (ICP-MS), inductively coupled plasma-atomic emission spectrometry (ICP-AES) and neutron activation analysis (NAA). These methods present high sensitivity, but the instruments and the analysis are costly, need trained operators, and the sample preparation is time-consuming since it very often requires separation and preconcentration steps[74,75].

In this work, a Paper-based Analytical Device (PAD) was developed for the determination of Pd(II) in water solutions. PAD sensing devices exploit the capillary properties of paper provided by the cellulosic fiber network, eliminating the necessity of pumping methods. In addition, the papers' availability, biodegradability, low price, and ease of surface functionalization make them an attractive substrate for sensors' development[76–78].

The device was developed by modifying the surface of filter paper with the diazo dye TazoC (disodium 2-[(1H-5-tetrazolyl)azo]-1,8-dihydroxynaphtalene-3,6 disulphonate), the molecular structure is reported in Figure 15.

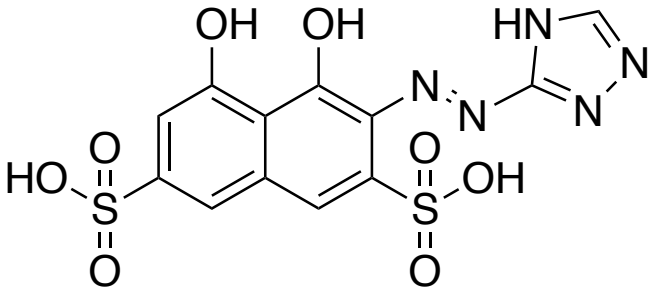

Figure 15. TazoC (disodium 2-[(1H-5-tetrazolyl)azo]-1,8-dihydroxynaphtalene-3,6 disulphonate) molecular structure

TazoC is not commercially available, but it has already been studied as a complexing ligand for several metal ions; in particular, it forms a stable 1:1 complex with Pd(II) even in strongly acid solutions (pH=2); the complex configuration is reported in Figure 16[79–81].

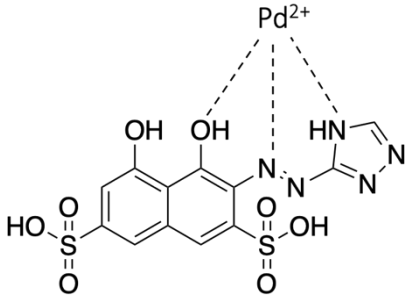

Figure 16. Molecular structure of 1:1 TazoC:Pd(II) complex[82]

The complex Pd(II)/TazoC is purple-blue, very different from the free ligand's red-orange: this color change is the propriety used in optical sensors development. At pH higher than 2 the ligand can complex other cations such as Cu(II) and Ni(II) in addition to Pd(II). A multivariate approach was necessary to quantify Pd(II) in the presence of interferent species. Partial Least Square regression was used as a multivariate tool to relate the UV-vis spectra of the solid device to the concentration of Pd(II) in solution[10,83–85].

2.4.2 Material and methods

2.4.2.1 Ligand and sensor preparation

TazoC was synthesized and purified according to previously described procedures[86]; its empirical formula and molecular weight (536.34 g/mol) were confirmed by elemental analysis. A 1 mM ligand stock solution was prepared by dissolving the weighted solid in ultrapure water. Tap water samples were obtained from the drinking water supply of Pavia, Italy. Samples were collected from the lab's sink (Department of Chemistry, University of

Pavia, Italy) after flushing cold water for 15 min; they were subsequently acidified to pH 2 with HCl.

The cellulose filter paper was cut into 2 cm-sided squares using scissors. Each square, placed on a flat and clean surface, was drop-coated with 0.05 mL of 1 mM TazoC solution and left to air dry. The so-obtained PADs were immersed in 2.5 mL of aqueous metal-ion solution and kept under gentle stirring on a reciprocating shaker for 30 min (the time required to obtain a homogeneous and stable coloration of the PAD). The PADs were removed from the solution using plastic tweezers and left to air dry for 2-3 minutes on a flat and clean surface (the temperature fluctuation affects the PAD's spectrum, so the measurements were performed at 25°C setting the air conditioning at the value and using the PADs not completely dry but slightly moistened). Subsequently, the PADs were inserted into the sample holder using plastic tweezers for the UV-vis analysis. The spectrum was registered in the wavelength range from 300 to 800 nm (bandwidth 0.2nm, scan rate200nm/min) against a blank PAD wetted only with the buffer solution.

2.4.2.2 Chemometric data treatment

Partial Least Square regression (PLS) was used for the chemometric data treatment to correlate the information contained in the UV-vis spectra to the concentration of Pd(II) in the solution. The PLS models were built by selecting a suitable data set (training set) obtained measuring Pd(II) solutions at different concentrations to cover the entire experimental domain homogeneously; three PLS models were developed at three different pH values: pH 2, pH 4 and pH 5.5. The training set used for each PLS model comprised the data of three replicates of 8-point calibrations (24 rows and 103 columns, eight concentrations and three replicates each and the absorbance values per 103 wavelengths). Each PLS model was tested by a cross-validation procedure on the training set and then with an external test set. The test set matrix comprised 9 rows (3 concentrations per 3 replicates) and 103 columns (absorbance values for 103 wavelengths).

The sensing device was also tested with mixtures at different concentrations of Pd(II) and Cu(II) at pH 4 and Pd(II), Cu(II) and Ni(II) at pH 5.5. Another training set was prepared using tap water spiked with different concentrations of Pd(II); from the concentrations predicted by the model, the recovery percentages were calculated.

All the data used for PLS models were only centered and not scaled, as usually done with the spectroscopic data set, and analyzed using CAT[32]. The tables reporting the metal-ion concentration in each sample are in Appendix III – PLS data (Training set, Test set compositions, and model performances) of the TazoC-PADs for Pd(II) determination (paragraph 2.4).

2.4.3 Results and discussion

The PADs were obtained by cutting a sheet of filter paper into two cm-sided squares and using TazoC as a chromophore receptor. The receptor forms a purple-blue-colored stable 1:1 complex with Pd(II) also in very acidic media; this behavior was exploited to develop the present devices. Until pH 2, only Pd(II) is complexed by TazoC, while Cu(II) and Ni(II) are not, as can be observed by the UV-vis spectra in Figure 17. It means that competition by other metal ions, complexed by TazoC at higher pH values, is not exerted in the acidic region and can be exploited for selectivity purposes.

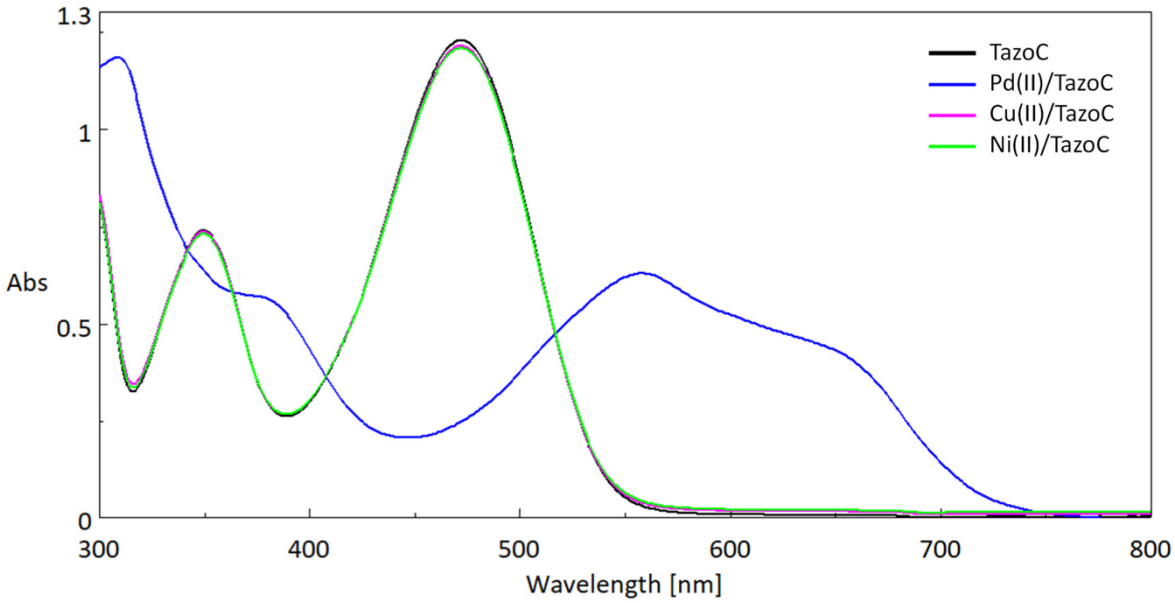

Figure 17.UV-vis spectra (absorbance (Abs, a.u.) vs Wavelength (nm)) in aqueous solutions at pH2 (HCl 0.01M) of 75 μM TazoC (black line); 75 μM TazoC and 75 μM Pd(II) (blu line); 75 μM TazoC and 75 μM Cu(II) (pink line); 75 μM TazoC and75 μM v Ni(II) (green line).

As can be observed in Figure 17, the typical peak of the free ligand at about 475 nm (ε = 17.333 cm^{-1} M^{-1}) is in agreement with the data previously reported [80], and the spectrum does not change if other cations than Pd(II) are added at pH 2 (they all overlap to the spectrum of the free ligand), at least until 1:1 ratio. The absorption peak of the complex with palladium(II) undergoes a red shift compared to that of the free ligand. Moreover, the

peak of the free ligand disappears when an equimolar amount of metal ion is added, as expected by the prevalent 1:1 stoichiometry of the TazoC complexes[80].

Figure 18 reports the three different UV-vis spectra obtained when a TazoC solution was added with an equimolar amount of Pd(II), Cu(II) and Ni(II) at pH 4 and 5.5

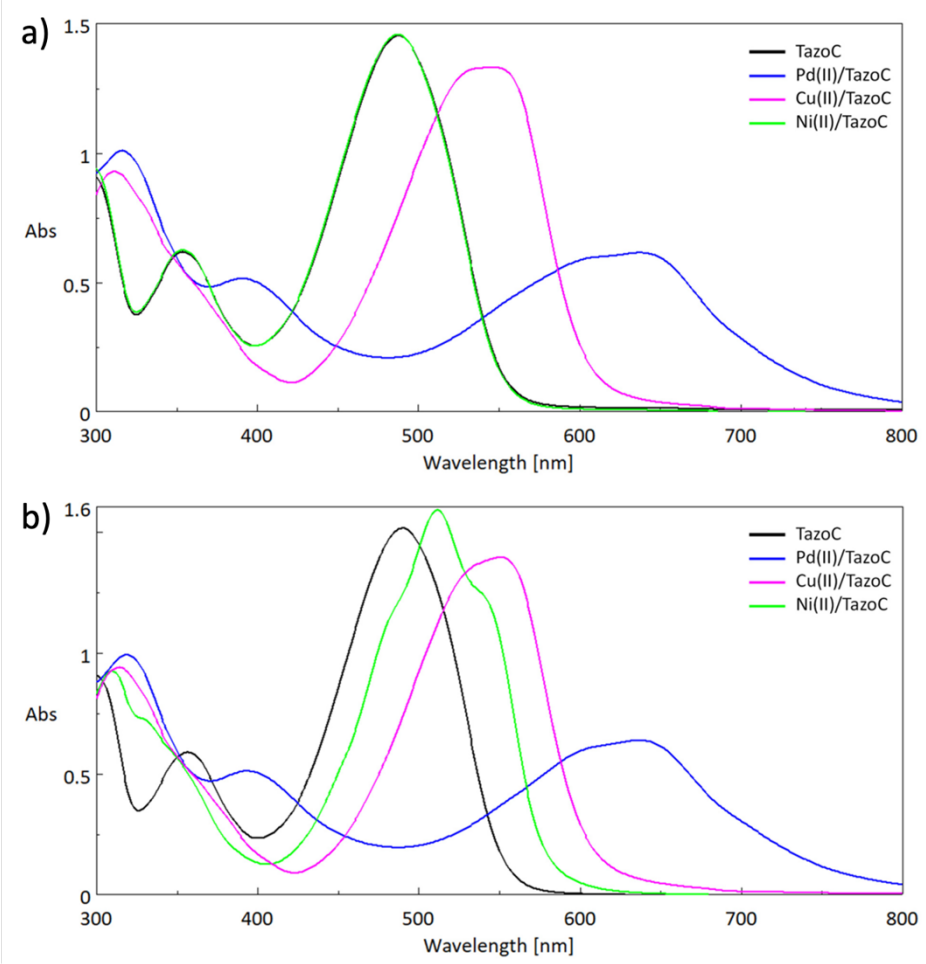

Figure 18. UV-vis spectra (absorbance (Abs, a.u.) vs Wavelength (nm)) in aqueous solutions of 75 μM TazoC (black line); 75 μM TazoC and 75 μM Pd(II) (blu line); 75 μM TazoC and 75 μM Cu(II) (pink line); 75 μM TazoC and75 μM v Ni(II) (green line), (a) acetate buffer pH 4, (b) acetate buffer pH 5.5.

From these spectra, where only an effect of one metal at a time at an equimolar amount with respect to the ligand is shown, the interference of Cu(II) and both Cu(II) and Ni(II) increasing the pH is expected.

As described elsewhere, filter paper cut in squares was loaded with 0.05 mL of 1mM TazoC water solution to build the sensor since that volume was enough to cover the PAD's surface entirely without obtaining overflow of the ligand. Some trials were performed by plunging the paper square in 2.5 mL of 1mM TazoC solution, but lower sorption kinetics and inhomogeneity of the PADS's color were verified.

Moreover, deciding the modality with which the sample was loaded on the sensing device was necessary. The drop coating using 0.5 mL and the immersion in 2.5 mL of sample were tried. The best results were obtained with the second strategy adopted for all the experiments, as verified in the previous pH assessment sensor. The time required to obtain uniform PAD color, avoiding the leaching of the ligand, was about 30 minutes, leaving the samples gently shaking in a closed container on a reciprocating shaker.

The PADs are disposable devices and must be used immediately after their preparation. If stored in water for over 1 hour, the chromophore or its complexes may desorb from the paper.

In Figure 19, TazoC-PADs are reported after reaction with the metal ions solutions at different concentrations and pHs. Figure 20 shows the corresponding UV-vis spectra of the PADs collected as described above.

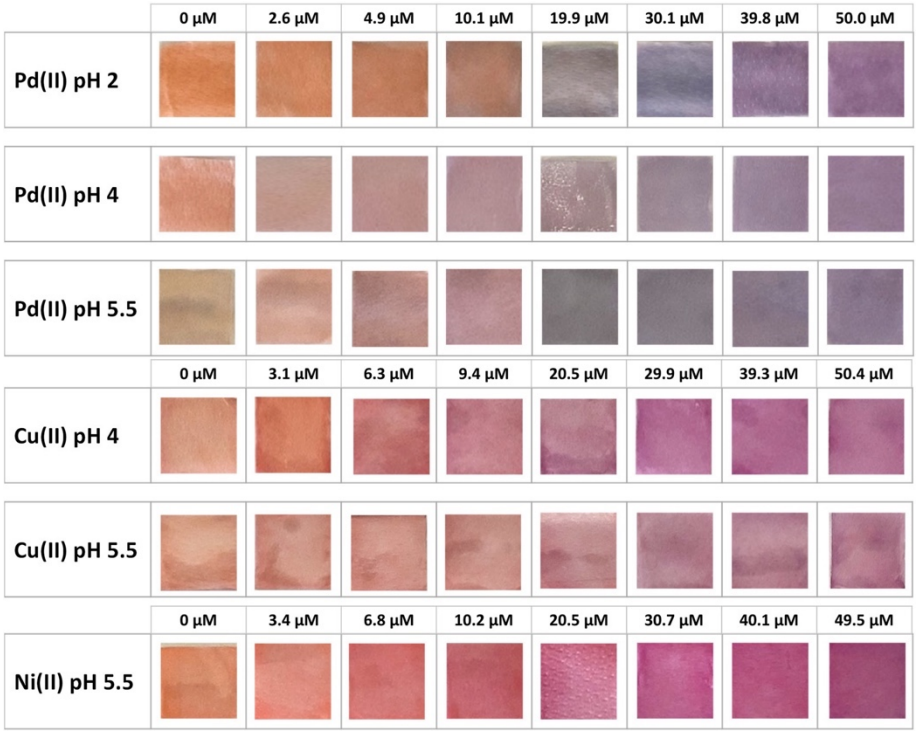

Figure 19. TazoC-PADs after immersion in Pd(II), Cu(II) and Ni(II) solutions at different concentrations and pHs.

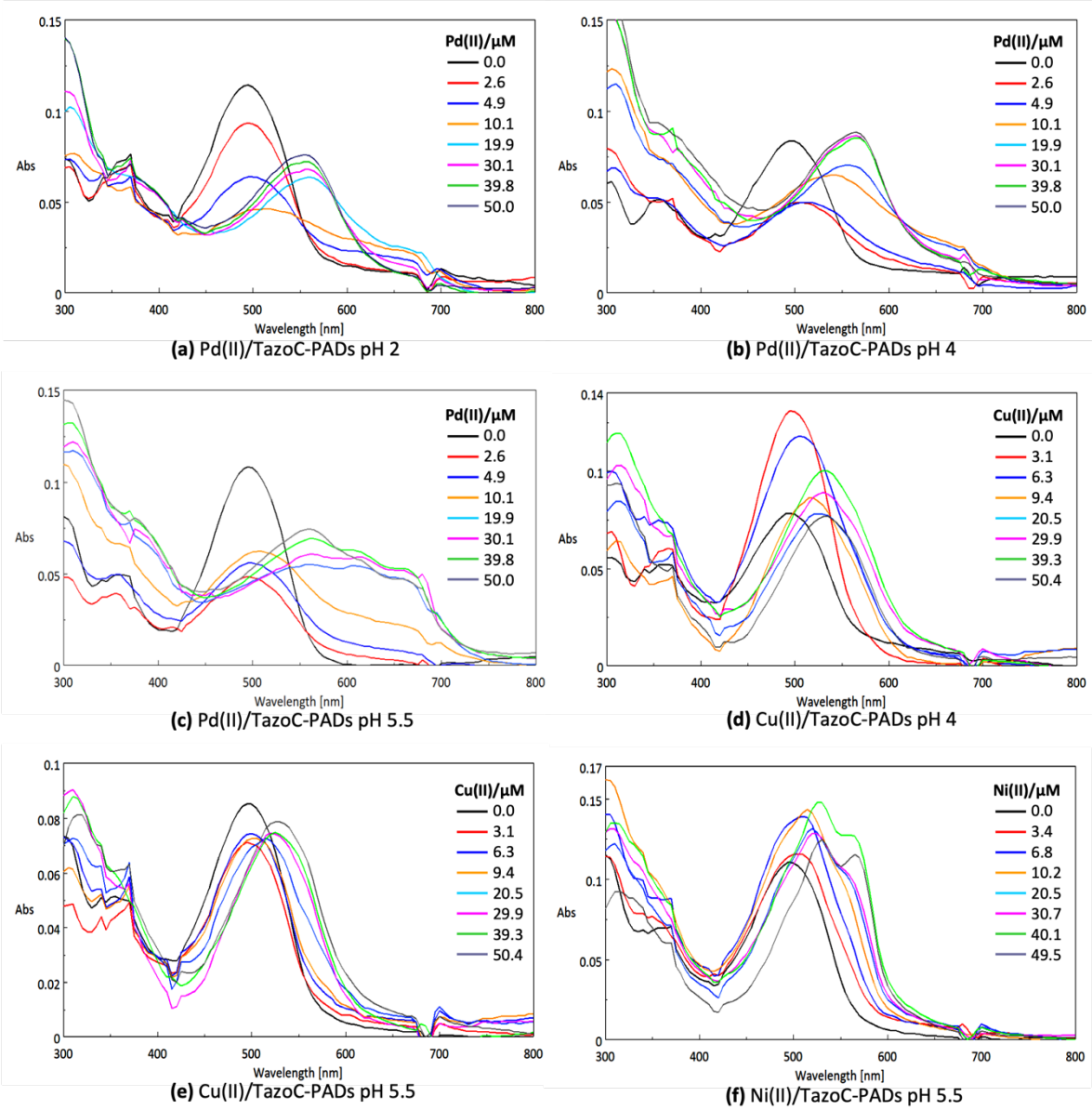

Figure 20. Spectra (Absorbance (Abs, a.u.) vs Wavelength (nm)) of TazoC-PADs after immersion in Pd(II), Cu(II) and Ni(II) solutions at different concentrations and pHs. The images of the PADs are shown in Figure 37.

It is evident that PAD spectra exhibit more disturbed signals when compared with those in aqueous solution, but the shapes of the peaks and the position are similar; this behavior confirms that the paper does not interfere with the TazoC in the formation of the complexes with metals and this is the main reason for employing Partial Least Square regression (PLS) instead of classical univariate analysis for metal quantification. Using the entire spectrum instead of the absorbance at the complex maximum is very usefull expecially when we deal with a very disturbed spectrum.

The first PLS model was built for the system Pd(II)/TazoC-PADs in aqueous solutions at pH 2 (HCl 0.01M).

This model was built using a training set composed of three replicates of an 8-point calibration with Pd(II) concentrations ranging from 2.6 to 50 μM.

The best model was considered that built with 5 latent variables that ensure the 98.61 % of explained variance in Cross-Validation (% Exp.Var.CV), a global Root Means Square Error in CV (RMSECV) 0f 2.05 μM and 1.86 μM of Root Mean Square Error in Prediction (RMSEP), using as a guideline the Figure 21.

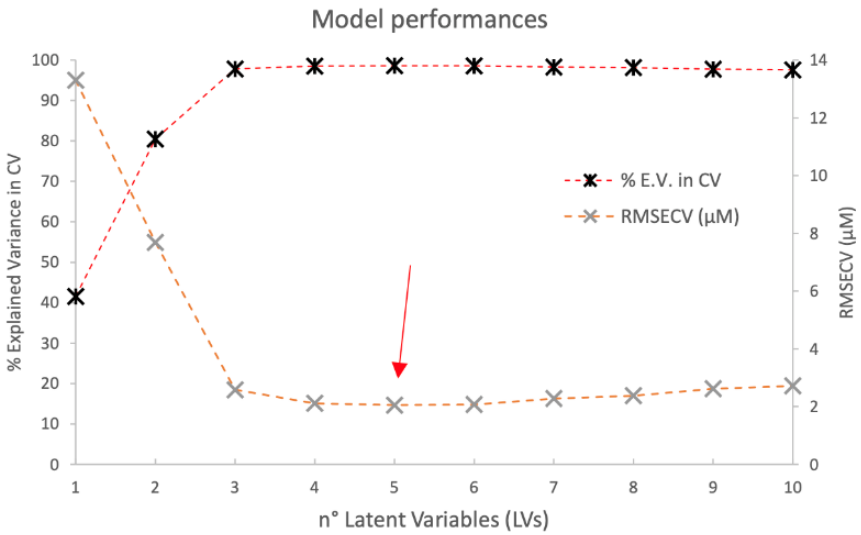

Figure 21.PLS model Pd(II)/TazoC.PADs pH 2: Model performances

An external data set was then used for further validation, obtained with three replicates of the measurements performed in solutions at 7.5, 25.2 and 42.5 μM.

In Figure 22(a), the Experimental vs. Fitted values for the training set (burgundy dots) and test set (blue dots) are reported: the data sets are distributed along the straight line Y = X without any trend; in Figure 22(b) the residuals plot is shown, and the residuals resulted randomly distributed around the 0 value (between -3 and 3).

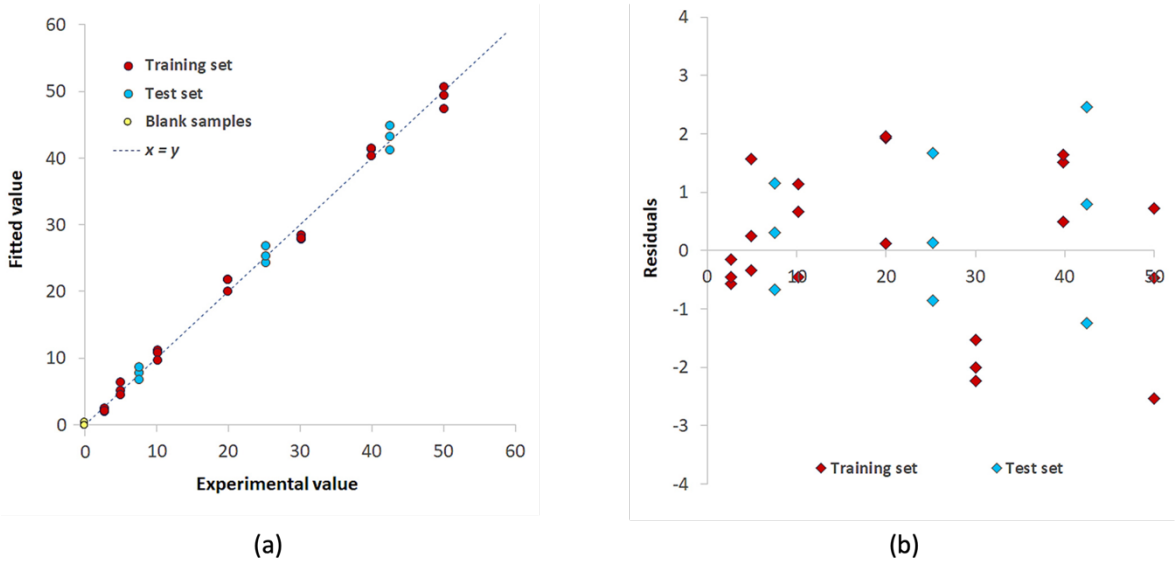

Figure 22. PLS model for Pd(II)/TazoC-PADs at pH=2 (a) Experimental vs Fitted values plot for the training set (burgundy dots) and test set (blue dots) and blank samples (yellow dots); (b) residuals for the training set (burgundy dots) and test set (blue dots).

In any analytical method, figures of merits regarding LOD and LOQ are fundamental.

As discussed in the PLS regression strategy, this issue is difficult to resolve. We decided to adopt a commonsense rule that, even if not rigorous, has a practical sense. The spectra of 10 blank samples (TazoC-PADs contacted with the solutions at pH 2 without Pd(II), see yellow dots in Figure 22(a)) are projected into the model, and the concentrations predicted. The limit of detection (LOD) and the limit of quantification (LOQ) were computed as 3.3 and 10 times, respectively, the standard deviation of the predicted blank concentrations as reported in eq.3 and eq. 5 in section 1.4.5. Limit of detection (LOD) and limit of quantification (LOQ).

PLS models were also obtained for Pd(II) concentration measurements at pH 4 and 5.5, following all the steps described for pH=2, using 8 latent variables for each model, followed by an external validation data set. For the sake of simplicity, in the following, we reported only the figures of Experimental vs Fitted values and that of residuals, reported in Figure 23. The data set, the model performances and residues are found in Appendix III – PLS data (Training set, Test set compositions, and model performances) of the TazoC-PADs for Pd(II) determination (paragraph 2.4); see tables T 6.3- 1 for pH 2; T 6.3- 2 for pH 4; T 6.3- 3 for pH 5.5 and the figures F 6.3- 1 for pH 4 and F 6.3- 2 for pH 5.

Also, LOD and LOQ were calculated for the PLS models at pH 4 and 5.5 using the same strategy used for data at pH 2. Table 7 summarizes the parameters of the PLS models in

Cross-Validation, in prediction according to the validation with the internal data seta, the LOD, and the LOQ for each model.

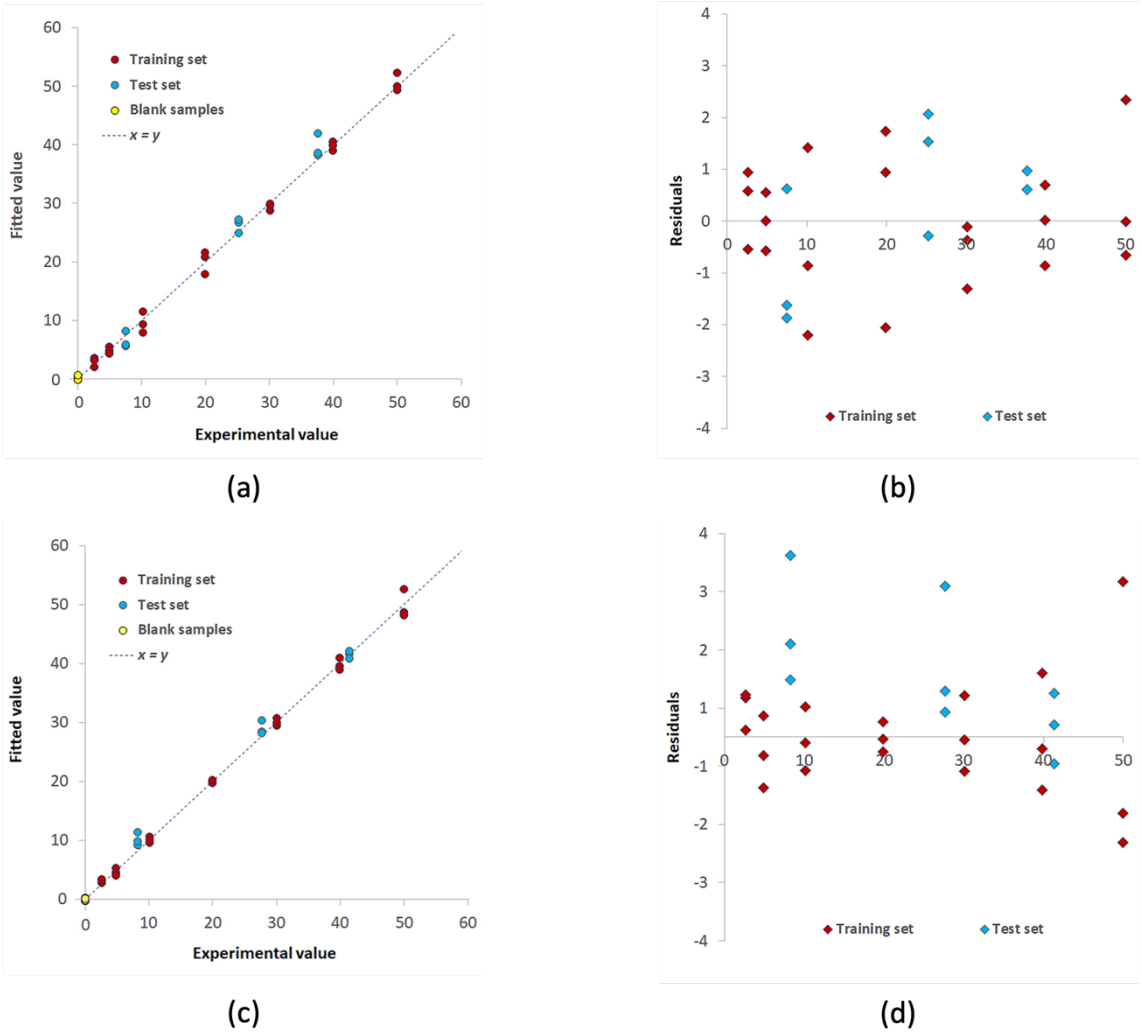

Figure 23. PLS models for Pd(II)/TazoC-PADs at pH 4 and Pd(II)/TazoC-PADs at pH 5.5 (a,c) Experimental vs Fitted values for the training set (burgundy dots), test set (blue dots) and blank samples (yellow dots); (b,d) residuals for the training set (burgundy dots) and test set (blue dots).

Table 7. Number of latent variables (LVs), % explained variance in cross-validation (%Exp.var.CV), Root Mean Square Error in CV (RMSECV), the correlation coefficient of the regression (r^2), the limit of detection (LOD) and the limit of quantification (LOQ) for the PLS model in figure 39 and 40

	Pd(II)/TazoC-PADs pH 2	**Pd(II)/TazoC-PADs pH 4**	**Pd(II)/TazoC-PADs pH 5.5**
LVs	5	8	8
%Exp.Var.CV	98.61	98.92	98.02
RMSECV (μM)	2.05	3.08	2.45
r^2 model	0.994	0.996	0.997
RMSEP (μM)	1.86	1.92	1.55
r^2 prediction	0.994	0.991	0.995
LOD (μM)	0.8	0.8	0.7
LOQ (μM)	2.3	2.4	2.0

Also, the PLS models at pH 4 and 5.5 are satisfactory, performing like those already commented for determination at pH=2.

According to the WHO threshold limit for Pd content in drug chemicals (from 47.0 μM to 94.0 μM, which means from 5 mg/L to 10 mg/L)[87] and the United Nations Food and Agriculture Organization (FAO) recommended maximum level for irrigation waters of 47.0 μM (5mg/L)[88], the lowest quantifiable Pd(II) concentration obtainable with the proposed PADs meet the requirements of both WHO and FAO for palladium(II) detection in that matrixes.

Focusing on Pd(II) determination, we choose to consider both Cu(II) and Ni(II) as interferents. Alternatively, we can also view their determination in a multi-calibration strategy, but it was out of our purposes.

As expected, at pH=4, it is impossible to ignore copper if present; otherwise, it happens as described below. If the PLS model for Pd(II)/TazoC-PADs at pH 4 is used to quantify the analyte in solutions containing Pd(II)/Cu(II) at different concentrations, the PLS model incorrectly predicted the concentration of Pd(II). In Figure 24, the PLS model for Pd(II)/TazoC-PADs at pH 4 (burgundy dots) and data predicted by the model for the mixture used as a test set (blue dots) are reported.

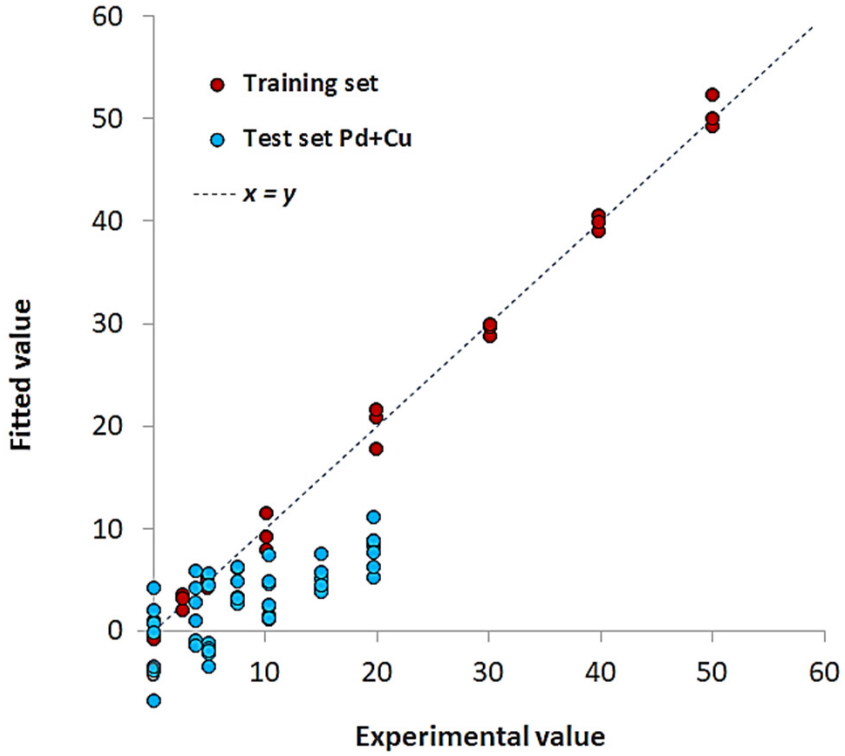

Figure 24.PLS model for Pd(II)/TazoC-PADs at pH 4 Experimental value vs Fitted values plot for the training set (burgundy dots) and Pd(II)/Cu(II) mixtures as test set samples (blue dots)

The strategy to overcome this issue is to build PLS models using as training sets the measurements performed in the same matrix of the samples, which means that tailored PLS models must be developed for solutions containing interferent species and for tap water samples.

In Figure 25 and Table 8, the PLS plots and parameters of the models named Pd(II)+Cu(II)/TazoC-PADs pH 4 and Pd(II)+Cu(II)+Ni(II)/TazoC-PADs pH 5.5 are reported. The mixtures are prepared so that concentrations of the metal cations are independent and different, both for the training and test sets. It is fundamental to vary interferent concentrations, even if they are limited to equimolar addition with respect to Pd(II). The tables reporting the metal-ion concentrations (T 6.3- 4 for Pd(II)+Cu(II) pH 4; T 6.3- 5 for Pd(II)+Cu(II)+Ni(II) pH 5.5) in each sample and the performance graph (F 6.3- 3 for Pd(II)+Cu(II) pH 4; F 6.3- 4 for Pd(II)+Cu(II)+Ni(II) pH 5.5)of the sensor are reported in the Appendix III – PLS data (Training set, Test set compositions, and model performances) of the TazoC-PADs for Pd(II) determination (paragraph 2.4)

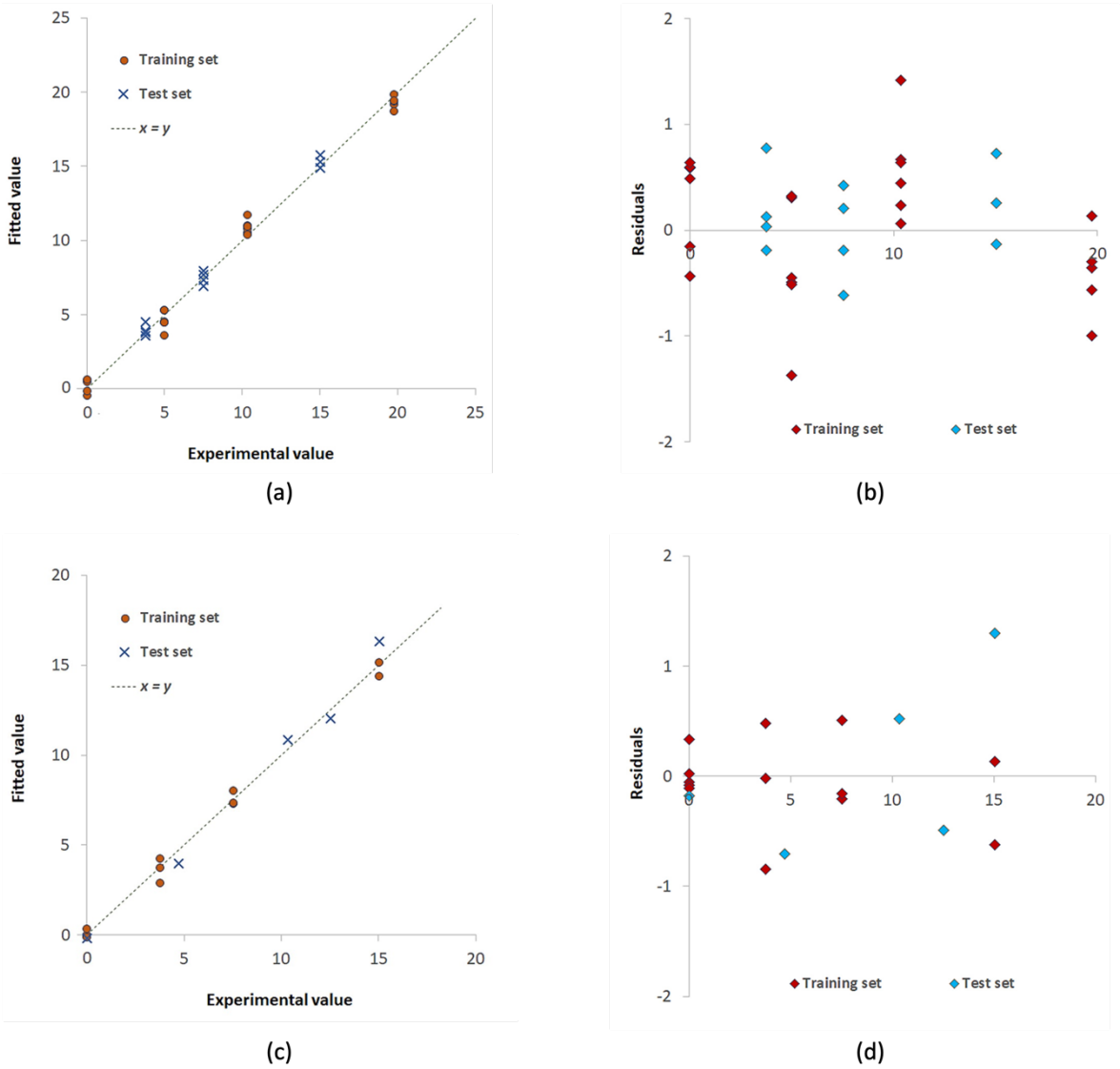

Figure 25.PLS models for Pd(II)+C u(II)/TazoC-PADs at pH 4 (a) and Psd(II)+Cu(II)+Ni(II)/TazoC-PADs at pH 5.5 (c) Experimental vs Fitted values for the training set (burgundy dots) and test set (blue dots); (b,d) residuals for the training set (burgundy dots) and test set (blue dots).

Table 8. Number of latent variables (LVs), % Explained Variance in Cross-Validation (%Exp. Var. CV) Root Mean Square Error in CV (RMSECV), Root Means Square Error in prediction (RMSEP) and the correlation coefficient of the regression (r^2), for the PLS model in figure 42.

		Pd(II)+Cu(II)/TazoC-PADs pH 4	**Pd(II)+Cu(II)+Ni(II)/TazoC-PADs pH 5.5**
Training set	LVs	8	7
	%Exp.Var.CV	93.07	74.2
	RMSECV (μM)	1.92	2.33
	r^2 model	0.992	0.995
Test set	RMSEP (μM)	1.41	0.86
	r^2 prediction	0.993	0.990

Both PLS models proved adequate in predicting Pd(II) concentrations even in the presence of interfering cations since there was pretty good agreement between experimental and fitted values.

As long as real sample analysis of Pd(II) is concerned, it is well known that for the preservation of water samples for metals' analysis rules[89], acidification at pH<2 is mandatory to avoid the precipitation of hydroxides; for this reason, the model that deserves our attention is that developed at pH= 2, where the possible interferences of other metal ions are limited, depending on their concentrations. According to this indication, the PLS model was built using tap water as a matrix acidified at pH2 and fortified with Pd(II) at different concentrations (model name: Pd(II)/TazoC-PADs TW). Three tap water samples were acidified and spiked with Pd(II) concentrations (7.5, 25.2 and 44.6 μM) and used as an external data set (3 replicates for each sample). The tables (T 6.3- 6) reporting the metal-ion concentrations in each sample and the sensor's performance graph (F 6.3- 5) are reported in Appendix III – PLS data (Training set, Test set compositions, and model performances) of the TazoC-PADs for Pd(II) determination (paragraph 2.4).

Table 9. Number of latent variables (LVs), % Explained Variance in Cross-Validation (%Exp. Var. CV) Root Mean Square Error in CV (RMSECV), Root Means Square Error in prediction (RMSEP) and the correlation coefficient of the regression (r^2), for the PLS model Pd(II)/TazoC-PADs TW in Figure 26

		Pd(II)/TazoC-PADs TW pH 2
Training set	LVs	5
	%Exp.Var.CV	98.73
	RMSECV (μM)	1.96
	r^2 model	0.995
Test set	RMSEP (μM)	2.06
	r^2 prediction	0.992

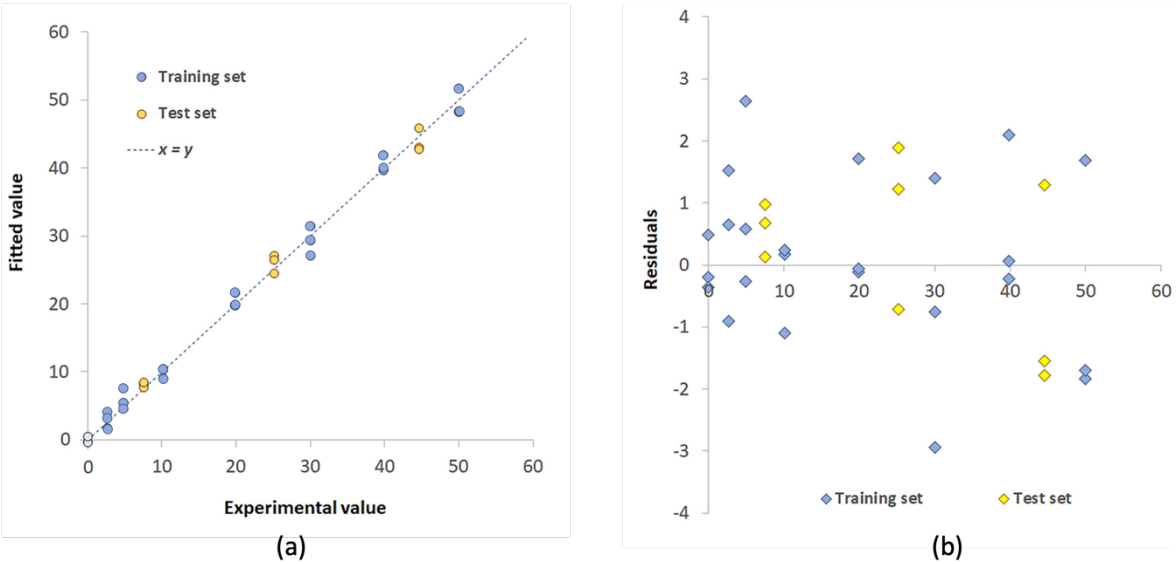

Figure 26.PLS model Pd(II)/TazoC-PADs TW pH 2 (a) Experimental value vs Fitted value plot for the training set (light blue dots) and test set (yellow dots); (b) residuals plot for the training set (light blue dots) and for the test set (yellow dots).

The results of the prediction of external samples can also be used to evaluate recoveries as reported in Table 10.

Table 10.Recovery Tes. The number in parenthesis is the standard deviation on the last digit (n=3)

Pd(II)added (μM)	Pd(II) found$_{ICP-OES}$ (μM)	Pd(II) found$_{TazoC-PADs}$ (μM)	RC%	E%
7.5	7.4(3)	8.1(5)	108	+8
25.2	25.0(4)	26(1)	103	+3
44.6	45.2(7)	44(2)	98	-2

The recoveries (RC %) for Pd(II) concentrations are between 80% and 110%, an acceptable recovery[90,91], demonstrating the sustainability of the proposed method for Pd(II) determination in drinking waters. The paramount advantage of the method developed here is its simplicity and costlessness compared to the instrumental analysis. The solid material, which I remember is paper, limited the possibility of decreasing the pH further. Lower pH, formally equal to zero (mineral acid equal to 1 M), would improve selectivity towards other metal ions when present several orders of magnitude higher compared to Pd(II)[79].

2.4.4 Conclusions

A cheap, selective, disposable colorimetric Paper-based Analytical Device (PAD) for Pd(II) sensing and quantification is proposed. The chromogenic receptor immobilized on the filter paper is a non-commercial azo-dye named TazoC ((disodium 2-[(1H-5-tetrazolyl)azo]-1,8-dihydroxy naphthalene-3,6 disulphonate); it has been selected since it forms strong and stable purple-blue colored complexes with Pd(II) in very acidic media (below pH 2).

The PLS chemometric tool was used to correlate the UV-vis spectra to the concentration of Pd(II) in solution; an advantage of using multivariate analysis is that the whole spectrum can be used as a signal, taking into account the changes in shape and height of spectrum peaks. Different tailored PLS models were developed and validated, highlighting the need to perform calibrations in the media of interest to avoid interferences and complex matrix problems.

The lowest quantifiable concentration value of about 2.5μM meets the WHO and FAO requirements for palladium(II) detection in drug chemicals and irrigation waters.

3 ELECTROCHEMICAL SENSORS

This section presents the electrochemical sensors developed. The first paragraph describes the transduction methods; in the second, the methods used to modify and characterize the working electrode surfaces and the techniques applied to characterize the electrochemical process at the electrode surface are presented. Finally, the last paragraphs describe the potentiometric and voltammetric sensors developed and applied to real samples.

3.1 Electrochemical transduction methods

Electrochemical sensors are a class of sensors in which the working electrode is the transducer[92]. The different typologies of sensors differ according to the electrochemical detection method. The methods used for the electrochemical sensors developed in this research are potentiometry and voltammetry.

3.1.1 Potentiometry

Potentiometric sensors are widespread devices for the determination of charged analytes thanks to the non-destructive nature of the technique. The measurements are performed by a two-electrode cell: the working and reference electrodes. Potentiometric sensors can be classified into three groups: Ion-Selective Electrodes (ISE), Coated Wire Electrodes (CWE) and Ion-Selective Field Effect Transistors (ISFET)[93]. The ISE devices comprise a well-stable reference electrode immersed in an inner solution of the analyte at a known concentration and a membrane working electrode in which a selective membrane for the target analyte separates the inner standard solution from the sample one. Redox processes do not occur at ISEs. The potential developed at the membrane results from an ion exchange process occurring at each interface between the membrane and solution. The most known ISE is the glass electrode for pH measurements[94]. The membrane potential measured by an ISE can be modeled by a similar Nernst equation[94] (Eq. 1) that correlates the potential to the activity of the ion in the sample solution.

$$E(V) = k' + \frac{2.303RT}{z_i F} \cdot \log(a_i) \quad (7)$$

k' is a constant including the potential of the reference electrode and the asymmetry potential of the membrane, R is the gas constant ($\frac{J}{K \cdot mol}$), T is the temperature (K), z_j is the

ion charge, and a_i is the analyte activity approximating the molar concentration for diluted solutions.

The Coated Wire Electrode (CWE) is another typology of potentiometric sensors characterized by the direct contact of the polymeric membrane with the surface of the working electrode, forming an electrode/polymer interface. This family of potentiometric sensors is less stable than the ISEs due to the blocked interface between the conductive material of the electrode and the polymer[95]; moreover, they suffer from a small interfacial sensing contact area, the possible formation of aqueous layer between the conductive metal substrate and the ion-selective membrane and the residual current passing through the ion-selective membrane causes noise and large signal drift. Nevertheless, the solid-contact screen printed cells have been proposed to increase the potential stability, repeatability, and miniaturization possibility[96]; besides, low-cost, custom and disposable sensors can be obtained[97].

The ISFETs (Ion-Selective Field Effect Transistor) is the third typology of potentiometric sensors. Figure 27 reports a schematic representation of the components of the ISFET.

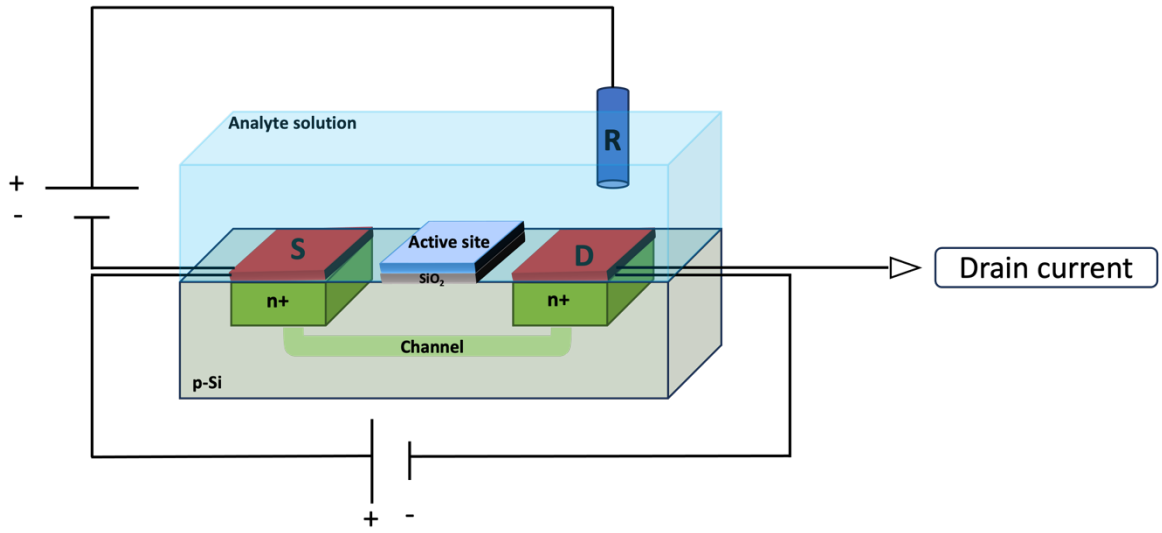

Figure 27. Schematic representation of components of ISFET devices.

The ISFET device comprises a mono-crystalline p-silicon wafer containing two silicon regions strongly n-doped called Source (S) and Drain (D). On top of the source and drain regions, two metallic disks constitute the electrodes S and D. The sensing site is a SiO_2 film modified with the active area that can be a polymer, a membrane or a self-assembled monolayer. The sample solution is in contact with the sensing surface and a reference

electrode (R), generally an Ag/AgCl/KCl electrode. A well-defined potential is applied between the R and S to generate a charge separation between the electrons and the holes in the p-Si wafer, forming an electron channel that connects the two n^+ regions; the potential applied is called threshold potential (V_T). A potential between S and D is applied to generate a current flow. When the ionic analyte is in contact with the active sites on the surface, its presence generates a new distribution of charges in the p-Si wafer; if the analyte is a cation, it attracts the electrons in the electrical channel and the drain current increases, vice versa if the analyte is an anion, the electrons are repelled and the drain current decreases.

These devices can be used in two operation modes: at fixed potential and fixed current.

If the device is used in the potentiostatic mode, the R-S and the S-D potentials are fixed at a specific value, and the drain current change is used as the analytical signal. If the device maintains the drain current fixed at a specific value, the analytical signal is the external potential that must be applied to maintain the current at that value. The output potential is proportional to the logarithm of the analyte's activity in solution; for this reason, Eq. (7) can be used to correlate the signal with the analyte concentration in solution[98,99].

3.1.2 Voltammetry

In voltammetry, the classical three-electrode cell consists of a working electrode (WE), a reference electrode (RE), and a counter electrode (CE).

Voltammetry is a widespread electrochemical technique that relies on a basic rule: in the three-electrode cell, when a potential scan is applied between the reference and the working electrodes in a solution containing electroactive species, the anodic or cathodic reactions that occur at the working electrode surface generate a faradic current flowing between the working and counter electrodes that can be used as analytical signal.

If a fixed potential is applied between the reference and the working electrodes, and the obtained current is used as the analytical signal, the method is called amperometry.

The voltammetric techniques differ in how the potential between the WE and the RE is applied. In DC (Direct Current) voltammetry, a linear scan of the potential in time is applied. If potential pulses are over-imposed on a linear potential scan, the technique is called Differential Pulse Voltammetry (DPV) or Square Wave Voltammetry (SWV) if square wave pulses are applied.

The technique is called Cyclic Voltammetry (CV) if a triangular potential waveform is applied, for example, a forwarding scan in the anodic direction (increasing potential) and a reverse scan in the cathodic direction (decreasing potential).

Figure 28 shows the different excitation signals, i.e., potential vs time, for the different voltammetric techniques.

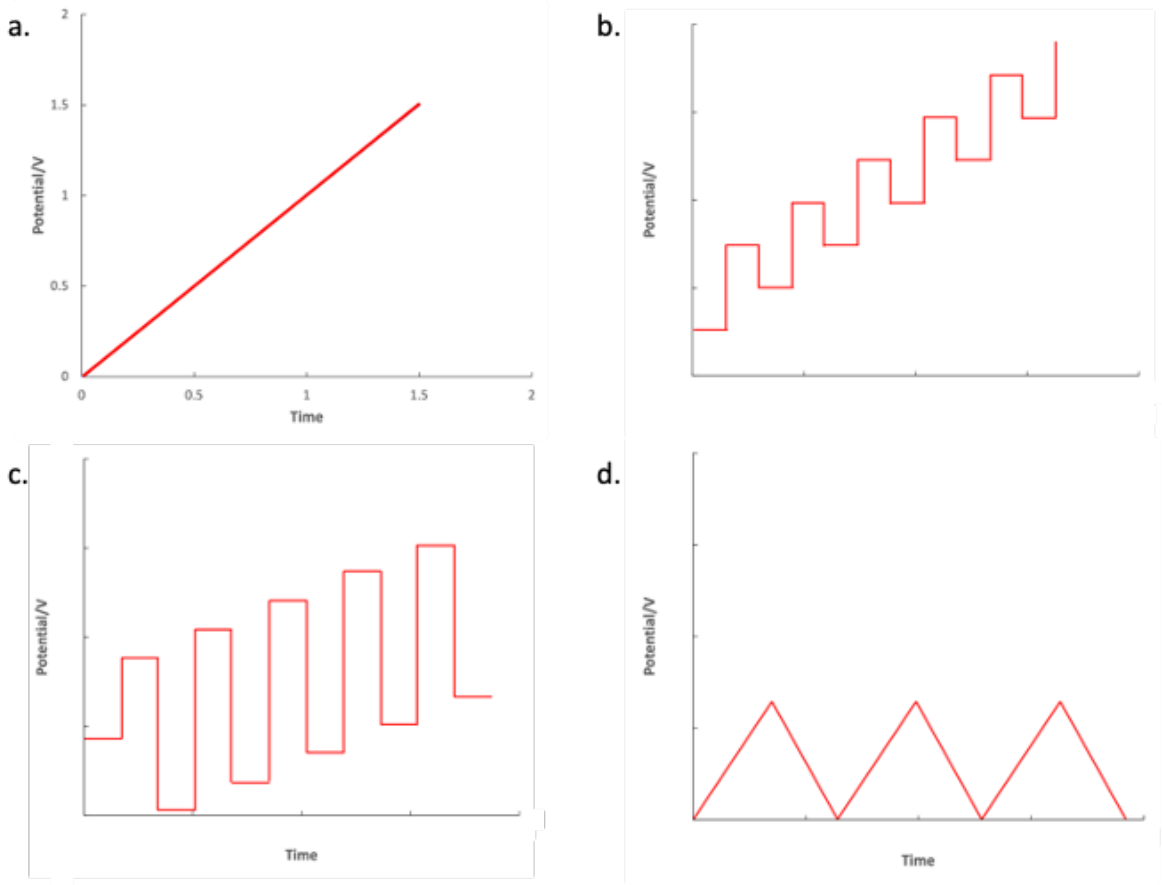

Figure 28. Potential imposition methods in voltammetry: a) Linear Voltammetry, b) Differential Pulse Voltammetry (DPV), c) Square Wave Voltammetry (SWV) and d) Cyclic Voltammetry (CV).

The choice of electrochemical technique depends on the analyte's electrochemical behavior; for example, if the analyte undergoes a reversible electrochemical process, the most suitable technique, in terms of sensitivity, is SWV. CV is instead helpful in characterizing the analyte's electrochemical process.

Different working electrodes can be used for voltammetric analysis, such as glassy carbon, platinum, copper and gold; the reference electrodes can be SCE (saturated calomelan electrode) or Ag/AgCl/KCl, while the counter electrode is, in general, a platinum wire. In the last twenty years, screen-printed cells (SPC) have often been applied in developing electrochemical sensors. They are manufactured by printing different types of ink on

plastic or ceramic substrates, for example, graphite or gold ink for the working and counter electrode and Ag/AgCl ink for the pseudo reference electrode. SPCs are easy to handle, cheap and can be applied for in situ analysis.

3.2 Electrochemical Sensors Development

In this project, screen-printed cells (SPCs) were used to develop electrochemical sensors. SPCs consist of a plastic, paper or ceramic substrate on which the electrodes are printed. The working, counter and reference electrodes can be made of different inks, such as graphite, silver, copper, gold and platinum.

In particular, two different inks were employed to print the working electrodes of the SPCs: graphite and gold; in both kinds of SPCs, the pseudo-reference electrode was of Ag/AgCl ink, and the counter electrode was printed with graphite ink.

The SPCs' working electrodes in graphite were modified with molecularly imprinted polymers, while the SPCs' working electrodes in gold were modified with self-assembled monolayers (SAM).

The following paragraphs report the methods employed to modify the electrode surface, the techniques used to characterize the electrode surface, and the approach employed to study the electrochemical process of the selected analytes.

3.2.1 Molecularly Imprinted polymers (MIP)

Molecularly imprinted polymers (MIP) are a family of polymers able to mimic the specific recognition mechanism of biological systems[54]. The molecular imprinting process involves the polymerization of functional monomers and crosslinkers in the presence of a target analyte that acts as a template[101]. After the polymerization, the subsequent template removal leaves specific cavities in the polymer, complementary in size and shape to the target molecule. Therefore, the free MIP's cavities can rebind specifically the analyte or closely related molecules when in contact with a sample solution[102,103]. A scheme of the synthesis and the desorption/rebinding process is shown in Figure 29.

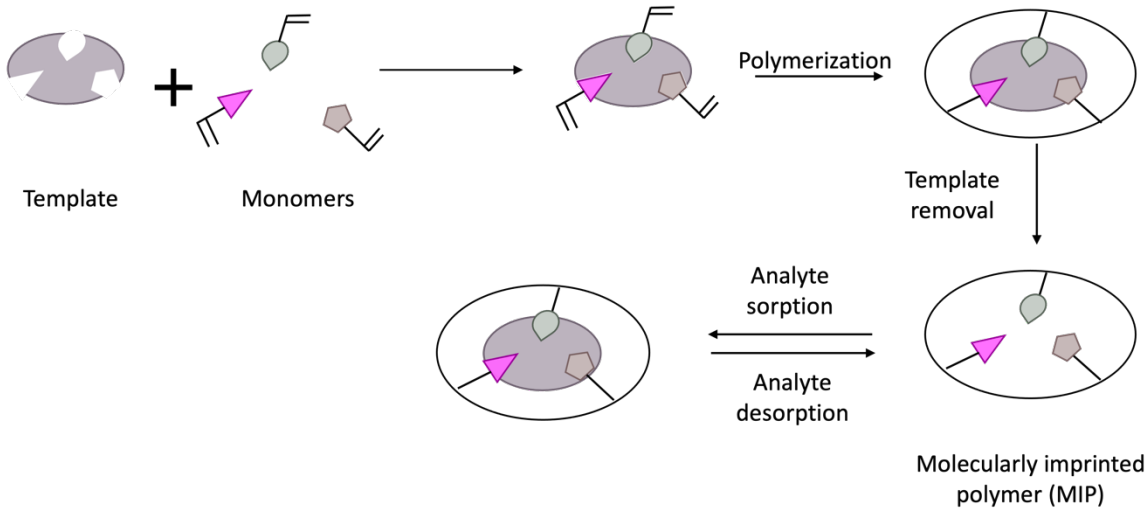

Figure 29. Molecularly Imprinted Polymer synthesis and desorption/rebinding process.

MIPs are appealing thanks to their recognition properties, stability, availability, and versatility; in fact, MIPs can be developed for many molecules[104].

Three approaches to the MIPs' synthesis can be used: non-covalent, covalent and semi-covalent.

Molecularly imprinted polymers are obtained starting from a pre-polymeric solution containing the template, monomers, crosslinkers, a suitable solvent and, when necessary, a radical initiator. The most widespread polymerization technique is based on the free radical mechanism that can be photo-, thermal-induced or electrochemical.

The MIPs applied to modify the electrode surface of the sensors developed in the present research are based on the non-covalent (weak bounds like Van der Waals and hydrophobic forces, hydrogen bonding and ionic interactions) between the template and the recognition cavities[105]. They were obtained using thermal initiation or electro-polymerization.

A crucial point in obtaining a well-performing MIP is to remove the template molecules once the polymerization is completed. The template molecules can be removed using appropriate washing solutions (generally ethanol/acetic acid solution 4:1) or electrochemically by applying a fixed potential to break the template molecule, causing leakage from the active sites.

3.2.2 Self-Assembled Monolayer (SAM)

Self-assembled monolayers (SAMs) are thin films obtained by the spontaneous adsorption of amphiphilic adsorbates onto an appropriate substrate, forming ordered aggregates[106]. The assembly is due to the chemical affinity between the adsorbates and the substrates. The most common self-assembled monolayers are those of carboxylic acids on aluminum oxide or silver, alcohols, amine and isonitriles on platinum, dialkyl disulfides on gold, alkanethiols on gold, silver and copper. SAMs have several vantages: they are easy to generate, densely packed and precisely oriented; moreover, the surface properties can be adjusted using standard organic synthetic methods[106]. Figure 30 shows a schematic representation of a self-assembly of thiol molecules on a gold substrate.

Figure 30. Schematic representation of a self-assembly of thiol molecules on a gold substrate.

SAM grafting is a very used method for the modification of electrode surfaces[107]. Two different sensors were developed in this research based on the gold screen-printed electrode surface modification with SAMs, as described in the following paragraphs.

3.2.3 Characterization of the electrode surface and after chemical modification

3.2.3.1 Determination of the electrochemically active area of the electrode

The electrochemically active area of a working electrode can be determined by cyclic voltammetry (CV), registering the voltammogram at different scan rates and employing a reversible electrochemical probe[108]. Generally, the most used probes are ferrocene 1 mM, 5 mM $K_3Fe(CN)_6$/0.1 mM KCl or the $Ru(NH_3)_6$ (II)/(III) 5 mM. The obtained anodic and cathodic peak currents are plotted vs. the square root of the scan rate, and the active area was calculated by applying the Randles-Sevick equation[109] (eq.8)

$$i_p = F \cdot n \cdot 0.4463 \cdot C \cdot A \cdot \sqrt{\frac{n \cdot F \cdot vD}{R \cdot T}} \qquad (8)$$

I_p peak current anodic or cathodic, Faraday constant (C/mol), n number of electrons, C probe concentration in mol/cm^3, D diffusion coefficient (cm^2/s), v scan rate (V/s), A active area (cm^2), T temperature (K), R gas constant (J/molK), F faraday constant (C/mol).

3.2.3.2 Determination of the capacitance of the double layer of the working electrode

The double-layer capacitance (C_{dl}) can be obtained from the EIS Nyquist plot or by cyclic voltammetry.

From the Nyquist plot and the relative Randles circuit obtained by Electrochemical Impedance Spectroscopy (see paragraph 3.2.3.4), the C_{dl} can be computed. The measurements are generally performed using an electrochemical probe solution.

Using the second approach, the C_{dl} is determined by CV scanning the potential from +0.5 to −0.5 V in 0.1 M NaCl solution (in which the lowest faradic current is expected) at different scan rates. The difference between the anodic and cathodic current (ia-ic = Δi) read at +0.02 V was plotted vs. the scan rate; the slope of the straight line is equal to twice the double layer capacitance[110].

3.2.3.3 Determination of the surface coverage (Γ) and the electron transfer rate (k°) for SAM-modified electrode

The surface coverage (Γ) of a working electrode modified with a Self-Assembled Monolayer (SAM) is determined by the integration of the cathodic peak from the desorption curve in KOH 0.1 M registered in cyclic voltammetry (CV from 0 to -1.4 V, scan rate 0.1 V/s)[111,112], by applying equation (9):

$$\Gamma = Q \cdot n \cdot F \cdot A \qquad (9)$$

where Q is the quantity of charge (C) required to break the S–Au bounds, n is the number of electrons involved in the process (n = 1), F is the Faraday constant (C/mol), and A is the electrode area (cm^2).

The electrode coverage with an electro-active metal sorbed on the SAM from the cyclic voltammetry scans can be obtained using eq.9 or the following eq.10[113].

$$I_p = \frac{n^2 F^2 v\, A\Gamma}{4RT} \qquad (10)$$

I_p is the intensity of the peak of the metal in CV measured in V, n is the number of electrons, F is the Faraday constant, v is the scan rate in V/s, A is the area expressed in cm^2, Γ is the

coverage expressed in mol/cm^2, R is the gas constant in J/molK and T is the temperature in Kelvin[113].

The electron transfer rate (k°) is evaluated by cycling voltammetry employing an electroanalytical probe, for example, 5 mM $[Fe(CN)_6]^{3-}$ in 0.5 M KNO_3/0.1 M phosphate buffer solution at pH 7 (E_{start} = -0.5 V, E_{end} = +0.5 V, 20 scan rates from 0.01V/s to 2 V/s), applying the following equation (11)[114]:

$$k^\circ = 2.18\left(\frac{D\alpha nFv}{RT}\right)^{0.5} exp\left[-\frac{\alpha^2 nF}{RT}(\Delta E)\right] \quad (11)$$

where k° is the electron transfer rate, D the diffusion coefficient (cm^2/s), α is the charge transfer coefficient (α = 0.5), n the electrons involved in the process (n = 1), F is the Faraday constant (C/mol), v is the scan rate (V/s), R the gas constant (J/K·mol), T the temperature (K) and ΔE is the peak separation (V).

3.2.3.4 Characterization by Electrochemical Impedance Spectroscopy (EIS)

Electrochemical Impedance Spectroscopy (EIS) is an electrochemical technique mainly used to evaluate the electrochemical behavior of the electrode/electrolyte interface but has recently been applied for sensing purposes too. When a charged electrode is immersed in a solution, ions, solvent molecules, and electrons form a double layer, and the presence of these charges on the surface of the electrode perturbates the quiet state of the solution, generating two theoretical planes on which molecules are disposed: l'*Inner Helmholtz Plane (IHP)* e l'*Outer Helmholtz Plane* (OHP) as reported in Figure 31[115].

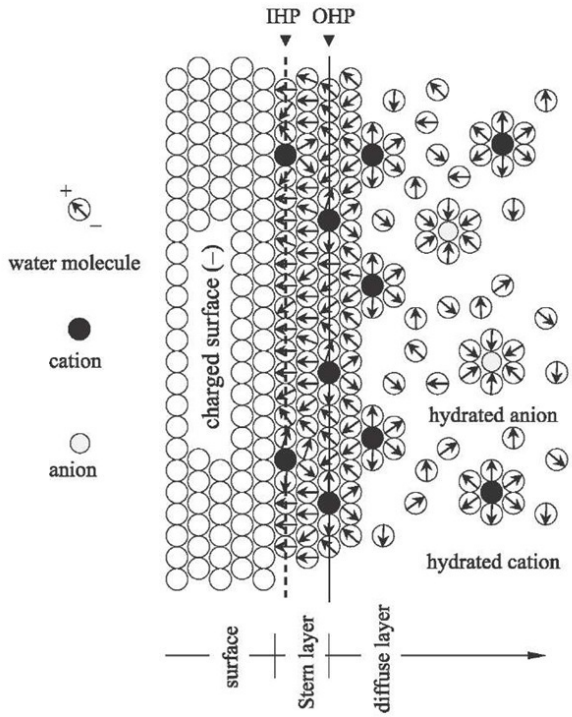

Figure 31. Phenomena at the electrode/electrolyte interface[116].

On the first imaginary plane (IHP), solvent dipoles and the nude ions without the hydration sphere are oriented depending on the surface charge of the electrode, while the ions with the hydration sphere are disposed on the second imaginary plane (OHP). Gradually passing from the OHP to the bulk, the solution becomes homogeneous and electrically neutral[116]. The charge distribution influences the potential and the resistance at the electrode/electrolyte interface. If an electrical stimulus (that can be a voltage or a current) is applied to the working electrode, an electrical response is obtained depending on the working electrode's or electrolyte's characteristics. When an electrical stimulus is applied to an electrochemical cell, several processes can occur; for example, electrons can flow through the electrodes or cross the electrode/electrolyte interface, causing oxidation or reduction of species in solution[116]. If an AC voltage is applied, a current response is obtained; thanks to these two sine waves, the impedance and the phase shift are calculated. The impedance changes depend on transformations at the electrode surface and reactions across the interface. Generally, the applied AC potential frequencies are scanned, and the impedance is collected for each frequency. The Nyquist plot is the most used method to display how impedance changes with frequencies. The Nyquist plot is obtained by plotting the negative imaginary impedance against the real impedance, and

depending on the shape of the obtained curve, different phenomena at the electrode surface can be determined. For example, for an electrode where polarization is due to a combination of kinetic and diffusion processes the classical shape of the Nyquist plot is that reported in Figure 32.

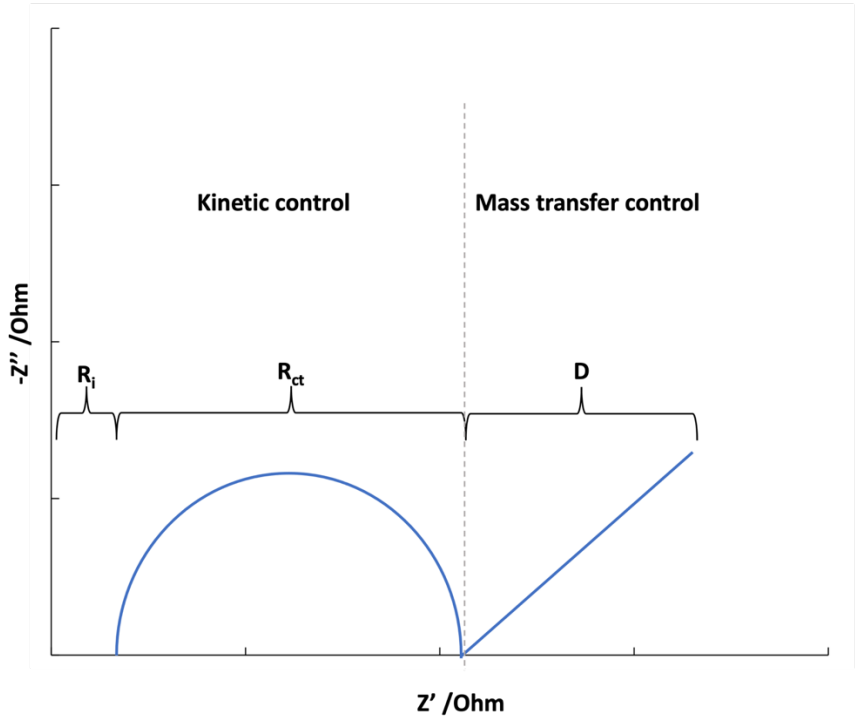

Figure 32.The theoretical Nyquist plot for an electrode where polarization is due to a combination of kinetic and diffusion processes. Ri is the resistance at the interface, R_{ct} is the resistance at the charge transfer, and D is the diffusion coefficient.

The R_i is the resistance at the electrode/electrolyte interface, the R_{ct} is the resistance at charge transfer, and D is the diffusion in the bulk. All the phenomena represented in the Nyquist plot can be schematized in a Randles equivalent circuit. Electrical circuit elements are assigned to each chemical/physical phenomenon that occurs at the electrode/electrolyte interface and in solution. For example, the resistance at the electrode/electrolyte interface is represented by a resistor (R_i), the resistance at charge transfer is represented by a resistor (R_{ct}) in parallel with the capacitor, representing the double layer capacitance (C_{dl}), while the diffusion is represented by the Warburg element (typical of electrochemical impedance spectroscopy)[117]. Figure 33 shows the Randles equivalent circuit of the Nyquist plot reported in Figure 32.

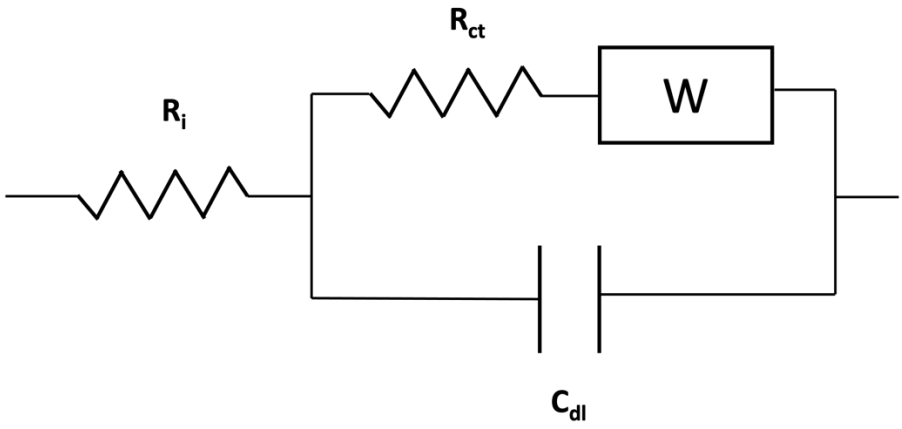

Figure 33. The Randles equivalent circuit of the Nyquist plot reported in Figure 6

The Rct depends on the characteristics of the working electrode surface, so its variation can be helpful in developing sensors, for example, to verify if the electrode surface modification has been successful or to quantify the interaction with the analyte and the receptor used to the electrode surface modification [118–120].

3.2.4 Characterization of the electrochemical process to the electrode surface (for irreversible analytes)

3.2.4.1 Determination of the number of electrons involved in the electrochemical process by controlled potential electrolysis (CPE)

The number of electrons involved in the electrochemical process of the analyte can be evaluated by controlled potential electrolysis (CPE)[121,122] by electrolyzing the compounds at a potential slightly higher (50 or 100 mV) than the oxidation or reduction peak in a three-electrode cell under a static nitrogen atmosphere. A Pt gauze is generally used as the working electrode, a Pt wire as the counter electrode and Ag/AgCl/3 M NaCl as the reference electrode.

The number of electrons involved in the electrochemical step is evaluated by calculating the charge Q necessary to electrolyze the analyte exhaustively, i.e. when the current was reduced to 5% of the initial value.

3.2.4.2 Cyclic voltammetry experiments

The CV measurements at different scan rates are performed in a solution at a constant analyte concentration (generally 2.5 mM or 5 mM) to obtain information regarding the electrochemical redox process. In particular, The relationships between log i_p and log v, the variation of the peaks potential (E_p) vs. the logarithm of scan speed (log v), the relationships $i_p \cdot v^{-1/2}$ *vs.* v (namely, the "current function") and log i_p *vs.* log v are investigated; moreover, to evaluate whether the electrochemical process is diffusion-controlled, plots of current intensity (i_p) vs. square root of the scan speed ($v^{0.5}$) or vs. scan speed (v) are performed.

Determination of the E°′ potential of the analyte

The formal potential *E°′* for a reversible process can be estimated according to the following equation 12 proposed in the literature[122,123]:

$$E^{\circ\prime} = \frac{E_{pa}+E_{pc}}{2} \qquad (12)$$

where E_{pa} and E_{pc} are, respectively, the anodic and the cathodic peak potentials.

For irreversible processes, the formal potential can be roughly estimated from the intercept of the E_p vs. v graph, extrapolating the value of E_p on the ordinate axes at the value equal to zero of the scan speed[124].

Determination of the charge transfer coefficient (α)

The charge transfer coefficient α can be determined for irreversible and quasi-reversible electrochemical processes via the Tafel slope, **b**:

$$\mathbf{b} = \partial Ep/\partial \log v = 2.303RT/\alpha n_\alpha F \qquad (13)$$

From the E_p vs. log v plot, the slope b can be obtained. Substituting the values of the constants T, R, and F and determining the number of electrons involved in the rate-determining step (n_α) from the CPE experiments or literature data, the following equation 14 is obtained:

$$\alpha = 0.059/n_\alpha \mathbf{b} \qquad (14)$$

As α is evaluable only for irreversible reactions, this procedure can be used for quasi-reversible processes using the CV data at high scan speed values, i.e., when the process

becomes more irreversible, and the slope of the plot E_p vs. log v is different from zero[125].

Determination of the diffusion coefficient (D)

From the CV scans at different scan rates, the first (anodic) peak potential was used to evaluate the diffusion coefficient, according to the following equation 15[126] for irreversible processes and to Randles-Sevcik equation 16 for reversible processes.

$$i_p = 2.99 \cdot 10^5 n\sqrt{(1-\alpha)}A[C]_\infty\sqrt{D}\sqrt{v} \quad (15)$$

$$i_p = 2.69 \cdot 10^5 n^{\frac{3}{2}}A[C]_\infty\sqrt{D}\sqrt{v} \quad (16)$$

D (cm^2/s) is obtained from the slope of the graph i_p vs. $v^{0.5}$

i_p is the anodic peak intensity (A), *n* the number of electrons exchanged per molecule, α the charge transfer coefficient (V), A the active area (cm^2), $[C]_\infty$ the concentration of the bulk solution (mol/cm^3), and v the scan rate (V/s).

Determination of the kinetic electron transfer constant (k°)

According to the literature[127], the value of the kinetic electron transfer constant *k*° can be calculated for irreversible electrochemical processes by using the Matsuda-Ayabe (equation 17):

$$E_p = \frac{RT}{\alpha nF}\left[0.78 - ln\frac{k^0}{\sqrt{D}} + \frac{1}{2}ln\frac{\alpha nFv}{RT}\right] \quad (17)$$

The value of k° was obtained from the intercept of the linear part of the graph obtained by plotting $\frac{E_p nF\alpha}{RT}$ vs. $0.5ln\frac{\alpha nFV}{RT}$.

E_p is the potential of the redox peak, R is the gas constant (J/molK), T is the temperature (K), α is the charge transfer coefficient (V), F is the Faraday constant (C/mol), D is the diffusion coefficient (cm^2/s), *n* is the number of electrons exchanged per molecule and v is the scan rate (V/s).

Determination of the reaction order

The reaction order is calculated from the voltammetric measurement used for the analyte quantification (i.e., square wave voltammetry, SWV or differential pulse voltammetry, DPV) by plotting log i_p vs. concentration of the analyte. The slope of the linear part of the graph corresponds to the reaction order[126].

3.3 MIP-modified screen-printed potentiometric sensors for Atrazine and phenoxy herbicides

3.3.1 Introduction

Two potentiometric sensors are developed to determine Atrazine and phenoxy herbicides such as 2-methyl-4-chlorophenoxyacetic acid (MCPA). Both are solid-contact screen-printed cells, i.e., characterized by the direct contact of the polymeric membrane with the surface of the working electrode, forming an electrode/polymer interface. Two-electrode screen-printed cells (SPCs) with graphite-ink working (WE) and Ag/AgCl-ink pseudo-reference (RE) electrodes are used. In both cases, the WE has been modified with an acrylic Molecularly Imprinted Polymer (MIP) as an ion-selective membrane.

The selected analytes are two herbicides already employed in agriculture in some countries, but they are highly toxic and dangerous.

Atrazine (2-chloro-4-athylamino-6-isopropylamino-1,3,5-triazine) is a triazine pesticide. The term pesticide includes herbicides, insecticides, fungicides and plant growth regulators[128]. Atrazine is a toxic compound that has been banned in some countries since it is an endocrine disrupter, can provoke several types of cancers, can interrupt regular hormone functions, can cause reproductive tumors, weight loss of embryos and mothers and congenital disabilities[129,130].

MCPA (2-methyl-4-chlorophenoxyacetic acid) was the first synthetic herbicide synthesized in England around 1941. It is a selective phenoxy herbicide that controls broadleaf weeds in arable and cereal crops. MCPA can mimic auxin, encouraging uncontrolled growth and subsequent death of certain plants[131]. MCPA has a soil half-life of 24 days and a water-octanol partition coefficient of 0.2-1mL/g, but some environmental pH and temperature values may facilitate the sorption and the degradation[132]. A warning behavior of MCPA is that it can form stable complexes with toxic metal ions such as lead and cadmium in environmental pH ranges[133]. MCPA has a very low bioconcentration factor (BCF) 1-14[134]; the human symptoms due to MCPA poisoning are fatigue, weakness, anoxia, nausea, vomiting, diarrhea, lowering of blood pressure, and body temperature disturbance. Progressive hypotension, ataxia, neuromuscular inability, and convulsion[135]. The human lethal oral concentration is around 814 mg/Kg[136].

Therefore, the monitoring of Atrazine and MCPA in the environment is of paramount importance.

The most common techniques used to quantify herbicides in water bodies and soils are high-performance liquid chromatography coupled with mass spectrometry (HPLC-MS)[137,138], ultra-performance liquid chromatography (UPLC)[139,140] and gas chromatography coupled with mass spectrometry[141–143]. These techniques are costly; the measurements are time-consuming, and they can not be done in situ and need trained personnel. Considering all these disadvantages, the development of low-cost, easy-to-use, disposable and quick-responsive sensors is desirable.

In this scenario, potentiometric electrochemical sensors based on screen-printed cells (SPCs) with the WE modified with acrylic molecularly imprinted polymers that act as ion-selective membranes are proposed.

3.3.2 Material and methods

3.3.2.1 MIP and NIP prepolymeric mixtures preparation and modification of the SPC

The MIP prepolymeric solutions are prepared by mixing the template, functional monomer (methacrylic acid, MAA), and cross-linker (ethylene glycol dimethacrylate, EGDMA) in the opportune ratio (as reported in Table 11) and adding the radical initiator (2,2,-azobisissobutyronitrile, AIBN) just before starting the thermal polymerization.

Table 11. *MIPs' prepolymeric mixtures composition and molar ratio Template: Functional Monomer: Cross-Linker*

	Template (mg)	**MAA** (µL)	**EGDMA** (µL)	**AIBN** (mg)
Atrazine	25	48	95	28
molar ratio	*1*	*5*	*4*	
MCPA	28	175	175	35
molar ratio	*1*	*15*	*7*	

Each mixture is deaerated with a gentle flow of N_2 for 5 minutes and sonicated to dissolve the template and AIBN completely. The minimum amount of toluene (0.2 mL) is added to facilitate the dissolution of the components. The NIPs (non-imprinted polymers) prepolymeric mixtures are prepared following the same procedure as the MIP but without adding the template.

Each graphite screen printed cell is washed in ethanol and left dry at room temperature under a hood. 7 µL of prepolymeric mixture (of MIP or NIP) is drop-coated on the clean surface of the working electrode, and the screen printed cell is placed in a vacuum desiccator before subsequent thermal polymerization to avoid oxygen adsorption. Then, the thermal polymerization is carried out in an oven at 70°C overnight.

The modified screen-printed cell is subjected to 5 cleaning cycles by immersion of the electrodes for 30 min in 10 mL of an ethanol/acetic acid (4:1) mixture to remove the template and unreacted monomers. The schematic representation of the procedure for the working electrode's functionalization is reported in Figure 34. The modified SPCs are stored at room temperature and hydrated in ultrapure water for 10 minutes before use.

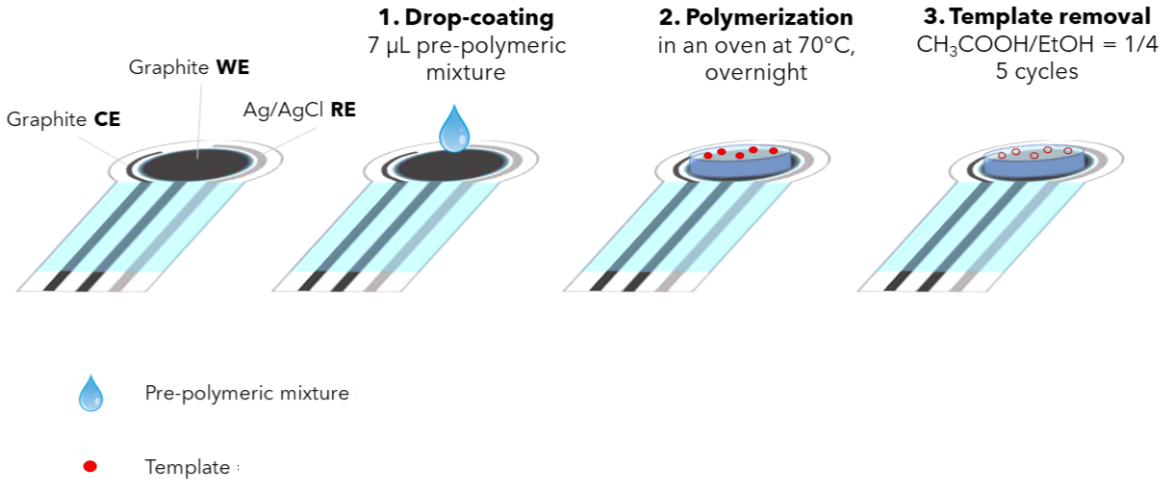

Figure 34. Schematic representation of the working electrode's functionalization with the MIP prepolymeric mixture.

3.3.2.2 Characterization of the working electrode surface

The working electrode surface of the screen-printed cell is characterized before and after the functionalization with the polymeric layers (MIP and NIP). The electrochemically active area determined by experiments in cyclic voltammetry (see paragraph 3.2.4.2) and the electrochemical impedance spectroscopy (EIS) measurements (see paragraph 3.2.3.4) are performed both employing the electrochemical probe 5mM $K_3Fe(CN)_6$/0.1M KCl at pH7.2.

3.3.2.3 Potentiometric measurements

Potentiometric measurements are performed by connecting the screen-printed cells to the potentiostat/galvanostat EmStat4s-PalmSens BN (Houten-The Netherlands) by immersing

the MIP-modified screen-printed cell for atrazine in 15mL of HCl (or other inorganic acids) at pH = 1.5 and adding portions of 10 μL atrazine standard solution 0.47 mM in methanol, and for MCPA in 15 mL of PBS buffer at pH 5.5 and adding portions of 20 μL of MCPA standard solution 25 nM under gentle stirring.

At each addition of analyte, the potential is recorded, and the average of the values sampled in the last 60 s after waiting 3-5 minutes for the steady-state is considered the response signal (stability criterium $\Delta E/\Delta t$ = 0.02 mV/s).

3.3.3 Results and discussion

3.3.3.1 MIP-modified screen-printed sensor for Atrazine

As described before, the working electrode surface is functionalized by drop-coating the prepolymeric mixture of the MIP or NIP, followed by a thermal polymerization at 70°C.

A physical-chemical characterization is performed to check if the polymerization occurred correctly with the formation of the recognition cavities. The modified working electrode surface is observed using SEM (Scanning Electron Microscopy), and the images are compared to those of the bare electrode. SEM images are reported in Figure 35.

For the bare electrode (panels a-d), a homogenous layer of grains (panels c and d) or large platelets (panel b) can be observed due to the gold spattered on the surface, as required for the measurements. For other sensors (panels e-h for MIP-modified electrode and panels i-n fo>r NIP-modified electrode), compact particles are superimposed on the fine grains layer, forming clusters of different sizes and shapes. In particular, the MIP-based electrode has both filamentous and compact particles of 10/20 microns above the material's surface. Compared to NIP, MIP has an irregular, rough morphological structure due to the presence of binding cavities. Conversely, the NIP has a regular structure, more similar to that of the bare electrode, due to the absence of imprinted sites.

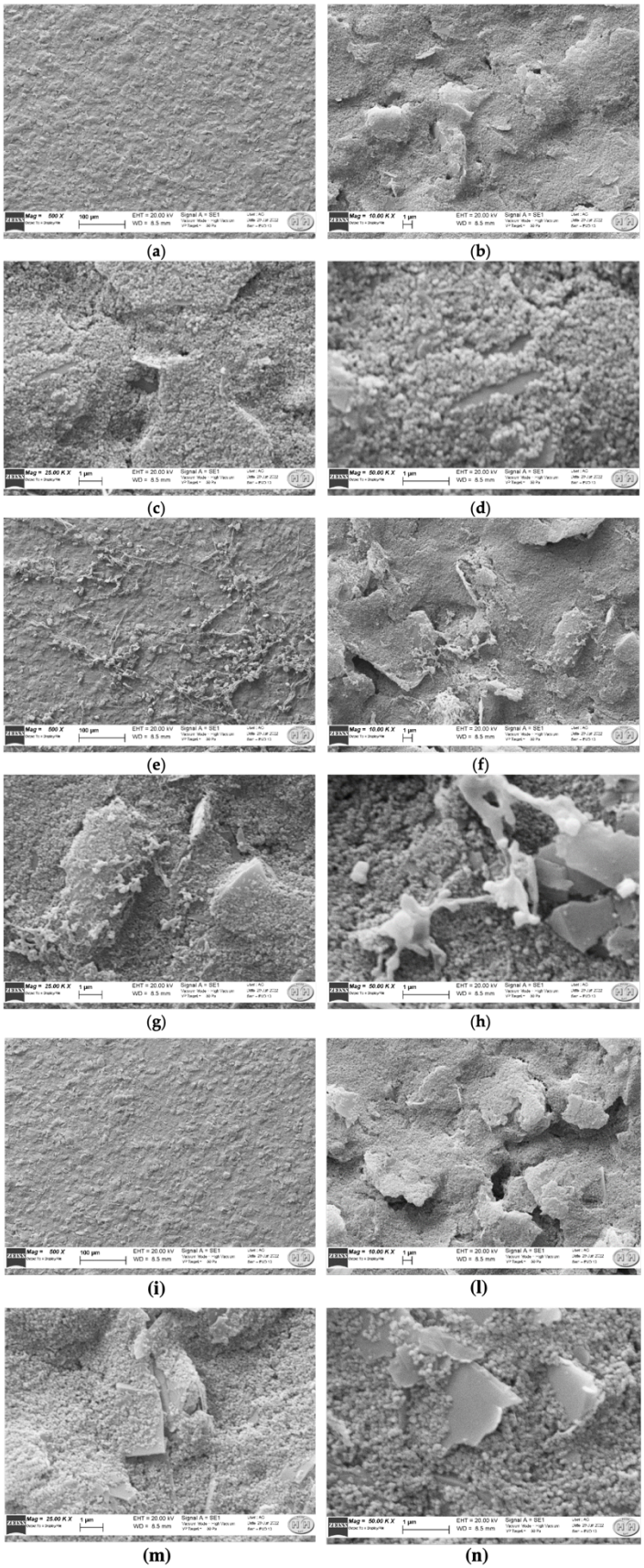

Figure 35. SEM images of the sensors: bare (a-d), MIP-modified electrode (e-h), and NIP-modified electrode (i-n).

The working electrode surface is also characterized by determining the electrochemically active area before and after the functionalization; the Randles-Sevick equation (eq.8) is applied for the computation, obtaining the results reported in Table 12.

Table 12.Active area values calculated using the Randles-Sevick equation 8. The standard deviations on the mean are reported in brackets.

	Active area (mm^2)
Bare SPC	50(1)
MIP-modified SPC	4.0(8)
NIP-modified SPC	2.3(3)

As can be noticed, the values of the active area of the modified SPC are very different compared to that of the bare SPC. This result can be interpreted with the non-conductive nature of the polymer deposited on the electrode surface, which reduces the electronic transfer capability of the graphite. Moreover, a slightly higher area is obtained for the MIP-functionalized electrode, justifiable by the higher porosity than the NIP.

Electrochemical Impedance Spectroscopy (EIS) is used to characterize the electrochemical response of the modified surface. The data obtained from the EIS plot can be correlated to the physical and chemical properties of the electrode surface, modeling the electrochemical responses by an equivalent electrical circuit (Randles circuit). Figure 36 shows the Nyquist plot (imaginary impedance Z'' vs. real impedance Z') obtained for the unmodified electrode (bare electrode), the MIP-modified electrode before and after the sorption of atrazine at two different concentration levels and the NIP-modified electrode.

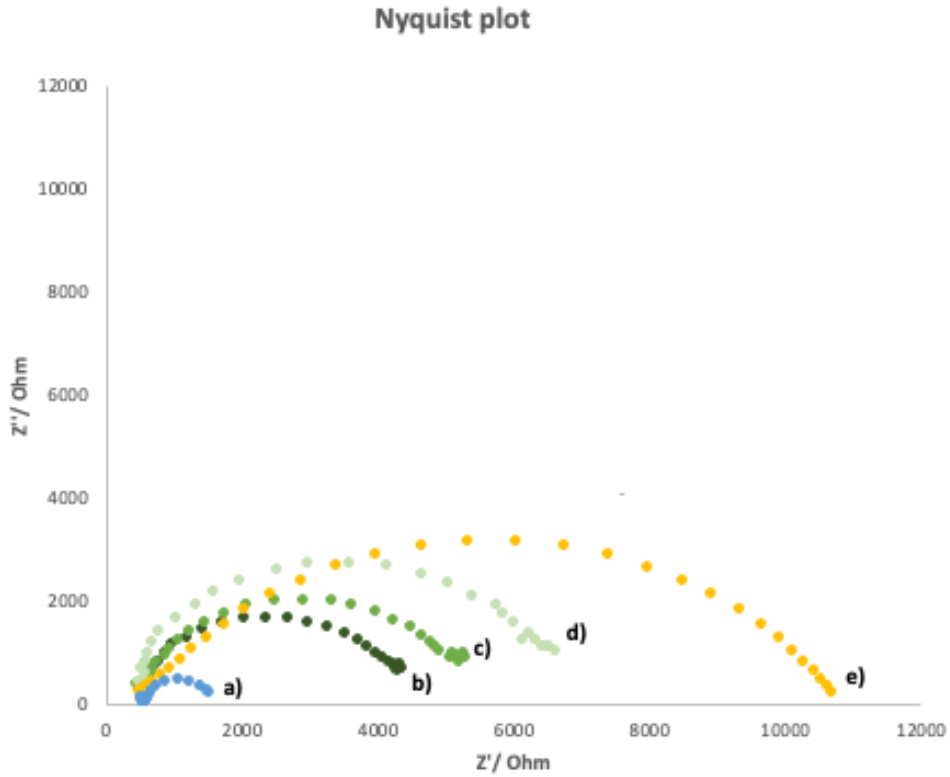

Figure 36.Nyquist plot of (a) bare electrode, (b) MIP-modified electrode, (c) MIP-modified electrode after equilibration with 10^{-6}M atrazine, (d) MIP-modified electrode after equilibration with $7.7 \cdot 10^{-6}$M atrazine and (e) NIP modified electrode. Measurements performed in 5mM $K_3Fe(CN)_6$/0.1M KCl solution; frequency range 100kHz÷10mHz; signal amplitude = 50mV.

All phenomena at the MIP and NIP-modified and bare electrode surfaces may be schematized, respectively, with the Randles circuits shown in Figure 37a) and Figure 37b). R_1 corresponds to the solution resistance, R_2 is the electron transfer resistance (diameter of the semi-circle in the Nyquist plot), C1 is the double-layer capacitance, and Z_w is the Warburg element, i.e., the element added to justify the mass transfer diffusion-limited process.

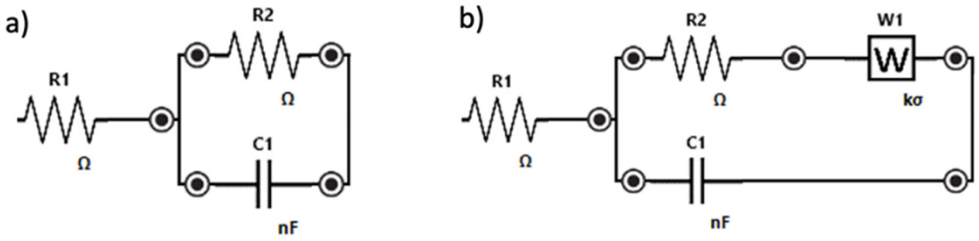

Figure 37. Randles equivalent circuit of (a) MIP and NIP-modified electrode, (b) bare electrode

As can be observed in Figure 36, the linear part of the Nyquist plot characteristic for a process limited by mass diffusion is evident only for the bare electrode. Moreover, it has the lowest charge transfer resistance since graphite is a good conductor. The resistance

increases if a polymeric film on the working electrode surface prevents the electrons' transfer. Since the MIP possesses the recognition cavities, a lower resistance is observed for the cleaned MIP-modified electrode compared to those that have the cavities partially occupied by the analyte. This behavior can be explained by considering the atrazine molecules as shutters of the polymer's cavities that obstruct the charge transfer; in fact, the resistance increases by increasing the atrazine concentration. The NIP-modified electrode has the highest charge transfer resistance due to the absence of cavities that facilitate the charge transfer across the polymeric structure.

After the working electrode's characterization, the potentiometric measurements are undertaken.

As mentioned before, the molecularly imprinted polymer can act as an ion-selective membrane on the surface of the working electrode if the analyte is in its ionic form. In order to have the most atrazine protonated (pK_a = 1.7)[144], measurements are performed at pH 1.5 in HCl as the ionic medium. Figure 38 reports the protonation equilibrium of Atrazine.

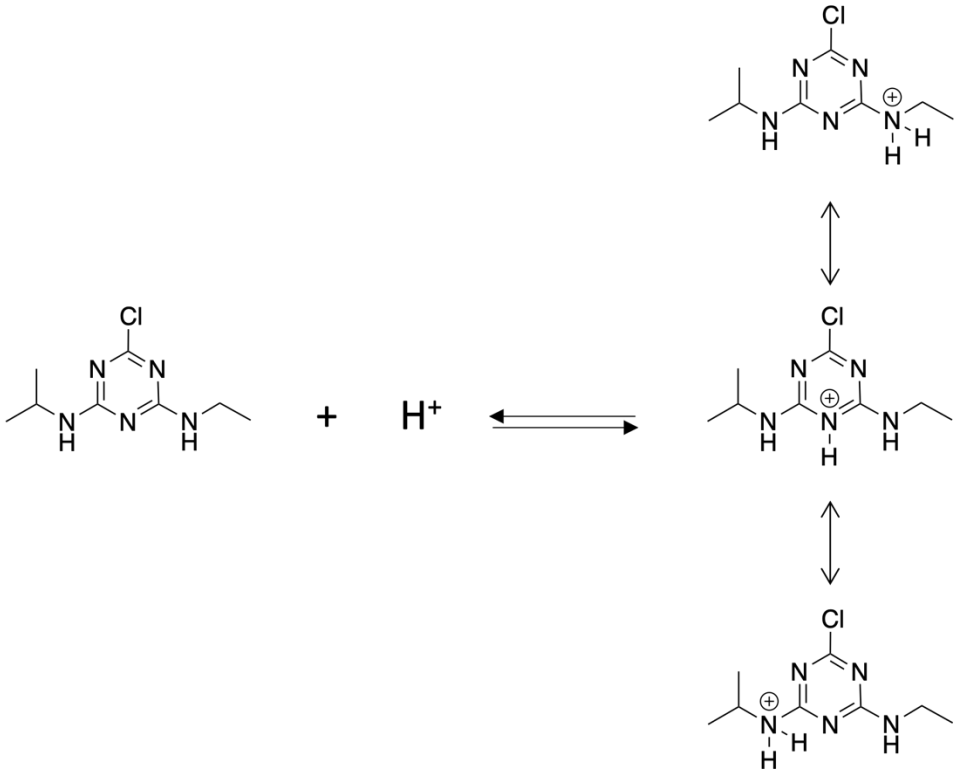

Figure 38. Protonation equilibrium of Atrazine.

For example, Figure 39 shows the potentiometric response of the MIP-based screen-printed cell at different Atrazine concentrations.

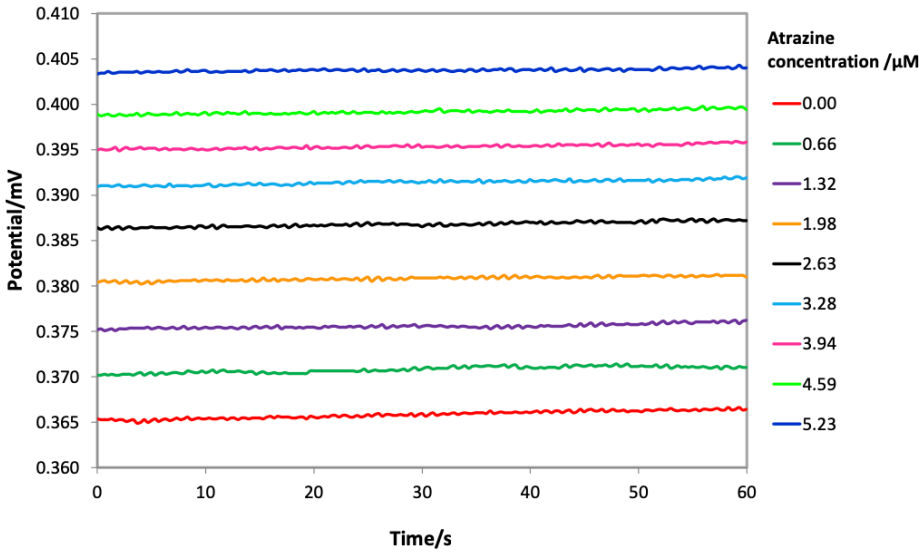

Figure 39. Potentiometric response of a MIP-based screen-printed cell at different Atrazine concentrations in HCl solution at pH =1.5. Steady state reached in 5 min. Cell potential registered in the last 60 seconds.

At each atrazine addition, the potential linearly increased with the logarithm of the concentration of analyte according to the well-known pseudo-Nernst's law (eq.7). Calibration measurements are performed using five different MIP-screen printed cells modified with the same strategy since the devices are disposable. The calibration curve reported in Figure 40 shows the average of the potential values (mV) vs. the logarithm of the Atrazine concentration; error bars represent the standard deviation of the measurements performed with five different sensors.

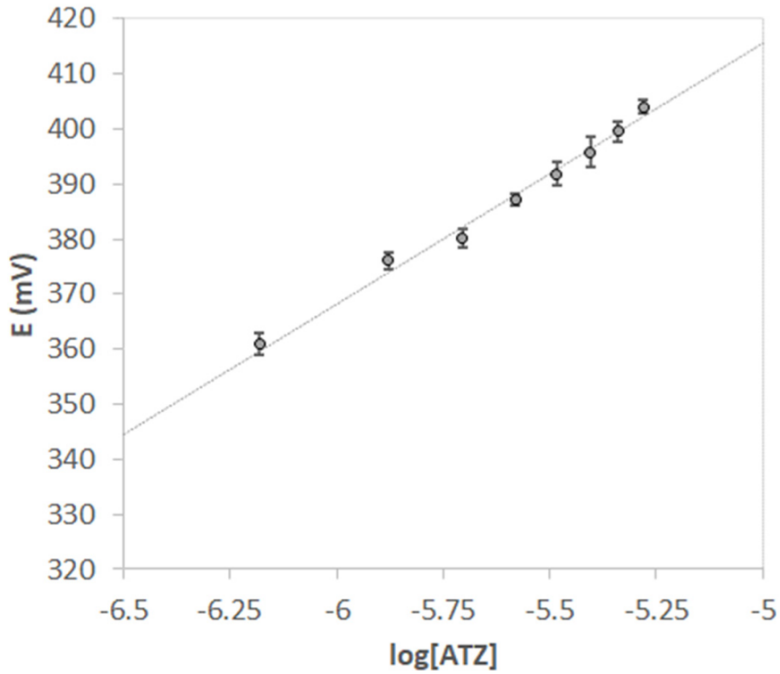

Figure 40. Nernst's plot E vs log[ATZ]. V = 15 mL, HCl pH 1.5. Each point is the mean of 5 measurements obtained with different screen-printed cells. Error bars correspond to the standard deviation of the measurements.

The limit of detection (LOD) is calculated from the linearized Nernst's plot ($10^{E/slope}$ vs. [ATZ]) as reported in eq.4 in section 1.4.5. Limit of detection (LOD) and limit of quantification (LOQ). The value of the LOD obtained from the five electrodes calibration is 0.40(2) μM.

Although the low detection limit is obtained, the standardization curve's linearity range is relatively small, only one decade of concentration change, but enough to determine atrazine residuals in polluted environmental samples.

Analogous calibration curves are performed with the NIP-modified electrode; the slope near zero indicates the poor interaction with atrazine due to the absence of the specific recognition cavities in the polymer.

The graph of Figure 41 compares the calibration performed using the MIP-modified and the NIP-modified screen-printed cell.

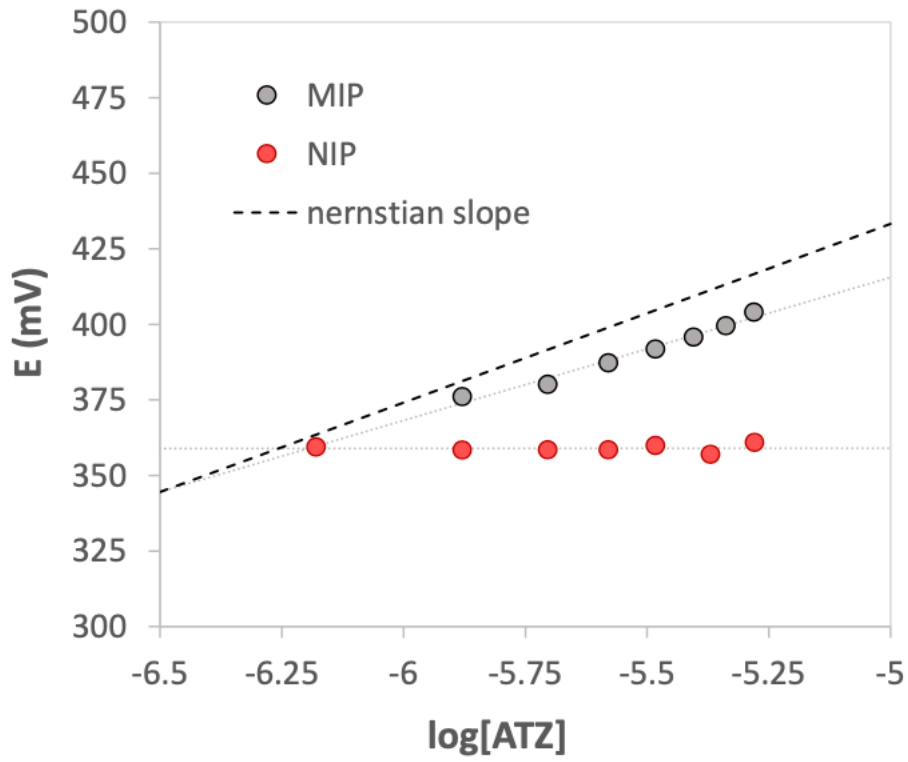

Figure 41. Nernst's plot E vs log[ATZ]. V = 15 mL of HCl pH = 1.5. Grey dots are the measurements performed using the MIP-modified screen-printed cell, and red dots are those performed using the NIP-modified screen-printed cell. The dotted straight line represents the theoretical Nernstian slope for monovalent cations.

Since Atrazine is a monoprotonated cation at pH 1.5, the theoretical slope of the straight line obtained by plotting E (mV) vs log[ATZ] should be 59.2 mV/dec; it is evident that a sub-Nernstian slope is obtained for the MIP-based electrode. As suggested by different authors, the sub-Nernstian slope is justified for neutral ion-selective membranes, considering the

effect of ions of opposite charge to the primary one, which can interact with the active site of the polymer. The same interpretation was proposed for both classical ISEs and potentiometric screen-printed electrodes[145–147].

So, by assuming the MIP film over the screen-printed electrode as a neutral membrane (since the carboxylic groups of the methacrylic acid, i.e., the functional monomer of the MIP is undissociated at pH 1.5), we questioned how anions could reach the cavities of the MIP. Presumably, an ion pair is formed between the protonated atrazine and the anion (conjugate base) of the acid used as the ionic medium.

Therefore, measurements are performed at pH 1.5 using different inorganic acids (HCl, HNO_3, $HClO_4$, H_2SO_4, H_3PO_4) to confirm this theory.

An interesting linear correlation is obtained by plotting the standardization curve's slope as a function of the anion volume (calculated using Gaussian 6.0 software)[148], as reported in Figure 42. In particular, as the size of the anion increases, the slope decreases. The larger size of the ion pair probably results in greater difficulty for the analyte to reach the recognition cavities of the polymer; indeed, the best sensitivity (the highest slope) is obtained using the smallest anion Cl^-.

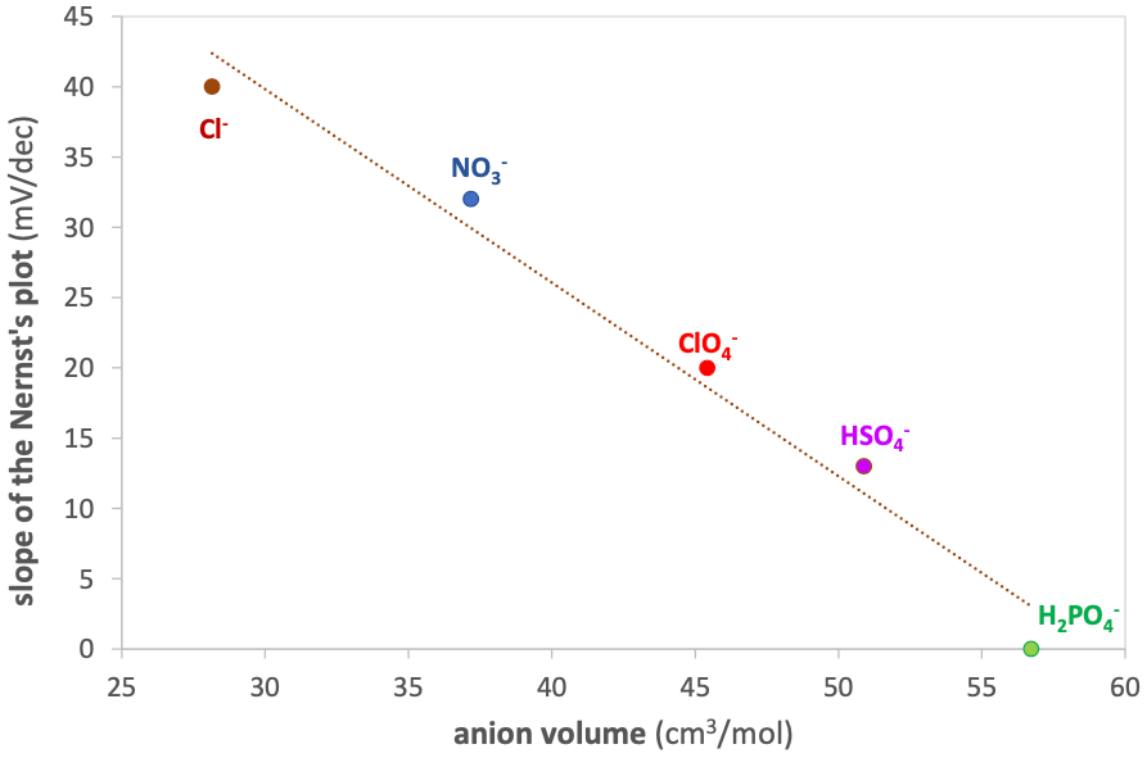

Figure 42. The slope of the Nernst's plot (mV/dec) vs anion volume (cm^3/mol) of the inorganic acids used as the ionic medium. Anion volume computed using Gaussian software[148].

Selectivity tests are performed using three different pesticides as interferent species: Simazine, Ametryn and Bentazone. The first two molecules are triazine herbicides, while the third is diazinic; the three molecular structures are reported in Figure 43.

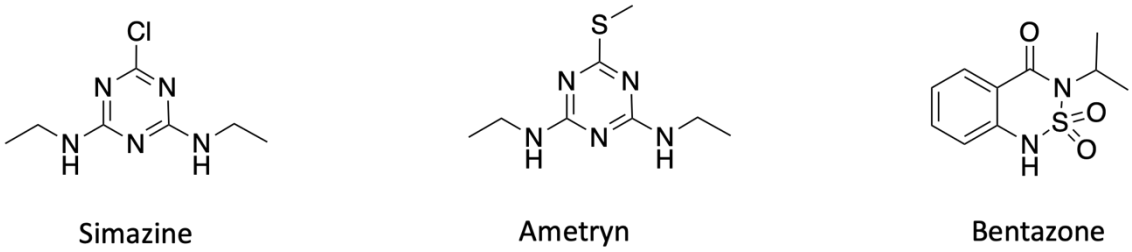

Figure 43. Molecular structures of the interferent species

Table 13 summarizes the slopes of the standardization curves (E (mV) vs. log[interferent]) obtained by analyzing solutions of each of the three pesticides taken individually; the results are compared to the slope of the calibration for Atrazine. As can be observed, the Bentazone does not cause interference; in fact, the variation of the potential in the presence of different amounts of Bentazone is irrelevant. This behavior is predictable since its molecular structure differs significantly from that of Atrazine. Ametryn and Simazine are more similar to Atrazine structure; indeed, the signal varies proportionally with the increasing concentration of interferent. The slopes are lower than that obtained for Atrazine but not enough to define their presence as negligible. This result is also relatively unsurprising, and for samples containing triazine pesticides, the proposed method cannot distinguish between them, and only a total concentration can be obtained.

Table 13. Slope standardization curves (in HCl at pH1.5) for the pesticides analyzed as interferents: Simazine, Ametryn and Bentazone. For comparison, the slope of the standardization curve for Atrazine is reported. Numbers in the brackets are the standard deviations on the last digit.

Pesticide	**Slope (mV/dec)**
Simazine	13(1)
Ametryn	30(2)
Bentazone	5(3)
Atrazine	40(6)

Measurements are also performed on tap water samples fortified with atrazine to demonstrate the applicability of the proposed sensor; for these tests, the standard additions method was applied. Tap water from the lab sink (Pavia, Italy) is acidified at pH 1.5, and different concentrations of Atrazine standard solution are added. The results are

summarized in Table 14. Recovery experiments. Portions of a tap water sample acidified at pH 1.5 with HCl and fortified with Atrazine. It can be observed that the % recovery values are between 91.7 % and 105.1 %, and the highest error is 4.3 %; these results confirm the good performances of the sensor and the potential for its application to atrazine detection in contaminated environmental samples.

Table 14. Recovery experiments. Portions of a tap water sample acidified at pH 1.5 with HCl and fortified with Atrazine

Spike (μM)	Found (μM, $\bar{x}\pm$ CI[1])	%RDS	% Recovery
0.462	0.47 ± 0.05	4.3	101.7
0.524	0.55 ± 0.05	3.6	105.1
0.642	0.59 ± 0.06	4.2	91.7
0.954	0.96 ± 0.07	2.9	100.8

[1]CI = 95% confidence interval. For 3 replicated, *t* = 4.3.

3.3.3.2 MIP-modified screen printed sensor for phenoxy herbicides[18]

Analogously to the previously developed MIP-modified screen-printed sensors for atrazine, the working electrode surface was characterized before and after modification with the MIP or NIP film. The differences in the SEM analysis of the bare and modified electrodes confirmed, even in this case, the successful imprinting of the polymer. Moreover, electrochemical impedance spectra similar to those obtained for the atrazine sensor confirmed the same behavior of the electrode surface before and after modification.

Once characterized, the modified screen-printed cell is used to perform potentiometric measurements. The molecularly imprinted polymer film on the working electrode surface acts as an anion-selective membrane since MCPA has a p*K*a=3.07 and, working in phosphate buffer pH 5.5, the predominant species at this pH is the negatively charged deprotonated form[149]. Figure 44a shows the structure of the deprotonated MCPA, while Figure 44b reports the graph of the species distribution in the function of pH.

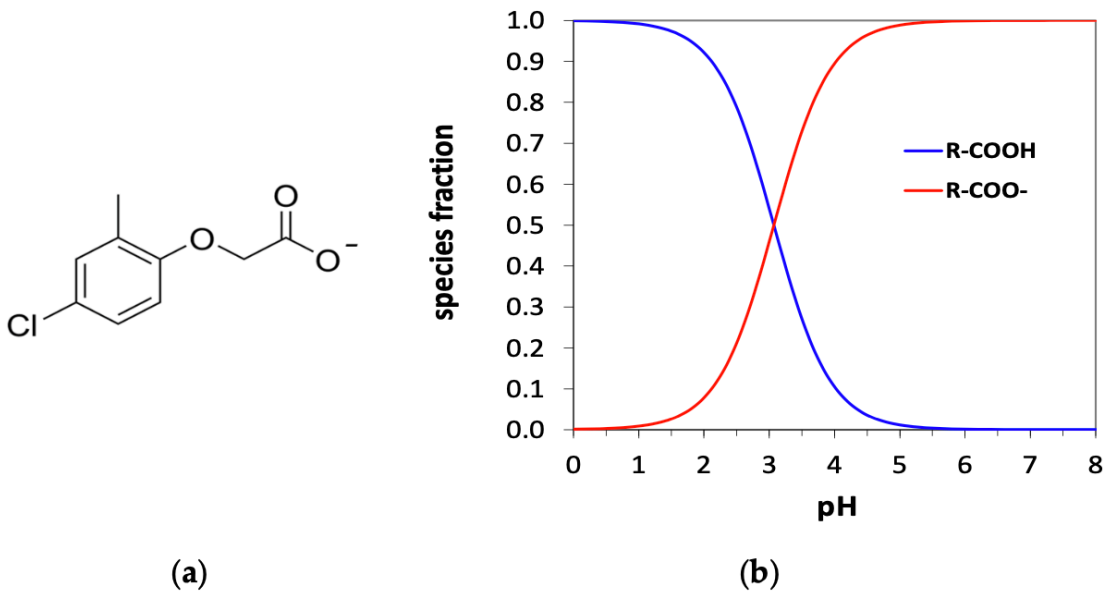

Figure 44. a) Negatively charged deprotonated form of MCPA; b) Graph of species distribution in function of the pH for MCPA.

Calibrations are obtained using three different MIP or NIP-modified screen-printed cells (SPCs). Each SPC is used twice, so the standard deviation is calculated on the slopes obtained from the resulting six different calibrations.

Figure 45 shows an example of the calibration curves obtained for MIP and NIP functionalized electrodes.

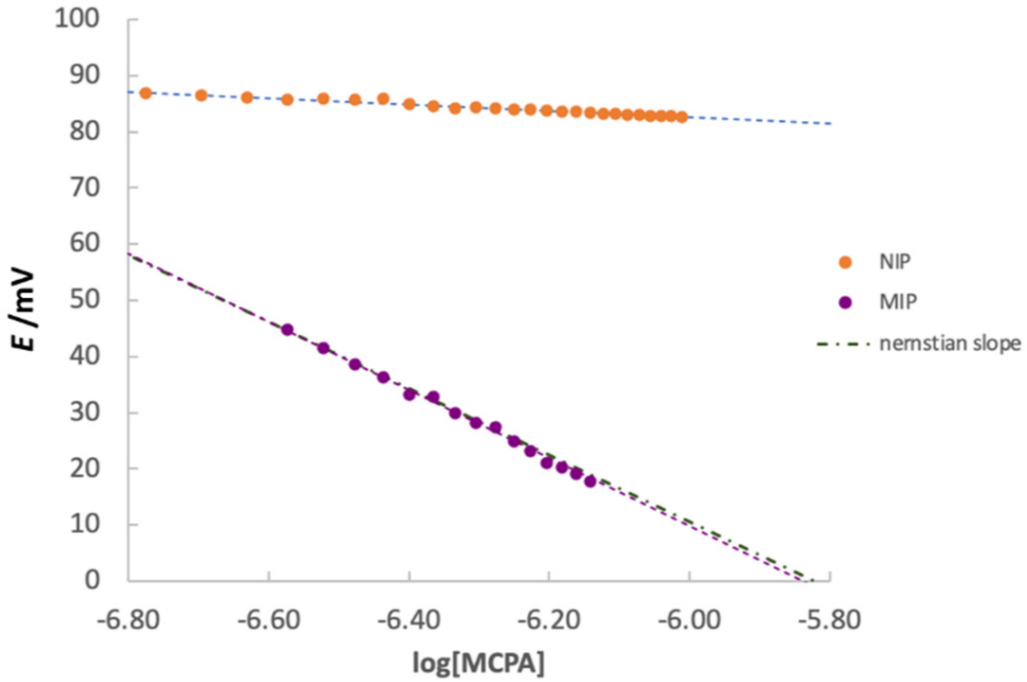

Figure 45. The calibration curve of MCPA of a screen-printed cell was modified with MIP (purple dots), NIP (orange dots), and the theoretical Nernstian slope (dotted green line). Experimental conditions: 15 mL phosphate buffer pH 5.5, additions of 0.02 mL MCPA std 25µM.

The average value of the slopes of the six calibration plots for the MIP-modified electrode is -59(1) mV/dec, very similar to the theoretical -59.2 mV/dec, expected from the pseudo-Nernst equation (eq.7). Conversely, the slope of the NIP-modified electrodes is much lower (of about -9(11) mV/dec; this means that these electrodes are poorly sensitive to the presence of MCPA in solution due to the unspecific interactions between the analyte and the polymeric film. The limits of detection and quantification are calculated as reported in eq 4 and eq 6 (see section 1.4.5*)* by considering the linearized Nernst equation $10^{E/slope}$ vs. MCPA (M). The LOD and LOQ obtained are 13 nM and 40 nM, respectively, demonstrating the high sensitivity of the sensor, although it is a potentiometric method.

Subsequent tests are performed investigating the three herbicides structurally analogs to MCPA, i.e., Mecoprop, Dichloroprop and 2,4-D Pestanal (see their structure in Figure 46) and one of a different structure, Bentazone, to evaluate the selectivity degree of the sensor.

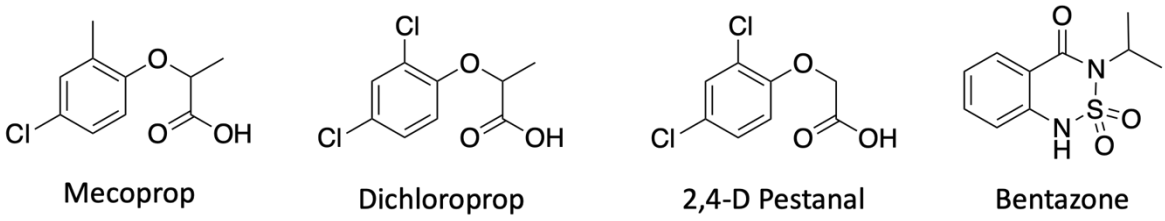

Figure 46. Molecular structure of interferents

Table 15 summarizes the slope value of the calibration curves (E/mV vs. log[pesticide]) obtained by analyzing the interferents without MCPA.

Table 15. Slope value of the calibration curves for each pesticide (average values obtained for three calibration curves for each pesticide). Numbers in brackets are the standard deviation on the last digit.

Pesticide	**Slope (mV/dec)**
Mecoprop	-54 (3)
Dichloroprop	-57 (5)
2,4-D Pestanal	-55 (3)
Bentazone	-1.3 (2)
MCPA	-59 (1)

As expected, the phenoxy-based molecules, similar to MCPA, show a slope very close to the theoretical one of -59.2 mV/dec, while the MIP-functionalized screen-printed cell is not sensitive to the presence of Bentazone; indeed, in this case, the slope is about -1mV/dec.

To corroborate these results, measurements are performed in solutions containing a constant concentration of interferent (0.5 μM) and increasing quantities of MCPA. As expected, the sensor is sensitive to the presence of both MCPA and another phenoxy herbicide when they are in solution together, while it is sensitive to only MCPA in solutions containing both MCPA and Bentazone. Table 16 shows the slope value of these calibrations. For the phenoxy herbicides, in the *x*-axis the logarithm of the sum of both herbicide concentrations is reported.

Table 16. Slope value of the calibration curves performed in solutions containing 0.5μM of MCPA and increasing quantities of each interferent. For the phenoxy herbicides, in the x-axis of the calibration plots, the logarithm of the sum of both the herbicides' concentrations is reported. Numbers in parentheses are the standard deviations on the last digit.

Pesticide	**Slope (mV/dec)**
MCPA + Mecoprop	-57(2)
MCPA + Dichloroprop	-55(3)
MCPA + 2,4-D Pestanal	-57(4)
MCPA + Bentazone	-60(2)
MCPA	-59(1)

As can be deduced from the values reported in Table 16, the MIP-based sensor is selective to phenoxy herbicides with similar structure and chemical behavior to the template MCPA; consequently, the sensor could be applied to evaluate the total degree of contamination from similar substances.

To verify the applicability of the sensor to environmental samples, some recovery tests are performed using tap water samples fortified with MCPA; for the quantification, the standard addition technique is applied. The tap water samples' pH is adjusted to 5.5 and spiked with different concentrations of MCPA. Table 17 summarizes the results.

Table 17. Recovery experiments. Tap water samples adjusted to pH 5.5 with phosphate buffer solution and spiked with different concentrations of MCPA

Spike Concentration (μM)	Found (μM, x ± CI[1])	% RDS	% Recovery
0.169	0.16 ± 0.04	2.5	98.5
0.101	0.10 ± 0.05	4.6	103.6
0.531	0.53 ± 0.02	0.5	100.5
0.918	0.93 ± 0.03	1.1	101.1

[1]CI = 95% confidence interval. For 3 replicates, *t* = 4.30.

The standard additions plots have slope values ranging from -57(3) mV/dec and -62(2) mV/dec, so the sample's matrix does not affect the sensor's response. As can be observed from Table 17, the % recovery ranged from 98.5% to 103.6%, and the precision was good since the highest value is around % RDS 4.6; therefore, these results are promising for practical applications of the developed potentiometric sensor for environmental samples contaminated by phenoxy herbicides.

3.3.4 Conclusions

New potentiometric MIP-based screen-printed sensors for Atrazine and phenoxy herbicides detection are proposed. The polymeric film covering the working electrode surface acts as an ion-selective membrane. Before and after the modification, the working electrode surface is characterized by determining the active area and evaluating the electrochemical impedance spectra. In both cases, the non-conductive nature of the acrylic polymer film coverage is confirmed.

For the atrazine sensor, the active ion is positively charged protonated form, so the determination is carried out at pH 1.5 in HCl. The obtained detection limit is 0.4 μM and the calibration curves' slope value is 40 mV/dec, i.e., a sub-Nernstian response. The experiments aimed at interpreting this behavior corroborate the hypothesis of a possible interaction of the anion of the acid used as the ionic medium with the polymer cavities. Indeed, it has been demonstrated that as the size of the anion increases, the slope decreases, deviating more and more from the Nernstian value.

The sensor selectivity is closely related to the size and geometry of the polymer cavities; indeed, the sensor can not discriminate herbicides with molecular structures similar to Atrazine.

For the phenoxy herbicides potentiometric sensor, the molecule used as the template is MCPA and, in this case, the active ion is the deprotonated form, so the measurements are performed in phosphate buffer at pH 5.5.

From the calibration curves, a slope value of -59 mV/dec, similar to the theoretical one, is obtained.

The interferent tests highlight similar sensing properties for the sensor toward phenoxy pesticides structurally similar to MCPA, i.e., Mecoprop, Dichloroprop and 2,4-D Pestanal; thereby, the sensor could be applied for the determination of the total degree of contamination coming from these herbicides. Conversely, the sensor does not respond to molecules with molecular structures different from MCPA, such as Bentazone.

The pretty good analytical figures of merits obtained are promising for the applications of both sensors to contaminated environmental samples.

3.4 SAM-modified screen-printed gold electrode for Fe(III) detection

3.4.1 Introduction

Deferoxamine (DFO) is immobilized as a functionalized self-assembled monolayer of a thiol (SAM) on the gold surface of the working electrode of a screen-printed cell to develop a voltammetric sensor for iron(III).

Deferoxamine (DFO) is a natural siderophore tri-hydroxamate produced by the bacteria *Streptomyces pilosus*[150]; it is a bidentate ligand that strongly binds hard cations like Fe(III) through its oxygen atoms. It has a low molecular weight, and it is water soluble. Deferoxamine is the active principle of Desferal®, a drug employed in the treatment of acute or chronic iron overload due to blood transfusion. Figure 47a shows the molecular structure of Deferoxamine, and Figure 47b shows the molecular model of the complex Fe(III): DFO.

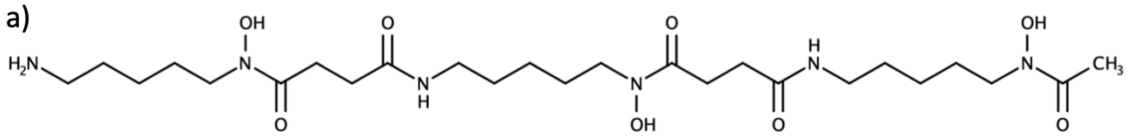

Figure 47. a) Deferoxamine molecular structure; b) molecular model of the complex Fe(III):DFO.

Deferoxamine properties have also encouraged the development of functional materials used as sorbents or sensors mainly for Fe(III), for example, mesoporous silica MCM-41[151,152], filter paper[153] or synthetic polymers and hybrid materials[154,155].

In the present study, deferoxamine is linked to a self-assembled monolayer (SAM) of a thiol (3-mercaptopropionic acid) on the gold surface of the working electrode of a screen-printed cell to develop a voltammetric sensor for iron(III).

3.4.2 Material and methods

3.4.2.1 Functionalization of the working gold electrode

The procedure for preparing a DFO-SAM on the gold electrode is adapted from that previously reported for an SPR deferoxamine-based sensor[156]. 7 μL of 20 mM MPA aqueous solution is drop-coated and soaked overnight to form the thiol SAM on the cleaned gold electrode surface. Then, the Au-MPA SAM is activated by drop-coating 7 μL of 0.1 M phosphate buffer solution (PBS) at pH 5.5, containing 2 mM EDC and 5 mM NHS for 1.5 h. The activated SAM layer was rinsed with PBA and used for functionalization by drop-coating 7 μL of 2 mM DFO aqueous solution and left to react for 2 h at room temperature. The functionalized electrode was rinsed carefully with ultrapure water to eliminate physically adsorbed species and dried in an N_2 atmosphere. When not immediately used, the functionalized electrode is stored in a 2 mM DFO solution.

3.4.2.2 Characterization of the working electrode surface

The working gold electrode surface of the screen-printed cell is characterized before and after the functionalization with the SAM layer. The electrochemically active area is determined by experiments in cyclic voltammetry employing the electrochemical probe 5mM $K_4Fe(CN)_6$/0.1M KCl at pH 7.2 (see paragraph 3.2.4.2) and the double layer capacitance is evaluated from CV experiments in 1 M acetic buffer at pH 4 (start potential +0.4 V, end potential +1 V, scan rate from 0.025 a 0.5 V/s) according to the procedure reported in paragraph 3.2.4.2.

3.4.2.3 Fe(III) determination by Differential Pulse Voltammetry (DPV)

Fe(III) is accumulated onto the functionalized gold electrode by immersion of the screen-printed cell in 15 mL of 0.01 M HNO_3 solution at different Fe(III) content for 2 min, at the open circuit, under gentle stirring. Then, the DPV measurements are performed in 0.1 M acetate buffer at pH 3.5, containing 0.1 M $NaClO_4$ as a supporting electrolyte. Electrochemical conditions are: Starting potential +0.9 V, end potential -0.1 V, scan rate 1000 mV/s, pulse amplitude 50 mV, pulse time 0.04 s. Figure 48 shows a schematic representation of the Fe(III) determination procedure.

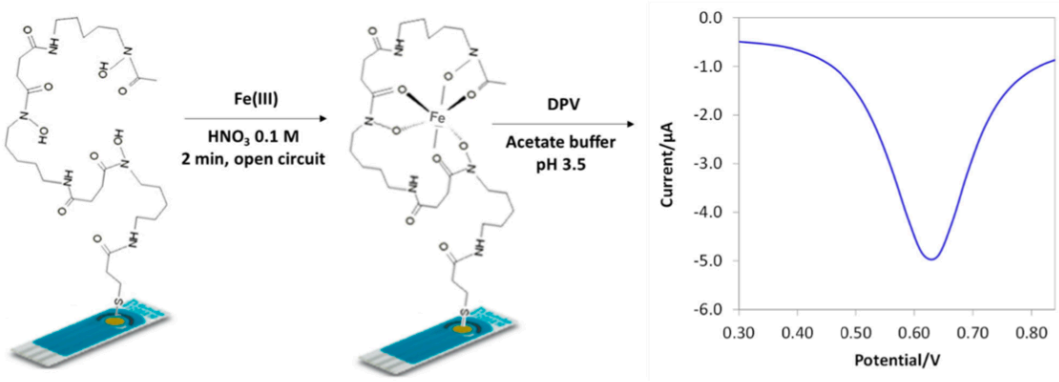

Figure 48. Schematic representation of Fe(III) determination procedure

3.4.3 Results and discussion

When working with a screen-printed cell, the main issue is to functionalize the single working electrode, avoiding contamination of the pseudo-reference and auxiliary electrodes; consequently, it is impossible to soak the whole cell in the reagents' solutions. The best option is to drop-coat the surface of the working electrode with the solutions containing the modifiers.

The second issue is to decide the soaking time. To form the thiol monolayer, 7µL of MPA solutions is left to dry at room temperature overnight. An experimental design is performed to optimize the soaking time needed for the second and third steps; in particular, a 2^2 full factorial design is applied. Table 18 reports the level definitions for the parameters under investigation.

Table 18. Full factorial design 2^2: level definitions for the parameters under investigation.

Parameter	Minimum level (-1)	Maximum level (+1)
Time second step (t_2 min)	90	180
Time third step (t_3 min)	60	120

As response, the current intensity of the peak obtained in DPV analysis is evaluated. The data obtained are processed by the open-source program CAT[32]. Figure 49 shows the graph representing the significance of the model's coefficients.

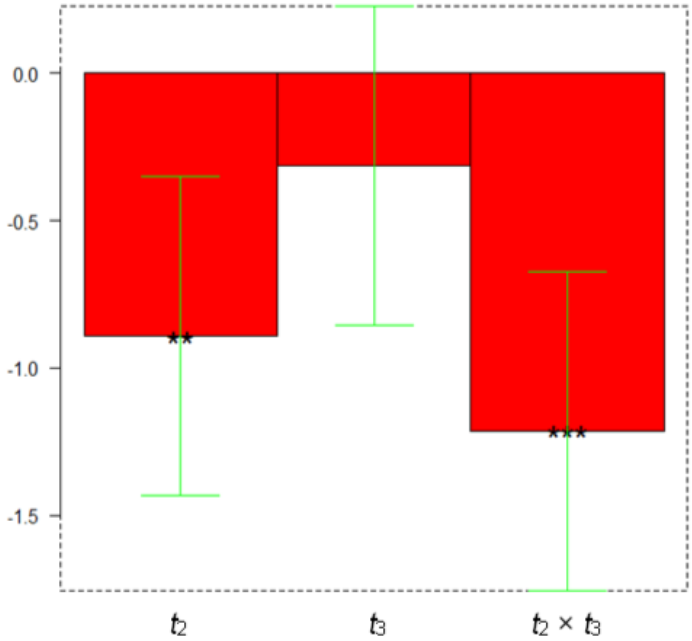

Figure 49. Experimental design to optimize the reaction times of the two functionalization steps of the working gold electrode: coefficients plot. The greatest values and little black stars (regardless of the sign) may suggest a significant influence of the respective parameter or interaction.

From the coefficient plot in Figure 49 it can be observed that the most significant coefficients are $b_{1,}$ related to t_2 (the reaction time of the second step), and b_{12}, related to $t_2 \cdot t_3$. The following equation describes the model: $R = b_0 + b_1 t_2 + b_2 t_3 + b_{12} t_2 t_3$. The interaction between the coefficients can also be evaluated from the isoresponse surface, which appears distorted, as shown in Figure 50.

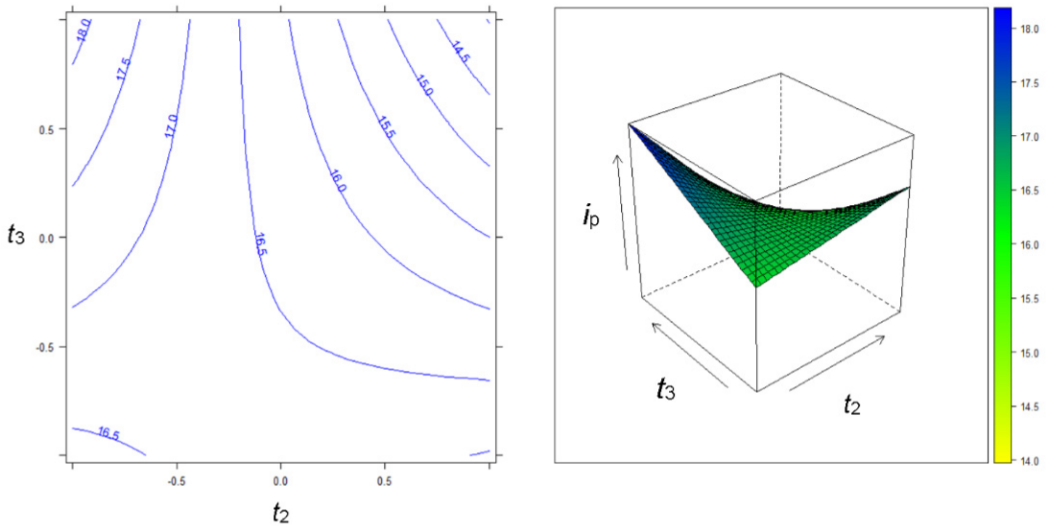

Figure 50. Experimental design to optimize the reaction time of the second and third steps for the gold electrode modification. The best sensor response was obtained for t_2 -1 (90 min) and t_3 +1 (120 min).

The best sensor response is obtained by modifying the screen-printed cell for 1.5 h in the second and 2 h in the third steps.

The working electrode is characterized before and after functionalization by determining the active area and the double-layer capacitance.

For the cleaned gold bare electrode, the computed area is equal to 0.12 (7) cm^2, which is not significantly different from the value provided by the manufacturer of 0.126 cm^2. The area is also determined after the functionalization with deferoxamine; in this case, a lower value is obtained equal to 0.11(7) cm^2. This experimental evidence can be justified considering that the deferoxamine monolayer above the working electrode reduces the electronic transfer capacity of gold.

The computed double-layer capacitance for the bare electrode is 2.7(1) μF while for the functionalized electrode is ten times higher about 28.81(4) μF. The capacitance of the double layer increases from the bare electrode to the functionalized one; this behavior is due to the presence of the DFO on the surface of the electrode, which can accumulate electrical charges on the electrode surface.

The DPV measurements are carried out by accumulating the Fe(III) without applying a deposition potential since only the metal cation is complexed by the ligand fixed on the working electrode surface. The acid pH of the solution is necessary to avoid the formation of Fe(III) hydrolysis products and to obtain less stable Fe(III)/DFO complexes, which can be reduced at less negative potentials. In the second step, the electrochemical reduction of the Fe(III) preconcentrated on the electrode surface is obtained by DPV in acetate buffer 0.1 M at pH 3.5, scanning the potential from +0.9 V to -0.1 V vs Ag/AgCl pseudo-reference electrode. A cathodic current peak appeared at about +0.63 V due to Fe(III) reduction to Fe(II). Figure 51 reports an example of DPV obtained for a calibration curve varying the Fe(III) concentration from 0 to 12 nM.

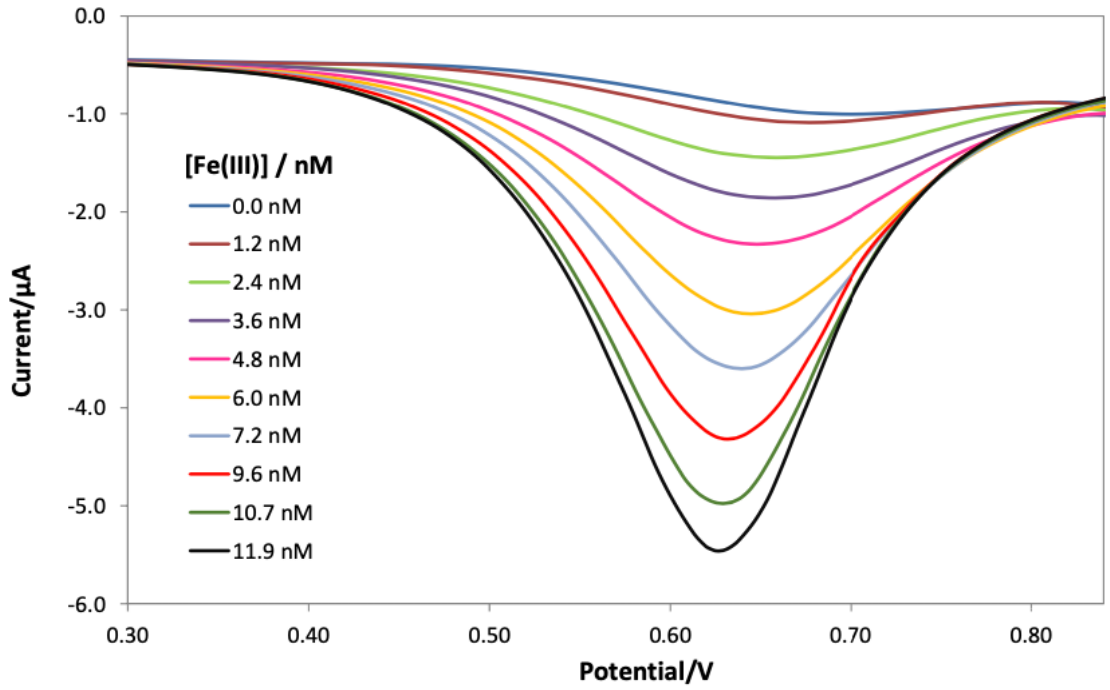

Figure 51. DPV plot obtained on the gold working electrode functionalized with DFO after immersion in Fe(III) standard solutions at pH 1 (from 0 to 12 nM); DPV measurements were performed in 0.1M acetate buffer at pH 3.5 containing 0.1M $NaClO_4$ as supporting electrolyte. Electrochemical conditions were: starting potential +0.9V, ending potential -0.1V, scan rate 100 mV/s, pulse amplitude 50 mV, pulse time 0.04s.

Calibration curves are realized using different screen-printed cells, all functionalized with the same procedure, since the removal of the thiol SAM would require electrochemical desorption in strong alkali or acid media. Figure 52 shows the calibration curve obtained by plotting the average of the peak currents values (absolute values, µA) against Fe(III) concentration (nM); error bars correspond to the standard deviation of the measurements performed with five electrodes. The equation of the straight line obtained from the five calibrations (dotted line in Figure 52) is reported below:

$|i_p| = 0.421(8)\cdot[Fe(III)] - 0.47(6) \quad R^2 = 0.997$

(numbers in parenthesis are the standard deviations reported as uncertainty on the last digit).

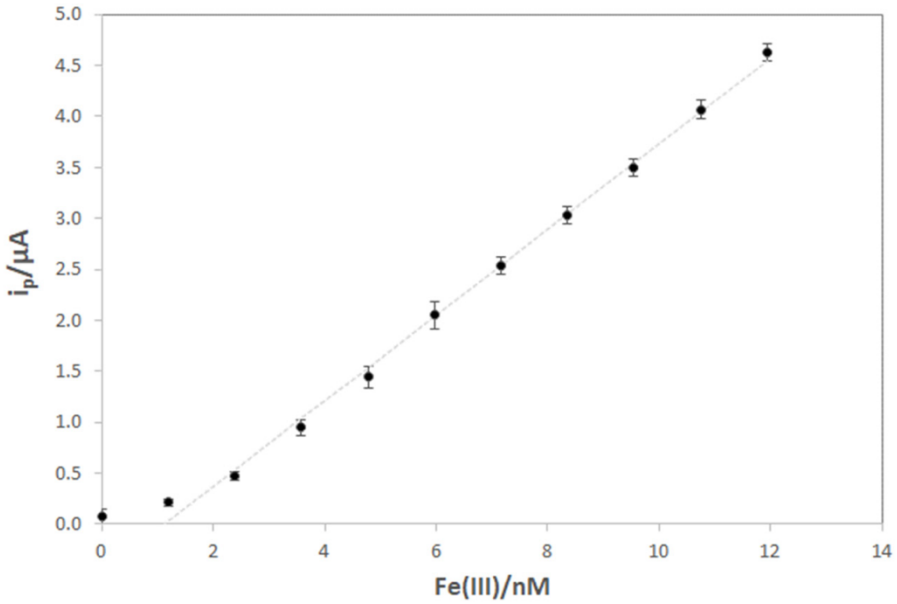

Figure 52.Calibration curve for Fe(III) determination by DPV. Each point is the average measurement value obtained with five screen-printed cells. Error bars correspond to the standard deviation of the measurements performed with five electrodes.

As can be observed in the graph, the linearity range is relatively small, covering only one order of magnitude, but enough to determine Fe(III) at a very low concentration. The detection limit is computed as reported in eq. 4 (see paragraph 1.4.5), obtaining a value of 0.47(6) nM (26(3) ng/L). Tests in the presence of interferents are then performed to verify the sensor's selectivity. Deferoxamine can form very strong complexes with metal ions usually present in real samples, for example, Al(III), Zn(II) and Cu(II); for this reason, measurements have been performed in the presence of these cations. Firstly, measurements are carried out on a sample containing only Fe(III) 0.2 µg/L (3.6 nM), and then after the addition of Al(III) 2 µg/L (74.1 nM), Zn(II) 2 µg/L (30.6 nM) and Cu(II) 2 µg/L (31.5 nM); the voltammogram is registered after each addition. As shown in Figure 53, the peak's position and intensity do not change. Definitely, the Fe(III) determination is not affected by the presence of a 10-fold increase in these cations.

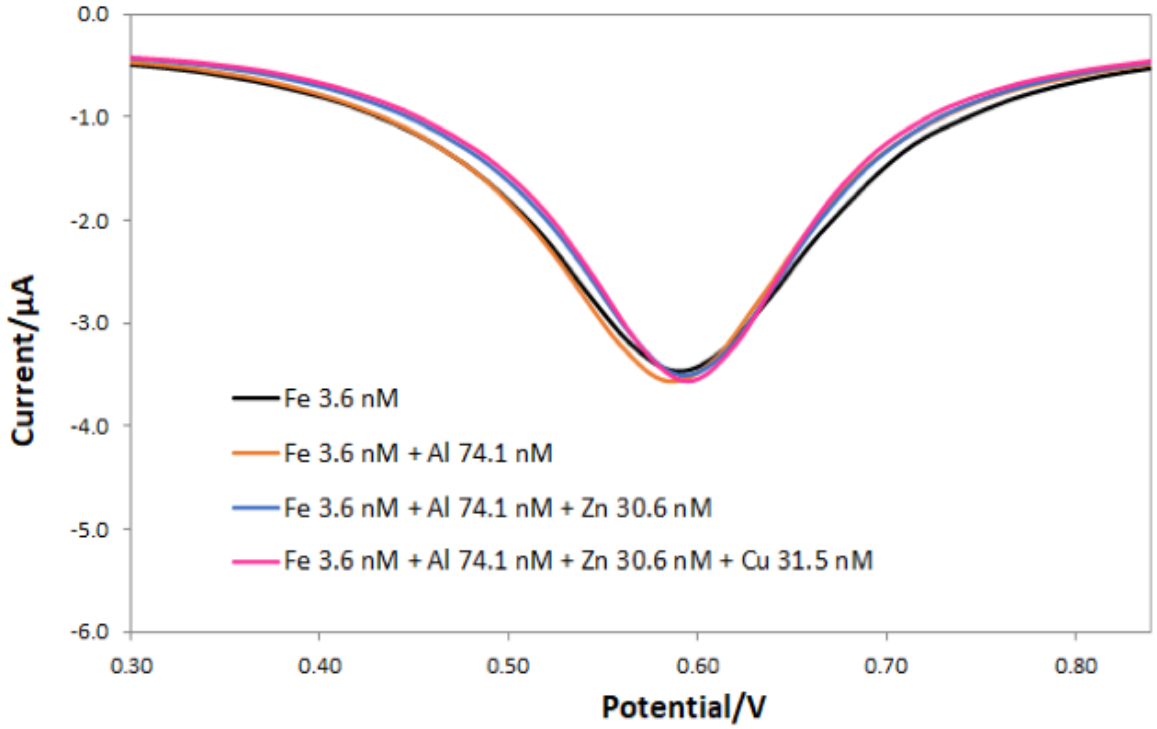

Figure 53. Differential Pulse voltammetry (DPV) of the gold screen-printed electrode modified with DFO SAM in solution containing only Fe(III) 3.6nM at pH1 (black line); Fe(III) 3.6 nM and Al(III) 74.1 nM at pH 1 (orange line); Fe(III) 3.6nM, Al(III) 74.1 nM and Zn(II) 30.6 nM; Fe(III) 3.6 nM, Al(III) 74.1 nM, Zn(II) 30.6 nM and Cu(II) 31.5 nM at pH 1 (pink line); DPV measurements were performed in 0.1M acetate buffer at pH 3.5 containing 0.1M $NaClO_4$ as supporting electrolyte. Electrochemical conditions were: starting potential +0.9V, ending potential -0.1V, scan rate 100 mV/s, pulse amplitude 50 mV, pulse time 0.04s.

A simulated tap water sample without Fe(III) is analyzed to prove the sensor's selectivity further. A mix of metals is used as a matrix and submitted to the whole procedure to construct the calibration curve with increasing concentration of Fe(III) (2 min of accumulation in HNO_3 solution at pH 1, and DPV measurements in 0.1 M acetate buffer at pH 3.5 containing 0.1 M $NaClO_4$ as supporting electrolyte). The composition of the matrix solution is reported in Table 19; the sample is then diluted 10-fold before being used in the calibration measurements.

Table 19. Cations' content for the simulated tap water sample without Fe(III)

Cation	Na(I)	K(I)	Ca(II)	Ng(II)	Zn(II)	Al(III)
mg/L	12	1.3	42	8.5	0.035	0.025

Figure 54 reports the DPV measurements and the calibration curve performed in the simulated tap water sample. As can be observed, the slope of the straight line interpolating the experimental point is equal to 0.405(8) µA/nM), which is very close to the value obtained for the calibration curve with a solution of only Fe(III). This effect is due to the

highest affinity of DFO for Fe(III) compared to the other cations investigated at the pH of the medium used for both accumulation and analysis.

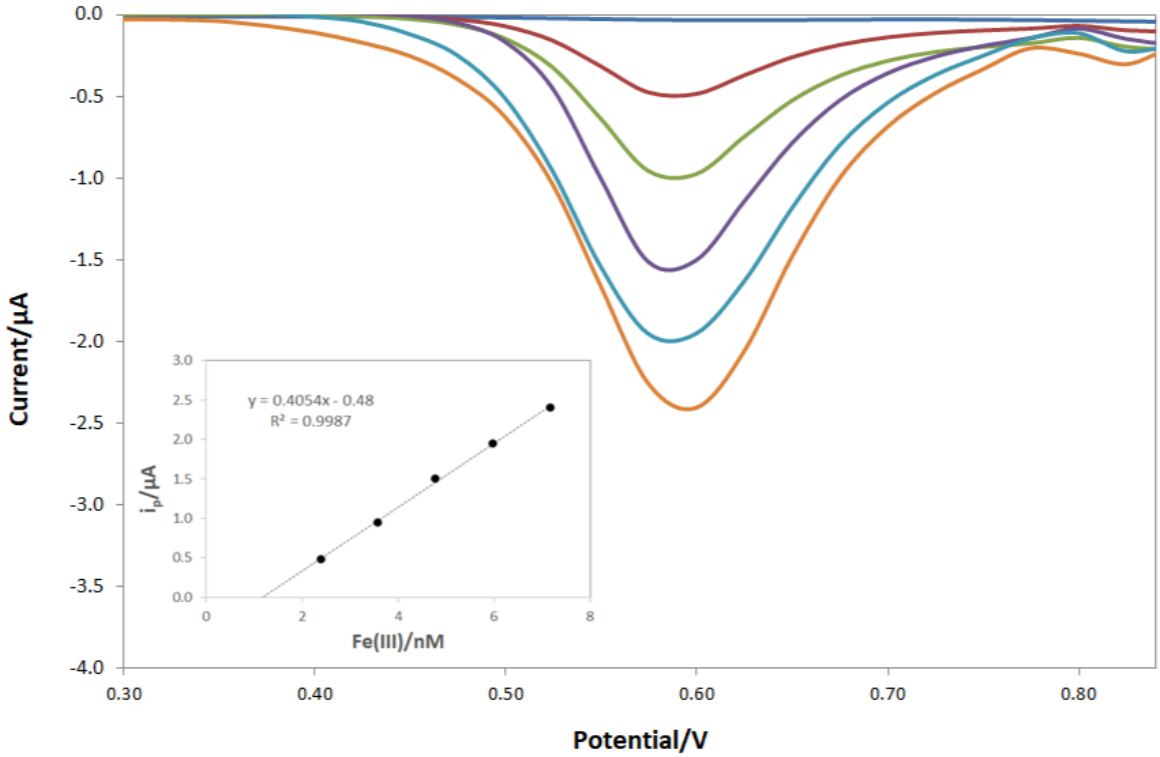

Figure 54. The DPV plot obtained on the gold working electrode modified with DFO after immersion in a simulated tap water sample diluted 10-fold with nitric acid solution at pH 1. Addition of Fe(III) from 0 to 7 nM. The calibration curve is reported as inset.

Further confirmation about the selectivity of the sensor under the condition of sorption and analysis of the metal cation is given by the distribution graphs for the cations/DFO complexes that highlights the predominance of the specie $FeHL^+$ at pH 3.5, while all other divalent cation at the same pH are present as free metal-ion specie, and only the complex $AlHL^+$ is present at the 10%. At pH 1 of the accumulation step, only Fe(III) can be complexed by DFO. Fe(II) does not give interference since it can not be complexed by deferoxamine. Figure 55 shows the distribution diagrams for Fe(III)/DFO, Al(III)/DFO, Cu(II)/DFO, Zn(II)/DFO, Ca(II)/DFO, Mg(II)/DFO, Fe(II)/DFO at 25°C and I=0.1M. protonation and complexation constants were obtained from[157].

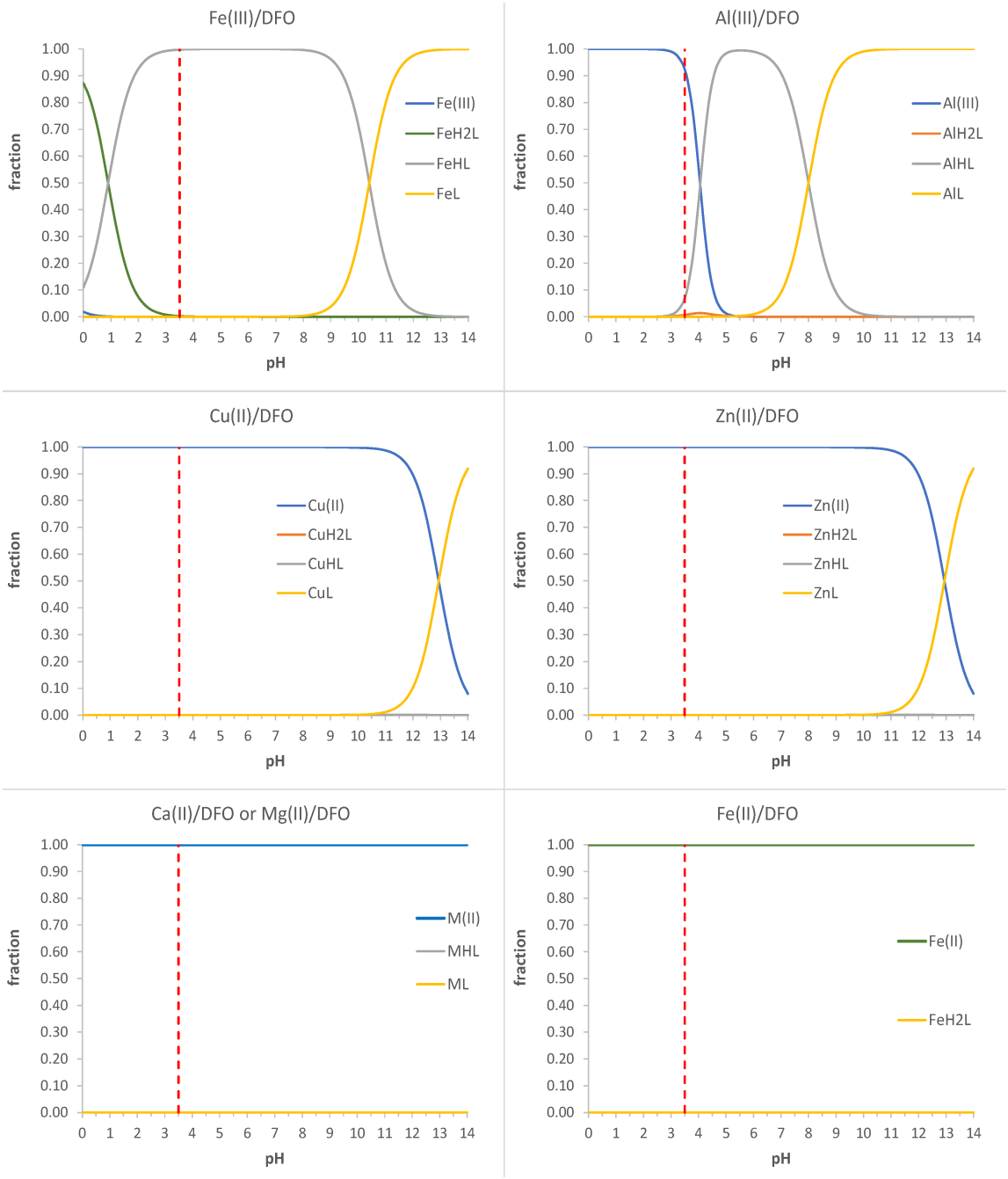

Figure 55. Distribution diagrams for the systems Fe(III)/DFO, Al(III)/DFO, Cu(II/DFO; Zn(II)/DFO, Ca(II)/DFO, Mg(II)/DFO, Fe(II)/DFO, at 25 °C and I = 0.1 M. Protonation and complexation constants obtained from ref. [157]

Finally, a tap water sample obtained from the laboratory sink is tested. The sample is diluted 100 times with ultrapure water before voltammetric measurements. The determination is performed in triplicate using three different modified gold screen printed cells and applying the standard addition method since it permits to prevent the errores caused by the eddy currents that change from electrode to electrode. The concentration of Fe(III) in the original sample, expressed as the mean of the values obtained with the

three electrodes, is 18(6) μg/L (0.3(1) μm), not significantly different from the value obtained by ICP-OES (17(5) μg/L, 0.30(9) μM).

3.4.4 Conclusions

The working gold electrode of screen-printed cells modified with a SAM of mercaptopropionic acid SAM functionalized with DFO is developed as a voltammetric sensor of Fe(III). The detection limit of the developed method is about 0.5 nM. The selectivity tests demonstrated that many inorganic cations in tap water do not interfere since DFO strongly interacts with Fe(III). The Fe(III) concentration measured in real tap water sample does not differ significantly from that measured in ICP-OES, demonstrating that the sensor developed could detect Fe(III) in environmental and biological samples at low metal-ion content.

3.5 Cysteamine-copper SAM-modified screen-printed gold electrode for glyphosate determination

3.5.1 Introduction

N-(phosphonomethyl)glycine, also known as Glyphosate, is a herbicide discovered in 1950 which became the most widely used worldwide. It is a systemic weed killer and crop desiccant that inhibits the plant enzyme 5-enolpyruvylshikimate-3-phosphate synthase[158–160]. In recent years, the use of this herbicide has been debated due to its long-term environmental impact. Glyphosate Is absorbed by the leaves; in this way, it gradually penetrates the entire food chain[161]. The EFSA (European Food Safety Authority) and the US EPA (Environmental Protection Agency) have set the maximum residue limits as 20 mg/L (EPA) in soybean, 0.1ng/mL (EFSA) and 700ng/mL (EPA) in drinking water[162].

Glyphosate is a tetra-protonated compound characterized by four pKa: 0.8, 2.23, 5.46 and 10.14; in natural waters, it is present in zwitterionic form[163]. Figure 56 shows the molecular structure of glyphosate.

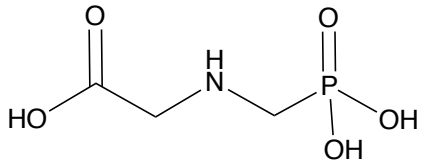

Figure 56. Glyphosate molecular structure

Glyphosate determination is generally performed by High-Performance Liquid Chromatography (HPLC) or Gas Chromatography (GC) coupled with mass spectrometry, UV-vis or fluorescence detectors. These typologies of techniques are very sensitive but expensive; the columns need derivatization, measurements can not be performed in real-time, and they need expert operators[164–166].

In this scenario, we proposed a gold screen-printed cell modified with a cysteamine-copper(II) self-assembled monolayer (SAM) for the voltammetric determination of Glyphosate. Since Glyphosate is non-electroactive, the electrochemical method must be indirect. The present method relies on the interaction of glyphosate with copper(II) ions complexed by a cysteamine SAM covering the working gold electrode surface of a screen-printed cell, which results in the decrease of the reduction signal of copper(II). Data treatment is performed using chemometric tools that are relatively uncommon for

processing electroanalytical data since the voltammograms strongly depend on the experimental parameters and suffer from poorer reproducibility and matrix effect.

3.5.2 Material and methods

3.5.2.1 Working electrode cleaning

Screen-printed cells (SPC) must be cleaned before use to remove any impurities and traces of oxides from the gold working electrode surface. For this purpose, SPC is submitted to electrochemical cleaning by cyclic voltammetry in sulfuric acid 0.1 M from - 1 V to +1 V, at 0.1 V/s, until reaching the stability of the voltammograms (overlap of the curves, which is typically observed after 20 cycles), rinsed with ethanol and dried under N_2.

3.5.2.2 Cysteamine-copper SAM formation on the gold working electrode

Cysteamine-Copper SAM is obtained in two steps. Firstly, 5 µL of cysteamine solution (5 mM in 99.9 % ethanol) are dropped on the cleaned gold working electrode surface (ensuring that the solution did not come into contact with the other two electrodes) and let stand for 12 h in a closed vessel to let the cysteamine molecules lining orderly up onto gold surface forming a self-assembled monolayer (SAM). The SAM-modified screen-printed cell is rinsed 3 times with ethanol (0.1 mL) and ultrapure water, then dried under N_2. 3 µL of 1 g/L copper(II) solution are deposited on the thiol SAM, let stand for 2 h, rinsed again 3 times with ethanol (0.1 mL), ultrapure water, and dried under N_2. The modified electrodes can be stored in a closed container for weeks without losing performance. Figure 57 schematizes the whole functionalization procedure.

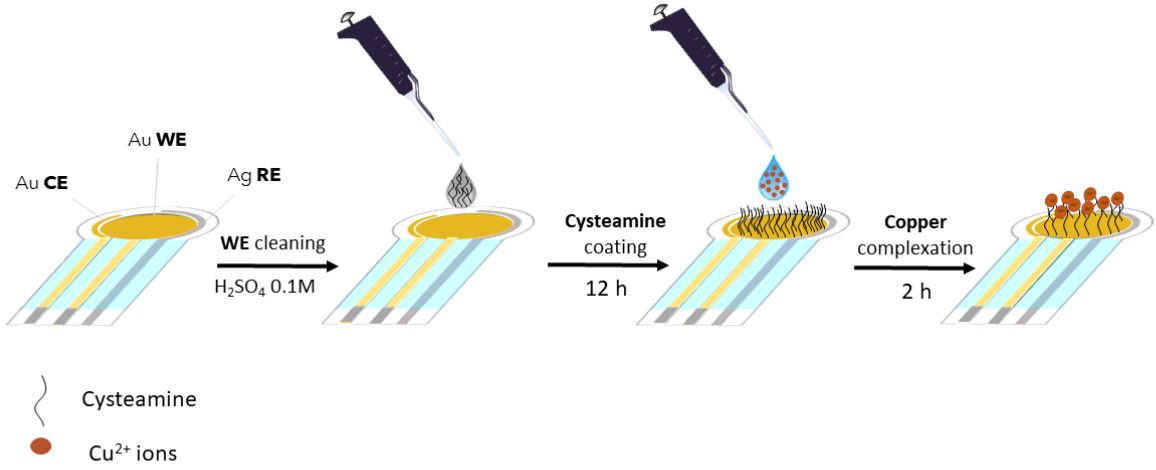

Figure 57. Schematic representation for the working electrode's functionalization with Cysteamine-copper SAM.

3.5.2.3 Characterization of the working electrode surface

Before and after the surface modification, the working gold electrode of the screen-printed cell is characterized by determining the active area according to the procedures described in paragraph 3.2.3.1, using ferrocene 1mM in acetonitrile containing 0.1 M tetrabutylammonium perchlorate as the electrochemical probe. Moreover, the surface coverage (Γ, mol/cm^2) before and after the formation of the cysteamine-SAM and the subsequent addition of Cu(II) and the electron transfer rate ($k°$) are evaluated as reported in paragraph 3.2.3.3.

Electrochemical Impedance Spectroscopy (EIS) measurements are even performed to further characterize the surface of the working electrode before and after the functionalization.

3.5.2.4 Glyphosate determination by cysteamine-copper SAM-modified screen-printed cell

The determination of Glyphosate with the working gold electrode of the screen-printed cell modified with a cysteamine-copper(II) SAM is carried out using the cyclic voltammetry in phosphate buffer 0.05 M, pH 8, as supporting electrolyte, scanning the potential from -1 V to +1.5 V with a scan rate of 0.1 V/s. Before starting the measurements, the modified screen-printed cell is submitted to 20 CV scans in the supporting electrolyte medium until signal stability. Subsequently, after each Glyphosate addition (from 5µM to 110µM), the solution is stirred for 3 min before recording the cyclic voltammograms. An electrode can be used for one calibration only since these kind of electrochemical sensors are disposable.

3.5.2.5 Chemometric data treatment

The chemometric method of Partial Least Square regression (PLS) is applied to extract quantitative information from the voltammograms. In particular, this tool is employed to develop models to relate the electroanalytical signals (the entire cyclic voltammogram) to the Glyphosate concentration. PLS is a technique that combines features from Principal Component Analysis (PCA) and Multiple Regression. PLS is commonly applied to the simultaneous analysis of two datasets, such as, in this case, cyclic voltammograms and concentration.

The methodology for building a PLS model starts by selecting a suitable data set, called the "training set," obtained by planning the preparation of glyphosate standard solutions at different concentrations to cover the entire experimental domain homogeneously.

The training set comprises the data of three different 11-point calibrations performed with as many modified electrodes (33 rows and 501 columns, i.e., 11 concentrations per three electrodes and the current values per 501 potentials). The PLS model is first tested by a cross-validated procedure on the training set and subsequently on an external data set (test set). A series of independent glyphosate solutions are prepared for this purpose; the dimensionality of the test set matrix is 7 rows (7 concentrations) and 501 columns (current values per 501 potentials).

A similar training set is prepared to develop the PLS model for matrix-matched solutions (tap water). Then, two tap water samples are fortified with different glyphosate concentrations (35 µM and 73 µM) and used as the external dataset. The recovery percentage is computed from the predicted concentration values. All the data are analyzed using the open-source software CAT[32].

3.5.3 Results and discussion

3.5.3.1 Electrochemical characterization of the working electrode surface

Before and after the surface modification, the working gold electrode of the screen-printed cell is characterized by determining the active area; in particular, the determination is performed for the bare gold electrode (Au bare), for that modified with cysteamine SAM (Au_Cys) and after addition of Cu(II) (Au_Cys_Cu) by applying the Randles-Sevick equation (eq.8). The obtained results are reported in Table 20.

Table 20.The active area values computed by the Randles-Sevick equation (eq.8). Electrochemical probe: 1mM ferrocene in acetonitrile containing 0.1M tetrabutylammonium perchlorate. The standard deviation on the last digit is reported in brackets.

	Active area (mm^2)
Au bare	5.0(4)
Au_Cys	3.8(4)
Au_Cys_Cu	6.0(6)

As can be observed from the values, the active area slightly decreases, passing from the bare to the Au_Cys electrode. This behavior is already being observed in other studies[113], and it may be due to the blocking effects of the cysteamine on the surface of the electrode. The active area in the presence of cysteamine-copper SAM is slightly higher than the bare

electrode; this effect may be attributed to the contribution of copper to the electron transfer acting as an electron bridge from the surface to the probe in solution.

The surface of the gold working electrode is also characterized by defining the coverage Γ (mol/cm^2) and the electron transfer rate *k*° (cm/s) values; the obtained values are reported in Table 21.

Table 21. Values of the surface coverage and electron transfer rate for the bare and modified electrodes

Electrode	Γ**(mol/cm^2)**	***k*° (cm/s)**
Au bare		$3.9(6)\cdot10^{-3}$
Au_Cys	$1.9\cdot10^{-9}$	$4.8(8)\cdot10^{-3}$
Au_Cys_Cu	$2\cdot10^{-9}$	$1.2(6)\cdot10^{-4}$

The surface coverage value for cysteamine and copper ions suggests a 1:1 stoichiometry of the complex, indicating the formation of a monolayer for both cysteamine and Cu(II). The electron transfer rate values (*k*°) for the bare and the cysteamine SAM-modified electrodes are not significantly different; otherwise, the value for the electrode covered with the thiol-copper monostrate is lower due to the less efficient tunneling effect determined by the cysteamine/copper complex, as also demonstrated by the following electrochemical impedance spectroscopy (EIS) measurements. EIS measurements are performed in electrochemical probe 5 mM $K_3Fe(CN)_6$/0.1 M KCl on the gold bare electrode, modified with cysteamine SAM (Au_Cys), with Cysteamine-Cu(II) SAM (Au_Cys_Cu) and with Cysteamine-copper SAM after equilibration in 110 µM Glyphosate solution. Figure 58 shows the Nyquist plot and the Randles equivalent circuit for the electrodes cited above. The values of the Randles equivalent circuit elements for each electrode used for the data fitting are reported in Table 22.

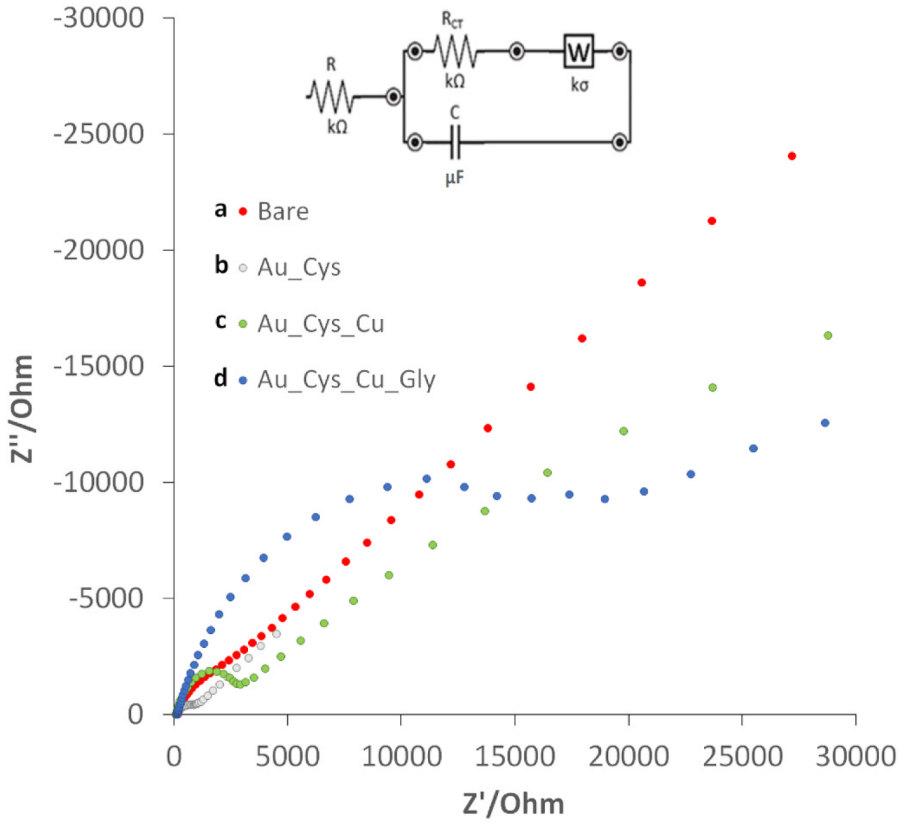

Figure 58. a) Nyquist plot of a)bare electrode, b) cysteamine-modified gold working electrode, c) cysteamine-copper modified gold working electrode, d) cysteamine-copper modified gold working electrode after equilibration in Glyphosate 110 μM solution. B) Randles equivalent circuit of the Nyquist plot. Measurements performed in 5 mM $K_eFe(CN)_6$/0.1 M KCl solution; frequency range 100 kHz ÷10 mHz; signal amplitude = 50 mV.

Table 22. Values of the Randles equivalent circuit elements for each electrode reported in Figure 67.

	R (kΩ)	R_{CT} (kΩ)	C (μF)	W (kσ)
Au bare	0.19	1.35	0.51	0.9
Au_Cys	0.27	3.00	0.33	0.35
Au_Cys_Cu	0.14	7.65	3.05	0.91
Au_Cys_Cu_Glyphosate	0.23	17.20	1.62	0.15

R=electrolyte resistance; R_{CT}=charge transfer resistance; C=double-layer capacitance; W=Warburg impedance

As can be observed in the Nyquist plot, the electrochemical behavior of each electrode is different from the others; for example, for the bare electrode, the Warburg diffusion predominates on the charge transfer resistance; indeed, the semicircle almost disappears due to the fast electrode reaction of the redox couple $Fe(CN)_6^{3-}/Fe(CN)_6^{4-}$. The charge transfer resistance toward the selected electrochemical probe for the other three modified electrodes is higher than in the bare electrode, as evidenced by the larger semicircle. The modification of the electrode surface by resistive monolayer changes the alternate current (ac) response[167]. The charge transfer resistance gradually increases, proceeding from the

Au_Cys electrode to the Au_Cys_Cu electrode; in this last case, the slight increase in the R_{CT} value can be justified by considering two effects: the electrostatic attraction due to the positively charged surface and negatively charged probe $Fe(CN)_6^{4-/3-}$ and the blocking effect determined by the cysteamine/copper complex, and the less efficient tunneling effect determined by the cysteamine/copper(II) complex, being the second one dominant. The addition of glyphosate to the solution and operating with the Cu-Cysteamine SAM provokes a considerable increase in the charge transfer resistance since no electrostatic interaction between the probe and electrode surface occurs due to the complexation of copper with the herbicide, remaining only the less efficient tunneling effect toward the electron transfer.

Figure 59 shows the cyclic voltammograms recorded in phosphate buffer 0.05M pH = 8 at each modification step.

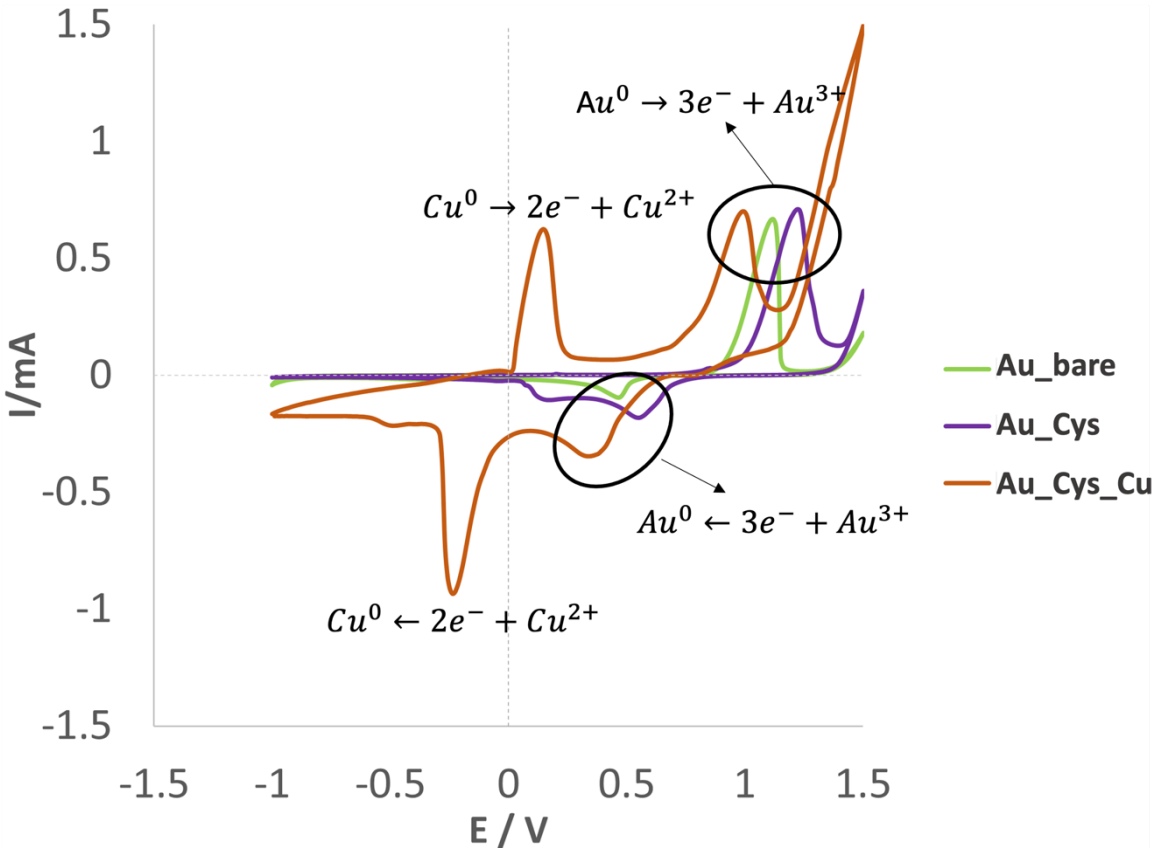

Figure 59. Cyclic voltammograms in phosphate buffer 0.05M, pH = 8 at each step of the modification. CV registered from -1V to +1-5V, scan rate 0.1V/s.

The cathodic peak attributable to the reduction of Cu(II) to Cu(0) appears at - 0.3 V; the peak at about +1 V and those in the reduction direction at about +0.45 V can be assigned to the gold redox processes. By operating in a different media, such as 0.1 M KNO_3 instead

of phosphate buffer, the CV profile became more complicated as the reduction of copper proceeds in two-wave steps, from Cu(II) to Cu(I) and from Cu(I) to Cu(0), for this reason, the measurements were performed in PBS buffer.

3.5.3.2 Voltammetric determination of glyphosate using SAM-modified screen-printed cell

Glyphosate, as stated before, is non-electroactive; for this reason, its electrochemical detection is challenging. The here-developed method describes an indirect strategy for glyphosate determination. The free amine of the cysteamine SAM, covering the gold surface of the working electrode, forms a complex with the copper(II) cations. When glyphosate is added to the supporting electrolyte solution, the reduction current of Cu(II) decreases since the interaction with glyphosate.

Indeed, glyphosate has three functional groups in its structure, i.e., carboxyl, amine, and phosphonic groups, that can strongly coordinate transition metal ions, such as copper(II)[168–171]. As an example, Figure 60 shows the cyclic voltammograms of one calibration.

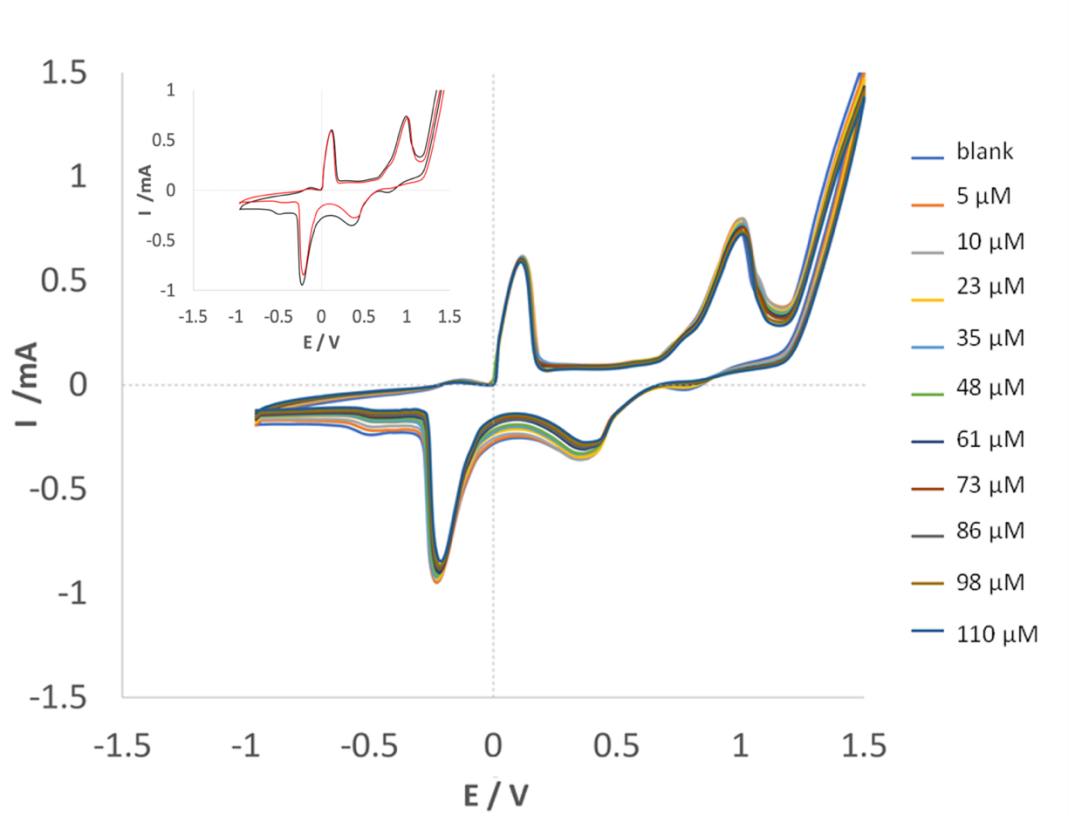

Figure 60. Cyclic voltammograms of the calibration for Glyphosate determination by the cysteamine-copper SAM-modified-screen printed cell. CV registered from -1 V to +1.5 V, scan rate 0.1 V/s in 10 mL of phosphate buffer 0.05 M pH=8 at different Glyphosate content. Before each measurement, the solutions are gently stirred for 3 minutes. In the insert are reported the cyclic voltammograms of the blank and the solution after the addition of 110 µM Glyphosate.

As shown in Figure 60, the Cu^{2+} cathodic peak decreases while the concentration of analyte increases, as expected, due to the competition between Glyphosate and cysteamine for copper(II) complexation. It can also be observed that besides the Cu(II) cathodic peak decreases, there is a shift and a shape change of the voltammogram; the univariate data treatment using the information given by the voltammograms is impossible. For this reason, a multivariate approach was chosen.

A data set was built using the voltammograms of three different 11-point calibrations performed with as many modified electrodes. The model was validated by predicting the test dataset and comparing the experimental values with the calculated ones.

The Partial Least Square regression analysis revealed that 6 latent variables represented the best compromise between the descriptive and predictive capability of the model; the figures of merit are reported in Table 23.

Table 23. The number of latent variables (LVs), % explained variance in cross-validation (%Exp.Var.CV), Root Mean Square Error in CV (RMSECV) and Root Mean Square Error in Prediction (RMSEP), and the correlation coefficient of the regression line (r^2) for the PLS model-glyphosate standard aqueous solutions.

PLS model (glyphosate standard aqueous solutions)		
Training set	LV_s	6
	%Exp.Var.CV	88.96
	RMSECV (µM)	12.3
	r^2 model	0.967
Test set	RMSEP (µM)	8.0
	r^2 prediction	0.992

Figure 61 compares experimental and predicted values for the training set (blue points) and test set (red points); predicted and experimental concentrations are not significantly different at 95 % of confidence. Table 24 summarizes the relative error % between the experimental Glyphosate concentration of the solutions used as the test set and the predicted values. All the concentrations are predicted with an error % lower than 10%.

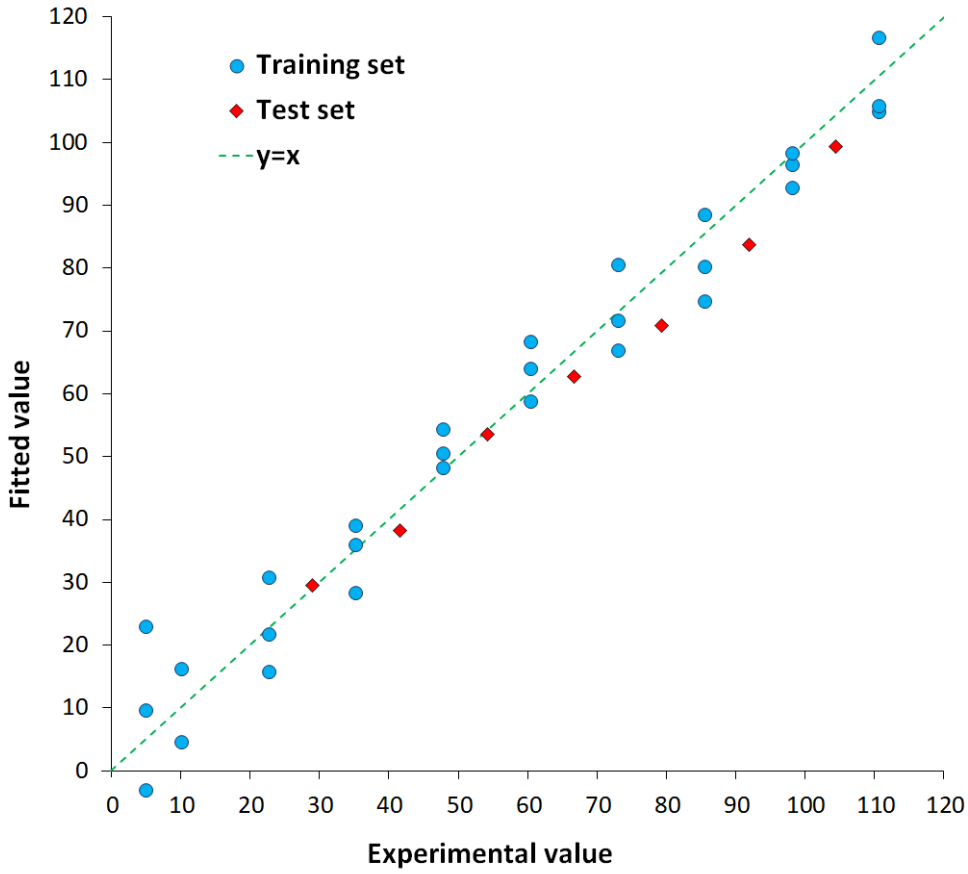

Figure 61. Experimental values vs. Fitted values plot for the training set (blue dots) and test set (red dots) samples of PLS model-Glyphosate standard aqueous solutions. Scales reference in μM concentrations.

Regarding the detection limit (LOD), there is currently no defined procedure for multivariate calibration. Defining an estimator for the LOD is more complex than extending the traditional univariate procedure; for this reason, only the lowest quantifiable concentration (LOQ) of glyphosate by the proposed method is reported, i.e., 5 μM. Since the glyphosate content in water should be below 4 μM according to the US standards, and the limit set by the European Union is below 0.6 nM, a pre-concentration step, for example, by a solid phase extraction (SPE) is needed before the application of the electrochemical sensors to uncontaminated waters.

Table 24. Validation of the PLS model: predicted values and prediction errors.

Nominal concentration (μM)	Predicted value (μM)	E%
28.9	29.5	1.9
41.5	38.2	7.9
54.1	53.5	1.2
66.7	62.8	5.9
79.2	70.8	10
91.9	83.7	8.8
104	99.3	4.9

The reliability of the proposed sensor was verified by analyzing tap water samples spiked with glyphosate. As well known, drinking waters contain cations such as Ca^{2+}, Mg^{2+}, K^{+} and Na^{+} that can interfere with Glyphosate detection since they can form complexes with it[169,171,172]. As the first trial, the cyclic voltammograms of the fortified tap water samples spiked with different concentrations of Glyphosate are projected in the PLS model previously developed. As expected, the predicted concentrations are definitively wrong, being highly overestimated (see Figure 62). Indeed, like for all analytical methods subject to interferences or when complex real matrices have to be analyzed, calibration with external standard solutions is unsuccessful for the analyte quantification. The standard additions method or matrix-matched calibrations are the usual strategies to overcome interferences and complex matrix problems. The second approach is adopted here. Therefore, a new PLS model is developed using matrix-matched solutions (tap water), adopting the same criteria assumed in the previous one. Two tap water samples are fortified with Glyphosate concentrations of 35μM and 73μM and used as an external dataset (3 replicates for each sample). In Figure 62b, the comparison between the experimental value vs. predicted value plot for the training set (blue dots) and test set (yellow dots) is shown, and the model's figures of merit are summarized in Table 25.

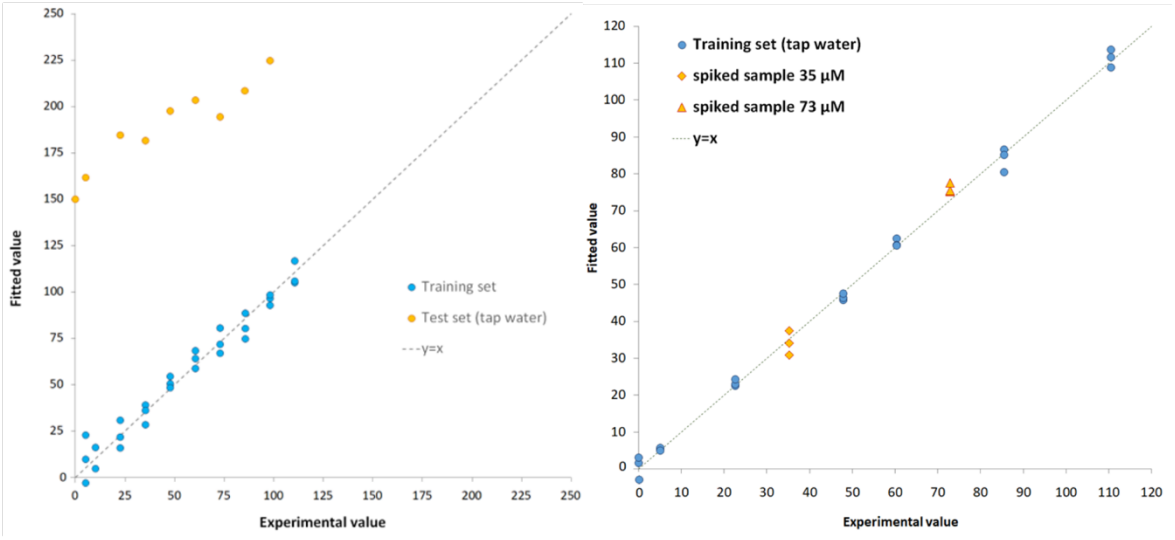

Figure 62. **(a)** Experimental vs. Fitted plot for the training set (blue dots) and test set (glyphosate-spiked tap water samples, yellow dots) of the PLS model-glyphosate standard aqueous solutions. **(b)** Experimental values vs fitted value plot for the training set (blue dots) and test set (yellow dots) samples of the PLS model-glyphosate tap water. Scales reference µM concentrations.

Table 25. Number of latent variables (LVs), % explained variance in cross-validation (%Exp.Var.CV), Root Mean Square Error in CV (RMSECV) and Root Mean Square Error in Prediction (RMSEP), and the correlation coefficient of the regression line (r^2) for the PLS model-glyphosate tap water.

PLS model (glyphosate tap water)		
Training set	LV_s	6
	%Exp.Var.CV	91.2
	RMSECV (µM)	10.9
	r^2 model	0.997
Test set	RMSEP (µM)	3.1
	r^2 prediction	0.991

The recovery percentage is computed from the predicted concentration values and reported in Table 26.

Table 26.Recovery test. The number in parenthesis is the standard deviation.

Added (µM)	**Found$_{LC-MS}$ (µM)**	**Found$_{SPC}$ (µM)**	**Rc%**	**E%**
35	35.7(8)	34(2)	97	-3.4
73	73.8(9)	76(1)	104	4.8

The obtained recovery values are between 80% and 110%, i.e., the acceptable recovery range[90,91] for each concentration, demonstrating that the proposed method is adequate for the quantification of Glyphosate in natural waters even in the presence of interferents, such as the cations macro constituents always present in natural water.

3.5.4 Conclusions

A gold screen-printed electrode modified with a cysteamine-copper(II) SAM is developed for Glyphosate detection in water samples. Since Glyphosate is a non-electroactive molecule, an indirect method is developed.

The gold-ink working electrode of the screen-printed cell is modified with a cysteamine-copper SAM, and the measurements are performed by Cyclic Voltammetry from -1 V to +1.5 V, 0.1 V/s in PBS 0.05 M at pH=8. When increasing concentrations of Glyphosate are added to the background electrolyte solution, the reduction peak of Cu(II) decreases due to the complexation reaction between copper(II) and glyphosate. Moreover, this complexation reaction provokes shifts and changes in the shape of the peak in the cyclic voltammograms, so the quantitative analysis with univariate calibrations is inapplicable, and it is necessary to resort to multivariate calibration methods. A PLS model is built to quantify Glyphosate in aqueous standard solutions with a LOQ of 5 μM. A tailored PLS model is built to quantify Glyphosate in tap water; this model can predict the concentration of real samples, obtaining recoveries between 80 % and 110 % even in the presence of interferent species.

3.6 MIP-based screen-printed electrode for Irbesartan sensing

3.6.1 Introduction

Irbesartan is a “sartan-family” drug often used by patients who suffer from hypertension, type 2 diabetes mellitus and nephropathy[173,174]. The EU has classified many drugs, including sartans, as emerging pollutants since the long-term effects on the environment and human health are not well known[175–177]. Losartan and Irbesartan are among the most prescribed antihypertensive medicines, especially for the older population. They are effective at low concentrations and are left unscathed by wastewater treatment plants[178]. For this reason, their monitoring and removal are of utmost importance. Figure 63 reports the molecular structure of Irbesartan.

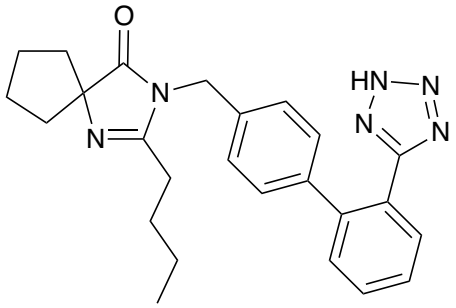

Figure 63. Molecular structure of Irbesartan

The most used techniques for Irbesartan determination in real samples are HPLC and UPLC coupled with the UV detector or MS/MS spectrometry[179,180]. These techniques are time-consuming, expensive, often require a large amount of solvents, and unsuitable for in situ analysis.

This study describes a voltammetric sensor based on a working graphite electrode of a screen-printed cell modified with a molecularly imprinted polymer. The MIP’s prepolymeric composition and the experimental parameters for the Square-Wave Voltammetry (SWV) analysis have been optimized using the Design of Experiments (DoE).

The reliability of the proposed method is proved by the analyses of tap water samples fortified with the drug.

3.6.2 Material and methods

3.6.2.1 Prepolymeric mixture and modification of the working electrode surface

The MIP prepolymeric solution is prepared according to the optimized procedure by mixing Irbesartan (IRB), MMA (methyl methacrylate), and EGDMA (ethylene glycol dimetharylate) with a molar ratio of 1:4:10 and adding the minimum amount of methanol to facilitate the dissolution of the components. The mixture is deaerated with a gentle flow of N_2 for 5 minutes, then AIBN is added, and the mixture is sonicated until a limpid solution is obtained. The NIP prepolymeric mixture is prepared following the same procedure but without including the template (IRB).

Each screen-printed cell (SPC) is washed with methanol and left to dry at room temperature under a hood. 3 μL MIP or NIP mixture is drop-coated on the surface of the working electrode, and then the polymerization is carried out in an oven at 60°C overnight.

The SPC is then subjected to 7 cleaning cycles by immersion for 1 h in 10 mL of a mixture of glacial acetic acid/methanol (1/4 molar ratio) to remove the template molecules and unreacted monomers. The functionalized SPCs are stored at room temperature and left hydrated for 10 min before use.

3.6.2.2 Characterization of the working electrode

The working electrode surface is characterized before and after modification by determining the active area according to the methodology described in paragraph 3.2.3.1 and by measurements in electrochemical impedance spectroscopy (EIS).

3.6.2.3 Irbesartan determination by square wave voltammetry (SWV)

Irbesartan concentration is measured by Square Wave Voltammetry (SWV) in 15 mL of 0.1 M acetate buffer solutions at pH 5.5, under gently stirring and applying the experimental conditions, optimized through a full factorial design of experiments (DoE). The optimized parameters are reported in Table 27.

Table 27. Experimental conditions, optimized through a Design of Experiments (DoE) approach, for Irbesartan analysis by SWV, using the MIP- or NIP- modified electrode.

Parameters	Bare electrode	MIP-/NIP-modified electrode
E_{start} (V)	+1.0	+1.0
E_{end} (V)	-1.5	-1.5
Frequency (Hz)	50	1.0
Impulse amplitude (V)	0.1	0.05
Equilibration time (s)	120	300

3.6.3 Results and discussion

3.6.3.1 Optimization of the prepolymeric mixture composition

The prepolymeric mixture composition is optimized for obtaining the most sensitive and selective polymer. A full factorial design 2^3 was applied. The parameters under investigation are the quantities of MAA, EGDMA and methanol. The current peak (ip, (A) obtained by SWV analysis is considered as the response. For data processing, the open-source software CAT[32] is used. Table 28 summarizes the level definitions for the parameters undergoing optimization, while in Figure 64, the graph showing the significance of the model's coefficients is reported.

Table 28. Optimization of the prepolymeric mixture by a full factorial design 2^3: level definitions for the parameters considered, keeping constant the Irbesartan content (0.05mmol)

Parameter	Minimum level (-1)	Maximum level (+1)
MAA[1] (mmol)	01	0.2
EGDMA[2] (mmol)	0.5	1.0
CH_3OH[3] (mL)	0.4	0.8

[1]MAA = methacrylic acid (functional monomer); [2]EGDMA = ethylene glycol dimethacrylate (cross-linker); [3]CH_3OH = methanol (solvent).

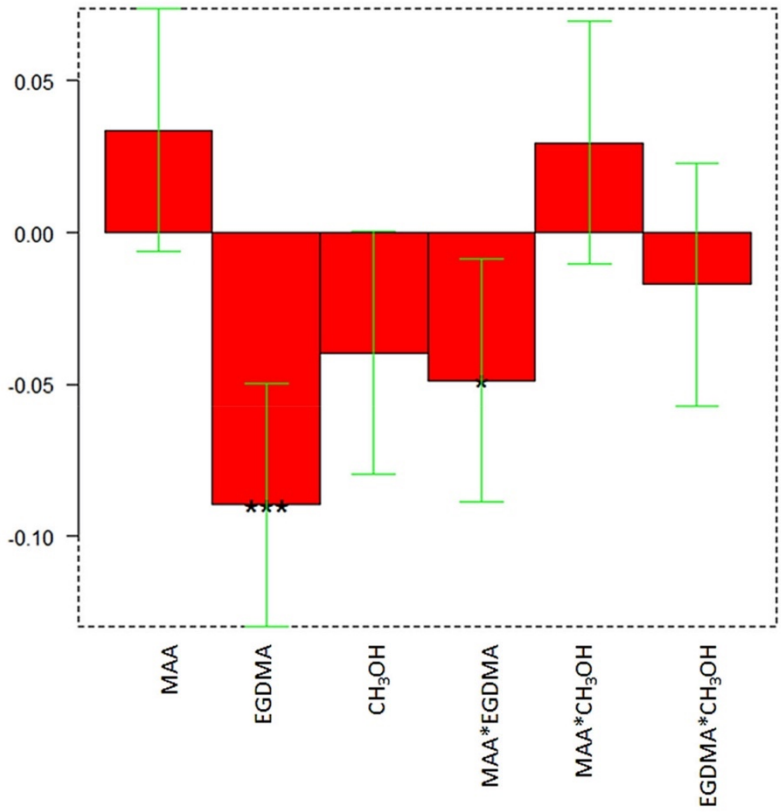

Figure 64. Experimental design to optimize the prepolymeric mixture: coefficients plot. The greatest values and little black stars (regardless of the sign) suggest a significant influence of the respective parameter or interaction and significance (*p≤'0.05,***p≤0.001).

The model equation can be written as follows:

$$i_p = b_0 + b_1[\mathrm{MAA}] + b_2[\mathrm{EGDMA}] + b_3[\mathrm{CH_3OH}] + b_{12}[\mathrm{MAA}][\mathrm{EGDMA}] + \\ + b_{13}[\mathrm{MAA}][\mathrm{CH_3OH}] + b_{23}[\mathrm{EGDMA}][\mathrm{CH_3OH}]$$

Table 29 reports the coefficient values and their significance.

Table 29. Coefficients and significance (*p≤'0.05,***p≤0.001) calculated for the optimization of the prepolymeric mixture by full factorial design 2^3.

Coefficient	Value	Significance
b_0	0.3462	
b_1	0.00337	
b_2	-0.0896	***
b_3	-0.0396	
b_{12}	-0.0487	*
b_{13}	0.0296	
b_{23}	-0.0171	

The coefficient plot highlights that the significant parameters/interactions are the mmol of EGDMA and the interaction between mmol MAA and EGDMA, while the solvent volume is irrelevant. From the parameters obtained in the DoE, the best amount of EGDMA is 0.5 mmol, while that of MAA is 0.2 mmol.

For the model validation, six replicates of the center point [0 0 0] are set up, and the average value, standard deviation and confidence interval (CI) at a 95% confidence level are reported in Table 30. Since the predicted value fits into the CI the model is validated.

Table 30.Optimization of the prepolymeric mixture by a full factorial design 2^3: model validation by six replicates at the center point [0 0 0], 0.15 MAA, 0.75 mmol EGDMA and 0.6 mL CH_3OH. CI = confidence interval 95% confidence level.

	I_p (μA)
Average	0.33
Standard deviation	0.02
Upper bound CI	0.35
Lower bound CI	0.31
Predicted response b_0	0.3462

Therefore, the optimal prepolymeric mixture had the following composition IRB: MAA: EGDMA = 0.05 mmol: 0.2mmol: 0.5mmol = 1: 4: 10. As previously stated, the volume of methanol is irrelevant, and the maximum value of 0.8 mL is selected to be sure to solubilize all the mixture components well.

3.6.3.2 Characterization of the working electrode surface before and after the modification

The active area is computed using the Randles-Sevick equation (eq.8) for the bare, MIP-, and NIP-modified electrodes. Each obtained value was compared to the theoretical one. The values are reported in Table 31.

Table 31. The active area values calculated by the Randles-Sevick equation (eq.8). Measure performed in electrochemical probe 5 mM $K_3Fe(CN)_6$/0.1 M KCl pH 7.2. The number in parenthesis is the standard deviation on the last digit.

	Active area (mm^2)
Bare electrode	12.3(3)
MIP-modified electrode	9.59(2)
NIP-modified electrode	8.80(3)
Theoretical	12.6

The values reported suggest that the active area decreases when the electrode is coated with a non-conductive polymer. As expected, the active area of the MIP-modified electrode is higher than that of the NIP-modified electrode; this is due to the presence of the recognition cavities in the MIP, which are, on the contrary, absent in the NIP.

The surface of the working electrode is further characterized by Electrochemical Impedance Spectroscopy (EIS) using, for the measurements, 5 mM $K_3Fe(CN)_6$/0.1 M KCl as the electrochemical probe/electrolyte solution. The NIP-modified electrode, the MIP-modified electrode after the template removal and the same electrode after equilibration with the analyte solution are analysed. Figure 65 shows the Nyquist plot for each electrode; the corresponding Randles' equivalent circuit is reported as insert.

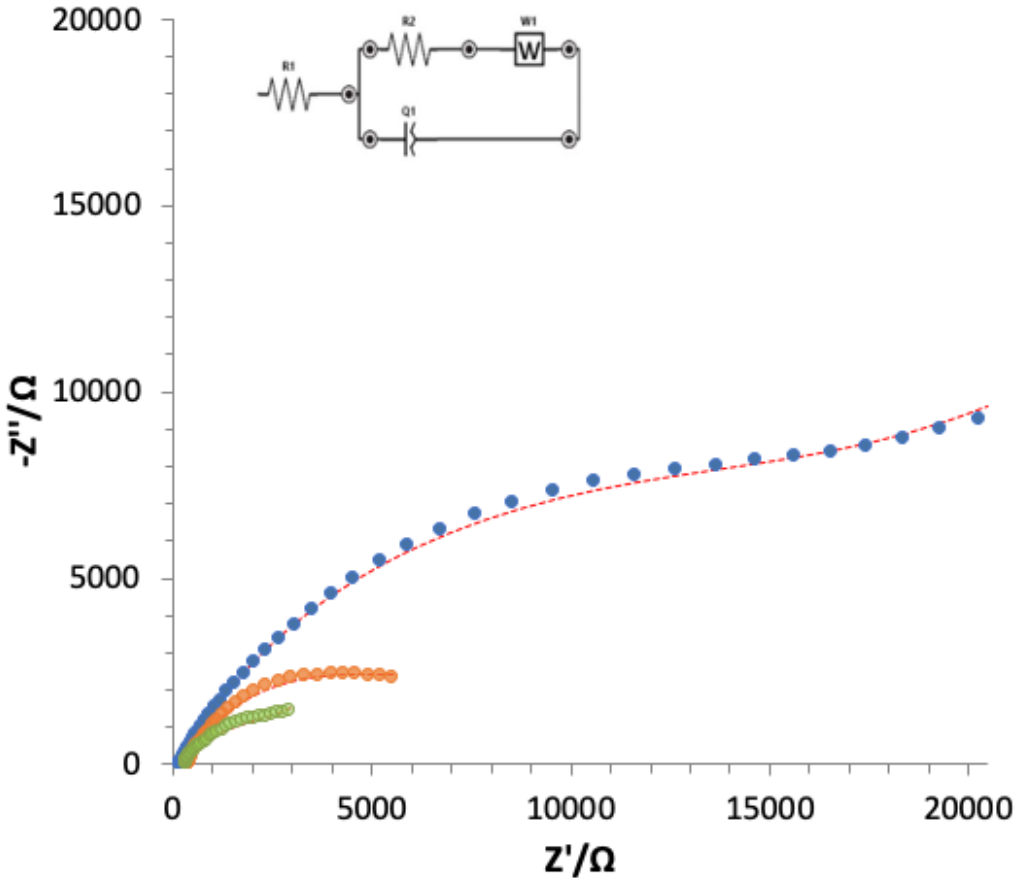

Figure 65.Nyquist plot of the NIP-modified electrode (blue dots) MIP-modified electrode after template removal (green dots) and after equilibration with IRB solution (orange dots). Measurements performed in the following electrochemical probe solution: 5 mM $K_3Fe(CN)_6$/0.1 M KCl, pH 7.2.

As can be observed from the Nyquist plot, the charge transfer resistance increases from the electrode covered with the MIP after the template removal to the MIP after equilibration with the IRB solution. This behavior may be due to the presence of the analyte in the recognition cavities that prevents the electric charges from reaching the working electrode surface. This behavior is amplified using the NIP-modified electrode, which has a lower porosity than the MIP.

3.6.3.3 Irbesartan Determination by Square-Wave Voltammetry (SWV): Optimization of the Procedure, Calibration and Real Sample Analysis

Once the screen-printed cell (SPC) is modified with the MIP, and before its use for the voltammetric measurements, it is washed several times with the mixture of methanol/glacial acetic acid ≥ 99% = 1/4 to remove the template molecule. Calibration measurements are performed on the bare electrode and the MIP-and NIP-modified ones. The experiments are carried out in 30 mL of 0.1 M acetate buffer at pH 5.5 using SWV. The voltammogram is recorded after an equilibration time of 120 and 300 s, respectively, for the bare electrode and the MIP-/NIP- modified ones. For the MIP-modified electrode, the equilibration time corresponds to the incubation period necessary for the Irbesartan molecule to reach the cavities of the polymeric film. A full factorial 2^3 Design of Experiments (DoE) was carried out to define the best experimental conditions, and the current peak (i_p, μA*)* is evaluated as the response. The levels of the variables, the coefficient plots and their significance and the model equation are reported in Appendix IV – Optimization data (levels of variables, coefficient plots and their significance and the model equation) for SWV experimental conditions for bare and MIP-modified electrodes for Irbesartan detection (paragraph 3.6). The best experimental conditions are summarized in Table 27.

Figure 66a shows the calibration curve obtained for the MIP- and NIP-modified electrodes by plotting the cathodic current peak (i_p, μA) vs. Irbesartan concentration (μM) and Figure 66b the SW voltammograms of the calibration curve for one MIP-modified electrode.

The straight-line equations of the calibrations reported in Figure 66a are:

i_p [μA] = 1.30(3) + 6.9(2)·[IRB, μM] R^2 = 0.994 for the MIP-modified electrode;

i_p [μA] = 1.23(3) − 0.4(3)·[IRB, μM] R^2 = 0.168 for the NIP-modified electrode

(The number in round brackets is the standard deviation of the last digit).

As expected from the experiments performed with the NIP-modified electrode, only a residual current independent of the Irbesartan concentration is registered.

The detection (LOD) and quantification (LOQ) limits are computed by equations 4 and 6, as reported in paragraph 1.4.5. LOD and LOQ are the average values obtained from three different calibration curves.

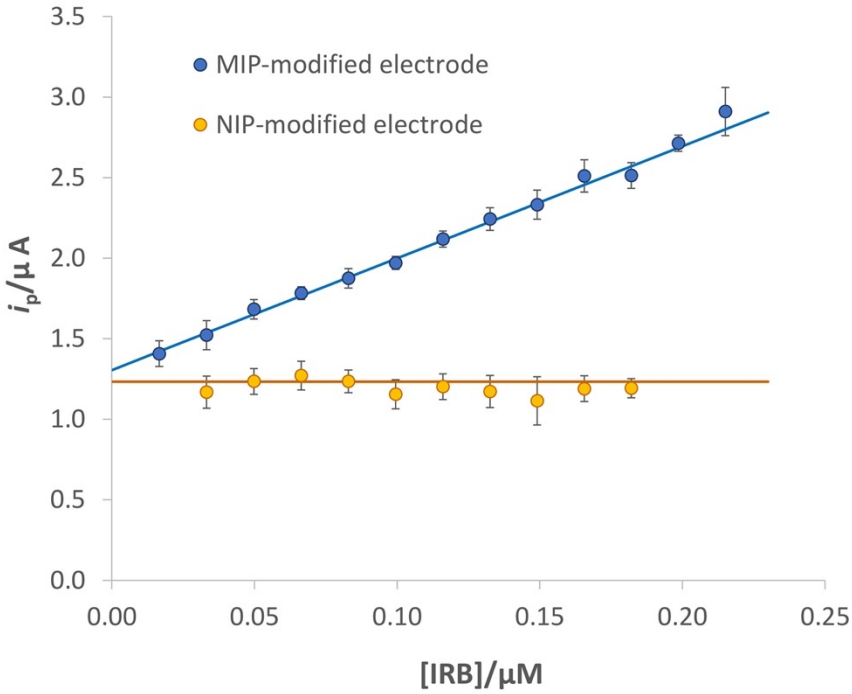

(a)

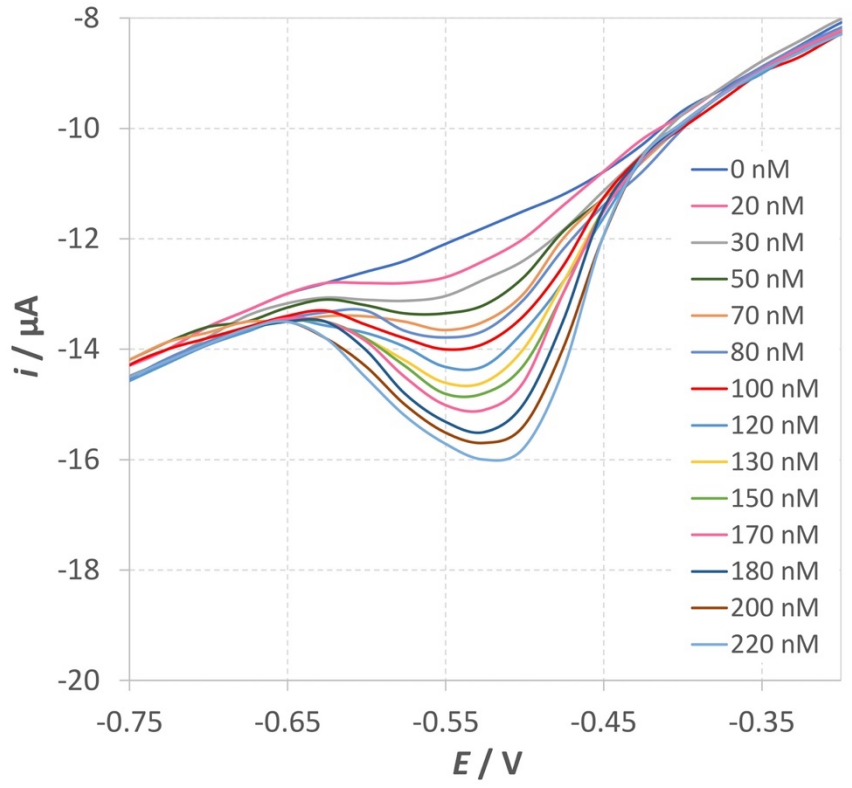

(b)

Figure 66. a) Calibration curves of the MIP-modified electrode (blue dots) and NIP-modified electrode (orange dots). b) SW voltammograms of the calibration curve for one MIP-modified electrode

Some calibrations are also performed with the bare electrode, applying the optimized experimental conditions summarized in Table 27.

The linearity range obtained employing the bare electrode is slightly wider than that achieved with the MIP-modified electrode, but higher LOD and LOQ values are obtained. Table 32 summarizes the LOD, LOQ, LOL (limit of linearity) values and the sensitivity (slope of the calibration curve) for each electrode.

Table 32. Limits of Detection (LOD), Limits of Quantification (LOQ) and Limits of Linearity (LOL) for bare and MIP-modified screen-printed electrodes. LOD and LOQ are the average values obtained from three different calibration curves. The number in parenthesis is the standard deviation..

	bare	**MIP**
Sensitivity (μA/μM)	5.4(1)	6.9(2)
LOD (μM)	0.09(2)	0.012(3)
LOQ (μM)	0.26(5)	0.03(1)
LOL (μM)	0.26-4	0.03-0.3

Two fortified tap water samples with two different concentrations of Irbesartan are analyzed to verify the applicability of the MIP-modified screen-printed cell for environmental analyses. The recovery % and the error% are calculated for each sample and summarized in Table 33.

Table 33. Recovery% and error% using SPC-bare and SPC-MIP of tap water adjusted to pH 5.5 and fortified with different concentrations of Irbesartan.

	$C_{nominal}$/M	$C_{experimental}$/M	**Recovery %**	**Error%**
MIP-modified electrode	$3.6 \cdot 10^{-7}$	$3.37(6) \cdot 10^{-7}$	93.6	-6.4
Bare electrode	$3.6 \cdot 10^{-7}$	$1.2(1) \cdot 10^{-7}$	33.3	-66.7
MIP-modified electrode	$1.4 \cdot 10^{-7}$	$1.2(2) \cdot 10^{-7}$	92.8	-7.1
Bare electrode	$1.4 \cdot 10^{-7}$	$3.9(5) \cdot 10^{-7}$	278	178

Table 33 shows good recoveries and a maximum error of 7.1% for the MIP-modified electrode, while the bare one is not a selective sensor since the recoveries were unsatisfactory. The bad results obtained with the bare electrode could be due to the interference of electroactive substances in the real samples; the presence of the specific

MIP's cavities reduces the chance of such interferents reaching the electrode surface, making more accurate measurements possible.

3.6.4 Conclusions

A voltammetric MIP-based screen-printed cell for Irbesartan determination is proposed. Before and after modification, the working electrode surface was characterized by EIS and the active area was calculated. The results of both methods demonstrated the covering of the surface with the MIP layer.

From the calibration measurements performed under optimized conditions, a LOD of 0.012(3) µM and a LOQ of 0.04(1) µM were obtained.

The applicability of the sensor for environmental analyses was tested by detecting Irbesartan in fortified tap water samples, obtaining good recoveries.

3.7 Ascorbic acid sensing by e-MIP-modified screen-printed electrodes

3.7.1 Introduction

Ascorbic acid (L enantiomer), known as vitamin C, is a hydrosoluble vitamin characterized by well-established antioxidant properties[181]. These antioxidant properties are due to the reducing nature of the molecule, which acts as an electron donor[182–184]. Figure 67 shows the molecular structure of Ascorbic acid (AA).

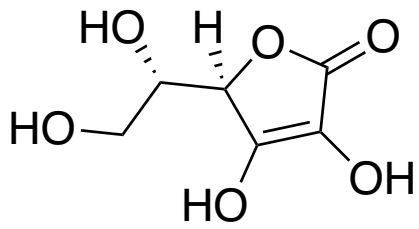

Figure 67. Molecular structure of Ascorbic acid (AA).

Ascorbic acid is found in many foods, such as fresh vegetables, fruits and legumes. It is involved in collagen synthesis, iron absorption and immune response activation; moreover, vitamin C participates in osteogenesis and wound healing[182–184]. Ascorbic acid is commonly used as an antioxidant in the foodstuff industry to inhibit undesired changes in the flavor or color of foods[185,186].

Excess Ascorbic acid can cause gastric irritations, and its metabolite, oxalic acid, can provoke renal problems[181]. For this reason, monitoring Ascorbic acid, especially in the foodstuff industry, is crucially important.

The classical methods for Ascorbic acid determination include the redox titrations with oxidants such as potassium iodide or bromate and dichlorophenol indophenol[187,188] while the more modern ones use HPLC techniques with amperometric or fluorimetric detection[189–191]. Compared to the bulky and expensive instruments used for HPLC measurements, the electrochemical methods are more portable and rapid and permit the measurement to be performed in situ.

Significant progress has also been made in developing electrochemical sensors for ascorbic acid detection, and in some of them, the electrode surface was modified by molecularly imprinted polymers. Recently, several studies have reported on applying electrosynthesized MIPs (e-MIPs) to develop electrochemical sensors.

Electropolymerized MIPs (e-MIPs) present several advantages; for example, the rapid polymerization performed by simple electrochemical techniques such as cyclic voltammetry or amperometry, the thickness of the polymer can be tuned by changing the experimental conditions, and the polymerization can be conducted in an aqueous medium (decreasing the use of toxic agents)[192,193].

Other electrochemical procedures can also be applied to enhance these e-MIPs. One of them, which is very useful, is overoxidation, performed by the electrochemical treatment of the MIP film by positive electrode potentials much higher than those required for the polymerization reaction. Overoxidation is advantageous in MIPs' preparation since it allows the formation of carboxyl, carbonyl, and hydroxy groups that can interact with the template molecule by hydrogen bonds, promoting the formation of more selective cavities[194].

The most frequently electropolymerized imprinted films are primary polypyrrole, followed by polyaniline and polythiophene derivatives[195]. The focus on polypyrrole is due to its water solubility and ease of oxidation; moreover, polypyrrole possesses several valuable characteristics, such as good environmental stability, conductivity, and redox properties[196]. When submitted to high positive potentials, it can be over-oxidized, and the incorporation of carbonyl groups into the polymer's backbone occurs, causing a loss of electric conductivity and the filling of pinholes and defects. At the same time, higher control of the film thickness arises, and the background currents are more stable[192,196–198].

In this context, an electrochemical sensor based on electrosynthesized polypyrrole, molecularly imprinted with ascorbic acid and overoxidated, was developed. The polymeric film was electrodeposited on the graphite working electrode of a screen-printed cell, obtaining a selective and simple method for AA sensing.

Differential pulse voltammetry (DPV) was selected for the analyte detection, and the electrochemical parameters were optimized by a Design of Experiments (DoE).

Interference tests and trials with drugs were performed to assess the selectivity and reliability of the proposed method.

3.7.2 Material and methods

3.7.2.1 Preparation of the e-MIP and e-NIP sensors

Before modification, each screen-printed cell (SPC) is washed with ethanol and left to dry at room temperature under a hood.

The e-MIP-modified electrode is prepared by electrodeposition on the surface of the clean SPC using cyclic voltammetry (CV) in the potential range −0.6 ÷ 0.8 V during five cycles (scan rate 0.1 V/s) in an aqueous solution of 0.1 M $LiClO_4$, 15 mM pyrrole, and 10 mM ascorbic acid (AA). The polypyrrole-imprinted film was overoxidized by applying a fixed potential of +1.2 V for 2 min in 0.1 M $LiClO_4$ solution. The extraction of the template was performed in two steps. Firstly, the modified SPC was placed in PBS solution 0.05 M at pH 7.5 for 20 min, under gentle stirring on an orbital shaker, followed by 10–15 cycles of cyclic voltammetry, scanning the potential from −1 to +1 V (scan rate 0.1 V/s) in PBS solution 0.05M/KCl 0.1M at pH = 7.5.

Electropolymerized, not-imprinted polymer films on the working electrode of the SPC (e-NIPs) were prepared under the same conditions but without adding the template, i.e., AA, in the polymerization solution.

3.7.2.2 Characterization of the working electrode surface

The working electrode surface is characterized by determining the active area and the double layer capacitance according to the methods reported in paragraph 3.2.3.2; moreover, electrochemical impedance spectroscopy (EIS) measurements are performed.

3.7.2.3 Ascorbic acid determination by Differential Pulse Voltammetry (DPV)

Differential pulse voltammetry (DPV) is used as the voltammetric method for the determination of ascorbic acid in 10 mL of 0.05 M PBS/ 0.1 M KCl solutions at pH7.5, applying the following experimental conditions, optimized by a Design of Experiments (DoE) approach: E_{start}: -0.5 V, E_{end}: 0.3 V, E_{step}: 0.01 V, E_{pulse}: 0.025 V, t_{pulse}: 0.25 s, scan rate: 0.02 V/s.

3.7.3 Results and discussion

3.7.3.1 Optimization of the DPV experimental conditions for Ascorbic acid analysis

A full factorial design 2^3 was applied to optimize the DPV experimental conditions: pulse potential (E_p, V), pulse time (t_p,s) and scan rate (v, V/s). Table 34 reports the minimum and

maximum levels of the conditions under investigation, while Figure 68 shows the significance plot of the model's coefficients, whose values are reported in Table 35. Three-point calibration curves are performed for each experiment, and the slope of the straight line is used as the response of the DoE (since the higher the slope, the more sensitive the measure). The data treatment is performed by using the open-source software CAT[32].

Table 34. Optimization of the DPV experimental conditions by full factorial design 2^3: level definitions for the parameters considered, keeping constant the range of the potential scan (from -0.5V to +0.3V).

Parameter	**Maximum level (-1)**	**Maximum level (+1)**
E_{pulse} (E_p, V)	0.015	0.025
t_{pulse} (t_p,s)	0.15	0.25
Scan rate (v, V/s)	0.01	0.02

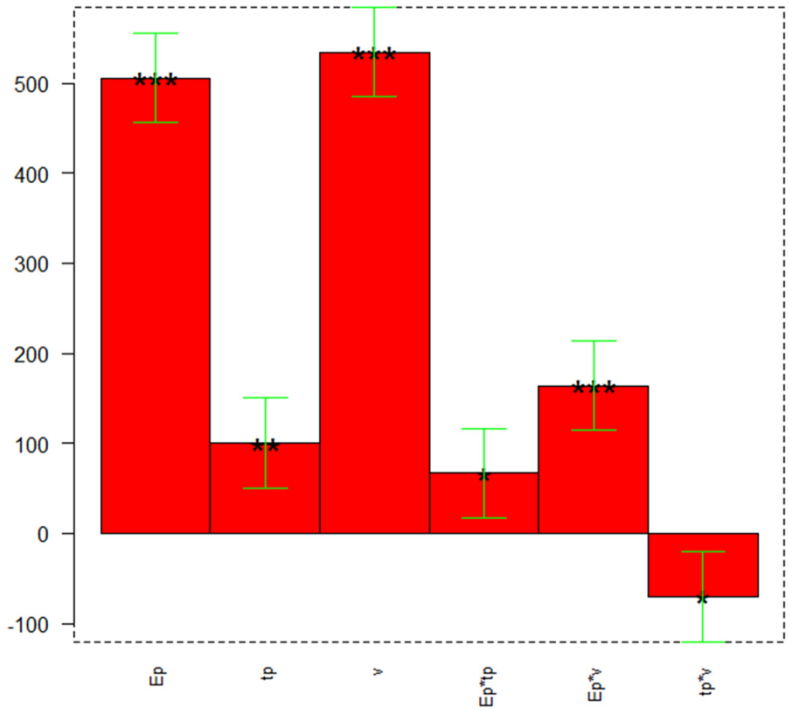

Figure 68. DoE to optimized the DPV parameters: coefficients plot. The greatest values and little black stars (regardless the sign) indicate a significant influence of the respective parameters or their interaction and significance (*p≤'0.05, **p≤0.01,***p≤0.001).

Table 35. Optimization of the DPV parameters by full factorial design 2^3: coefficient values and their significance(*p≤'0.05, **p≤0.01,***p≤0.001).

Coefficient	Value	Significance
b_0	932	
b_1	505.74	***
b_2	100.13	**
b_3	534.08	***
b_{12}	66.96	*
b_{13}	164.07	***
b_{23}	-70.49	*

The DoE model can be expressed by the equation:

$$slope = b_0 + b_1 \cdot E_p + b_2 \cdot t_p + b_3 \cdot v + b_{12} \cdot E_p \cdot t_p + b_{13} \cdot E_p \cdot v + b_{23} \cdot t_p \cdot v$$

From the coefficients plot of Figure 68, it can be observed that all parameters are important and have a positive effect on the response, so they must be set at the maximum value (+1). The most significant interaction is between the pulse potential (E_p) and the scan rate (v), presenting a significant positive effect on the response.

Three replicates of the center point [0 0 0] are performed; Table 36 reports the average, the standard deviation and the confidence interval (CI) at the 95% confidence level. Since the predicted response b_0 is included in the CI the model is validated; therefore, the optimized parameters are E_p: 0.025 V, pulse time (t_p) 0.25 s and v 0.02 V/s.

Table 36. Optimization of the DPV experimental, conditions by a full factorial design 2^3: model validation by three replicates at center point [0 0 0], E_p=0.02 V, t_p=0.2s, v=0.015 V/s. CI = confidence interval at 95% confidence level.

	Slope ($\mu A \cdot M^{-1}$)
Average	975
Standard deviation	49
Upper bound CI	1024
Lower bound CI	926
Predicted response b_0	932

3.7.3.2 Characterization of the working electrode surface

The electrochemically active area and the double-layer capacitance are determined before and after the working electrode modification with e-MIP or e-NIP. Moreover, Electrochemical Impedance Spectroscopy (EIS) measurements are implemented to evaluate the electron transfer kinetics of the bare and modified electrodes.

Active area and double-layer capacitance values are summarized in Table 37.

Table 37. Active area values calculate by the Randles-Sevick equation 8. Electrochemical probe solution: 5mM $K_3Fe(CN)_6$/KCl 0.1M pH 7.5. Potential scan from -1 to +1V; scan rate form 0.025 to 0.5 V/s.

	Active area (mm^2)	**Capacitance (μF)**
Bare electrode	3.8(2)	0.5(3)
e-MIP-modified electrode	2.4(2)	2.15(5)
e-NIP-modified electrode	1.3(1)	1.52(6)
Geometric area (circular shape electrode ∅1.1mm)	3.8	7

As can be observed from the values reported in Table 37, the active area decreases after coating the electrode with the polymer. As expected, the active area of the e-NIP-modified electrode is lower than that of the e-MIP. Indeed, the absence of the polymer's recognition cavities leads to a decrease in the electroactive surface. The double-layer capacitance increased from the bare electrode to the overoxidized e-NIP and e-MIP functionalized electrodes; this implies that the presence of the polymer layer increases the possibility of accumulating electrical charges.

The characterization of the bare and modified electrodes is also implemented by EIS measurements; the Nyquist plot is reported in Figure 69.

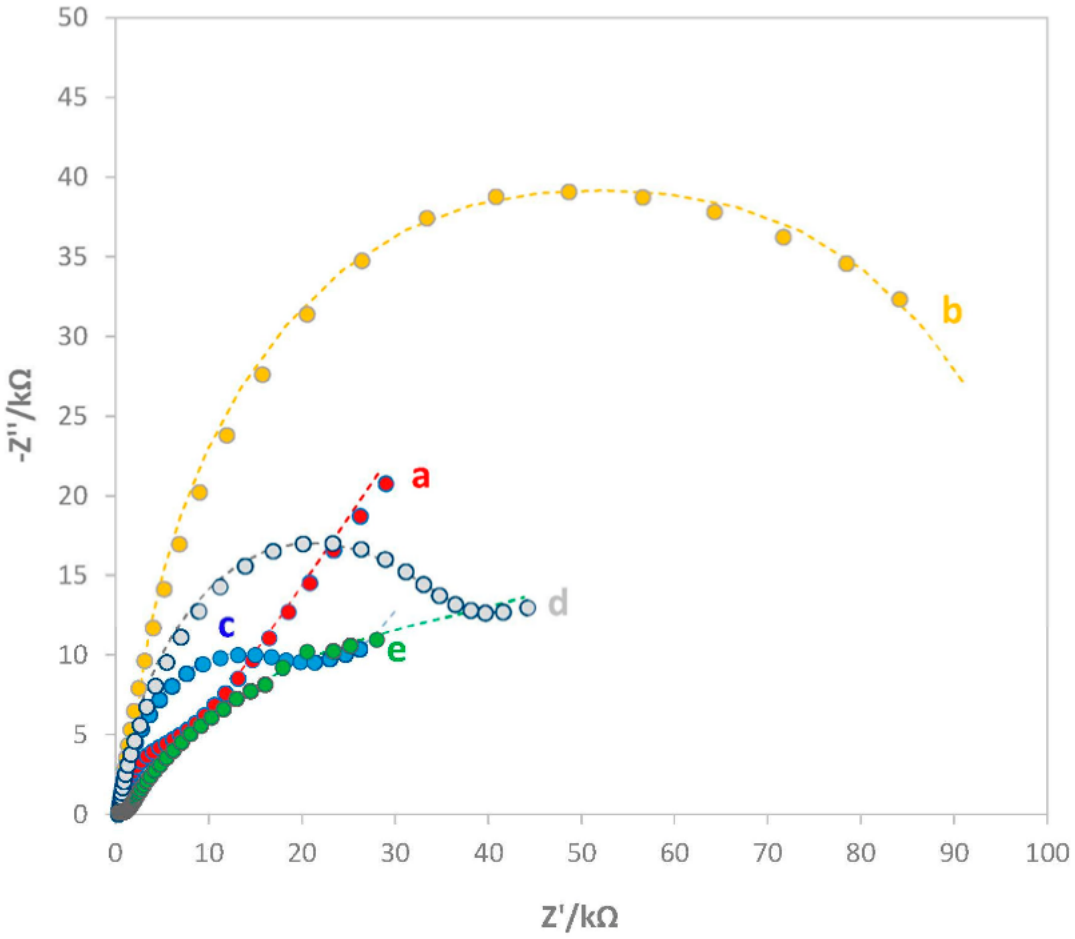

Figure 69. Nyquist plot of (a) bare electrode, (b) e-MIP modified electrode, (c) e-MIP-modified electrode after template removal, (d) e-MIP-modified electrode after rebinding with AA 3mM, (e) e-NIP-modified electrode. Measurements were performed in 5mM $K_3Fe(CN)_6$(KCl 0.1M solution. Frequency range 100 kHz-10 mHz with a sinusoidal potential modulation of 0.05 V superimposed on a dc potential of 0.2 V.

As can be observed from Figure 69, the presence of the polymeric films influenced the impedance behavior of the electrode surface at both high and low frequencies. The bare electrode displays a low $R_{CT,}$ while the other modified electrode shows a higher resistance to the charge transfer, indicating that after overoxidation, the conductive properties of the polymer are lost. The curves (b) and (e), i.e., those related to the e-MIP before template removal and the e-NIP modified electrodes, show a similar behavior. The mass diffusion process is almost absent due to the massive R_{CT} of the uniform polymer films on the working electrode. The curves (c), (d), and (a), related to the e-MIP-modified electrode after template removal, the same electrode after rebinding with 3 mM AA solution and the bare electrode have the working electrode surface more exposed to the solution; for this reason, the mass transfer diffusion process is more significant. The Randles equivalent circuits reported in Figure 70 schematize the two different trends. In both circuits, the

electrode/electrolyte resistance (R), the charge transfer resistance (R_{CT}, which influences the diameter of the semicircle in the Nyquist plot) and the double layer capacitance (C) are present. In the Randles circuit of Figure 70b, the Warburg element (W) representing the contribution of the mass-diffusion-limited process is also present.

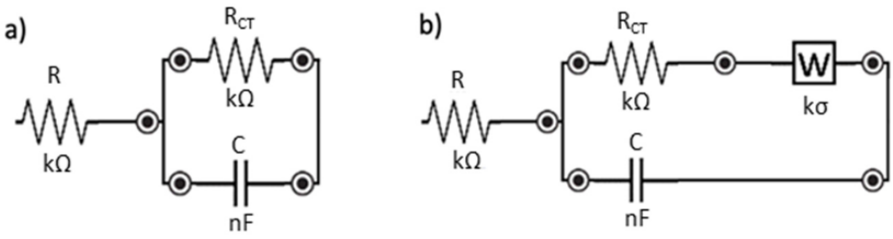

Figure 70. Randles equivalent circuits for modeling the Nyquist plots of figure 79. a) for e-NIP (**e)**and e-MIP-modified electrode(**b**), b) for e-MIP-modified electrode after template removal(**c**), the same electrode after rebinding with 3mM AA (**e**)and bare electrode (**a**).

3.7.3.3 Electrochemical Detection of Ascorbic acid: Evaluation of the analytical parameters. Selectivity Test and Analyses of Commercial Products

As stated above, DPV is selected for ascorbic acid detection. Calibration curves are obtained, registering the voltammograms in 10 mL of 0.05 M PBS/0.1 M KCl solutions at pH 7.5 at increasing ascorbic acid concentration and applying the experimental parameters optimized by the DoE approach described above. To compare the analytical figures of merit, bare, e-MIP, and e-NIP electrodes are tested. The voltammograms obtained for the three different electrodes and even the graph for a non-overoxidated e-MIP are reported in Figure 71.

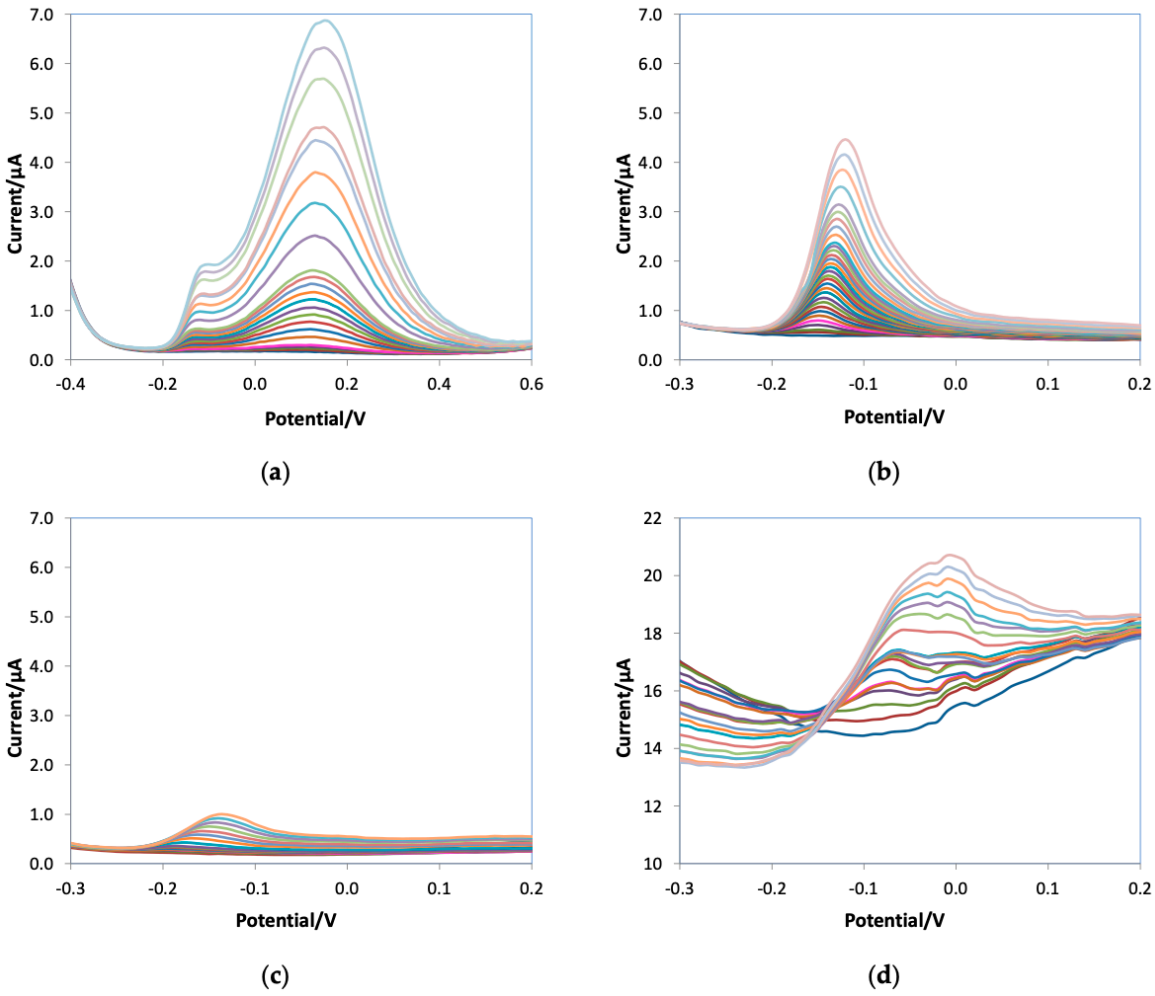

Figure 71. DPV voltammograms of (a) bare, (b) e-MIP, (c) e-NIP, (d) non-overoxidized e-MIP registered in 10 mL of 0.05 M PBS/0.1 KCl solutions at pH 7.5 at increasing ascorbic acid concentration from 0 to 5mM.

As can be observed in the voltammograms obtained with the non-overoxidated e-MIP (Figure 71d), disturbed signals and high background current are evident, so experiments with this type of modified electrodes have not been continued. Figure 72 shows the calibration graphs (i_p(µA) vs. [AA](mM)) obtained using the bare electrode, the e-MIP- and e-NIP-modified screen printed cells, while in Table 38, the parameters of the obtained straight lines are summarized.

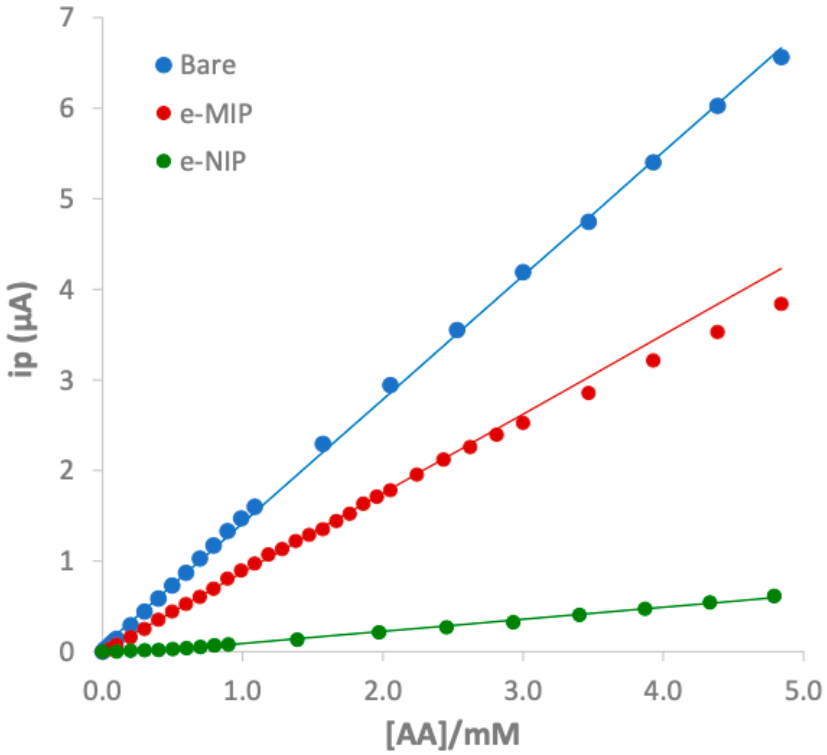

Figure 72. Calibration graphs for bare, e-MIP and e-NIP obtained, respectively, from the DPV data of figure 81 a-c.

Table 38.Analytical parameters evaluated from the linea regression of the DPV data. Results obtained from three different calibration curves using three screen-printed cells for each type (bare, e-MIP and e-NIP) in 10 mL of 0.05 M PBS/0.1 M KCl solutions at pH 7.5. In brackets is reported the standard deviation on last digit

Electrode	Slope (µa, mM^{-1})	R^2	LOD[a] (µM)	LOQ[a] (µM)	Linear range (µM)
Bare	1.34(7)	0.999	35	106	20-4800
e-MIP	1.02(6)	0.999	21	64	30-2400
e-MIP[b]	98(2)	0.998	1.2	3.6	2-100
e-NIP	0.13(2)	0.997	150	450	400-800

[a]LOD calculated as reported in eq.4 while LOQ as reported in eq.6.
[b]calibration performed in 100mL of solution

From the values reported in Table 38, the bare electrode seems to be slightly more sensitive compared to the overoxidized e-MIP; however, the linear range, the LOD and the LOQ are relatively similar, a little better for e-MIP. Some other calibrations are performed using ten times higher volume, obtaining an improved LOD. The poor sensitivity of the e-NIP is an added advantage since the non-imprinted polymer acts as a barrier to the analyte reaction at the electrode surface.

The repeatability of the measurements is also tested. Figure 73 reports the calibration graphs of five replicates with the same scree-printed cell. It can be observed that the differences among the replicates are not significant (RDS<5%).

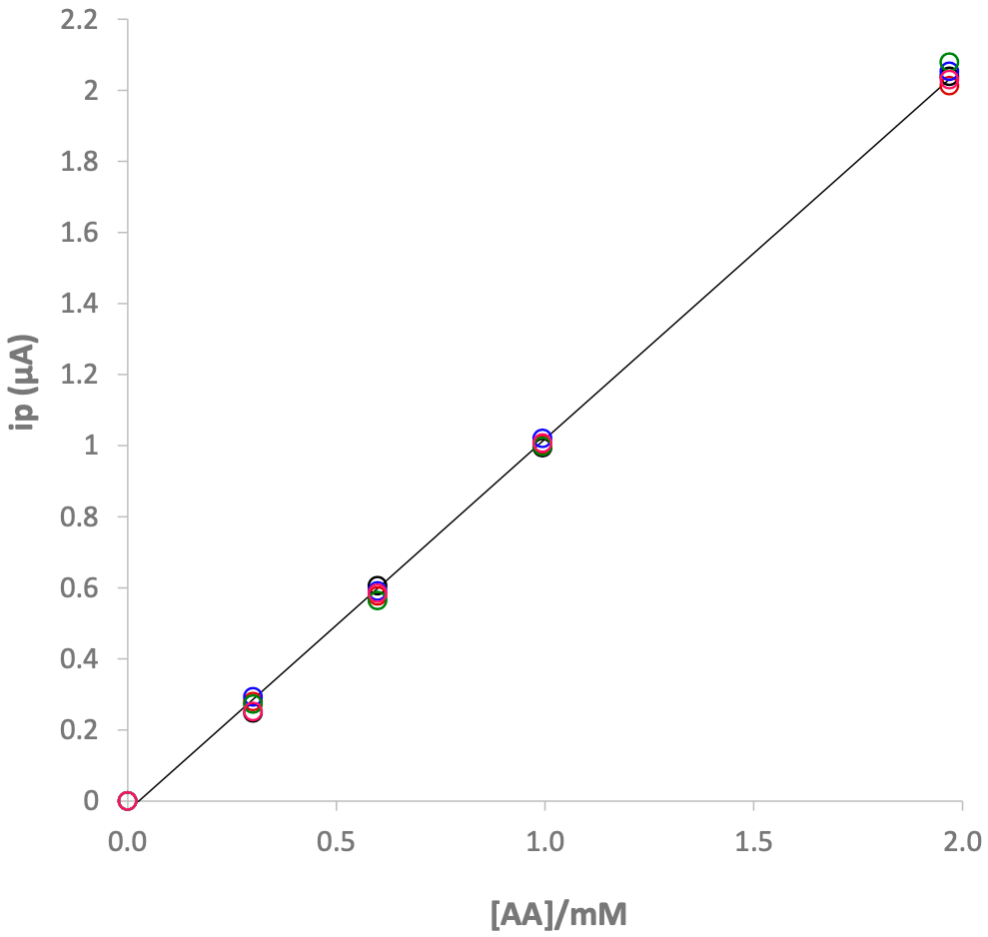

Figure 73. Five replicates of calibration obtained with a single e-MIP modified screen-printed cell. Data point of each replicate at the same concentration are reported with dots in different colour.

Selectivity tests are performed in the presence of interferents in the solution containing Ascorbic acid. As interferents, dopamine and uric acid are chosen since the oxidation reactions occur at close potentials[199–201]. Figure 74 shows the voltammograms of the measurements performed with the bare electrode in a solution of 0.5 mM of ascorbic acid with different concentrations of interferents. As can be observed, the oxidation peaks of the interferent species overlap with the signal of the ascorbic acid; under these conditions, the bare electrode can not be used for the ascorbic acid determination.

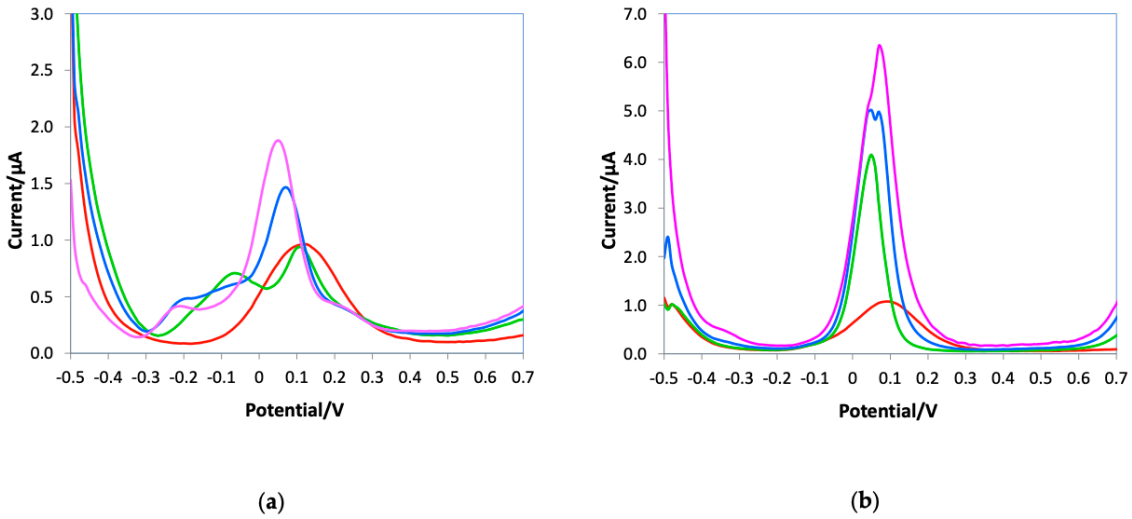

Figure 74. DPV voltammograms of the e-MIP electrode registered in 10 mL of 0.05M PBS/0.1M KCl solutions at pH 7.5, (**a**) 0.5 mM AA (red line), 0.5mM AA + 0.3 mM uric acid (green line), 0.5 mM AA + 0.5 mM uric acid (blue line), 0.5 mM AA+0.8 mM uric acid (pink line;, (**b**)0.5mM AA(red line), 0.5mM + 0.3 mM dopamine (green line), 0.5mM AA+0.5mM dopamine (blue line), + 0.5mM AA + 0.8 mM dopamine (pink line).

The same measurements were performed using the e-MIP-modified screen-printed cell, and the results are surprisingly different compared to those obtained with the bare electrode. Figure 75 reports the voltammograms of the measurements using the e-MIP-modified screen-printed cell in (a) solutions containing a fixed concentration of uric acid and different concentrations of ascorbic acid and (b) in solutions containing fixed concentrations of ascorbic acid and different concentrations of dopamine.

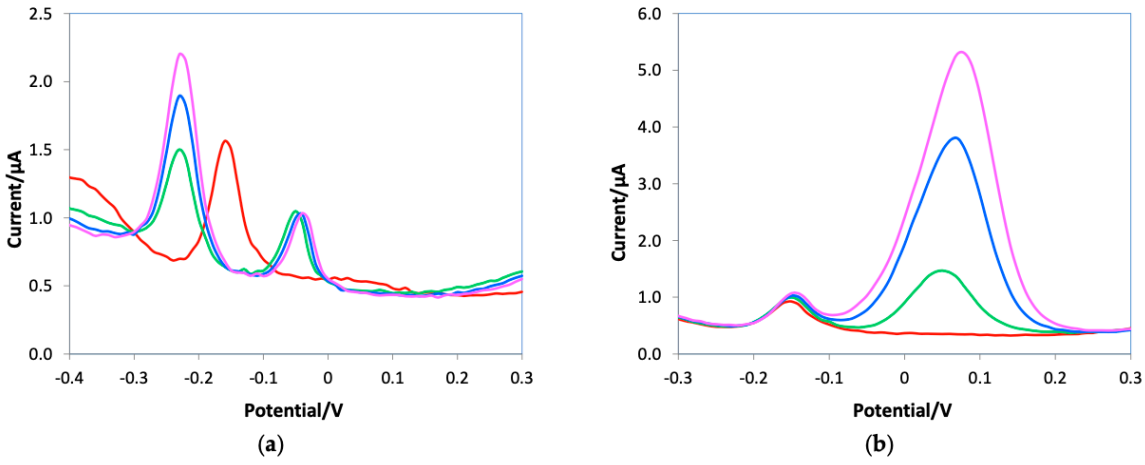

Figure 75. DPV voltammograms of the bare electrode registered in 10 mL of 0.05M PBS/0.1M KCl solutions at pH 7.5, (**a**) 1 mM AA (red line), 1mM AA + 0.4 mM uric acid (green line), 1.2 mM AA + 0.4 mM uric acid (blue line), 1.5 mM AA + 0.4 mM uric acid (pink line;, (**b**)1mM AA(red line), 1mM + 0.1 mM dopamine (green line), 1mM AA+0.2mM dopamine (blue line), + 1mM AA + 0.3 mM dopamine (pink line).

As can be clearly observed in the voltammograms reported in Figure 75, the presence of the e-MIP on the surface of the working electrode permits the peak's separation of the analyte from those of the interferent species, allowing the quantification of the ascorbic acid without interference problems.

To assess the reliability of the proposed method, two different drug tables with known ascorbic acid content were analyzed. The standard additions method is applied, and the results are reported in Table 39.

Table 39.Ascorbic acid detection in farmaceutical products. CI = confidence interval at 95% con-fidence level. Three replicates for each sample using the same e-MIP screen-printed cell.

	VIVIN C ® **AA content (mg)**	**TIOBEC®** **AA content (mg)**
Average (*n=3)*	210	30
Standard deviation	5	2
Upper bound CI	222	35
Lower bound CI	197	24
Declared content	200	30

For both the commercial products, the obtained results are in good agreement with the declared ascorbic acid content; moreover, the low standard deviation reveals a significant reproducibility of the measurements, considering that the same e-MIP-based screen-printed cell was used for both determinations.

3.7.4 Conclusions

A molecularly imprinted electrosynthesized polymer (e-MIP) on screen-printed electrodes for ascorbic acid detection by the DPV method is developed.

The best results are obtained after polypyrrole overoxidation, performing the measurements in a phosphate buffer solution of 0.05 M/KCl 0.1 M at pH 7.5 and applying optimized experimental conditions for the voltammetric detection.

The graphite working electrode surface is characterized before and after modification, measuring the active area and the double-layer capacitance. The results of both determinations demonstrate the electrode surface coverage by the e-MIP layer.

The analytical parameters evaluated from the calibration curves demonstrate good sensitivity and a detection limit that is not significantly different from that achievable with the non-modified electrode (bare). The LOD obtained is about 20 µM if the sample volume is 10 mL, but the value can be reduced if a higher sample volume is analyzed (e.g.,1.2 µM if the sample volume is 100 mL).

Selectivity tests are undertaken considering dopamine and uric acid as interferents, proving the possibility for the e-MIP-based electrode to quantify ascorbic acid without interference problems or to determine the three analytes simultaneously if all are present in the same sample.

To assess the proposed method's reliability, two pharmaceutical products with known ascorbic acid content are analyzed, and the results agree with the declared ascorbic acid content.

3.8 e-MIP-modified screen-printed electrodes for the voltammetric detection of MCPA

3.8.1 Introduction

As reported in paragraph 3.3, MCPA in an herbicide synthesized in England around 1941. It is a selective phenoxy herbicide that controls broadleaf weeds in arable and cereal crops. MCPA can mimic auxin, encouraging uncontrolled growth and subsequent death of certain plants[131]. The potentiometric sensor developed for the determination of MCPA in water samples reported in paragraph 3.3., can detect MCPA at low concentrations since the detection limit (LOD) is equal to 10 nM, but it is not able to quantify the analyte in the presence of other phenoxy herbicides having a similar molecular structure and shape. The voltammetric sensor here presented aimed to quantify MCPA even in the presence of interferent species. This sensor is based on a screen-printed cell with the graphite working electrode modified by a molecularly imprinted electro-synthesized polymer (e-MIP).

Differential Pulse Voltammetry (DPV) is the technique employed, exploiting the irreversible oxidation peak of the analyte at about + 1.2 V in phosphate buffer at pH 5.5. Due to the high background currents observed in these experimental conditions that could limit the possibility of detecting concentrations below 10 µM, multivariate data treatment is effectively used. In particular, Partial Least Squares regression is the tool applied, preceded by the Savitzky–Golay smoothing (first-derivative function) of the DPV signals.

As highlighted in recent reviews[202–204], chemometrics in electrochemistry research is still underutilized. However, chemometrics can improve the analytical performance of electrochemical sensors, cut the cost of sensor fabrication and analysis by optimization through experimental design, reduce the dimensionality of the data, and eliminate drift effects or interference problems. It can also be applied to the development of multivariate models for quantitative analysis.

The potential and effectiveness of chemometric tools have been verified in this study, developing tailored PLS models in synthetic aqueous solutions (buffered at pH 5.5) and tap water samples fortified with MCPA and other pesticides as possible interferents.

3.8.2 Material and methods

3.8.2.1 Working electrode modification by e-MIP or e-NIP

The prepolymeric mixture of 15 mM pyrrole and 1 mM MCPA (template) in 10 mL 0.1 M $LiClO_4$ is stirred for 30 min to let the template molecules interact with the monomer. The molar ratio template/monomer is 1:15. Analogous mixture but without the template is prepared to obtain the non-imprinted polymer (e-NIP).

Before modification, each screen-printed cell (SPC) is rinsed with ethanol and left to dry at room temperature.

The e-MIP and e-NIP are obtained by electropolymerizing the correspondent prepolymeric mixture onto the clean working electrode of the SPC. 5 scans of cyclic voltammetry from -0.2 V to +0.8 V at 0.1 V/s are sufficient to obtain a homogeneous coating and a film not too thick. The screen-printed cells are left to dry overnight at room temperature. The template is removed from the e-MIP by placing the modified SPC in 10 mL of an ethanol/acetic acid solution (4:1) for 20 min, three times, and then washing it with deionized water.

These modified screen-printed cells are disposable, so they do not need further processing after use.

3.8.2.2 Characterization of the working electrode surface and the electrochemical process of the analyte to the electrode surface

The working electrode surface of the bare and modified electrodes is characterized by determining the active area (using 5 mM potassium hexacyanoferrate(III)/0.1 M KCl at pH 7 as the electrochemical probe solution) and the double-layer capacitance (in NaCl 0.1 M solution) according to the methods presented in paragraphs 3.2.3.1. and 3.2.3.2. Further characterization is performed by electrochemical impedance spectroscopy (EIS) according to the methodology reported in paragraph 3.2.3.4.

The electrochemical process of the analyte to the electrode surface of the bare and modified electrodes is characterized by determining the number of electrons exchanged during the electrochemical process (*n*), the charge transfer coefficient (α), the E° potential, the kinetic electron transfer constant (k°), the diffusion coefficient (D), and the reaction order (r.o.) according to the procedure and the equations reported in paragraphs 3.2.4.1 and 3.2.4.2, in 10 mL of 2.5 mM MCPA/0.1 M PBS solution at pH 5.5.

3.8.2.3 MCPA determination by Differential Pulse Voltammetry (DPV)

Differential pulse voltammetry (DPV) is employed to quantify MCPA in aqueous solutions. The parameters used were: potential range from 0 V to 1.5V, 0.1V/s, step potential 0.025 V, potential pulse 0.2 V and pulse time 0.05 s. All the measurements were performed in 10mL of PBS buffer solution at pH 5.5 or tap water samples by adding an increasing quantity of MCPA; the solution was kept under stirring for 15 min, and then the voltammogram was registered.

3.8.2.4 Chemometric data treatment

Chemometric tools are applied to analyze the DPV voltammograms obtained at different MCPA concentrations and in different ionic media. A double-technique approach is selected, combining an unsupervised technique, the principal component analysis (PCA), with the supervised partial least square regression (PLS). Both chemometric data treatments are performed using the open-source R-based software CAT (Chemometric Agile Tool)[32].

PCA is used to reduce the large dataset's dimensionality while retaining most of the information about the data variation. The 2D graphical output allows a more straightforward interpretation of the differences or similarities among the data.

In the present work, PCA is run on the entire dataset (i.e., 58 rows – concentrations of MCPA, and 21 columns – current value for each potential (from 0.6 V to 1.1 V)).

The PCA tool cannot be used for quantitative analysis but helped define the four tailored PLS models to be developed for MCPA quantification in each media.

To develop a PLS model, a suitable data set, called the "training set," has to be prepared; in this case, the training set is obtained by MCPA standard solutions at different concentrations to cover the whole experimental domain homogeneously. The validation of the PLS model is firstly performed by a cross-validation procedure on the training set and then predicting an external data set (validation set) obtained by preparing independent MCPA solutions at different concentrations than those of the training set.

Moreover, the Savitsky-Golay filter is used to smooth the data, obtaining the first derivative of the DPV voltammograms.

Similar training and external sets were prepared to develop tailored PLS models for matrix-matched solutions, i.e., tap water or tap water spiked with atrazine, glyphosate and dichloroprop.

3.8.3 Results and discussion

3.8.3.1 Working electrode modification and characterization

Electropolymerization of the molecularly imprinted polypyrrole is performed via cyclic voltammetry in the potential range -0.2 V to +0.8V at 0.1V/s in an aqueous solution of 15 mM pyrrole, 1 mM MCPA and 0.1 M $LiClO_4$. Five scans are selected as a good compromise between an insufficient formation of the imprinted cavities with fewer scans and a polymer film too thick with less accessible recognition sites, achievable with more than 7-10 scans. Electrochemical Impedance Spectroscopy (EIS) is used to verify the actual modification of the working electrode surface of the screen-printed cell with the e-MIP or e-NIP. Impedimetric measurements are performed in an electrochemical probe solution (0.05 M $K_3Fe(CN)_6$/0.1 M KCl at pH 7) from 100 kHz to 10 mHz using the non-modified electrode (bare), and those modified by the e-MIP or e-NIP. The modified screen-printed electrode is characterized under different conditions: using the e-MIP-based electrode before and after the complete removal of the template and after equilibration with two different concentrations of analyte (10 µM and 50 µM) to understand how the electrochemical behavior of the modified electrode changes depending on the number of occupied cavities by the analyte. Besides, the bare and the e-NIP-modified electrodes are studied. The data obtained from the EIS analysis are shown in the Nyquist plot of Figure 76; the same figure reports the related Randles equivalent circuit.

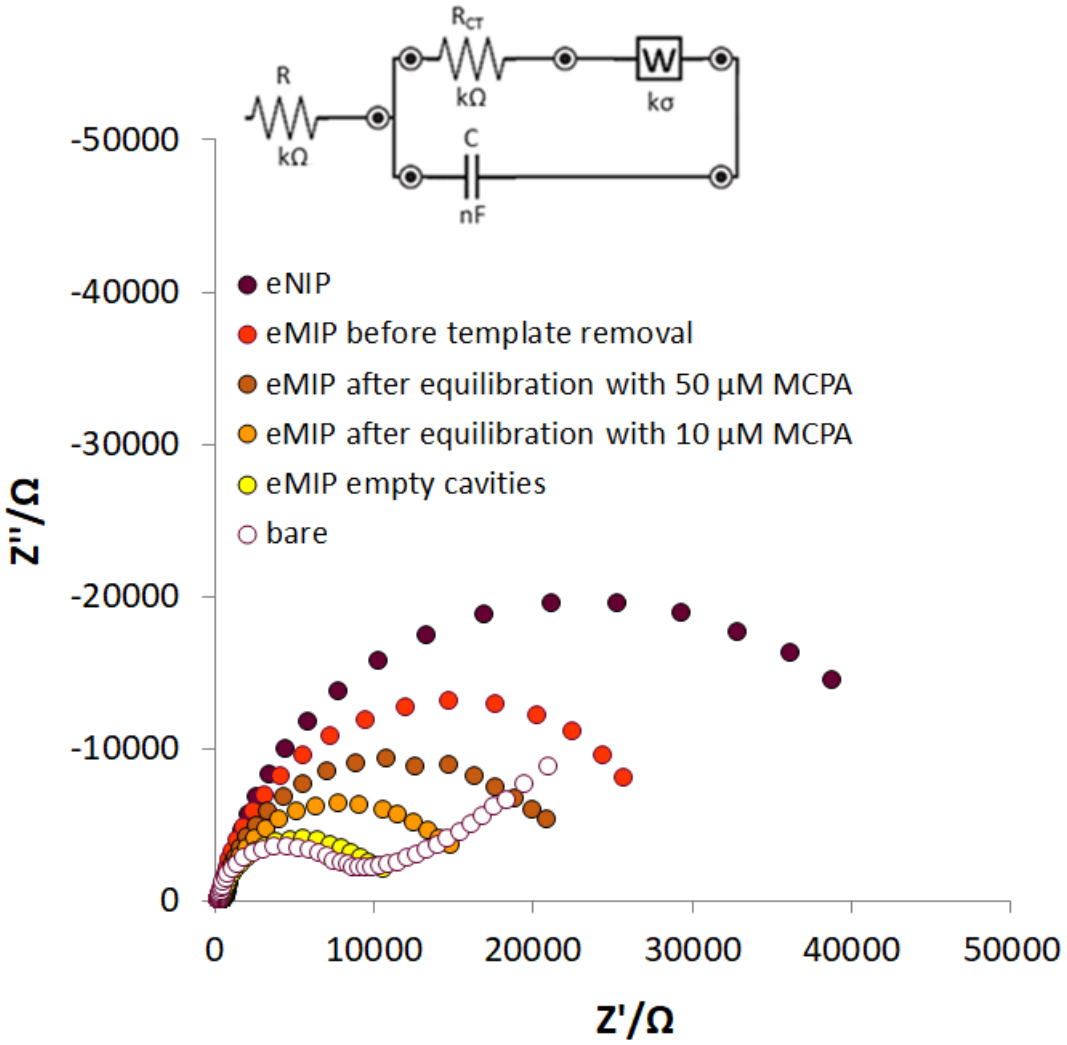

Figure 76.Nyquist plot of bare and modified working electrode of the screen-printed cell. In the inset: Randles equivalent circuit.

The Nyquist plots in Figure 76 report the measurements performed with differently modified working electrodes. The bare electrode trend represented by grey dots is very similar to the theoretical one, while the behavior of the polymer-modified screen-printed electrodes changes. In particular, in the modified screen-printed electrode, the charge transfer resistance increases (the diameter of the semi-circle increases), and the straight line of the diffusion is not visible, probably due to the thickness of the polymers on the electrode's surface. Focusing on the R_{CT}, it can be observed that the resistance increases from the e-MIP-modified electrode after removing the MCPA (yellow dots) to the same electrode where the template occupies all the cavities (red dots). This behavior may be because MCPA ions (given that the MCPA pK_a= 3.07, the predominant species at pH 7 is the

negatively charged deprotonated form[149]) in the polymer cavities prevent the electrochemical probe ions from reaching the surface of the working electrode.

The highest resistance is measured with the e-NIP-modified electrode (black dots); this behavior can be explained considering that the polymeric film does not possess the selective cavities for the analyte, so the probe ions are prevented from reaching the sensing surface. As shown in Figure 76, the R_{CT} for the e-MIP-modified electrode increases proportionally to the MCPA concentration in solution, so in principle, this technique could be used for quantitative analysis.

The working electrode surface before and after modification is characterized by determining the active area and the double-layer capacitance; the results are summarized in Table 40.

Table 40. *Characterization of the working electrode surface: active area and double-layer capacitance measured before and after electrode's modification. The active area was determined by CV from -1.0V to +1.0V at different scan rates from 0.2 V/s to 0.5 V/s in 5 mM $K_3Fe(CN)_6$/0.1 M KCl at pH 7. The double-layer capacitance was determined by CV from -0.5V to +0.5V at different scan rates from 0.2 V/s to 0.5 V/s in 0.M NaCl.*

	Active Area (mm^2)	**Double layer capacitance (μF)**
bare	3.7(1)	1.07(3)
e-MIP	3.3(1)	9.9(9)
e-NIP	1.9(1)	3.2(5)

As can be observed from Table 40, the active area is higher for the bare electrode than that of the e-MIP and e-NIP-modified screen-printed electrode; this is due to the presence of a polymeric film on the surface of the working electrode that prevents (partially for the eMIP and totally for the eNIP) the ions of the electrochemical probe from reaching the surface of the electrode. The active area of the eNIP-modified electrode is lower than that of the e-MIP-based one because the polymer is less porous and does not possess the recognition cavities. The double-layer capacitance is higher for the e-MIP and e-NIP-modified electrodes since a conductive polymer is deposited on the surface, facilitating the formation of the double-layer of charges. The more the polymer is porous, the higher the double-layer capacitance because there are more sites where charges can be accumulated.

3.8.3.2 *Characterization of the electrochemical process of MCPA at the bare and e-MIP-modified electrode surface*

The electrochemical redox process of MCPA at the bare and e-MIP-modified electrodes is characterized by determining the number of electrons exchanged during the oxidation process (*n*), the charge transfer coefficient (*α*), the E° potential, the diffusion coefficient (D), the kinetic charge transfer constant (*k*°) and the reaction order (r.o.). The results are reported in Table 41.

Table 41. *Characterization of the electrochemical process at the bare and eMIP-modified electrode surface. Measurements are performed in CV from 0V to +1.5V at different scan rates from 0 to 1.8 V/s, in 2.5 mM MCPA, PBS 0.1 M at pH 5.5. The number of electrons exchanged (n) is determined by the controlled potential electrolysis at a fixed potential (+1.2 V) in 2.5 mM MCPA, PBS 0.1 M at pH 5.5.*

	n	***α* (V)**	**E° (V)**	**D (cm^2/s)**	***k*°**	**r.o.**
bare	1	0.31	1.08	0.0019	$3 \cdot 10^{-5}$	1
e-MIP	1	0.36	0.99	0.0018	$1 \cdot 10^{-5}$	1

The charge transfer coefficient is similar for both electrodes; in fact, the material of the working electrode is the same. The E° potential slightly decreases when the polymer is deposited on the surface of the working electrode; this behavior was also observed in previous studies[17]. The diffusion coefficient of MCPA is slightly lower when measured using the e-MIP-modified electrode, probably because the presence of the polymer slows down the mobility of the analyte toward the electrode surface.

Similarly, the kinetic charge transfer coefficient (*k*°) is lower for the eMIP-modified electrode because the polymer on the surface prevents a few MCPA molecules from reaching the working electrode's surface. Since the redox process involves only MCPA, the first order of the reaction was confirmed, obtaining a slope near 1 by plotting the logarithm concentration of MCPA vs. the logarithm of the peak current. From the graphs log i_p vs. log *v*, a linear trend is verified for both electrodes, confirming that the process at the electrode surface is mainly diffusive.

Figure F 6.5- 1 a) and b) (Appendix V - e-MIP-modified screen-printed electrodes for the voltammetric detection of MCPA (electrode characterization and PLS model performaces)) show the CV curves for the bare and e-MIP-modified electrodes; Table T 6.5-1(Appendix V - e-MIP-modified screen-printed electrodes for the voltammetric detection of MCPA (electrode characterization and PLS model performaces) summarizes the regression line

equations of the various graphs from CV data used to evaluate the parameters reported in Table 41.

3.8.3.3 Quantitative determination of MCPA by the e-MIP-modified sensor

The characterized eMIP-modified electrode was then used for quantitative analysis by Differential Pulse Voltammetry (DPV) measurements.

Firstly, the method's feasibility was tested in synthetic standard solutions of MCPA. Aiming to define the suitable ionic medium for the analysis, acetate buffer at pH 4.5 and phosphate buffers at pH 5.5 and 7 were considered. The calibration data for each solution were compared, and the medium in which the dose-response curve has the highest slope of the straight line was chosen (see Appendix V - e-MIP-modified screen-printed electrodes for the voltammetric detection of MCPA (electrode characterization and PLS model performaces), F 6.5- 2). Highest sensitivity was obtained in phosphate buffer solution at pH 5.5; for this reason, further DPV measurements were performed in this ionic medium with increasing concentrations of MCPA, recording the voltammogram from 0 V to 1.5 V and 0.1 V/s scan rate.

At low analyte concentrations in solution, it was difficult to identify the anodic peak with the naked eye; for this reason, Partial Least Suare regression (PLS) coupled with the Savitsky-Golay first derivative smoothing filter (S-G)[205] was used as the chemometric tool for the data treatment. In this way, lower analyte concentrations can be detected. Figure 77 shows an example of voltammograms before and after S-G smoothing.

DPV measurements were performed in PBS 0.1 M at pH 5.5 with increasing concentrations of MCPA from 7.4 µM to 103 µM, recording the voltammogram from +0 V to 1.5V and 0.1V/s scan rate. The PLS model was created after applying the S-G filter to each voltammogram.

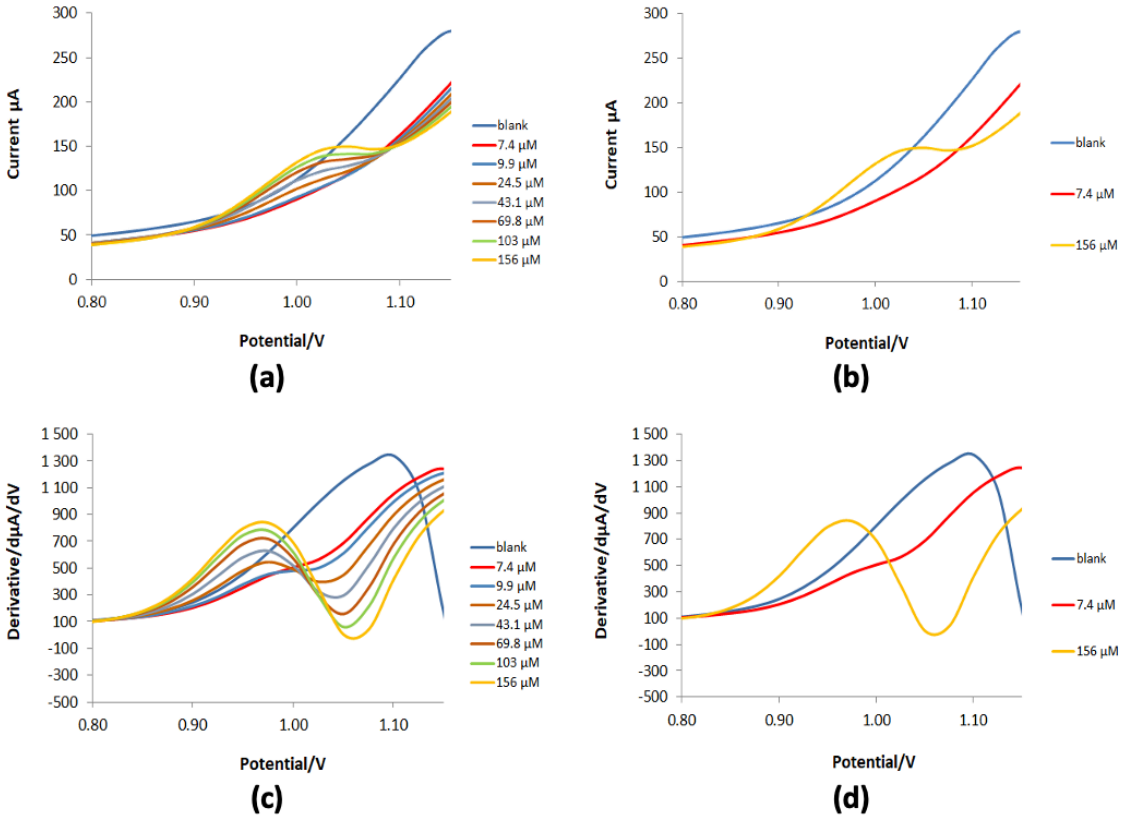

Figure 77. Voltammograms performed in PBS 0.1 M pH 5.5 with increasing concentrations of MCPA using the e-MIP_SPC for measurements. a) voltammogram of the calibrations measurements, b) voltammograms of the blank (PBS), at 7.4 µM and 156 µM MCPA concentrations, c) Savitsky-Golay smoothed voltammogram of the calibration measurements, d) Savitsky-Golay smoothed voltammogram of the blank (PBS), at 7.4 µM and 156 µM MCPA concentrations.

The PLS/S-G model was built with a training set comprising the data of five replicates (five different eMIP-modified electrodes) of a 4-point calibration with MCPA concentrations ranging from 7.4 µM to 103 µM. The external dataset to validate and prove the model's robustness comprised five replicates of measurements performed in solutions at 9.9 µM and 69.8 µM MCPA concentrations.

A 4-latent variables model was realized: it ensures 94.7% of explained variance in Cross-Validation (% E.V. in CV), a global Root Mean Square Error in CV (RMSECV) of 8.3 µM and 5.5 µM of Root Mean Square Error in Prediction (RMSEP) for the external dataset. Figure S4a (Supplementary Material) shows the model performance graph.

Figure 78 reports the Experimental vs. Fitted values plot for the training set (light blue-colored points) and external dataset (yellow-colored points); the points are similarly distributed alongside the y=x straight line, and no significant difference in the fitting error appears. The correlation coefficient of the regression (r^2) for the model and prediction is 0.983 and 0.985, respectively; these values are strongly affected by the higher

irreproducibility of the measurements at lower analyte content, taking into account that modified disposable screen-printed cells were used.

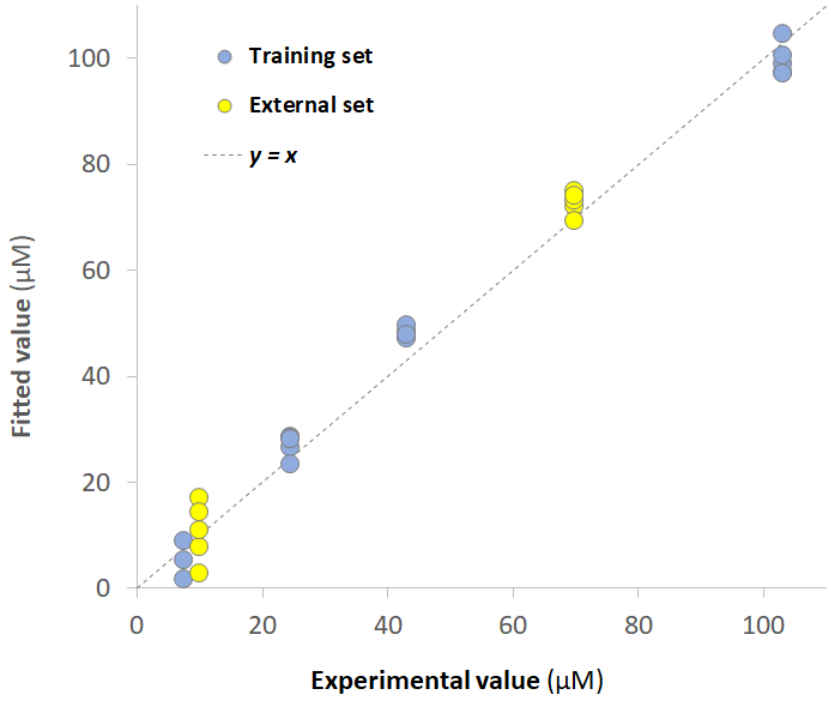

Figure 78. PLS/S-G model in phosphate buffer solution 0.1 M pH 5.5 with increasing concentrations of MCPA from 7.4 µM to 103 µM: Experimental values vs. Fitted values plot for the training set (light blue-colored points) and external set (yellow-colored points).

3.8.3.4 MCPA detecition in tap water samples

As stated in the introduction, the purpose of the work is the MCPA determination in environmental samples.

It has to be highlighted that, like all quantitative methods subject to interferences or when complex sample matrices must be analyzed, calibration with external standards is ineffective. Therefore, matrix-matched calibrations or the standard additions method have to be used. The first approach was adopted here to quantify MCPA in tap water samples by the eMIP-modified sensor. A PLS/S-G model was developed from the DPV measurements in unaltered tap water samples (without the addition of buffer or electrolyte solutions) and adding MCPA from 2.5 µM to 65.4 µM.

The training set comprises the data of two replicates of a 9-point calibration, and the external dataset to validate the model comprised two replicates of measurements performed in solutions at 7.4 µM and 47.6 µM MCPA concentrations.

Figure 79 shows the Experimental vs. Fitted values plot for the training set (blue-colored points) and external dataset (pink-colored points), and Table 42 summarizes the number of latent variables used to develop the model (LVs), the % Exp. Var. CV, the RMSECV, the RMSEP, the correlation coefficient of the regression, the F-test (comparison RMSECV vs. RMSEP) and the limit of quantification LOQ). Figure F 6.5- 3 b) (Appendix V - e-MIP-modified screen-printed electrodes for the voltammetric detection of MCPA (electrode characterization and PLS model performaces)) shows the model performance graph.

Regarding the detection limit (LOD) evaluation, no defined procedure for multivariate calibration exists currently. Establishing a LOD's computation in multivariate methods is more challenging than extending the classical univariate approach. Various strategies have been proposed, but there is not yet a unique method universally accepted by the scientific community. For these reasons, the lowest quantifiable concentration (LOQ) of MCPA was reported for the present method, as shown in Table 42.

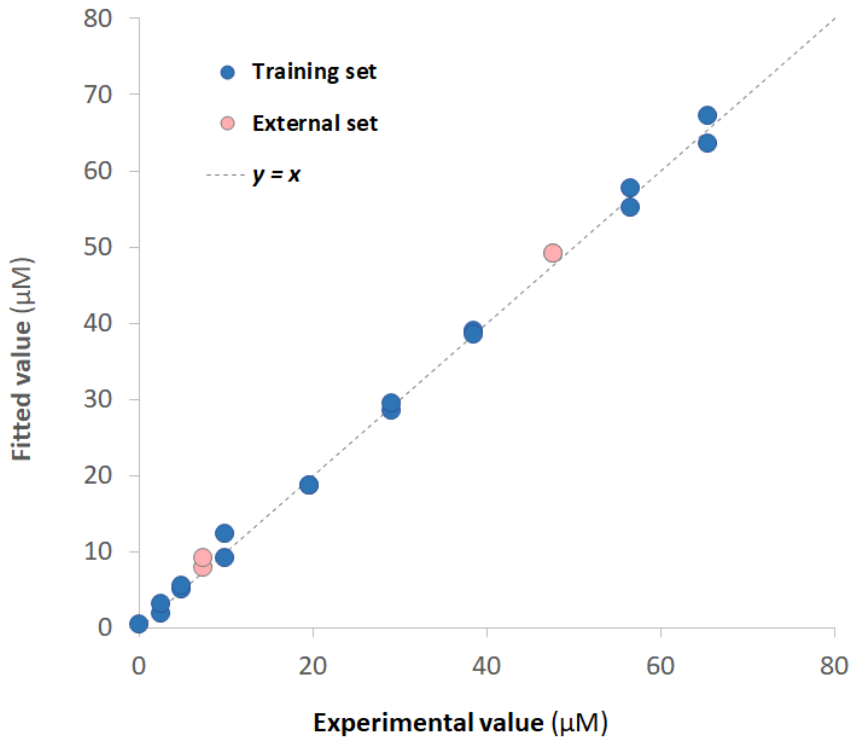

Figure 79. PLS/S-G model in tap water samples with increasing concentrations of MCPA from 2.5 µM to 65.4 µM: Experimental values vs. Fitted values plot for the training set (blue-colored points) and external set (pink-colored points).

Table 42. Number of latent variables (LVs), % explained variance in cross-validation (% Exp. Var. CV), Root Mean Square Error in CV (RMSECV), Root Mean Square Error in prediction (RMSEP), correlation coefficient of the regression (r^2), F-test (comparison RMSECV vs. RMSEP; alpha= 0.05) and limit of quantification (LOQ) for the PLS/S-G model of Figure 79.

PLS/S-G model in tap water		
Training set	LV_s	4
	% Exp.Var. CV	98.51
	RMSECV (µM)	2.8
	r^2 model	0.998
External set	RMSEP (µM)	1.4
	r^2 prediction	0.999
F-test RMSECV vs. RMSEP	calculated F-value	3.9
	critical F-value	8.2
	LOQ (µM)	2.5

The model's robustness and predictive ability were demonstrated; indeed, the training set and external set samples are analogously distributed alongside the y = x straight line, and no significant differences in the fitting errors arise, as confirmed by the F-test; indeed, the precision in cross-validation and prediction is not significantly different, being the calculated F-value lower than the threshold of significance for the alpha = 0.05.

The lowest quantifiable concentration is 2.5 µM corresponding to 500 µg/L; therefore, the sensors cannot directly detect MCPA present in environmental waters at concentrations compared to the World Health Organization (WHO) guideline value (2 µg/ L) or the European Commission Drinking Water Directive 98/83/EC, concerning the quality of water for human consumption, i.e., 0.1 µg/ L[206]; to detect so low analyte concentrations, a preconcentration step is required.

Tap water samples spiked with other pesticides were then analyzed to test the sensor's selectivity.

As interferents, atrazine, glyphosate and dichloroprop were considered. The first two are not electroactive in the potential range applied for the DPV measurements, whereas dichloroprop is a structural analog of MCPA and undergoes irreversible oxidation at a similar potential.

The experiments were carried out by spiking the water samples with a constant quantity of interferents and adding increasing concentrations of MCPA (from 2.5 to 103 µM). Two levels of interferent concentrations were evaluated: high concentration level, i.e., 50 µM

of one interferent and low concentration level, i.e., from 0.5 to 3 µM of interferents (single or in a mixture). Table 43 reports the composition of these solutions

Table 43. Interferent test: composition of the tap water samples used as media for MCPA calibrations.

	Atrazine (µM)	Glyphosate (µM)	Dichloroprop (µM)
1	50	0	0
2	0	50	0
3	0	0	50
4	1	1	1
5	0.5	1	1.5
6	0	0	2

The voltammograms of the experiments with interferents and those previously obtained in unmodified tap water were submitted to PCA analysis; the score plot is shown in Figure 80.

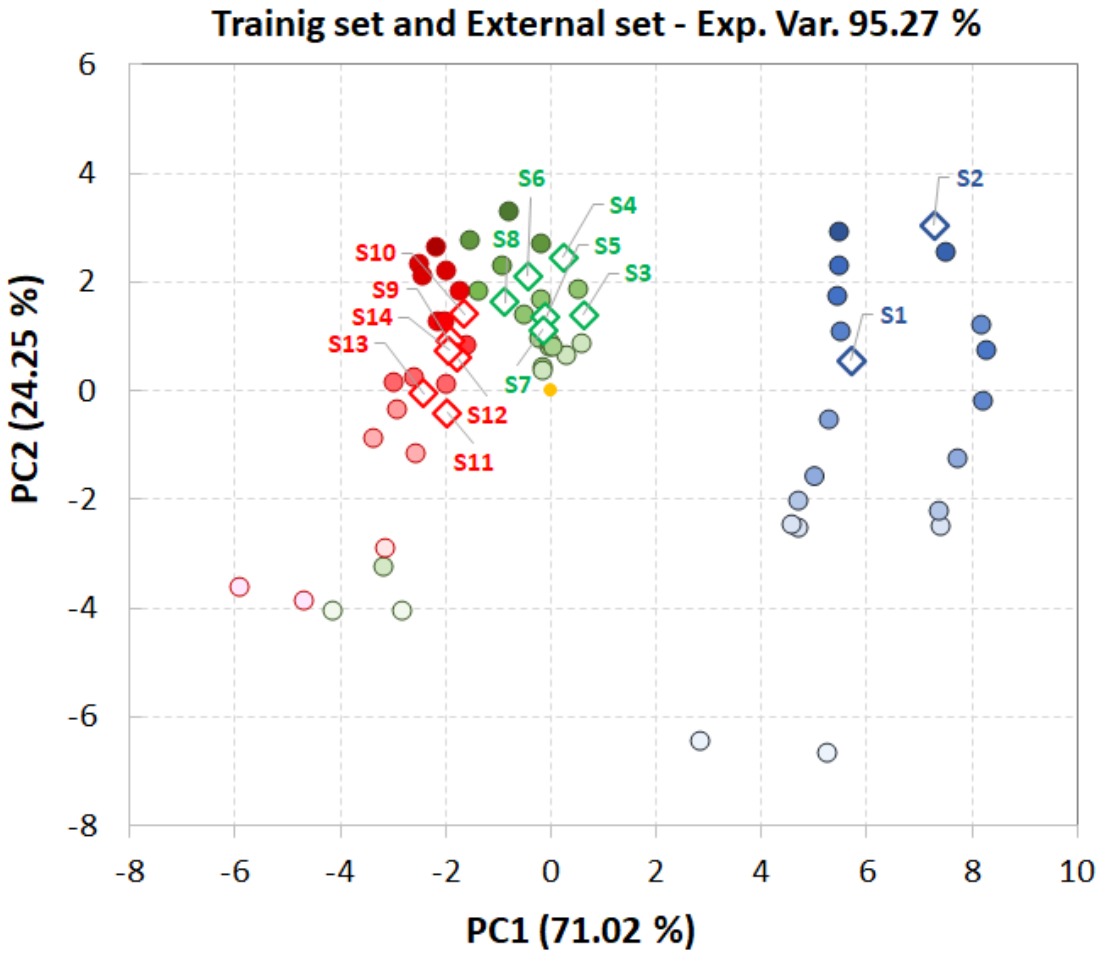

Figure 80. The score plot of the PCA model on the first two principal components is built on the training set (bullet symbol) and validated by a projection of the external dataset (diamond symbol).

The model was obtained considering only the first two components, which explain 95.27 % of the experimental variance. Three groups can be identified along the PC1 axis: the group represented by blue bullets corresponding to the two calibrations performed in unmodified tap water, the one represented by green bullets, i.e., the tap water samples spiked with the high level of interferents, and the group represented by red bullets corresponding to tap water samples spiked with the low level of interferents. The score in PC2 differentiated the samples depending on the MCPA concentration: the PC2 value decreases as the concentration decreases.

The PCA model was validated by a projection of an external dataset (diamond symbol in Figure 80; their composition is reported in Table 44): all samples are correctly located in the corresponding group of the score plot.

Table 44. Composition of the samples S1-S14 used to validate the PCA model.

	Atrazine (μM)	**Glyphosate (μM)**	**Dichloroprop (μM)**	**MCPA (μM)**
S1	0	0	0	29.1
S2	0	0	0	65.4
S3	50	0	0	24.4
S4	50	0	0	69.8
S5	0	50	0	24.4
S6	0	50	0	69.8
S7	0	0	50	24.4
S8	0	0	50	69.8
S9	0	0	2	7.4
S10	0	0	2	24.4
S11	1	1	1	7.5
S12	1	1	1	25
S13	0.5	1	1.5	7.5
S14	0.5	1	1.5	25

It is interesting to highlight that the three groups are distinguished based on interferents' concentration levels, independent of whether they are electroactive.

Moreover, the groups identified suggested the need for three different PLS-tailored models; in other terms, the PLS model built with unmodified tap water samples is ineffective for predicting the MCPA concentrations in the samples containing interferents.

Figure 81 shows the Experimental vs. Fitted values plot for the two PLS/S-G models developed for each interferent concentration level; figures F 6.5- 3 c) and d)(Appendix V - e-MIP-modified screen-printed electrodes for the voltammetric detection of MCPA (electrode characterization and PLS model performaces)) show the model performance graphs and Table 45 summarizes the figures of merit for both models.

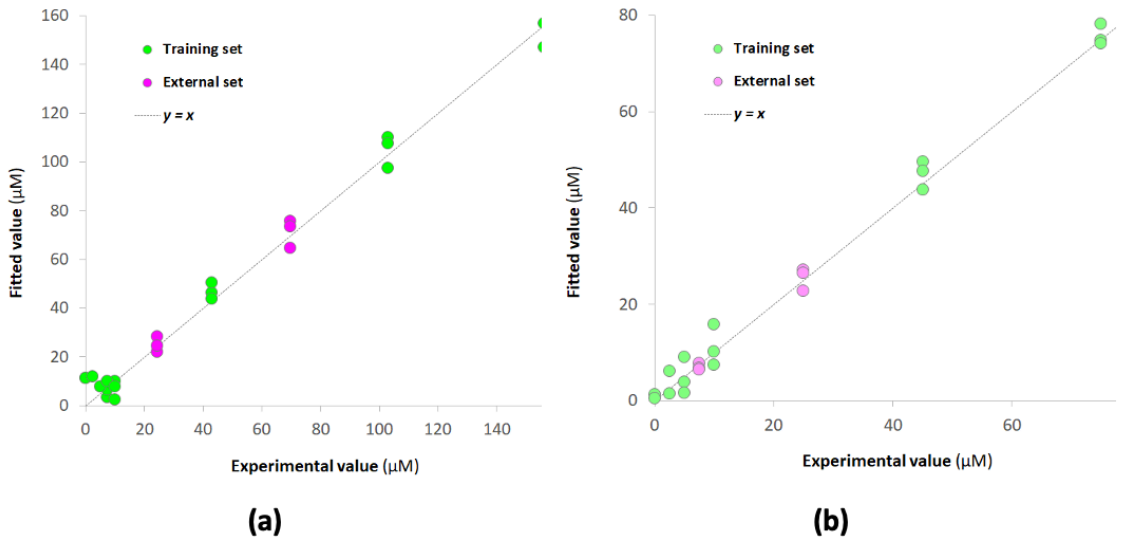

Figure 81. PLS/S-G models (a) in tap water samples spiked with the high level of interferents. External set: samples from S3 to S8 (b) in tap water samples spiked with the low level of interferents. External set: samples from S9 to S14. Experimental values vs. Fitted values plot.

Table 45. Number of latent variables (LVs), % explained variance in cross-validation (% Exp. Var. CV), Root Mean Square Error in CV (RMSECV), Root Mean Square Error in prediction (RMSEP), correlation coefficient of the regression (r^2), and F-tests (alpha= 0.05) for the PLS/S-G models of Figure 81.

		PLS/S-G model High-Level Interferents	**PLS/S-G model Low-level interferents**
Training set	LV_s	2	4
	% Exp.Var. CV	94.47	95.83
	RMSECV (µM)	12.3	5.5
	r^2 model	0.979	0.991
External set	RMSEP (µM)	4.6	3.5
	r^2 prediction	0.973	0.976
F-test RMSECV vs. RMSEP	calculated F-value	7.2	2.5
	critical F-value	4.6	4.6
F-test $RMSECV_{HL}$ vs. $RMSECV_{LL}$	calculated F-value	4.9	
	critical F-value	2.3	
F-test $RMSEP_{HL}$ vs. $RMSEP_{LL}$	calculated F-value	1.7	
	critical F-value	2.3	

Both PLS models proved adequate in predicting the MCPA concentrations even in the presence of interferents since there was pretty good agreement between experimental and fitted values. The fitting error value in cross-validation for the model at High-Level Interferents is higher than that in prediction and also higher than the fitting error in cross-validation for the model at Low-level interferents, as expected since the more concentrated the interferents, the more disturbed and poorer reproducible the measurements. In any case, the RMSEP values are not significantly different for both models, confirming their good predictive capability.

The predicted concentrations of MCPA in the samples from S1 to S14 obtained by projecting these samples in the appropriate PLS/S-G model are reported in Table 46 within the corresponding recovery percentages.

Table 46. Recovery test for the samples used as external datasets in the PLS/S-G models: S1 and S2 for the model in unmodified tap water; S3-S8 for the model High-Level interferents; S9-S14 for the model Low-Level interferents.

	Experimental MCPA (μM)	**Fitted MCPA (μM)**	**Recovery %**
S1	29.1	29.5	101
S2	65.4	63.6	97
S3	24.4	21.9	90
S4	69.8	75.5	108
S5	24.4	26.4	108
S6	69.8	73.6	105
S7	24.4	24.4	100
S8	69.8	64.6	93
S9	7.4	7.7	104
S10	25	22.7	91
S11	7.5	6.8	90
S12	25	27.2	109
S13	7.5	6.4	85
S14	25	26.5	106

The percentage of recoveries for each sample is between 80% and 110%, which is the acceptable recovery range, demonstrating the suitability of the proposed method for MCPA determination in contaminated environmental waters.

3.8.4 Conclusions

A voltammetric sensor for the herbicide MCPA (4-chloro-2-methylphenoxy acid) is developed by modifying the working electrode of a screen-printed cell (SPC) with an electropolymerized molecularly imprinted polymer (e-MIP). In particular, a polypyrrole MIP is synthesized using the MCPA as the template. In the first part of the work, the electrode surface is characterized before and after coating with the MIP, determining the active area and double-layer capacitance. As for the area, there is a decrease in the active surface from the unmodified electrode (bare) to the polymer-modified one, as expected since the polymer film allows the achievement of electroactive species at the electrode only through the cavities present and, therefore, not all the geometric area of the electrode is available. The capacitance of the double layer also increases from the bare electrode to the functionalized one; this means that the functionalization of the electrode with the e-MIP provokes an increased ability to accumulate electrical charges to the electrode and, therefore, an increase in sensor efficiency.

The characterization of the electrochemical process at the bare and e-MIP-modified electrodes is performed: the electron transfer coefficient, the electronic transfer kinetic constant, the potential standard E, the reaction order, the reaction coefficient and the number of electrons involved in the reaction are determined. These measurements showed that the electrochemical reaction is an irreversible oxidation, which occurs with the exchange of 1 electron. After the process characterization, the electrochemical method for the quantification of MCPA in aqueous solution is developed. The selected voltammetric technique was DPV (pulse differential voltammetry). Preliminary measurements have shown that the best ionic medium for conducting experiments is phosphate buffer at pH 5.5. However, even in such a supporting electrolyte, the oxidation peak of MCPA is poorly defined, wide and not symmetrical.

For this reason, the classical monovariate calibration would have failed for the analyte's quantification. Therefore, it is decided to apply a multivariate analysis, and in particular, the Partial Least Square regression (PLS) that allows correlation between the entire

voltammogram and the analyte concentration. To further improve the merit figures of the method, the voltammetric signals are pretreated via a first derivative smoothing filter: the Savitsky-Golay.

The PLS model is built with solutions at different MCPA concentrations in phosphate buffer at pH 5.5 (training set), and it is validated with independent samples at analyte concentrations other than those used for model construction (validation set). The results showed that the model had a good predictive capability.

Subsequently, measurements are performed in a real matrix, i.e., tap water fortified with various pesticides, such as atrazine and glyphosate (non-electroactive molecules) and dichloroprop (structural analog of MCPA and electroactive) and adding increasing amounts of MCPA. The voltammograms of these experiments were submitted to PCA analysis.

Three groups can be identified: the group corresponding to the calibrations performed in unmodified tap water, the one of the tap water samples spiked with a high level of interferents, and the group corresponding to tap water samples spiked with a low level of interferents. Consequently, the need to create ad hoc PLS models for the different types of samples analyzed has emerged. All these matrix-matched models have also proven robustness and have good predictive capabilities. From the results of these models, the percentage recoveries for the samples used as a validation test are calculated, and the values range from 80 % to 110 %, which is the limit of acceptability for the recovery yields in environmental samples.

4 CONCLUSIONS AND FUTURE PERSPECTIVES

This research project presents the development and applications of disposable and low-cost colorimetric and electrochemical sensors for the detection of analytes of environmental and food interest.

Two examples of colorimetric Paper-based Analytical Devices (PADs) are described.

The first one is a completely green array of PADs for pH detection, obtained by impregnating filter paper scraps with aqueous vegetable extracts, allowing rapid and economical preparation[10]**.** Natural dyes extracted from red cabbage (Brassica oleracea) and butterfly pea flower (Clitoria ternatea) are selected because of a wide range of color variations with pH changes. The RGB space model was applied to correlate the PADs' color variation with the pH of aqueous solutions**.** Multi-technique chemometric models are developed to determine the pH value, starting from the RGB triplet of each sensing PAD. Unsupervised techniques are first applied to visualize and rationalize the overall data set, i.e., Three-way Principal Components Analysis (3WPCA) and Principal Components Analysis (PCA). This approach allows for identifying pH subintervals and thus developing tailored Partial Least Square regression (PLS) models. The models obtained are validated by applying them to the analysis of real samples of different pH (natural waters, soft drinks, face lotions, etc.), and, despite scarce precision, a good agreement between the pH values is obtained. The pretty good results are promising and allow us to assert that the PLS models at pH intervals for the PADs' array are suitable for measuring pH in real aqueous samples, as long as they are not colored.

The second colorimetric sensor is the TazoC-PAD in which the receptor is an azoic ligand, (2-(tetrazolylazo)-1,8 dihydroxy naphthalene-3,6,-disulphonic acid), termed TazoC and the substrate the filter paper. The sensor is developed for the selective Pd(II) determination from very acidic aqueous solutions[82]. A proper application of the chemometric tool, PLS, permits the building spectrum/Pd(II) concentration correlation models, using the whole spectrum as the signal accounting for changes in shape and height of the spectrum peaks. Different tailored PLS models are developed and validated, highlighting the need to

perform calibrations in the media of interest to overcome interferences and complex matrix problems. The developed PLS models are adequate for predicting the Pd(II) concentrations even in the presence of interfering cations and in real matrices since there is pretty good agreement between experimental and fitted values.

Other minor contributions of mine, always in the colorimetric sensors field, are in 11 research papers[22,23,207,25–29,35,82,155] and 6 reviews[46,207,209–212] written in collaboration with my research group during the COVID-19 lockdown period.

The central part of the research project is devoted to the development and application of electrochemical sensors, both potentiometric and voltammetric. In all cases, screen-printed cells are employed, aiming to realize disposable, easy-to-handle, and adaptable to on-site analysis devices. The surfaces of the working electrodes are modified to improve the selectivity and, in some cases, even the method's sensitivity.

Two different kinds of electrode modifications are applied: the surface covering with a self-assembled monolayer (SAM) of a functionalizable thiol or a molecularly imprinted polymer (MIP).

The first two devices developed are potentiometric sensors in which the molecularly imprinted polymer over the working electrode surface acts as an ion-selective membrane[18,19].

The sensors are designed to detect atrazine and phenoxy herbicides. In both cases, before and after the modification, the working electrode surface is characterized by determining the active area and evaluating the electrochemical impedance spectra; the non-conductive nature of the acrylic polymer film coverage is confirmed. The pretty good analytical figures of merits obtained are promising for the applications of both sensors to contaminated environmental samples.

In the subsequent two voltammetric sensors, the gold working electrode surface of screen-printed cells is covered by a SAM of a thiol. In the first case, the direct detection of Fe(III) is proposed by exploiting the complexation of the metal cation with the deferoxamine residual linked to the carboxylic group of the 3-mercaptopropionic acid immobilized as a SAM on the gold electrode[214]. The surface of the working electrode is characterized before and after functionalization by determining surface properties such as the area and the double-layer capacitance. The Fe(III) detection is performed by DPV analysis after preconcentration of the cation at the open circuit potential in solution at pH = 1 for two

minutes. The method is applied to the iron(III) quantification in natural water samples, giving promising results.

The other SAM-modified sensor is developed for the indirect detection of glyphosate[215]. The challenge in this case is due to the non-electroactive nature of the analyte. For this purpose, a chemically modified gold working electrode of the screen-printed cell is obtained by covering the electrode surface with a cysteamine-copper self-assembled monolayer (SAM). The method exploits the interaction of glyphosate with copper ions complexed by cysteamine, which results in a decrease in the intensity of copper redox current. Cyclic voltammetry is employed as the measuring technique. When dealing with voltammograms with numerous peaks changing in shape and size, it is difficult to define which signal is the most significant for the analyte determination; in these cases, a helpful approach is chemometrics. Although chemometrics is still poorly applied in the electroanalytical field, in this work, PLS (Partial Least Square regression) is applied to build models to correlate the signal with the glyphosate concentration in standard aqueous solutions and tap water samples (matrix-matched calibration). The method's figures of merits are evaluated, obtaining a limit of quantification of about 5 µM. The reliability of the proposed sensor is verified by analyzing tap water spiked with glyphosate, and recoveries higher than 90 % are achieved.

The last three voltammetric sensors are all realized, covering the graphite working electrode surface of the screen-printed cell with a molecularly imprinted polymer.

Only the sensor for the Irbesartan detection is based on an acrylic MIP[16]. In this case, the composition of the prepolymeric mixture of template, functional monomer and cross-linker is optimized by a full factorial experimental design. The optimal mixture is drop-coated on the working electrode surface, and the thermal polymerization is carried out. The square wave voltammetry (SWV) Is the technique applied. The whole analysis is replicated with different SPCs, obtaining similar results, which highlight the good reproducibility potential. These sensors are applied to determine Irbesartan in fortified tap water samples, obtaining high recovery percentages. Given the good results, the method is promising for quantifying Irbesartan at a trace level.

Finally, the last two sensors are based on screen-printed cells in which the working electrode is modified with electropolymerized molecularly imprinted polypyrrole (e-MIP).

The first is devoted to the determination of ascorbic acid[17]; differential pulse voltammetry (DPV) is the selected method for the analysis. The ascorbic acid molecules are successfully entrapped in the polypyrrole film, creating the recognition sites. The best results are obtained after polypyrrole overoxidation. A comparison with the bare and the not-imprinted polypyrrole-modified electrodes shows that the e-MIP-based sensor has the highest selectivity and reproducibility. The developed method is applied to assess ascorbic acid in farmaceutical products, obtaining values that are not significantly different from the declared content by the pharmaceutical companies.

The last e-MIP-based voltammetric sensor is developed for the selective detection of the MCPA herbicide. Differential pulse voltammetry (DPV) is the technique employed, exploiting the irreversible oxidation peak of the analyte at about + 1.2 V in phosphate buffer at pH 5.5. Due to the high background currents observed in these experimental conditions that could limit the possibility of detecting concentrations below 10 µM, multivariate data treatment is effectively used. Therefore, it is decided to apply a multivariate analysis, and in particular, the Partial Least Square regression (PLS) that allows correlation between the entire voltammogram and the analyte concentration. To further improve the merit figures of the method, the voltammetric signals are pretreated via a first derivative smoothing filter: the Savitsky-Golay. The PLS model is built firstly with solutions at different MCPA concentrations in phosphate buffer at pH 5.5; subsequently, measurements are performed in a real matrix, i.e., tap water fortified with various pesticides and adding increasing amounts of MCPA. By projecting the DPV voltammograms of these experiments into the PLS model in phosphate buffer, it was found that the model cannot correctly predict MCPA concentrations in real matrix samples. The need to create ad hoc PLS models for the different types of samples analyzed has emerged. All these matrix-matched models have also proven robustness and have good predictive capabilities. From the results of these models, the percentage recoveries for the samples used as a validation test are calculated, and most of these values range from 80 % to 110 %; only in some cases are slightly higher than the limits of acceptability for the recovery yields in environmental samples. This work will be submitted to “A special issue to honor contributions of women to the field of Sensors and Actuators” (Journal *Sensors and Actuators Reports*, Elsevier).

Regarding both parts (colorimetric and electrochemical sensors), my three-year research production is summarised in 19 research articles published in international peer-reviewed journals[16,17,29,31,35,45,76,82,152,155,207,215,18,216,217,19,22,23,25–28].

Moreover, I had consistent participation to Italian and International conferences as the presenting author in oral and poster contributions concerning my research.

Although pretty good results are obtained, some other experiments must be done mainly to improve the reproducibility and sensitivity of both colorimetric and electrochemical sensors. Moreover, the development of sensor arrays will be a future challenge for the realization of the devices and for the data processing that will be entirely performed with chemometric techniques.

5 REFERENCES

1. Ohashi T, Dai L. Chapter 15 - C60 and carbon nanotube sensors. In: Dai L, ed. *Carbon Nanotechnology*. Elsevier; 2006:525-575. doi:https://doi.org/10.1016/B978-044451855-2/50018-8
2. Kweon S-J, Park J-H, Park C-O, Yoo H-J, Ha S. Wireless Kitchen Fire Prevention System Using Electrochemical Carbon Dioxide Gas Sensor for Smart Home. *Sensors*. 2022;22(11). doi:10.3390/s22113965
3. Schröder C, Förster R, Zwahlen DR, Windisch P. The Apple Watch spO2 sensor and outliers in healthy users. *npj Digit Med*. 2023;6(1):63. doi:10.1038/s41746-023-00814-x
4. Bhattacharjee T, Jiang H, Behdad N. Sensor design for water hardness detection. In: *SENSORS, 2013 IEEE*. ; 2013:1-4. doi:10.1109/ICSENS.2013.6688443
5. Tomei MR, Arduini F, Neagu D, Moscone D. Carbon black-based disposable sensor for an on-site detection of free chlorine in swimming pool water. *Talanta*. 2018;189:262-267. doi:https://doi.org/10.1016/j.talanta.2018.07.005
6. Seo G, Lee G, Kim MJ, et al. Rapid Detection of COVID-19 Causative Virus (SARS-CoV-2) in Human Nasopharyngeal Swab Specimens Using Field-Effect Transistor-Based Biosensor. *ACS Nano*. 2020;14(4):5135-5142. doi:10.1021/acsnano.0c02823
7. Nagl S, Wolfbeis OS. Classification of Chemical Sensors and Biosensors Based on Fluorescence and Phosphorescence BT - Standardization and Quality Assurance in Fluorescence Measurements I: Techniques. In: Resch-Genger U, ed. Springer Berlin Heidelberg; 2008:325-346. doi:10.1007/4243_2008_022
8. Hulanicki A, Glab S, Ingman F. Chemical sensors: definitions and classification. *Pure Appl Chem*. 1991;63(9):1247-1250. doi:doi:10.1351/pac199163091247
9. Mandoj F, Nardis S, Di Natale C, Paolesse R. Porphyrinoid Thin Films for Chemical Sensing. In: Wandelt K, ed. *Encyclopedia of Interfacial Chemistry*. Elsevier; 2018:422-443. doi:https://doi.org/10.1016/B978-0-12-409547-2.11677-4
10. Magnaghi LR, Alberti G, Pazzi BM, Zanoni C, Biesuz R. A green-PAD array combined with chemometrics for pH measurements. *New J Chem*. 2022;46(40):19460-19467. doi:10.1039/d2nj03675d
11. Bakhshpour-Yucel M, Gür SD, Seymour E, Aslan M, Lortlar Ünlü N, Ünlü MS. Highly-Sensitive, Label-Free Detection of Microorganisms and Viruses via Interferometric Reflectance Imaging Sensor. *Micromachines*. 2023;14(2). doi:10.3390/mi14020281
12. Nangare SN, Patil AG, Chandankar SM, Patil PO. *Nanostructured Metal–Organic Framework-Based Luminescent Sensor for Chemical Sensing: Current Challenges and Future Prospects*. Vol 13. Springer Berlin Heidelberg; 2023. doi:10.1007/s40097-022-00479-0
13. Gutiérrez A, Burgos JA, Moltó E. Development of an immunosensor based on the measurement of fluorescence. *Sensors Actuators, B Chem*. 2008;131(2):621-626. doi:10.1016/j.snb.2007.12.049
14. Alberti G, Spina S, Arcadio F, et al. MIP-Assisted 3-Hole POF Chip Faced with SPR-POF Sensor for Glyphosate Detection. *Chemosensors*. 2023;11(7):1-13. doi:10.3390/chemosensors11070414

15. Zeng J, Bian A, Chen A, et al. A miniaturized aerosol sizing sensor using light-scattering angular spectrum. *Opt Lasers Eng*. 2023;160(August 2022):107257. doi:10.1016/j.optlaseng.2022.107257
16. Zanoni C, Rovida R, Magnaghi LR, Biesuz R, Alberti G. Voltammetric Detection of Irbesartan by Molecularly Imprinted Polymer (MIP)-Modified Screen-Printed Electrodes. *Chemosensors*. 2022;10(12):1-14. doi:10.3390/chemosensors10120517
17. Alberti G, Zanoni C, Magnaghi LR, Biesuz R. Ascorbic Acid Sensing by Molecularly Imprinted Electrosynthesized Polymer (e-MIP) on Screen-Printed Electrodes. *Chemosensors*. 2023;11(6). doi:10.3390/chemosensors11060348
18. Zanoni C, Spina S, Magnaghi LR, Guembe-Garcia M, Biesuz R, Alberti G. Potentiometric MIP-Modified Screen-Printed Cell for Phenoxy Herbicides Detection. *Int J Environ Res Public Health*. 2022;19(24). doi:10.3390/ijerph192416488
19. Alberti G, Zanoni C, Spina S, Magnaghi LR, Biesuz R. MIP-Based Screen-Printed Potentiometric Cell for Atrazine Sensing. *Chemosensors*. 2022;10(8):339. doi:10.3390/chemosensors10080339
20. Kenny T. Chemical Sensors. *Sens Technol Handb*. Published online 2004:181-191. doi:10.1016/B978-075067729-5/50047-1
21. Lavigne JJ, Anslyn E V. Sensing A Paradigm Shift in the Field of Molecular Recognition: From Selective to Differential Receptors. *Angew Chemie Int Ed*. 2001;40(17):3118-3130. doi:https://doi.org/10.1002/1521-3773(20010903)40:17<3118::AID-ANIE3118>3.0.CO;2-Y
22. Magnaghi LR, Zanoni C, Alberti G, Quadrelli P, Biesuz R. Freshness Traffic Light for Fish Products: Dual-Optode Label to Monitor Fish Spoilage in Sales Packages. *ACS Food Sci Technol*. 2022;2(6):1030-1038. doi:10.1021/acsfoodscitech.2c00097
23. Magnaghi LR, Capone F, Zanoni C, Alberti G, Quadrelli P, Biesuz R. Colorimetric Sensor Array for Monitoring, Modelling and Comparing Spoilage Processes of Different Meat and Fish Foods. *Foods*. 2020;9(5). doi:10.3390/foods9050684
24. Magnaghi LR, Alberti G, Capone F, et al. Development of a Dye-Based Device to Assess the Poultry Meat Spoilage. Part II: Array on Act. *J Agric Food Chem*. 2020;68(45):12710-12718. doi:10.1021/acs.jafc.0c03771
25. Magnaghi LR, Zanoni C, Alberti G, Quadrelli P, Biesuz R. Towards intelligent packaging: BCP-EVOH@ optode for milk freshness measurement. *Talanta*. 2022;241:123230. doi:10.1016/j.talanta.2022.123230
26. Magnaghi LR, Zanoni C, Bellotti D, Alberti G, Quadrelli P, Biesuz R. Quick and Easy Covalent Grafting of Sulfonated Dyes to CMC: From Synthesis to Colorimetric Sensing Applications. *Polymers (Basel)*. 2022;14(19). doi:10.3390/polym14194061
27. Magnaghi LR, Alberti G, Capone F, et al. Development of a dye-based device to assess the poultry meat spoilage. Part II: Array on act. *J Agric Food Chem*. 2020;68(45):12710-12718. doi:10.1021/acs.jafc.0c03771
28. Magnaghi LR, Alberti G, Quadrelli P, Biesuz R. Development of a dye-based device to assess poultry meat spoilage. Part I: Building and testing the sensitive array. *J Agric Food Chem*. 2020;68(45):12702-12709. doi:10.1021/acs.jafc.0c03768
29. Magnaghi LR, Zanoni C, Bancalari E, et al. pH-Sensitive Sensors at Work on Poultry Meat Degradation Detection: From the Laboratory to the Supermarket Shelf. *AppliedChem*. 2022;2(3):128-141. doi:10.3390/appliedchem2030009
30. Magnaghi LR, Capone F, Zanoni C, Alberti G, Quadrelli P, Biesuz R. Colorimetric sensor array for monitoring, modelling and comparing spoilage processes of

different meat and fish foods. *Foods*. 2020;9(5). doi:10.3390/foods9050684
31. Magnaghi LR, Alberti G, Milanese C, Quadrelli P, Biesuz R. Naked-Eye Food Freshness Detection: Innovative Polymeric Optode for High-Protein Food Spoilage Monitoring. *ACS Food Sci Technol*. 2021;1(2):165-175. doi:10.1021/acsfoodscitech.0c00089
32. Leardi, R.; Melzi, C.; Polotti G. G. CAT (Chemometric Agile Tool). G. CAT (Chemometric Agile Tool). http://www.gruppochemiometria.it/index. php/software/19-download-the-rbased-chemometric-software
33. G. Brereton R. Calibration. In: *Chemometrics*. ; 2003:271-338. doi:https://doi.org/10.1002/0470863242.ch5
34. Leardi R, Armanino C, Lanteri S, Alberotanza L. Three-mode principal component analysis of monitoring data from Venice lagoon. *J Chemom*. 2000;14(3):187-195. doi:https://doi.org/10.1002/1099-128X(200005/06)14:3<187::AID-CEM593>3.0.CO;2-0
35. Magnaghi LR, Capone F, Alberti G, et al. EVOH-Based pH-Sensitive Optode Array and Chemometrics: From Naked-Eye Analysis to Predictive Modeling to Detect Milk Freshness. *ACS Food Sci Technol*. 2021;1(5):819-828. doi:10.1021/acsfoodscitech.1c00065
36. Henrion R. N-way principal component analysis theory, algorithms and applications. *Chemom Intell Lab Syst*. 1994;25(1):1-23. doi:https://doi.org/10.1016/0169-7439(93)E0086-J
37. Abdi H, Williams LJ. Partial Least Squares Methods: Partial Least Squares Correlation and Partial Least Square Regression BT - Computational Toxicology: Volume II. In: Reisfeld B, Mayeno AN, eds. Humana Press; 2013:549-579. doi:10.1007/978-1-62703-059-5_23
38. Helland IS. Some theoretical aspects of partial least squares regression. *Chemom Intell Lab Syst*. 2001;58(2):97-107. doi:https://doi.org/10.1016/S0169-7439(01)00154-X
39. Desimoni E, Brunetti B. *L'elaborazione Deidati Nel Laboratorio Di Analisi Chimiche*. CLUEB; 2010.
40. Felipe-Sotelo M, Cal-Prieto MJ, Ferré J, Boqué R, Andrade JM, Carlosena A. Linear PLS regression to cope with interferences of major concomitants in the determination of antimony by ETAAS. *J Anal At Spectrom*. 2006;21(1):61-68. doi:10.1039/B506783A
41. Ortiz MC, Sarabia LA, Sánchez MS. Tutorial on evaluation of type I and type II errors in chemical analyses: From the analytical detection to authentication of products and process control. *Anal Chim Acta*. 2010;674(2):123-142. doi:https://doi.org/10.1016/j.aca.2010.06.026
42. Boqué R, Larrechi MS, Rius FX. Multivariate detection limits with fixed probabilities of error. *Chemom Intell Lab Syst*. 1999;45(1-2):397-408. doi:10.1016/S0169-7439(98)00195-6
43. Allegrini F, Olivieri AC. IUPAC-Consistent Approach to the Limit of Detection in Partial Least-Squares Calibration. *Anal Chem*. 2014;86(15):7858-7866. doi:10.1021/ac501786u
44. Piriya V S A, Joseph P, Daniel S C G K, Lakshmanan S, Kinoshita T, Muthusamy S. Colorimetric sensors for rapid detection of various analytes. *Mater Sci Eng C Mater Biol Appl*. 2017;78:1231-1245. doi:10.1016/j.msec.2017.05.018
45. Liu B, Zhuang J, Wei G. Recent advances in the design of colorimetric sensors for

environmental monitoring. *Environ Sci Nano*. 2020;7(8):2195-2213. doi:10.1039/D0EN00449A
46. Alberti G, Zanoni C, Magnaghi LR, Biesuz R. Disposable and Low-Cost Colorimetric Sensors for Environmental Analysis. *Int J Environ Res Public Health*. 2020;17(22). doi:10.3390/ijerph17228331
47. Sørensen SPLSPL. . *C R Trav Lab Carlsb*. 1909;8.
48. Bergveld P. Thirty years of ISFETOLOGY: What happened in the past 30 years and what may happen in the next 30 years. *Sensors Actuators B Chem*. 2003;88(1):1-20. doi:https://doi.org/10.1016/S0925-4005(02)00301-5
49. Martinez AW, Phillips ST, Butte MJ, Whitesides GM. Patterned paper as a platform for inexpensive, low-volume, portable bioassays. *Angew Chem Int Ed Engl*. 2007;46(8):1318-1320. doi:10.1002/anie.200603817
50. Bordbar MM, Nguyen TA, Arduini F, Bagheri H. A paper-based colorimetric sensor array for discrimination and simultaneous determination of organophosphate and carbamate pesticides in tap water, apple juice, and rice. *Microchim Acta*. 2020;187(11):621. doi:10.1007/s00604-020-04596-x
51. Carneiro MCCG, Rodrigues LR, Moreira FTC, Sales MGF. Colorimetric Paper-Based Sensors against Cancer Biomarkers. *Sensors*. 2022;22(9). doi:10.3390/s22093221
52. Krishnan S, Syed Z ul Q. Colorimetric Visual Sensors for Point-of-needs Testing. *Sensors and Actuators Reports*. 2022;4:100078. doi:https://doi.org/10.1016/j.snr.2022.100078
53. Chaiyo S, Kalcher K, Apilux A, Chailapakul O, Siangproh W. A novel paper-based colorimetry device for the determination of the albumin to creatinine ratio. *Analyst*. 2018;143(22):5453-5460. doi:10.1039/C8AN01122B
54. Choudhary V, Philip L. Stable paper-based colorimetric sensor for selective detection of phosphate ion in aqueous phase. *Microchem J*. 2021;171:106809. doi:https://doi.org/10.1016/j.microc.2021.106809
55. Mukdasai S, Uppachai P, Srijaranai S. A novel colorimetric paper sensor based on the layer-by-layer assembled multilayers of surfactants for the sensitive and selective determination of total antioxidant capacity. *RSC Adv*. 2019;9(49):28598-28608. doi:10.1039/C9RA05642D
56. Pena-Pereira F, Velázquez A, Lavilla I, Bendicho C. A paper-based colorimetric assay with non-instrumental detection for determination of boron in water samples. *Talanta*. 2020;208:120365. doi:https://doi.org/10.1016/j.talanta.2019.120365
57. Chandran N, Janardhanan P, Bayal M, Pilankatta R, Nair SS. Development of a paper printed colorimetric sensor based on Cu-Curcumin nanoparticles for evolving point-of-care clinical diagnosis of sodium. *Sci Rep*. 2022;12(1):6247. doi:10.1038/s41598-022-09852-z
58. Firdaus ML, Aprian A, Meileza N, et al. Smartphone Coupled with a Paper-Based Colorimetric Device for Sensitive and Portable Mercury Ion Sensing. *Chemosensors*. 2019;7(2). doi:10.3390/chemosensors7020025
59. Zhao C, Li Y, Zhao J, et al. A “Test-to-Treat” Pad for Real-Time Visual Monitoring of Bacterial Infection and On-Site Performing Smart Therapy Strategies. *ACS Nano*. 2023;17(14):13296-13309. doi:10.1021/acsnano.3c01158
60. The GIMP Development Team. GNU Image Manipulation Program (GIMP), free software. Ver. 2.10.22. https://www.gimp.org
61. Diehl KL, Anslyn E V. Array sensing using optical methods for detection of chemical

and biological hazards. *Chem Soc Rev*. 2013;42(22):8596-8611. doi:10.1039/C3CS60136F
62. Rodríguez-Gonzálvez P, Guidi G. RGB-D Sensors Data Quality Assessment and Improvement for Advanced Applications BT - RGB-D Image Analysis and Processing. In: Rosin PL, Lai Y-K, Shao L, Liu Y, eds. Springer International Publishing; 2019:67-86. doi:10.1007/978-3-030-28603-3_4
63. Leardi R, Armanino C, Lanteri S, Alberotanza L. Three-mode principal component analysis of monitoring data from Venice lagoon. *J Chemom*. 2000;14(3):187-195. doi:10.1002/1099-128X(200005/06)14:3<187::AID-CEM593>3.0.CO;2-0
64. Wu X, Prior RL. Identification and characterization of anthocyanins by high-performance liquid chromatography-electrospray ionization-tandem mass spectrometry in common foods in the United States: vegetables, nuts, and grains. *J Agric Food Chem*. 2005;53(8):3101-3113. doi:10.1021/jf0478861
65. Wiczkowski W, Szawara-Nowak D, Topolska J. Red cabbage anthocyanins: Profile, isolation, identification, and antioxidant activity. *Food Res Int*. 2013;51(1):303-309. doi:https://doi.org/10.1016/j.foodres.2012.12.015
66. Fu X, Wu Q, Wang J, Chen Y, Zhu G, Zhu Z. Spectral Characteristic, Storage Stability and Antioxidant Properties of Anthocyanin Extracts from Flowers of Butterfly Pea (Clitoria ternatea L.). *Molecules*. 2021;26(22). doi:10.3390/molecules26227000
67. Qasem NAA, Mohammed RH, Lawal DU. Removal of heavy metal ions from wastewater: a comprehensive and critical review. *npj Clean Water*. 2021;4(1):36. doi:10.1038/s41545-021-00127-0
68. Nigam A, Sharma N, Tripathy S, Kumar M. Development of semiconductor based heavy metal ion sensors for water analysis: A review. *Sensors Actuators A Phys*. 2021;330:112879. doi:https://doi.org/10.1016/j.sna.2021.112879
69. Zamora-Ledezma C, Negrete-Bolagay D, Figueroa F, et al. Heavy metal water pollution: A fresh look about hazards, novel and conventional remediation methods. *Environ Technol Innov*. 2021;22:101504. doi:https://doi.org/10.1016/j.eti.2021.101504
70. Komendova R. Recent advances in the preconcentration and determination of platinum group metals in environmental and biological samples. *TrAC Trends Anal Chem*. 2020;122:115708. doi:https://doi.org/10.1016/j.trac.2019.115708
71. Ek KH, Morrison GM, Rauch S. Environmental routes for platinum group elements to biological materials—a review. *Sci Total Environ*. 2004;334-335:21-38. doi:https://doi.org/10.1016/j.scitotenv.2004.04.027
72. Ravindra K, Bencs L, Van Grieken R. Platinum group elements in the environment and their health risk. *Sci Total Environ*. 2004;318(1):1-43. doi:https://doi.org/10.1016/S0048-9697(03)00372-3
73. Kielhorn J, Melber C, Keller D, Mangelsdorf I. Palladium – A review of exposure and effects to human health. *Int J Hyg Environ Health*. 2002;205(6):417-432. doi:https://doi.org/10.1078/1438-4639-00180
74. Rao CRM, Reddi GS. Platinum group metals (PGM); occurrence, use and recent trends in their determination. *TrAC Trends Anal Chem*. 2000;19(9):565-586. doi:https://doi.org/10.1016/S0165-9936(00)00031-5
75. Gomez MB, Gomez MM, Palacios MA. Control of interferences in the determination of Pt, Pd and Rh in airborne particulate matter by inductively coupled plasma mass spectrometry. *Anal Chim Acta*. 2000;404(2):285-294.

doi:https://doi.org/10.1016/S0003-2670(99)00723-0
76. Magnaghi LR, Alberti G, Pazzi BM, Zanoni C, Biesuz R. A green-PAD array combined with chemometrics for pH measurements. *New J Chem*. 2022;46(40):19460-19467. doi:10.1039/D2NJ03675D
77. Tan W, Zhang L, Jarujamrus P, Doery JCG, Shen W. Improvement strategies on colorimetric performance and practical applications of Paper-based analytical devices. *Microchem J*. 2022;180:107562. doi:https://doi.org/10.1016/j.microc.2022.107562
78. Sri Sruthi P, Balasubramanian S, Senthil Kumar P, et al. Eco-friendly pH detecting paper-based analytical device: Towards process intensification. *Anal Chim Acta*. 2021;1182:338953. doi:https://doi.org/10.1016/j.aca.2021.338953
79. Biesuz R, Nurchi VM, Lachowicz JI, Alberti G. Unusual PLS application for Pd(ii) sensing in extremely acidic solutions. *New J Chem*. 2018;42(10):7901-7907. doi:10.1039/C7NJ05085B
80. Pesavento M, Riolo C, Biesuz R. Spectrophotometric determination of palladium(II) with four water-soluble heterocyclic azo dyes. *Analyst*. 1985;110(7):801-805. doi:10.1039/AN9851000801
81. Pesavento M, Profumo A. Evaluation of the activity coefficients of some sulfonated azo dyes and of their complexes with metal ions. *J Chem Soc{,} Perkin Trans 2*. 1992;(1):107-112. doi:10.1039/P29920000107
82. Alberti G, Magnaghi LR, Iurato M, Zanoni C, Biesuz R. Colorimetric Paper-Based Analytical Devices (PADs) Backed by Chemometrics for Pd(II) Detection. *Sensors*. 2023;23(17). doi:10.3390/s23177425
83. Jiménez-Carvelo AM, Salloum-Llergo KD, Cuadros-Rodríguez L, Capitán-Vallvey LF, Fernández-Ramos MD. A perfect tandem: chemometric methods and microfluidic colorimetric twin sensors on paper. Beyond the traditional analytical approach. *Microchem J*. 2020;157:104930. doi:https://doi.org/10.1016/j.microc.2020.104930
84. Pazzi BM, Pistoia D, Alberti G. RGB-Detector: A Smart, Low-Cost Device for Reading RGB Indexes of Microfluidic Paper-Based Analytical Devices. *Micromachines*. 2022;13(10). doi:10.3390/mi13101585
85. Hamedpour V, Postma GJ, van den Heuvel E, Jansen JJ, Suzuki K, Citterio D. Chemometrics-assisted microfluidic paper-based analytical device for the determination of uric acid by silver nanoparticle plasmon resonance. *Anal Bioanal Chem*. 2018;410(9):2305-2313. doi:10.1007/s00216-018-0879-z
86. Pesavento M, Riolo C, Soldi T, Cervo G. Spectrophotometric study of the equilibria between lanthanum (III) and three azodyes. *Ann Chim*. 1979;69:649-661.
87. Melber C, Keller D, Mangelsdorf I, on Chemical Safety IP. Palladium. Published online 2002:First draft prepared by Christine Melbeer, Detlef.
88. 3500-Pd PALLADIUM. In: *Standard Methods For the Examination of Water and Wastewater*. doi:10.2105/SMWW.2882.238
89. 3030 PRELIMINARY TREATMENT OF SAMPLES. In: *Standard Methods For the Examination of Water and Wastewater*. doi:10.2105/SMWW.2882.041
90. Huber L. *Validation and Qualification in Analytical Laboratories (2nd Ed.).* CRC Press; 2007. doi:10.3109/9780849382680
91. González AG, Herrador MÁ, Asuero AG. Intra-laboratory assessment of method accuracy (trueness and precision) by using validation standards. *Talanta*. 2010;82(5):1995-1998. doi:https://doi.org/10.1016/j.talanta.2010.07.071

92. Pablos JL, Sarabia LA, Ortiz MC, et al. Selective detection and discrimination of nitro explosive vapors using an array of three luminescent sensory solid organic and hybrid polymer membranes. *Sensors Actuators, B Chem*. 2015;212:18-27. doi:10.1016/j.snb.2015.01.103
93. Simões FR, Xavier MG. 6 - Electrochemical Sensors. In: Da Róz AL, Ferreira M, de Lima Leite F, Oliveira ON, eds. *Nanoscience and Its Applications*. Micro and Nano Technologies. William Andrew Publishing; 2017:155-178. doi:https://doi.org/10.1016/B978-0-323-49780-0.00006-5
94. Bratov A, Abramova N, Ipatov A. Recent trends in potentiometric sensor arrays-A review. *Anal Chim Acta*. 2010;678(2):149-159. doi:10.1016/j.aca.2010.08.035
95. Kahlert H. Potentiometry BT - Electroanalytical Methods: Guide to Experiments and Applications. In: Scholz F, Bond AM, Compton RG, et al., eds. Springer Berlin Heidelberg; 2010:237-256. doi:10.1007/978-3-642-02915-8_12
96. Hassan SSM, Kamel AH, Fathy MA. A novel screen-printed potentiometric electrode with carbon nanotubes/polyaniline transducer and molecularly imprinted polymer for the determination of nalbuphine in pharmaceuticals and biological fluids. *Anal Chim Acta*. 2022;1227:340239. doi:10.1016/j.aca.2022.340239
97. Bobacka J, Ivaska A, Lewenstam A. Potentiometric Ion Sensors. *Chem Rev*. 2008;108(2):329-351. doi:10.1021/cr068100w
98. Mansuriya BD, Altintas Z. 24 - Screen-printed electrochemical sensor platforms. In: Barhoum A, Altintas ZBT-F of ST, eds. *Woodhead Publishing Series in Electronic and Optical Materials*. Woodhead Publishing; 2023:745-774. doi:https://doi.org/10.1016/B978-0-323-88431-0.00027-2
99. Khaled E, Mohamed GG, Awad T. Disposal screen-printed carbon paste electrodes for the potentiometric titration of surfactants. *Sensors Actuators B Chem*. 2008;135(1):74-80. doi:https://doi.org/10.1016/j.snb.2008.07.027
100. Alberti G, Zanoni C, Magnaghi LR, Biesuz R. Low-cost, disposable colourimetric sensors for metal ions detection. *J Anal Sci Technol*. 2020;11(1). doi:10.1186/s40543-020-00221-x
101. Haupt K, Linares A V, Bompart M, Bui BTS. Molecularly imprinted polymers. *Top Curr Chem*. 2012;325:1-28. doi:10.1007/128_2011_307
102. Beltran A, Borrull F, Marcé RM, Cormack PAG. Molecularly-imprinted polymers: useful sorbents for selective extractions. *TrAC Trends Anal Chem*. 2010;29(11):1363-1375. doi:https://doi.org/10.1016/j.trac.2010.07.020
103. Alexander C, Andersson HS, Andersson LI, et al. Molecular imprinting science and technology: a survey of the literature for the years up to and including 2003. *J Mol Recognit*. 2006;19(2):106-180. doi:10.1002/jmr.760
104. Chen L, Wang X, Lu W, Wu X, Li J. Molecular imprinting: perspectives and applications. *Chem Soc Rev*. 2016;45(8):2137-2211. doi:10.1039/C6CS00061D
105. Kupai J, Razali M, Buyuktiryaki S, Kecili R, Szekely G. Long-term stability and reusability of molecularly imprinted polymers. *Polym Chem*. 2017;8(4):666-673. doi:10.1039/C6PY01853J
106. Creager S. Self-assembled Monolayer Films: Electrochemical Properties. In: Buschow KHJ, Cahn RW, Flemings MC, et al., eds. Elsevier; 2001:8299-8304. doi:https://doi.org/10.1016/B0-08-043152-6/01485-6
107. Edwards GA, Bergren AJ, Porter MD. 8 - Chemically Modified Electrodes. In: Zoski CGBT-H of E, ed. Elsevier; 2007:295-327. doi:https://doi.org/10.1016/B978-

044451958-0.50021-5
108. Profumo A, Zavarise F, Merli D, et al. Derivatized humic acids modified gold electrode: electrochemical characterization and analytical applications. *Anal Chim Acta*. 2007;598(1):58-64. doi:10.1016/j.aca.2007.07.035
109. Bard AJ, Faulkner LR, White HS. *Electrochemical Methods: Fundamentals and Applications*. John Wiley & Sons; 2022.
110. Bockris JOM, Reddy AKN, Gamboa-Aldeco ME. *Modern Electrochemistry 2A: Fundamentals of Electrodics*. Springer US; 2001. https://books.google.it/books?id=utDyTYpimkUC
111. Pensa E, Vericat C, Grumelli D, et al. New insight into the electrochemical desorption of alkanethiol SAMs on gold. *Phys Chem Chem Phys*. 2012;14(35):12355-12367. doi:10.1039/c2cp41291h
112. Dalmia A, Liu CC, Savinell RF. Electrochemical behavior of gold electrodes modified with self-assembled monolayers with an acidic end group for selective detection of dopamine. *J Electroanal Chem*. 1997;430(1):205-214. doi:https://doi.org/10.1016/S0022-0728(97)00223-4
113. Profumo A, Merli D, Pesavento M. Self-assembled monolayer modified gold electrodes for traces Cu(II) determination. *Anal Chim Acta*. 2006;557(1):45-51. doi:https://doi.org/10.1016/j.aca.2005.10.037
114. Klingler RJ, Kochi JK. Electron-transfer kinetics from cyclic voltammetry. Quantitative description of electrochemical reversibility. *J Phys Chem*. 1981;85(12):1731-1741. doi:10.1021/j150612a028
115. Guth U, Gerlach F, Decker M, Oelßner W, Vonau W. Solid-state reference electrodes for potentiometric sensors. *J Solid State Electrochem*. 2009;13(1):27-39. doi:10.1007/s10008-008-0574-7
116. Bockris JO, Khan SUM. Electrode Kinetics BT - Quantum Electrochemistry. In: Bockris JO, Khan SUM, eds. Springer US; 1979:41-79. doi:10.1007/978-1-4684-2493-5_2
117. Macdonald JR, Johnson WB. Fundamentals of Impedance Spectroscopy 1.1 BACKGROUND, BASIC DEFINITIONS, AND HISTORY 1.1.1 The Importance of Interfaces. Published online 2018.
118. Bakas I, Hayat A, Piletsky S, et al. Electrochemical impedimetric sensor based on molecularly imprinted polymers/sol–gel chemistry for methidathion organophosphorous insecticide recognition. *Talanta*. 2014;130:294-298. doi:https://doi.org/10.1016/j.talanta.2014.07.012
119. Abo-Elmagd IF, Mahmoud AM, Al-Ghobashy MA, et al. Impedimetric Sensors for Cyclocreatine Phosphate Determination in Plasma Based on Electropolymerized Poly(o-phenylenediamine) Molecularly Imprinted Polymers. *ACS Omega*. 2021;6(46):31282-31291. doi:10.1021/acsomega.1c05098
120. Shamsipur M, Moradi N, Pashabadi A. Coupled electrochemical-chemical procedure used in construction of molecularly imprinted polymer-based electrode: a highly sensitive impedimetric melamine sensor. *J Solid State Electrochem*. 2018;22(1):169-180. doi:10.1007/s10008-017-3731-z
121. O. Hammerich, B. Speiser O electrochemistry. *Organic Electrochemistry*. 5th ed. (CRC Press Taylor & Francis group, ed.).; 2016.
122. Milanesi CL, Protti S, Chiodi D, Profumo A, Merli D. Electrochemical characterization and voltammetric determination of aryl piperazine emerging as designer drugs. *J Electroanal Chem*. 2021;895:115480.

doi:https://doi.org/10.1016/j.jelechem.2021.115480
123. Brett CMA, Brett AMO. Electrochemistry: Principles, Methods, and Applications. In: ; 1993. https://api.semanticscholar.org/CorpusID:92734651
124. Wu Y, Ji X, Hu S. Studies on electrochemical oxidation of azithromycin and its interaction with bovine serum albumin. *Bioelectrochemistry*. 2004;64(1):91-97. doi:10.1016/j.bioelechem.2004.03.005
125. Laviron E. General expression of the linear potential sweep voltammogram in the case of diffusionless electrochemical systems. *J Electroanal Chem Interfacial Electrochem*. 1979;101(1):19-28. doi:https://doi.org/10.1016/S0022-0728(79)80075-3
126. Capucciati A, Burato A, Bersani C, Protti S, Profumo A, Merli D. Electrochemical Behavior and Voltammetric Determination of Two Synthetic Aroyl Amides Opioids. *Chemosensors*. 2023;11(3). doi:10.3390/chemosensors11030198
127. Klingler RJ, Kochi JK. Electron-transfer kinetics from cyclic voltammetry. Quantitative description of electrochemical reversibility. *J Phys Chem*. 1981;85(12):1731-1741. doi:10.1021/j150612a028
128. Aktar W, Sengupta D, Chowdhury A. Impact of pesticides use in agriculture: their benefits and hazards. *Interdiscip Toxicol*. 2009;2(1):1-12. doi:doi:10.2478/v10102-009-0001-7
129. Gebel T, Kevekordes S, Pav K, Edenharder R, Dunkelberg H. In vivo genotoxicity of selected herbicides in the mouse bone-marrow micronucleus test. *Arch Toxicol*. 1997;71(3):193-197. doi:10.1007/s002040050375
130. Kniewald J, Jakominić M, Tomljenović A, et al. Disorders of male rat reproductive tract under the influence of atrazine. *J Appl Toxicol*. 2000;20(1):61-68.
131. Moszczyński W, Białek A. Ecological Production Technology of Phenoxyacetic Herbicides MCPA and 2,4-D in the Highest World Standard. In: Hasaneen MNAE-G, ed. *Herbicides*. IntechOpen; 2012. doi:10.5772/32140
132. Paszko T. Pdf-88331-22189. 2009;18(6):1083-1091.
133. Bala T, Prasad BL V, Sastry M, Kahaly MU, Waghmare U V. Interaction of Different Metal Ions with Carboxylic Acid Group: A Quantitative Study. *J Phys Chem A*. 2007;111(28):6183-6190. doi:10.1021/jp067906x
134. NoMackay, D., Shiu, W.-Y., Shiu, W.-Y., & Lee SC. *Handbook of Physical-Chemical Properties and Environmental Fate for Organic Chemicals (2nd Ed.)*. (CRC Press., ed.).; 2006. doi:https://doi.org/10.1201/9781420044393
135. Gillespie S. *Drinking Water Radiochemistry Drinking Water Radiochemistry α*.
136. Grande Martínez Á, Arrebola Liébanas FJ, Santiago Valverde R, Hernández Torres ME, Ramírez Casinello J, Garrido Frenich A. Multifamily Determination of Phytohormones and Acidic Herbicides in Fruits and Vegetables by Liquid Chromatography–Tandem Mass Spectrometry under Accredited Conditions. *Foods*. 2020;9(7). doi:10.3390/foods9070906
137. Tan F, Zhao C, Li L, Liu M, He X, Gao J. Graphene oxide based in-tube solid-phase microextraction combined with liquid chromatography tandem mass spectrometry for the determination of triazine herbicides in water. *J Sep Sci*. 2015;38(13):2312-2319. doi:https://doi.org/10.1002/jssc.201500070
138. Mei M, Huang X, Yang X, Luo Q. Effective extraction of triazines from environmental water samples using magnetism-enhanced monolith-based in-tube solid phase microextraction. *Anal Chim Acta*. 2016;937:69-79.

doi:https://doi.org/10.1016/j.aca.2016.08.001
139. Chen D, Zhang Y, Miao H, Zhao Y, Wu Y. Determination of Triazine Herbicides in Drinking Water by Dispersive Micro Solid Phase Extraction with Ultrahigh-Performance Liquid Chromatography–High-Resolution Mass Spectrometric Detection. *J Agric Food Chem*. 2015;63(44):9855-9862. doi:10.1021/acs.jafc.5b03973
140. Rodríguez-González N, Beceiro-González E, González-Castro MJ, Alpendurada MF. On-line solid-phase extraction method for determination of triazine herbicides and degradation products in seawater by ultra-pressure liquid chromatography–tandem mass spectrometry. *J Chromatogr A*. 2016;1470:33-41. doi:https://doi.org/10.1016/j.chroma.2016.10.007
141. Hernandez F, Beltran J, Lopez FJ, Gaspar J V. Use of Solid-Phase Microextraction for the Quantitative Determination of Herbicides in Soil and Water Samples. *Anal Chem*. 2000;72(10):2313-2322. doi:10.1021/ac991115s
142. Brzezicki JM, Andersen ME, Cranmer BK, Tessari JD. Quantitative Identification of Atrazine and its Chlorinated Metabolites in Plasma. *J Anal Toxicol*. 2003;27(8):569-573. doi:10.1093/jat/27.8.569
143. Yokley RA, Mayer LC, Rezaaiyan R, Manuli ME, Cheung MW. Analytical Method for the Determination of Cyromazine and Melamine Residues in Soil Using LC-UV and GC-MSD. *J Agric Food Chem*. 2000;48(8):3352-3358. doi:10.1021/jf991231w
144. James TK, Ghanizadeh H, Harrington KC, Bolan NS. Degradation of atrazine and bromacil in two forestry waste products. *Sci Rep*. 2021;11(1):3284. doi:10.1038/s41598-021-83052-z
145. Rousseau CR, Bühlmann P. Calibration-free potentiometric sensing with solid-contact ion-selective electrodes. *TrAC Trends Anal Chem*. 2021;140:116277. doi:https://doi.org/10.1016/j.trac.2021.116277
146. Abdel-Haleem FM, Mahmoud S, Abdel-Ghani NET, El Nashar RM, Bechelany M, Barhoum A. Polyvinyl Chloride Modified Carbon Paste Electrodes for Sensitive Determination of Levofloxacin Drug in Serum, Urine, and Pharmaceutical Formulations. *Sensors*. 2021;21(9). doi:10.3390/s21093150
147. Shao Y, Ying Y, Ping J. Recent advances in solid-contact ion-selective electrodes: functional materials{,} transduction mechanisms{,} and development trends. *Chem Soc Rev*. 2020;49(13):4405-4465. doi:10.1039/C9CS00587K
148. Frisch, M.J.; Trucks, G.W.; Schlegel, H.B.; Scuseria, G.E.; Robb, M.A.; Cheeseman, J.R.; Scalmani, G.; Barone, V.; Petersson, G.A.; Nakatsuji H. Gaussian 16 Revision A 03 (software). Published online 2016.
149. Teixeira MC, Sá-Correia I. Saccharomyces cerevisiae resistance to chlorinated phenoxyacetic acid herbicides involves Pdr1p-mediated transcriptional activation of TPO1 and PDR5 genes. *Biochem Biophys Res Commun*. 2002;292(2):530-537. doi:10.1006/bbrc.2002.6691
150. Keberle H. The Biochemistry of Desferrioxamine and its Relation to Iron Metabolism. *Ann N Y Acad Sci*. 1964;119(2):758-768. doi:https://doi.org/10.1111/j.1749-6632.1965.tb54077.x
151. Alberti G, Emma G, Colleoni R, Pesavento M, Nurchi VM, Biesuz R. Novel DFO-functionalized mesoporous silica for iron sensing. Part 2. Experimental detection of free iron concentration (pFe) in urine samples. *Analyst*. 2014;139(16):3940-3948. doi:10.1039/C3AN01488F

152. Biesuz R, Emma G, Milanese C, et al. Novel DFO-SAM on mesoporous silica for iron sensing. Part I. Synthesis optimization and characterization of the material. *Analyst*. 2014;139(16):3932-3939. doi:10.1039/c4an00179f
153. Alberti G, Quattrini F, Colleoni R, Nurchi VM, Biesuz R. No Title. *Chem Pap*. 2015;69(8):1024-1032. doi:doi:10.1515/chempap-2015-0112
154. Pawlaczyk M, Schroeder G. Deferoxamine-Modified Hybrid Materials for Direct Chelation of Fe(III) Ions from Aqueous Solutions and Indication of the Competitiveness of In Vitro Complexing toward a Biological System. *ACS Omega*. 2021;6(23):15168-15181. doi:10.1021/acsomega.1c01411
155. Alberti G, Zanoni C, Magnaghi LR, Santos MA, Nurchi VM, Biesuz R. DFO@EVOH and 3,4-HP@EVOH: Towards New Polymeric Sorbents for Iron(III). *Chemosensors*. 2020;8(4). doi:10.3390/chemosensors8040111
156. Cennamo N, Alberti G, Pesavento M, et al. A Simple Small Size and Low Cost Sensor Based on Surface Plasmon Resonance for Selective Detection of Fe(III). *Sensors*. 2014;14(3):4657-4671. doi:10.3390/s140304657
157. Bellotti D, Remelli M. Deferoxamine B: A Natural, Excellent and Versatile Metal Chelator. *Molecules*. 2021;26(11). doi:10.3390/molecules26113255
158. Van Bruggen AHC, He MM, Shin K, et al. Environmental and health effects of the herbicide glyphosate. *Sci Total Environ*. 2018;616-617:255-268. doi:10.1016/j.scitotenv.2017.10.309
159. Richmond ME. Glyphosate: A review of its global use, environmental impact, and potential health effects on humans and other species. *J Environ Stud Sci*. 2018;8(4):416-434. doi:10.1007/s13412-018-0517-2
160. Sammons RD, Gaines TA. Glyphosate resistance: state of knowledge. *Pest Manag Sci*. 2014;70(9):1367-1377. doi:https://doi.org/10.1002/ps.3743
161. Agostini LP, Dettogni RS, Dos Reis RS, et al. Effects of glyphosate exposure on human health: Insights from epidemiological and in vitro studies. *Sci Total Environ*. 2020;705:135808. doi:10.1016/j.scitotenv.2019.135808
162. Valle AL, Mello FCC, Alves-Balvedi RP, Rodrigues LP, Goulart LR. Glyphosate detection: methods, needs and challenges. *Environ Chem Lett*. 2019;17(1):291-317. doi:10.1007/s10311-018-0789-5
163. Sidoli P, Baran N, Angulo-Jaramillo R. Glyphosate and AMPA adsorption in soils: laboratory experiments and pedotransfer rules. *Environ Sci Pollut Res Int*. 2016;23(6):5733-5742. doi:10.1007/s11356-015-5796-5
164. Sun L, Kong D, Gu W, et al. Determination of glyphosate in soil/sludge by high performance liquid chromatography. *J Chromatogr A*. 2017;1502:8-13. doi:10.1016/j.chroma.2017.04.018
165. Wang S, Liu B, Yuan D, Ma J. A simple method for the determination of glyphosate and aminomethylphosphonic acid in seawater matrix with high performance liquid chromatography and fluorescence detection. *Talanta*. 2016;161:700-706. doi:10.1016/j.talanta.2016.09.023
166. Zhang W, Feng Y, Ma L, et al. A method for determining glyphosate and its metabolite aminomethyl phosphonic acid by gas chromatography-flame photometric detection. *J Chromatogr A*. 2019;1589:116-121. doi:10.1016/j.chroma.2018.12.039
167. Campuzano S, Pedrero M, Montemayor C, Fatás E, Pingarrón JM. Characterization of alkanethiol-self-assembled monolayers-modified gold electrodes by electrochemical

impedance spectroscopy. *J Electroanal Chem*. 2006;586(1):112-121. doi:https://doi.org/10.1016/j.jelechem.2005.09.007
168. Coutinho CFB, Silva MO, Machado SAS, Mazo LH. Influence of glyphosate on the copper dissolution in phosphate buffer. *Appl Surf Sci*. 2007;253(6):3270-3275. doi:https://doi.org/10.1016/j.apsusc.2006.07.020
169. Glass RL. Metal complex formation by glyphosate. *J Agric Food Chem*. 1984;32(6):1249-1253. doi:10.1021/jf00126a010
170. E. M, C. M, M. B, L. M, T. U. Cu(II)-Glyphosate system: A study by anodic stripping voltammetry and the influence on Cu adsorption by montmorillonite. *Chemosphere*. 1994;28(12):2185-2196. doi:https://doi.org/10.1016/0045-6535(94)90186-4
171. Daniele PG, De Stefano C, Prenesti E, Sammartano S. Copper(II) complexes of N-(phosphonomethyl)glycine in aqueous solution: a thermodynamic and spectrophotometric study. *Talanta*. 1997;45(2):425-431. doi:https://doi.org/10.1016/S0039-9140(97)00156-2
172. Madsen HEL, Christensen HH, Gottlieb-Petersen C, et al. Stability Constants of Copper(II), Zinc, Manganese(II), Calcium, and Magnesium Complexes of N-(Phosphonomethyl)glycine (Glyphosate). *Acta Chem Scand*. Published online 1978:79-83. https://api.semanticscholar.org/CorpusID:95379353
173. Croom KF, Curran MP, Goa KL, Perry CM. Irbesartan. *Drugs*. 2004;64(9):999-1028. doi:10.2165/00003495-200464090-00011
174. Darwish IA, Darwish HW, Bakheit AH, Al-Kahtani HM, Alanazi Z. Chapter Five - Irbesartan (a comprehensive profile). In: Al-Majed Excipients and Related Methodology AABT-P of DS, ed. Vol 46. Academic Press; 2021:185-272. doi:https://doi.org/10.1016/bs.podrm.2020.07.004
175. Petrović M, Hernando MD, Díaz-Cruz MS, Barceló D. Liquid chromatography–tandem mass spectrometry for the analysis of pharmaceutical residues in environmental samples: a review. *J Chromatogr A*. 2005;1067(1):1-14. doi:https://doi.org/10.1016/j.chroma.2004.10.110
176. Malmborg J, Magnér J. Pharmaceutical residues in sewage sludge: Effect of sanitization and anaerobic digestion. *J Environ Manage*. 2015;153:1-10. doi:https://doi.org/10.1016/j.jenvman.2015.01.041
177. Gracia-Lor E, Sancho J V, Serrano R, Hernández F. Occurrence and removal of pharmaceuticals in wastewater treatment plants at the Spanish Mediterranean area of Valencia. *Chemosphere*. 2012;87(5):453-462. doi:https://doi.org/10.1016/j.chemosphere.2011.12.025
178. Loos R, Carvalho R, António DC, et al. EU-wide monitoring survey on emerging polar organic contaminants in wastewater treatment plant effluents. *Water Res*. 2013;47(17):6475-6487. doi:https://doi.org/10.1016/j.watres.2013.08.024
179. Francke DE. Journal of Pharmaceutical Sciences. *Am J Heal Pharm*. 1964;21(8):343-343. doi:10.1093/ajhp/21.8.343
180. Castro G, Rodríguez I, Ramil M, Cela R. Selective determination of sartan drugs in environmental water samples by mixed-mode solid-phase extraction and liquid chromatography tandem mass spectrometry. *Chemosphere*. 2019;224:562-571. doi:https://doi.org/10.1016/j.chemosphere.2019.02.137
181. Pisoschi AM, Pop A, Serban AI, Fafaneata C. Electrochemical methods for ascorbic acid determination. *Electrochim Acta*. 2014;121:443-460. doi:https://doi.org/10.1016/j.electacta.2013.12.127

182. SIES H, STAHL W, SUNDQUIST AR. Antioxidant Functions of Vitamins. *Ann N Y Acad Sci*. 1992;669(1):7-20. doi:https://doi.org/10.1111/j.1749-6632.1992.tb17085.x
183. Sebastian J. Padayatty Arie Katz YWPEOKJ-HLSCCCADSKD, Levine M. Vitamin C as an Antioxidant: Evaluation of Its Role in Disease Prevention. *J Am Coll Nutr*. 2003;22(1):18-35. doi:10.1080/07315724.2003.10719272
184. Cathcart RF. A unique function for ascorbate. *Med Hypotheses*. 1991;35(1):32-37. doi:https://doi.org/10.1016/0306-9877(91)90080-I
185. Bradshaw MP, Barril C, Clark AC, Prenzler PD, Scollary GR. Ascorbic Acid: A Review of its Chemistry and Reactivity in Relation to a Wine Environment. *Crit Rev Food Sci Nutr*. 2011;51(6):479-498. doi:10.1080/10408391003690559
186. Pisoschi AM, Cheregi MC, Danet AF. Total Antioxidant Capacity of Some Commercial Fruit Juices: Electrochemical and Spectrophotometrical Approaches. *Molecules*. 2009;14(1):480-493. doi:10.3390/molecules14010480
187. McHenry EW, Graham M. Observations on the estimation of ascorbic acid by titration. *Biochem J*. 1935;29(9):2013-2019. doi:10.1042/bj0292013
188. Deshmukh GS, Bapat MG. Determination of ascorbic acid by potassium iodate. *Fresenius' Zeitschrift für Anal Chemie*. 1955;145(4):254-256. doi:10.1007/BF00434121
189. Kall MA, Andersen C. Improved method for simultaneous determination of ascorbic acid and dehydroascorbic acid, isoascorbic acid and dehydroisoascorbic acid in food and biological samples. *J Chromatogr B Biomed Sci Appl*. 1999;730(1):101-111. doi:https://doi.org/10.1016/S0378-4347(99)00193-0
190. Iwase H, Ono I. Determination of ascorbic acid in food by column liquid chromatography with electrochemical detection using eluent for pre-run sample stabilization. *J Chromatogr A*. 1998;806(2):361-364. doi:https://doi.org/10.1016/S0021-9673(98)00062-4
191. Iwase H. Use of nucleic acids in the mobile phase for the determination of ascorbic acid in foods by high-performance liquid chromatography with electrochemical detection. *J Chromatogr A*. 2000;881(1):327-330. doi:https://doi.org/10.1016/S0021-9673(00)00057-1
192. Moreira Gonçalves L. Electropolymerized molecularly imprinted polymers: perceptions based on recent literature for soon-to-be world-class scientists. *Curr Opin Electrochem*. 2021;25:100640. doi:https://doi.org/10.1016/j.coelec.2020.09.007
193. Crapnell RD, Hudson A, Foster CW, et al. Recent Advances in Electrosynthesized Molecularly Imprinted Polymer Sensing Platforms for Bioanalyte Detection. *Sensors*. 2019;19(5). doi:10.3390/s19051204
194. Ramanavicius S, Ramanavicius A. Charge Transfer and Biocompatibility Aspects in Conducting Polymer-Based Enzymatic Biosensors and Biofuel Cells. *Nanomaterials*. 2021;11(2). doi:10.3390/nano11020371
195. Ramanavičius S, Morkvėnaitė-Vilkončienė I, Samukaitė-Bubnienė U, et al. Electrochemically Deposited Molecularly Imprinted Polymer-Based Sensors. *Sensors*. 2022;22(3). doi:10.3390/s22031282
196. Sadki S, Schottland P, Brodie N, Sabouraud G. The mechanisms of pyrrole electropolymerization. *Chem Soc Rev*. 2000;29(5):283-293. doi:10.1039/A807124A
197. Witkowski A, Freund MS, Brajter-Toth A. Effect of electrode substrate on the morphology and selectivity of overoxidized polypyrrole films. *Anal Chem*.

1991;63(6):622-626. doi:10.1021/ac00006a013
198. Hsueh C, Brajter-Toth A. Electrochemical Preparation and Analytical Applications of Ultrathin Overoxidized Polypyrrole Films. *Anal Chem*. 1994;66(15):2458-2464. doi:10.1021/ac00087a009
199. Tonelli D, Ballarin B, Guadagnini L, Mignani A, Scavetta E. A novel potentiometric sensor for l-ascorbic acid based on molecularly imprinted polypyrrole. *Electrochim Acta*. 2011;56(20):7149-7154. doi:https://doi.org/10.1016/j.electacta.2011.05.076
200. Yan C, Liu X, Zhang R, Chen Y, Wang G. A selective strategy for determination of ascorbic acid based on molecular imprinted copolymer of o-phenylenediamine and pyrrole. *J Electroanal Chem*. 2016;780:276-281. doi:https://doi.org/10.1016/j.jelechem.2016.09.046
201. Özcan L, Sahin M, Sahin Y. Electrochemical Preparation of a Molecularly Imprinted Polypyrrole-modified Pencil Graphite Electrode for Determination of Ascorbic Acid. *Sensors*. 2008;8(9):5792-5805. doi:10.3390/s8095792
202. Puthongkham P, Wirojsaengthong S, Suea-Ngam A. Machine learning and chemometrics for electrochemical sensors: moving forward to the future of analytical chemistry. *Analyst*. 2021;146(21):6351-6364. doi:10.1039/D1AN01148K
203. Liu J, Xu Y, Liu S, Yu S, Yu Z, Low SS. Application and Progress of Chemometrics in Voltammetric Biosensing. *Biosensors*. 2022;12(7). doi:10.3390/bios12070494
204. Desagani D, Ben-Yoav H. Chemometrics meets electrochemical sensors for intelligent in vivo bioanalysis. *TrAC Trends Anal Chem*. 2023;164:117089. doi:https://doi.org/10.1016/j.trac.2023.117089
205. Luo J, Ying K, Bai J. Savitzky-Golay smoothing and differentiation filter for even number data. *Signal Processing*. 2005;85(7):1429-1434. doi:10.1016/j.sigpro.2005.02.002
206. Morton PA, Fennell C, Cassidy R, et al. A review of the pesticide MCPA in the land-water environment and emerging research needs. *WIREs Water*. 2020;7(1):1-16. doi:10.1002/wat2.1402
207. Magnaghi LR, Alberti G, Zanoni C, Guembe-Garcia M, Quadrelli P, Biesuz R. Chemometric-Assisted Litmus Test: One Single Sensing Platform Adapted from 1–13 to Narrow pH Ranges. *Sensors*. 2023;23(3). doi:10.3390/s23031696
208. Alberti G, Zanoni C, Losi V, Magnaghi LR, Biesuz R. Current Trends in Polymer Based Sensors. *Chemosensors*. 2021;9(5). doi:10.3390/chemosensors9050108
209. Diouf A, Aghoutane Y, Burhan H, Sen F, Bouchikhi B, El Bari N. Tramadol sensing in non-invasive biological fluids using a voltammetric electronic tongue and an electrochemical sensor based on biomimetic recognition. *Int J Pharm*. 2021;593(November 2020):120114. doi:10.1016/j.ijpharm.2020.120114
210. Alberti G, Zanoni C, Magnaghi LR, Biesuz R. Gold and Silver Nanoparticle-Based Colorimetric Sensors: New Trends and Applications. *Chemosensors*. 2021;9(11). doi:10.3390/chemosensors9110305
211. Alberti G, Zanoni C, Magnaghi LR, Biesuz R. Deferoxamine-Based Materials and Sensors for Fe(III) Detection. *Chemosensors*. 2022;10(11). doi:10.3390/chemosensors10110468
212. Magnaghi LR, Zanoni C, Alberti G, Biesuz R. The colorful world of sulfonephthaleins: Current applications in analytical chemistry for “old but gold” molecules. *Anal Chim Acta*. 2023;1281:341807. doi:https://doi.org/10.1016/j.aca.2023.341807
213. Alberti G, Zanoni C, Spina S, Magnaghi LR, Biesuz R. Trends in Molecularly Imprinted

Polymers (MIPs)-Based Plasmonic Sensors. *Chemosensors*. 2023;11(2). doi:10.3390/chemosensors11020144

214. Alberti G, Zanoni C, Rovertoni S, Magnaghi LR, Biesuz R. Screen-Printed Gold Electrode Functionalized with Deferoxamine for Iron(III) Detection. *Chemosensors*. 2022;10(6). doi:10.3390/chemosensors10060214
215. Giancarla A, Zanoni C, Merli D, Magnaghi LR, Biesuz R. A new cysteamine-copper chemically modified screen-printed gold electrode for glyphosate determination. *Talanta*. 2024;269:125436. doi:https://doi.org/10.1016/j.talanta.2023.125436
216. Alberti G, Zanoni C, Rovertoni S, Magnaghi LR, Biesuz R. Screen-printed Gold Electrode Functionalized with Deferoxamine for Iron(III) Detection. *Chemosensors*. 2022;10(6). doi:10.3390/chemosensors10060214
217. Alberti G, Zanoni C, Losi V, et al. Kinetic and thermodynamic sorption studies of Fe(iii) and Zr(iv) by DFO@Purolite{,} a desferrioxamine B based chelating resin. *New J Chem*. 2023;47(28):13436-13449. doi:10.1039/D3NJ00903C

6 APPENDIX

6.1 Appendix I: Reagents and instruments

6.1.1 Reagents

6.1.1.1 Reagents for "Green-PAD array for pH measurements" and "TazoC-PADs for Pd(II) detection" (paragraphs 2.3 and 2.4)

- Distillated water (Chemistry Department, University of Pavia)
- The tap water (Chemistry Department, University of Pavia, Italy)
- Cellulose filter paper Whatman grade 1 (Laboindustria S.p.a., Arzergrande, Italy,)
- Red cabbage (*Brassica oleracea)* (Supermarket, Pavia, Italy)
- Butterfly pea flower *(Clitoria ternatea)* (Supermarket, Pavia, Italy)
- TazoC molecule (synthesized as reported in literature[86])
- Hydrochloric acid (Merk Life Science S.r.l., Milan, Italy, CAS:7647-01-0)
- Sodium orthophosphate (Merk Life Science S.r.l., Milan, Italy, CAS: 7558-79-4)
- Sodium hydroxide (Merk Life Science S.r.l., Milan, Italy, CAS: 1310-73-2)
- Palladium standard 1g/L, *Trace*CERT® (Supleco-Merk Life Science S.r.l., Milano, Italy, CAS: 207349)
- Copper standard 1g/L, *Trace*CERT®(Merk Life Science S.r.l., Milano, Italy, CAS: 68921)
- Nickel standard 1g/L, *Trace*CERT® (Merk Life Science S.r.l., Milano, Italy, CAS: 28944)
- Acetic acid (Merk Life Science S.r.l., Milano, Italy, CAS: 64-19-7)
- Ammonia cleaner (S.a.i.soc.alcoli Insutriali Sas, Italy)
- Tropical Aloe Vera drink (Eurofood S.p.A. Italy)
- Scheppes tonic water (Schweppes International Limited, Italy)
- Sprite (Coca-Cola S.r.L., Italy)
- White wine vinegar "Gaia" (Formec Biffi S.p.A., Italy)

6.1.1.2 Reagents for "MIP-modified screen-printed potentiometric sensors for Atrazine and phenoxy herbicides" and "MIP-based scree-printed electrode for Irbesartan sensing" (paragraphs 3.3 and 3.6)

- Methacrylic acid (MAA) (Merk Life Science S.r.l., Milan, Italy,, CAS: 79-41-4)
- Ethylene glycol dimethacrylate (EGDMA) (Merk Life Science S.r.l., Milan, Italy, CAS: 97-90-5)

- 2,2-azobisisobutyronitrile (AIBN) (Merk Life Science S.r.l., Milan, Italy, CAS: 78-67-1)
- Atrazine PESTANAL®analytical standard (Merk Life Science S.r.l., Milan, Italy, CAS:1912-24-9)
- Simazine PESTANAL®analytical standard (Merk Life Science S.r.l., Milan, Italy, CAS: 122-34-9)
- Ametryn PESTANAL®analytical standard (Merk Life Science S.r.l., Milan, Italy, CAS:834-12-8)
- Bentazone PESTANAL®analytical standard (Merk Life Science S.r.l., Milan, Italy, CAS: 24057-80-0)
- MCPA PESTANAL®analytical standard (Sigma-Aldrich, Milan, Italy, (Merk Life Science S.r.l., Milan, Italy, CAS: 94-74-6)
- Mecoprop PESTANAL®analytical standard (Sigma-Aldrich, Milan, Italy, (Merk Life Science S.r.l., Milan, Italy, CAS: 93-65-2)
- Dichloroprop PESTANAL®analytical standard (Sigma-Aldrich, Milan, Italy, (Merk Life Science S.r.l., Milan, Italy, CAS:15165-67-0)
- 2,4-D Pestanal PESTANAL®analytical standard (Sigma-Aldrich, Milan, Italy, (Merk Life Science S.r.l., Milan, Italy CAS: 94-75-7)
- Irbesartan (Merk Life Science S.r.l., Milan, Italy, CAS: 138402-11-6)
- Losartan (Merk Life Science S.r.l., Milan, Italy, CAS: 114798-26-4)
- Ethanol (Merk Life Science S.r.l., Milan, Italy, CAS:6 4-17-5)
- Methanol (Merk Life Science S.r.l., Milan, Italy, CAS: 67-56-1)
- Toluene (Merk Life Science S.r.l., Milano, Italy, CAS: 108-88-3)
- Acetic acid (Merk Life Science S.r.l., Milan, Italy, CAS: 64-19-7)
- Hydrochloric acid (Merk Life Science S.r.l., Milan, Italy, CAS:7647-01-0)
- Nitric acid (Merk Life Science S.r.l., Milan, Italy CAS: 7697-37-2)
- Sodium perchlorate (Merk Life Science S.r.l., Milan, Italy CAS: 7601-89-0)
- Sulfuric acid (Merk Life Science S.r.l., Milan, Italy CAS: 7664-93-9)
- Sodium dihydrogen phosphate (Merk Life Science S.r.l., Milan, Italy, CAS: 7558-80-7)
- Sodium hydroxide (Merk Life Science S.r.l., Milan, Italy, CAS: 1310-73-2)
- Sodium orthophosphate (Merk Life Science S.r.l., Milan, Italy, CAS: 7558-79-4)

- Potassium hexacyanoferrate (III) (Merk Life Science S.r.l., Milan, Italy, CAS: 13746-66-2)
- Tap water (Lab sink, Department of Chemistry, University of Pavia)
- Graphite screen-printed cells with three electrodes (Topflight Italia (S.P.A.), Vidigulfo, Italy)

6.1.1.3 Reagents for "SAM-modified screen-printed gold electrode for Fe(III) detection" and "Cysteamine-copper SAM-modified screen-printed gold electrode for glyphosate determination" (paragraphs 3.4 and 3.5)

- 3-Mercaptapropionic acid (MPA)(Merk Life Science S.r.l., Milano, Italy,CAS: 1291000)
- Cysteamine (Cys, $NH_2CH_2CH_2SH$, 95%) (Merk Life Science S.r.l., Milano, Italy, CAS: 60-23-1)
- *N*-(3-dimethylaminopropyl)-N′-ethylcarbodiimide hydrochloride (EDC) (Merk Life Science S.r.l., Milano, Italy, CAS: 25952-53-8)
- N-hydroxysuccinimide (NHS) (Merk Life Science S.r.l., Milano, Italy, CAS: 6066-82-6)
- Ethanol (Merk Life Science S.r.l., Milano, Italy, CAS: CAS:6 4-17-5)
- Potassium hexacyanoferrate (III) (Merk Life Science S.r.l., Milano, Italy, CAS: 13746-66-2)
- Sodium orthophosphate (Merk Life Science S.r.l., Milano, Italy, CAS: 7558-79-4)
- Sulfuric acid (Merk Life Science S.r.l., Milano, Italy, CAS: 7664-93-9)
- Sodium perchlorate (Merk Life Science S.r.l., Milan, Italy, CAS: 7601-89-0)
- Sodium hydroxide (Merk Life Science S.r.l., Milano, Italy, CAS: 1310-73-2)
- Iron standard 1g/L, *Trace*CERT®((Merk Life Science S.r.l., Milano, Italy, CAS: CAS: 43149)
- Copper standard 1g/L, *Trace*CERT®(Merk Life Science S.r.l., Milano, Italy, CAS: 68921)
- Deferoxamine mesylate salt (Desferal, DFO-Novartis Pharma S.p.A, Origgio (VA))
- Glyphosate powder (PESTANAL®, analytical standard, Merk Life Science S.r.l., Milano, Italy, CAS: 1071-83-6)
- Gold screen-printed three-electrode cells with ceramic support (Metrohm/DropSens, Metrohm Italiana Srl, Orig- gio (VA), Italy

6.1.1.4 *Reagents for "Ascorbic acid sensing by e-MIP-modified screen-printed electrodes" and "e-MIP-modified screen-printed electrode for the voltammetric detection of MCPA" (paragraphs 3.7 and 3.8)*

- Pyrrole (98%, Merk Life Science S.r.l., Milan, Italy, CAS: 109-97-7)
- Lithium perchlorate (Merk Life Science S.r.l., Milan, Italy, CAS:7791-03-9)
- Sodium dihydrogen phosphate (Merk Life Science S.r.l., Milan, Italy, CAS: 7558-80-7)
- MCPA PESTANAL®analytical standard (Merk Life Science S.r.l., Milan, Italy Italy, CAS: 94-74-6)
- Dichloroprop PESTANAL®analytical standard (Merk Life Science S.r.l., Milan, Italy, CAS:15165-67-0)
- Atrazine PESTANAL®analytical standard (Merk Life Science S.r.l., Milan, Italy,CAS:1912-24-9)
- Glyphosate powder (PESTANAL®, analytical standard, Merk Life Science S.r.l., Milano, Italy, CAS: 1071-83-6)
- L-Ascorbic acid (Supelco—Merk Life Science S.r.l., Milan, Italy,CAS: 50-81-7)
- Sodium orthophosphate (Merk Life Science S.r.l., Milan, Italy, CAS: 7558-79-4)
- Hydrochloric acid (Merk Life Science S.r.l., Milan, Italy, CAS:7647-01-0)
- Sodium hydroxide (Merk Life Science S.r.l., Milan, Italy, CAS: 1310-73-2)
- Ethanol (Merk Life Science S.r.l., Milano, Italy, CAS: CAS:6 4-17-5)
- Acetic acid (Merk Life Science S.r.l., Milan, Italy, CAS: 64-19-7)
- Potassium hexacyanoferrate (III) (Merk Life Science S.r.l., Milan, Italy, CAS: 13746-66-2)
- VIVIN C® tablets (Menarini Industrie Farmaceutiche Riunite S.r.l., Firenze, Italy)
- TIOBEC® 400 tablets (Laborest, Milan, Italy)
- Graphite screen-printed cells with three electrodes(Topflight Italia (S.P.A.), Vidigulfo, Italy)

6.1.2 Instruments

6.1.2.1 Instruments for colorimetric sensors

- pH meter (Mettler Toled mod. SevenMulti) equipped with a combined glass electrode (InLab Pro, Mettler Toledo S.p.A. – Milan, Italy)
- pH indicator paper, pH 1-14 Universal Indicator (Merk Life Science S.r.l. – Milan, Italy). iPad Pro 10.5 (Apple Inc., Italy)
- led-based lightbox (PULUZ, Shenzhen Puluz Technology Ltf, China)
- The GIMP software[60]
- Arduino-based RGB detector (designed by Eng. Dario Pistoia)
- Jasco V-750 spectrophotometer equipped with an FLH-740 film holder and a homemade clip designed to make the spectrum acquisition quick and easy
- Open-source R-based software CAT (Chemometric Agile Tool)

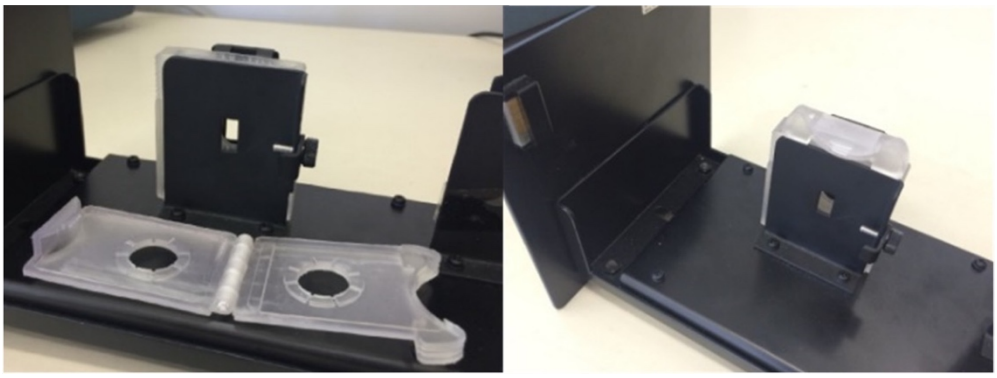

F6.1.2.1- 1. The homemade clip customized to the FLH-740 film holder of the Jasco V-750 UV-vis spectrophotometer.

6.1.2.2 Instruments for electrochemical sensors

- Ultrasonic bath AU-32 Argo Lab with ultrasound power 120 W(Tecno-Lab, Milan, Italy)
- pH-meter Mettler Toledo mod. SevenMulti, equipped with a combined glass electrode InLab Pro (Mettler Toledo, Milan, Italy)
- Potentiostat/galvanostat EmStat4s-PalmSens BN (Houten-The Netherlands https://www.palmsens.com/product/emstat4s/ (accessed on 7 June 2022)).
- Scanning electron microscopy (SEM) Zeiss EVO MA10 (Zeiss, Jena, Germany)

6.2 Appendix II – Green-PAD array for pH measurements (3-Way PCA matrixes, loadings of PCA Dataset description and visualization and ANOVA studies)

T 6.2- 1. Core matrix and superdiagonal core matrix of the 3-way PCA

Core Matrix

	1,1	2,1	1,2	2,2
1	-15.587	-1.7614	1.3805	-3.8604
2	-5.0311	1.3126	-0.99562	10.265

Superdiagonalized Core Matrix

	1,1	2,1	1,2	2,2
1	-16.448	0.21322	-0.4775	-0.56875
2	-0.22332	-0.81467	0.39549	-11.147

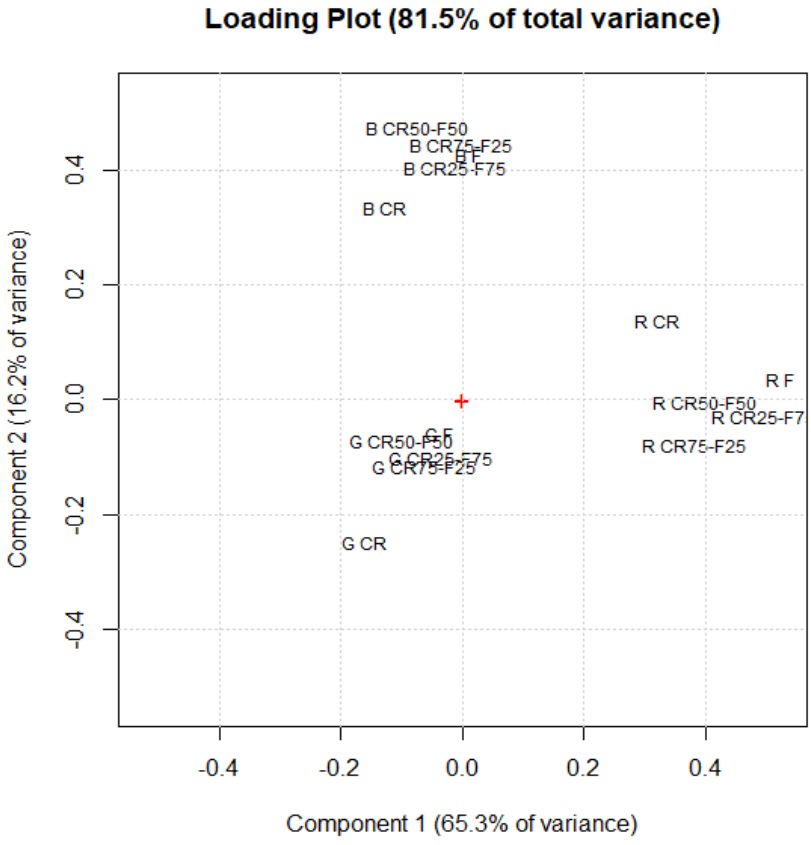

F 6.2- 1. Loading Plot of PC1 and PC2.

.

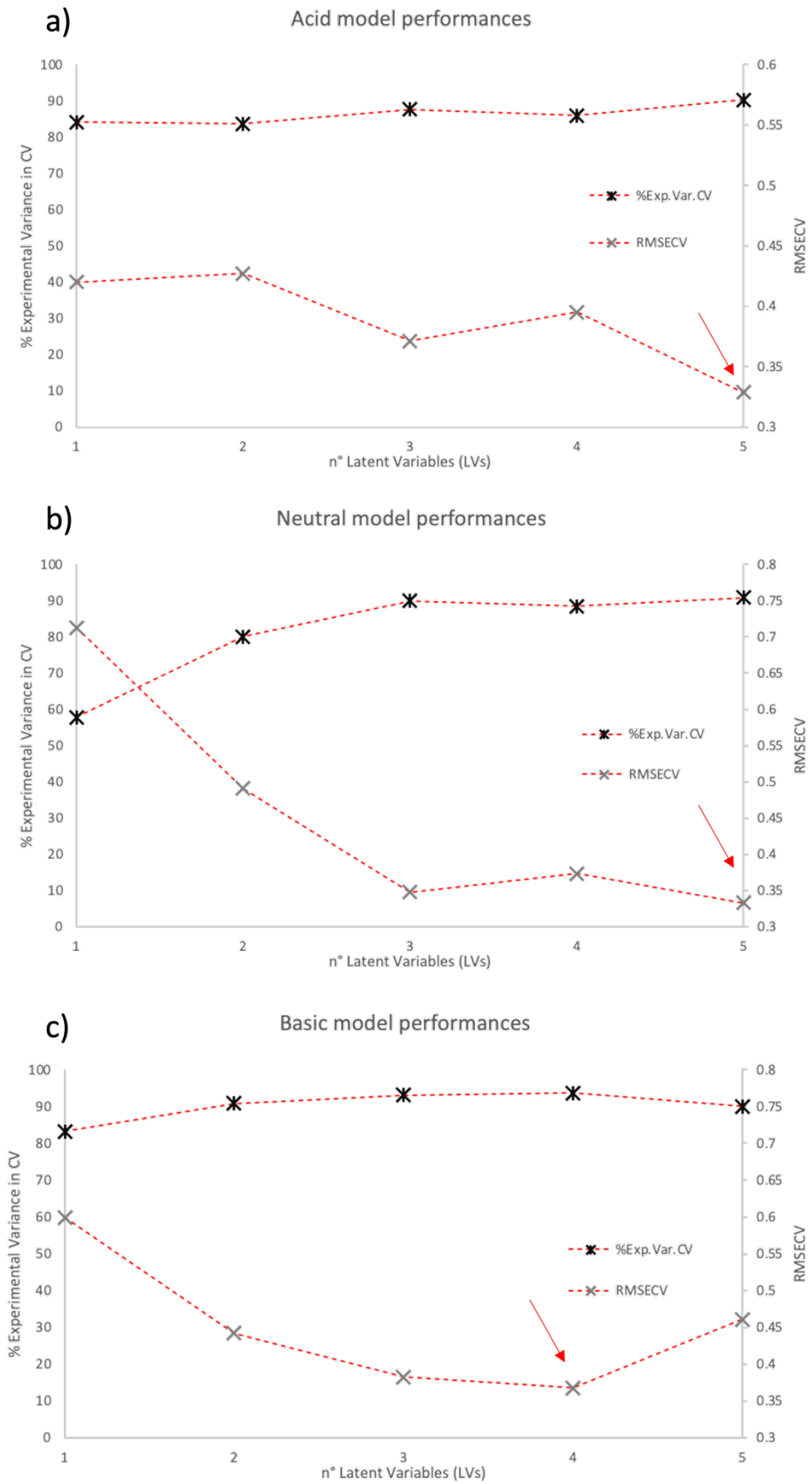

F 6.2- 2. Model performances in acid a), neutral b) and basic c) conditions. RGB indexes are obtained from pcitures of the sensors using GIMP software.

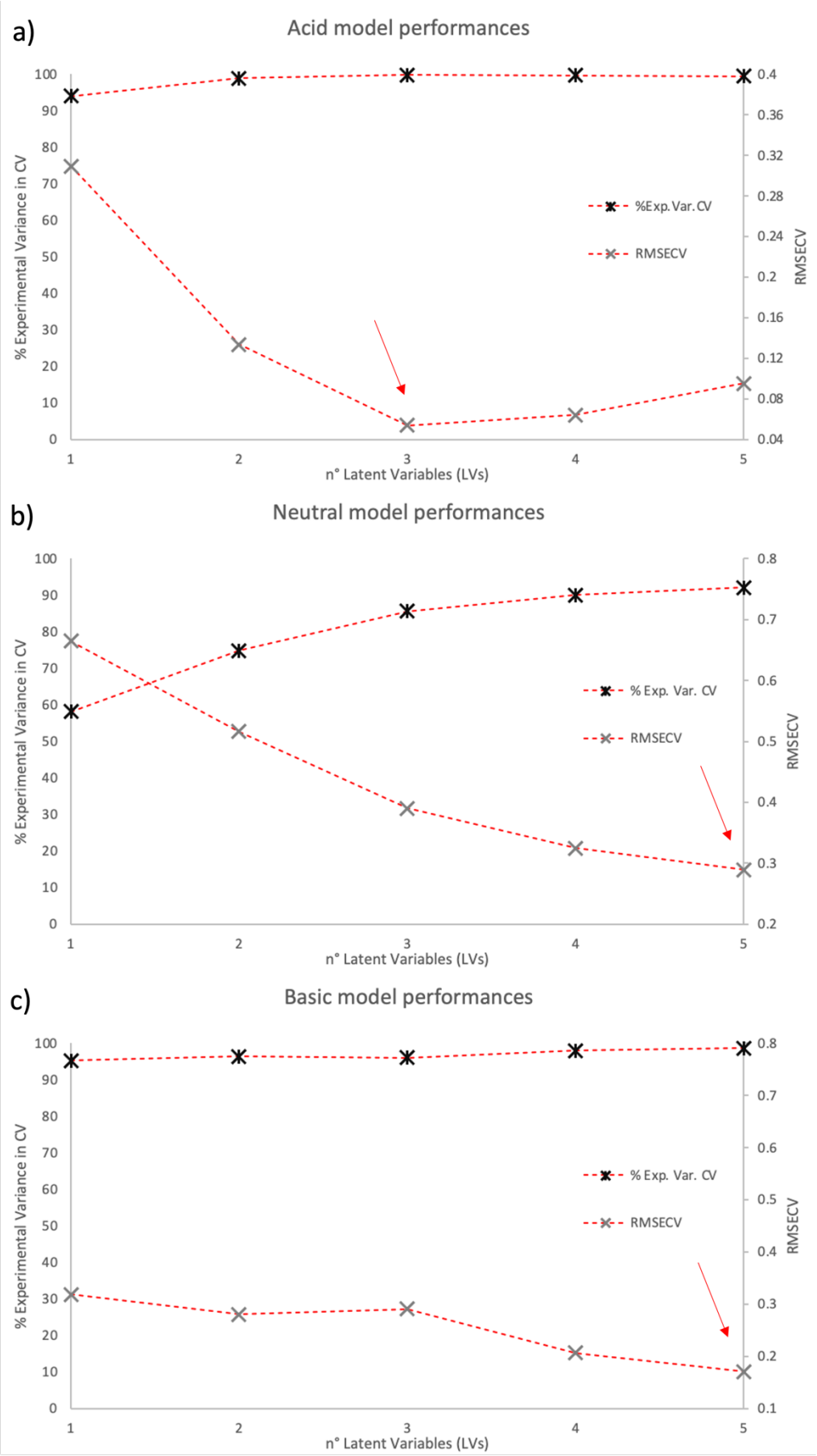

F 6.2- 3. Model performances in acid a), neutral b) and basic c) conditions. RGB indexes are obtained using the RGB detector.

T 6.2- 2. Results of the ANOVA used to compare the pH values obtained using the glassy carbon electrode (GE), the RGB values obtained from the pictures (GP1) and from the RGB detector (GP2) of the Green PADs.

	GE	GP(1)	GP(2)
1	2.39	2.4	2.35
2	2.72	2.9	2.84
3	3.05	2.8	3.03
4	3.55	4.5	3.51
5	7.68	7.3	7.77
6	10.73	10.7	10.8

SUMMARY	*Counting*	*Sum*	*Average*	*Variance*
1	3	7.2	2.4	0.001
2	3	8.5	2.8	0.008
3	3	8.9	3.0	0.019
4	3	10.6	3.5	0.001
5	3	22.8	7.6	0.062
6	3	32.2	10.7	0.003
GE	6	30.1	5.0	11.6
GP(1)	6	29.6	4.9	11.2
GP(1)	6	30.3	5.1	11.8

VARIANCE ANALYSIS

Origin of varaince	*SQ*	*gdl*	*MQ*	*F*	*Significance*	*F crit*
Rows	172.8848	5	34.57697	2403	4.66E-15	3.33
Colums	0.044044	2	20.022022	1.5	0.263098	4.10
Error	0.143889	10	100.014389			
Total	173.0728	17				

6.3 Appendix III – PLS data (Training set, Test set compositions, and model performances) of the TazoC-PADs for Pd(II) determination (paragraph 2.4)

T 6.3- 1. PLS model Pd(II)/TazoC-Pads pH 2: Experimental and fitted data

Training set		**Test set**	
Exp. [Pd] μM	Fit [Pd] μM	Exp. [Pd] μM	Fit [Pd] μM
2.6	2.1	7.5	7.8
2.6	2.5	7.5	8.7
2.6	2.2	7.5	6.8
4.9	5.1	25.2	24.3
4.9	6.5	25.2	26.8
4.9	4.5	25.2	25.3
10.1	11.3	42.5	43.4
10.1	10.8	42.5	41.2
10.1	9.7	42.5	44.9
19.9	21.9		
19.9	21.9		
19.9	20.0		
30.1	28.5		
30.1	27.8		
30.1	28.1		
39.8	41.4		
39.8	41.5		
39.8	40.3		
50.0	50.7		
50.0	47.4		
50.0	49.5		

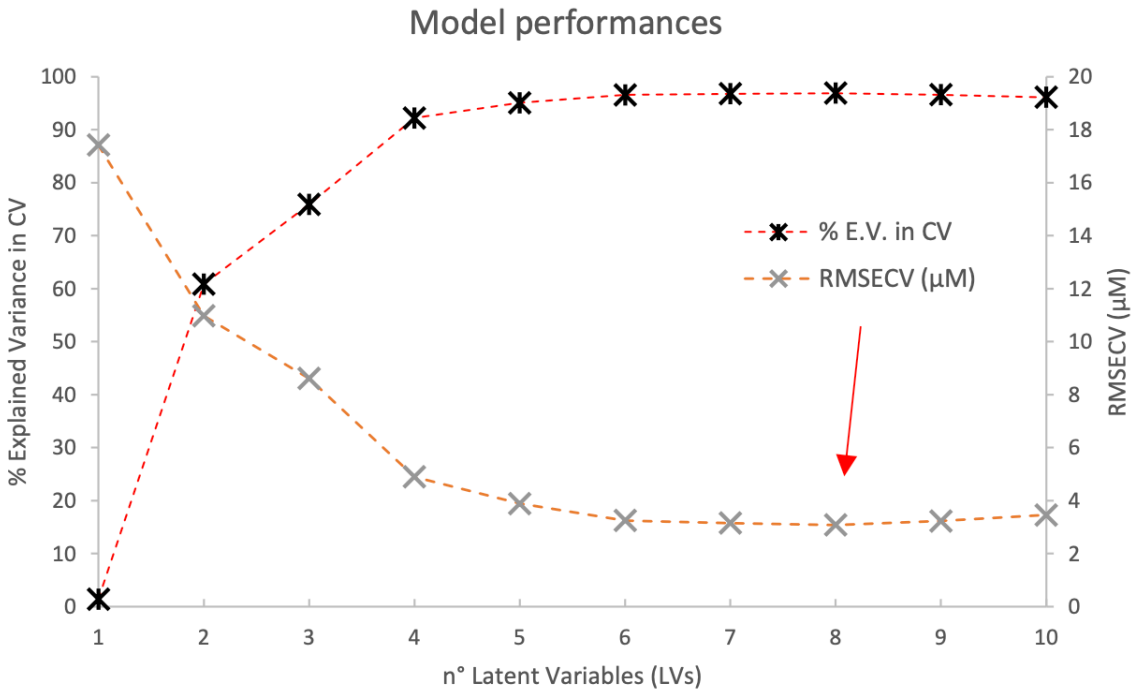

F 6.3- 1. PLS model Pd(II)/TazoC.PADs pH 4: Model performances

T 6.3- 2. PLS model Pd(II)/TazoC-Pads pH 4: Experimental and fitted data

Training set		**Test set**	
Exp. [Pd] µM	Fit [Pd] µM	Exp. [Pd] µM	Fit [Pd] µM
2.6	2.1	7.5	5.6
2.6	3.6	7.5	5.9
2.6	3.2	7.5	8.1
4.9	5.4	25.2	24.9
4.9	4.9	25.2	26.7
4.9	4.3	25.2	27.2
10.1	7.9	37.6	38.2
10.1	9.3	37.6	38.6
10.1	11.6	37.6	41.9
19.9	17.9		
19.9	20.9		
19.9	21.7		
30.1	28.8		
30.1	29.7		
30.1	30.0		
39.8	39.0		
39.8	40.5		
39.8	39.9		
50.0	52.3		
50.0	49.3		
50.0	50.0		

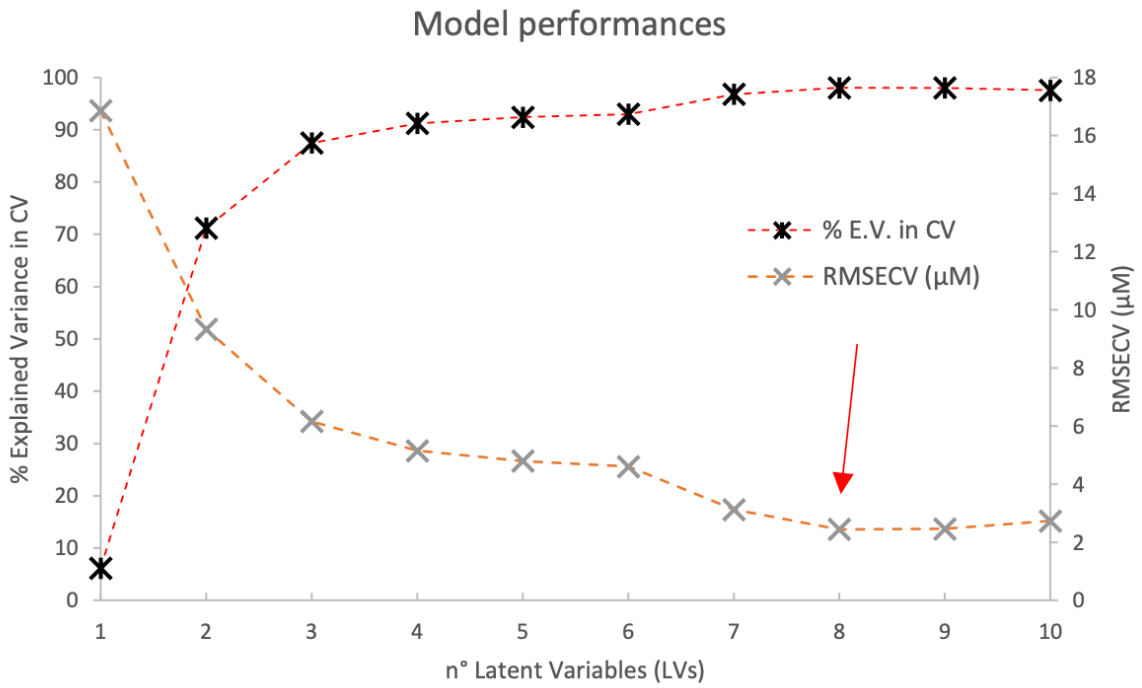

F 6.3- 2.PLS model Pd(II)/TazoC.PADs pH 5.5: Model performances

T 6.3- 3.PLS model Pd(II)/TazoC-Pads pH 5.5: Experimental and fitted data

Training set		**Test set**	
Exp. [Pd] µM	Fit [Pd] µM	Exp. [Pd] µM	Fit [Pd] µM
2.6	2.8	8.3	11.4
2.6	3.3	8.3	9.3
2.6	3.4	8.3	9.9
4.9	5.3	27.7	28.5
4.9	4.6	27.7	28.1
4.9	4.0	27.7	30.3
10.1	10.7	41.3	41.6
10.1	9.6	41.3	42.1
10.1	10.0	41.3	40.9
19.9	19.9		
19.9	19.7		
19.9	20.2		
30.1	29.5		
30.1	30.8		
30.1	30.0		
39.8	39.6		
39.8	40.9		
39.8	38.9		
50.0	48.7		
50.0	48.2		
50.0	52.7		

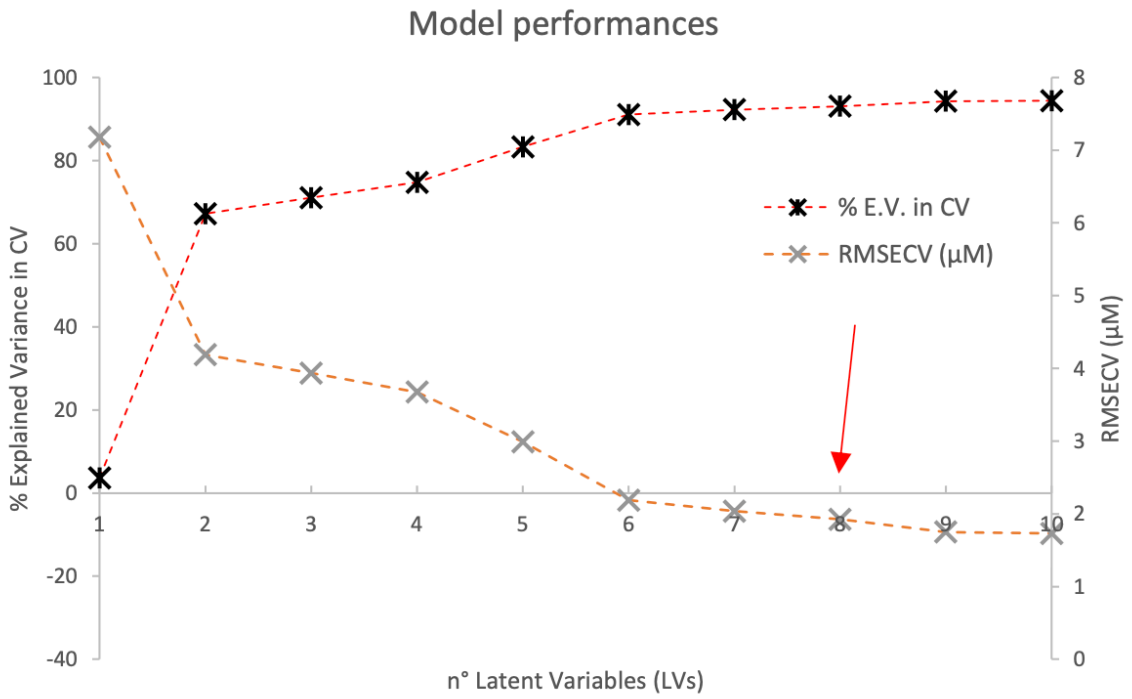

F 6.3- 3.PLS model Pd(II)+Cu(II)/TazoC.PADs pH 4: Model performances

T 6.3- 4.PLS model Pd(II)+Cu(II)/TazoC-PADs pH 4: Experimental and fitted data

Training set			**Test set**		
[Cu] µM	Exp.[Pd] µM	Fit [Pd] µM	[Cu] µM	Exp. [Pd] µM	Fit [Pd] µM
5.0	0.0	0.6	20.5	3.8	3.9
10.1	0.0	0.6	0.0	3.8	3.8
20.5	0.0	0.5	20.5	7.5	7.3
0.0	5.0	3.6	0.0	7.5	7.7
5.0	5.0	4.5	5.0	15.0	15.8
10.1	5.0	4.5	10.1	15.0	14.9
0.0	10.3	10.6	3.8	3.8	3.6
10.1	10.3	11.8	14.9	3.8	4.5
5.0	19.7	19.2	3.8	7.5	7.9
10.1	19.7	19.4	14.9	7.5	6.9
20.5	19.7	19.9	3.8	15.0	15.3
3.8	0.0	-0.4			
14.9	0.0	-0.2			
3.8	0.0	0.6			
7.6	5.0	4.5			
14.9	5.0	5.3			
7.6	5.0	5.3			
14.9	10.3	11.0			
0.0	10.3	10.8			
5.0	10.3	11.0			
10.1	19.7	10.4			
20.5	19.7	19.4			
5.0	19.7	18.7			

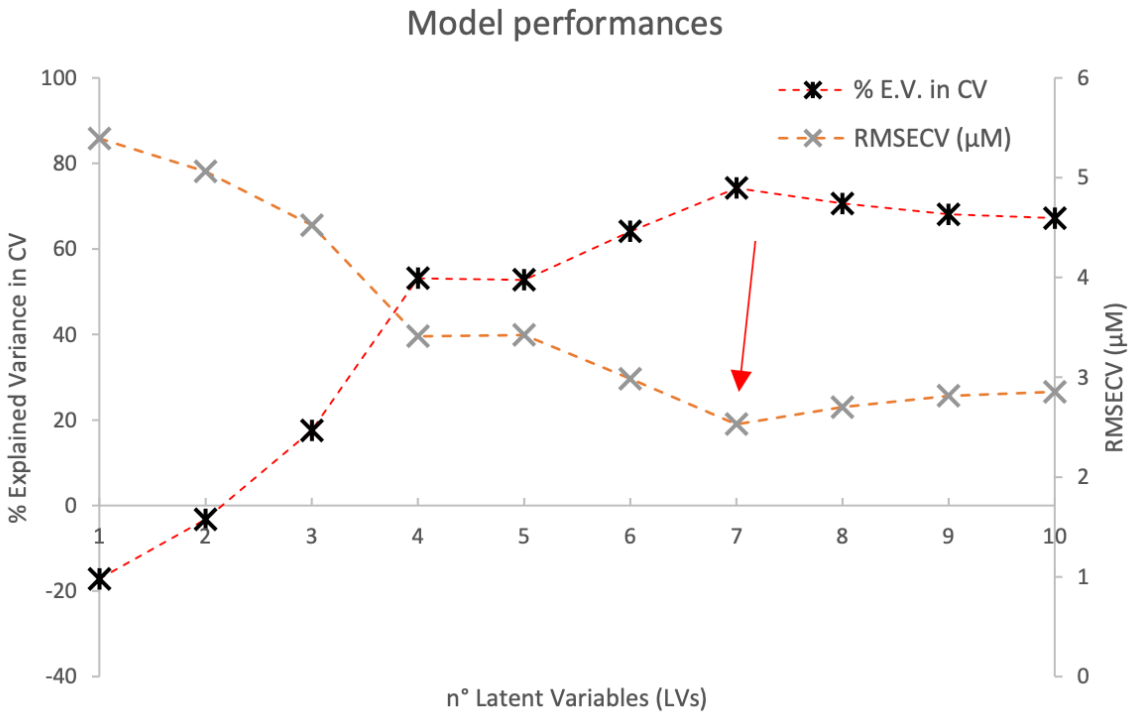

F 6.3- 4.PLS model Pd(II)+Cu(II)+Ni(II)/TazoC.PADs pH 5.5: Model performances

T 6.3- 5.PLS model Pd8II)+Cu(II)+Ni(II)/TazoC-PADs pH 5.5: Experimental and fitted data

Training set				**Test set**			
[Cu] µM	[Ni] µM	Exp.[Pd] µM	Fit [Pd] µM	[Cu] µM	[Ni] µM	Exp. [Pd] µM	Fit [Pd] µM
0.0	20.5	0.0	-0.1	4.7	30.7	0.0	-0.2
0.0	30.7	0.0	-0.1	0.0	30.7	4.7	4.0
0.0	40.1	0.0	0.0	15.7	3.7	12.5	12.0
7.9	30.7	0.0	0.3	0.0	30.7	10.3	10.9
9.4	30.7	0.0	-0.1	15.7	0.0	15.0	16.3
3.1	30.7	3.8	3.7				
7.9	15.7	3.8	2.9				
15.7	0.0	3.8	4.1				
0.0	30.7	7.5	7.3				
3.1	0.0	7.5	7.4				
7.9	20.5	7.5	8.0				
3.1	7.5	15.0	14.4				
7.9	0.0	15.0	15.2				

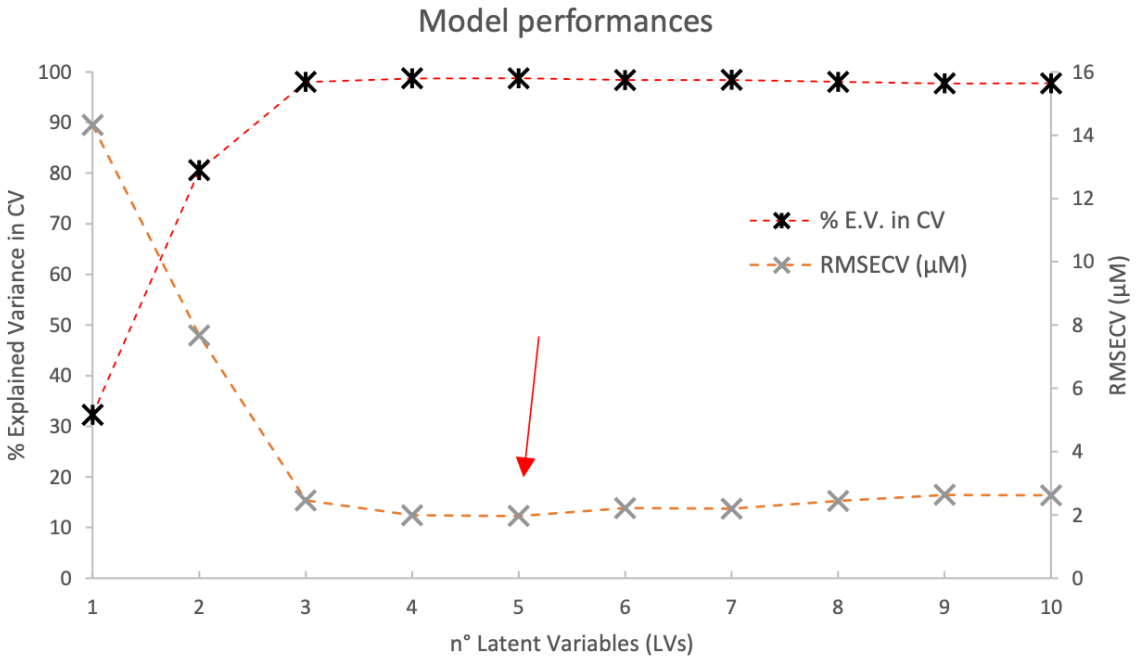

F 6.3- 5.PLS model Pd(II)/TazoC-PADs TW: model performances

T 6.3- 6. PLS model Pd(II)/TazoC-PADs TW: Experimental and fitted data

Training set		**Test set**	
Exp. [Pd] µM	Fit [Pd] µM	Exp. [Pd] µM	Fit [Pd] µM
2.6	1.7	7.5	8.2
2.6	4.1	7.5	7.6
2.6	3.3	7.5	8.5
4.9	7.5	25.2	27.1
4.9	5.5	25.2	24.5
4.9	4.6	25.2	26.4
10.1	9.1	44.6	45.9
10.1	10.3	44.6	43.0
10.1	10.4	44.6	42.8
19.9	19.8		
19.9	21.6		
19.9	19.9		
30.1	27.1		
30.1	29.3		
30.1	31.5		
39.8	39.6		
39.8	29.9		
39.8	41.9		
50.0	51.7		
50.0	48.2		
50.0	48.3		

6.4 Appendix IV – Optimization data (levels of variables, coefficient plots and their significance and the model equation) for SWV experimental conditions for bare and MIP-modified electrodes for Irbesartan detection (paragraph 3.6)

a) Optimization of the SWV experimental conditions for the bare electrode

T 6.4- 1.Optimization of the SWV experimental conditions for the bare electrode by a full factorial design 23: level definitions for the parameters considered.

Parameter	Minimum level (-1)	Maximum (+1)
Frequency (Fz, Hz)	1	50
Impulse amplitude (*A*, mV)	50	100
Equilibration time (*t*,s)	120	300

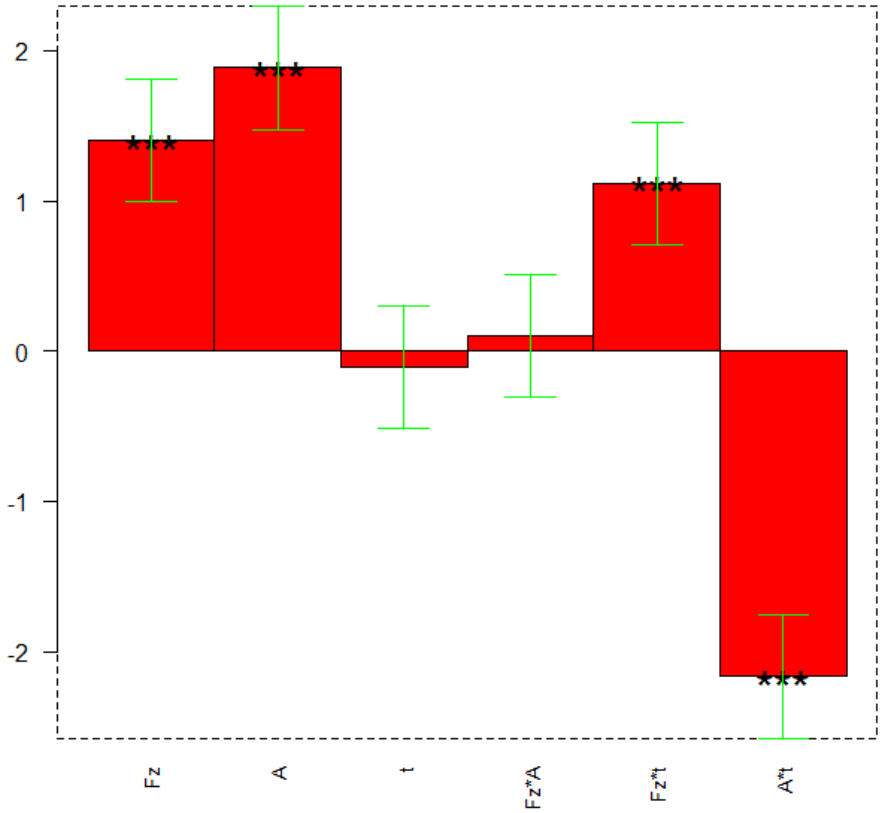

F 6.4- 1. DoE to optimize the SWV experimental conditions for the bare electrode. The greatest values and little black stars(regardless the sign) suggest a significant influence of the respective parameter or interaction and significance (*p≤'0.05,***p≤0.001).

Model equation can be written as follows:

$$i_p = b_0 + b_1 \cdot Fz + b_2 \cdot A + b_3 \cdot t + b_{12} \cdot Fz \cdot A + b_{13} \cdot F \cdot zt + b_{23} \cdot A \cdot t$$

T 6.4- 2. Coefficients and significance (*p≤'0.05,***p≤0.001) calculated for the optimization of the SWV experimental conditions for the bare electrode by full factorial design 2^3.

Coefficient	Value	Significance
b_0	5.586	
b_1	1.402	***
b_2	1.886	***
b_3	-0.104	
b_{12}	-0.102	
b_{13}	1.117	***
b_{23}	-2.166	***

T 6.4- 3. Optimization of the SWV experimental conditions for the bare electrode by a full factorial design 23: model validation by six replicates at the center point [0 0 0],Fz=25 Hz, A=75 mV and t=156 s. CI = confidence interval 95% confidence level.

	I_p (μA)
Average	0.33
Standard deviation	0.02
Upper bound CI	0.35
Lower bound CI	0.31
Predicted response b_0	0.3462

b) Optimization of the SWV experimental conditions for the MIP- and NIP-modified electrodes

T 6.4- 4. Optimization of the SWV experimental conditions for the MIP- and NIP- modified electrode by a full factorial design 2^3: level definitions for the parameters considered.

Parameter	Minimum level (-1)	Maximum (+1)
Frequency (Fz, Hz)	1	50
Impulse amplitude (*A*, mV)	50	100
Equilibration time (*t*,s)	210	300

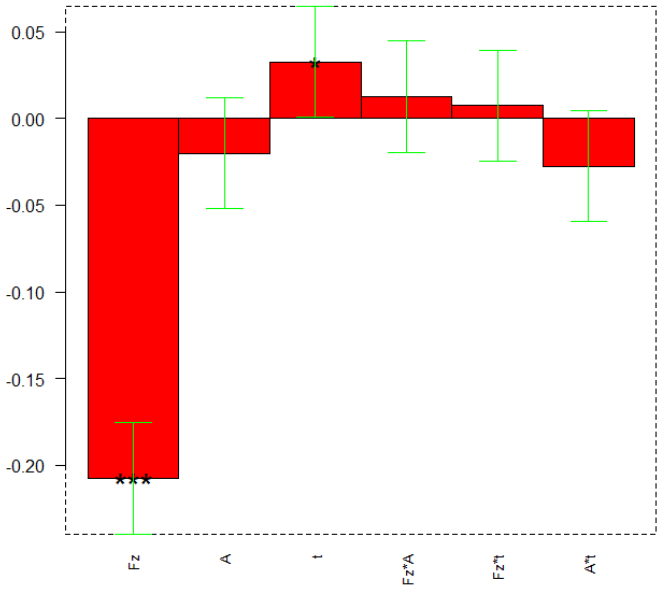

F 6.4- 2. DoE to optimize the SWV experimental conditions for the MIP- and NIP- modified electrode. The greatest values and little black stars(regardelss the sign) suggest a significant influence of the respective parameter or interaction and significance (*p≤'0.05,***p≤0.001).

Model equation can be written as follows<.

$$i_p = b_0 + b_1 \cdot Fz + b_2 \cdot A + b_3 \cdot t + b_{12} \cdot Fz \cdot A + b_{13} \cdot F \cdot zt + b_{23} \cdot A \cdot t$$

T 6.4- 5. Coefficients and significance (*p≤'0.05,***p≤0.001) calculated for the optimization of the SWV experimental conditions for the MIP- and NIP- modified electrode by full factorial design 2^3.

Coefficient	Value	Significance
b_0	0.2975	
b_1	-0.2075	***
b_2	-0.02	
b_3	0.0325	*
b_{12}	0.0125	
b_{13}	0.0075	
b_{23}	-0.0275	

T 6.4- 6. Optimization of the SWV experimental conditions for the MIP- and NIP- modified electrode by a full factorial design 2^3: model validation by six replicates at the center point [0 0 0],Fz=25 Hz, A=75 mV and t150 s. CI = confidence interval 95% confidence level.

	I_p (µA)
Average	0.299
Standard deviation	0.003
Upper bound CI	0.302
Lower bound CI	0.296
Predicted response b_0	0.2975

6.5 Appendix V - e-MIP-modified screen-printed electrodes for the voltammetric detection of MCPA (electrode characterization and PLS model performaces) (paragraph 3.8)

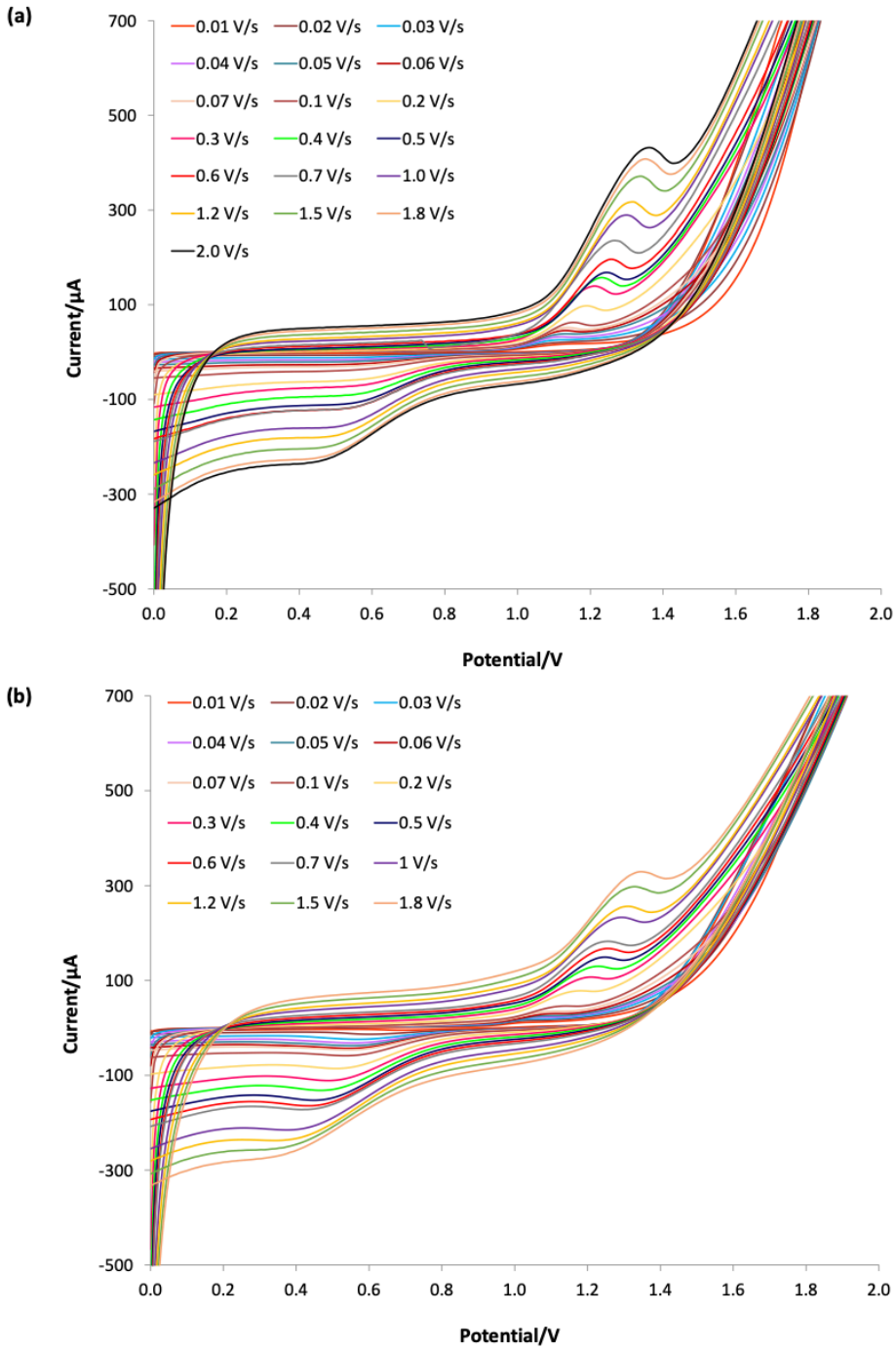

F 6.5- 1. CV at different scan speeds of MCPA, 2.5 mM MCPA, PBS 0.1 M at pH 5.5. **a)** bare working electrode; **b)** eMIP-modified working electrode

T 6.5-1. Regression line equations of the various graphs (see column 1) obtained from CVs data that were used to evaluate the electrochemical parameters related to the electrochemical process at the bare and eMIP-modified electrodes.
c = concentration (mg/L); v = scan speed ($V \cdot s^{-1}$); i= current intensity (A); E = potential (V). The number between parentheses refers to the uncertainty on the last digit.
*Obtained from the calibration curves, i_p (DPV) vs. c, concentration range from 10 mg/L to 200 mg/L.

	Bare electrode			**eMIP-modified electrode**		
	slope	intercept	R^2	slope	intercept	R^2
E vs. log *v*	0.19(2)	1.302(2)	0.990	0.165(3)	1.288(2)	0.996
E vs. *v*	0.76(6)	1.080(4)	0.959	1.3(1)	0.999(6)	0.954
log *i* vs. log *v*	0.65(1)	-4.15(2)	0.984	0.71(1)	-4.36(1)	0.995
***i* vs. $v^{1/2}$**	$7.3(2)\cdot10^{-5}$	$-4(2)\cdot10^{-6}$	0.986	$5.4(1)\cdot10^{-5}$	$-9.3(9)\cdot10^{-6}$	0.994
log *i* vs. log *c**	1.13(3)	+5.1(1)	0.998	1.38(5)	6.9(2)	0.999

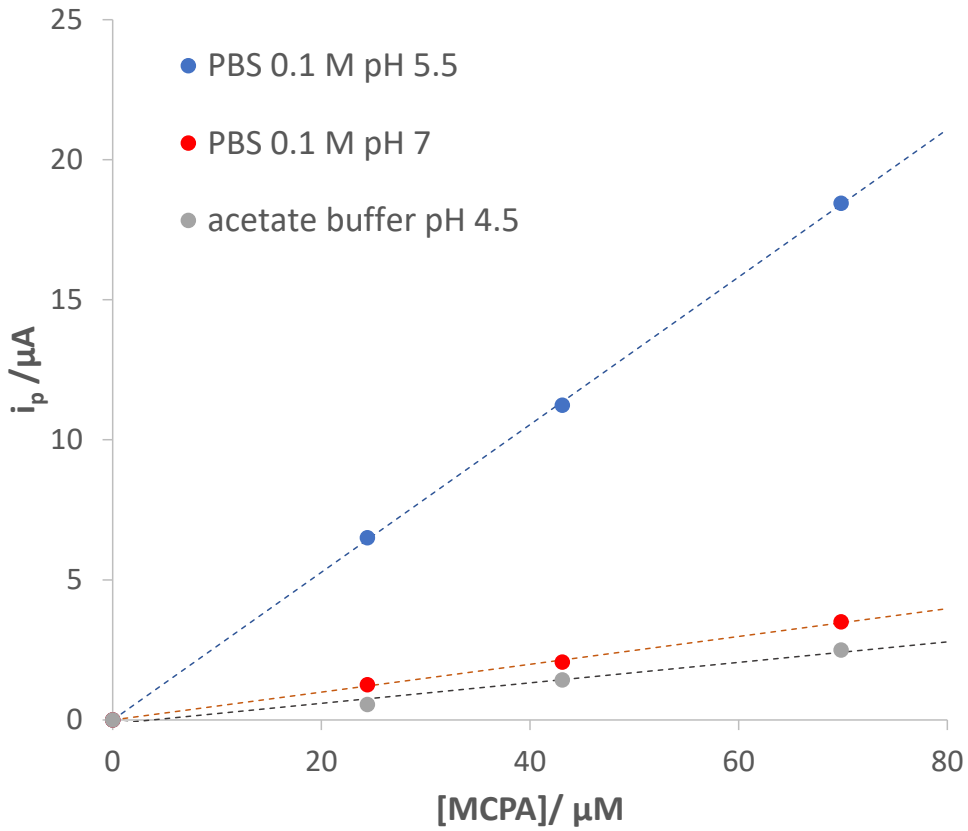

F 6.5- 2. Calibration curves in three different mediums: PBS 0.1 M at pH 5.5, PBS 0.1 M at pH 7, and acetate buffer at pH 4.5. DPV measurements: the anodic peak current at +0.9V is plotted vs. MCPA concentration.

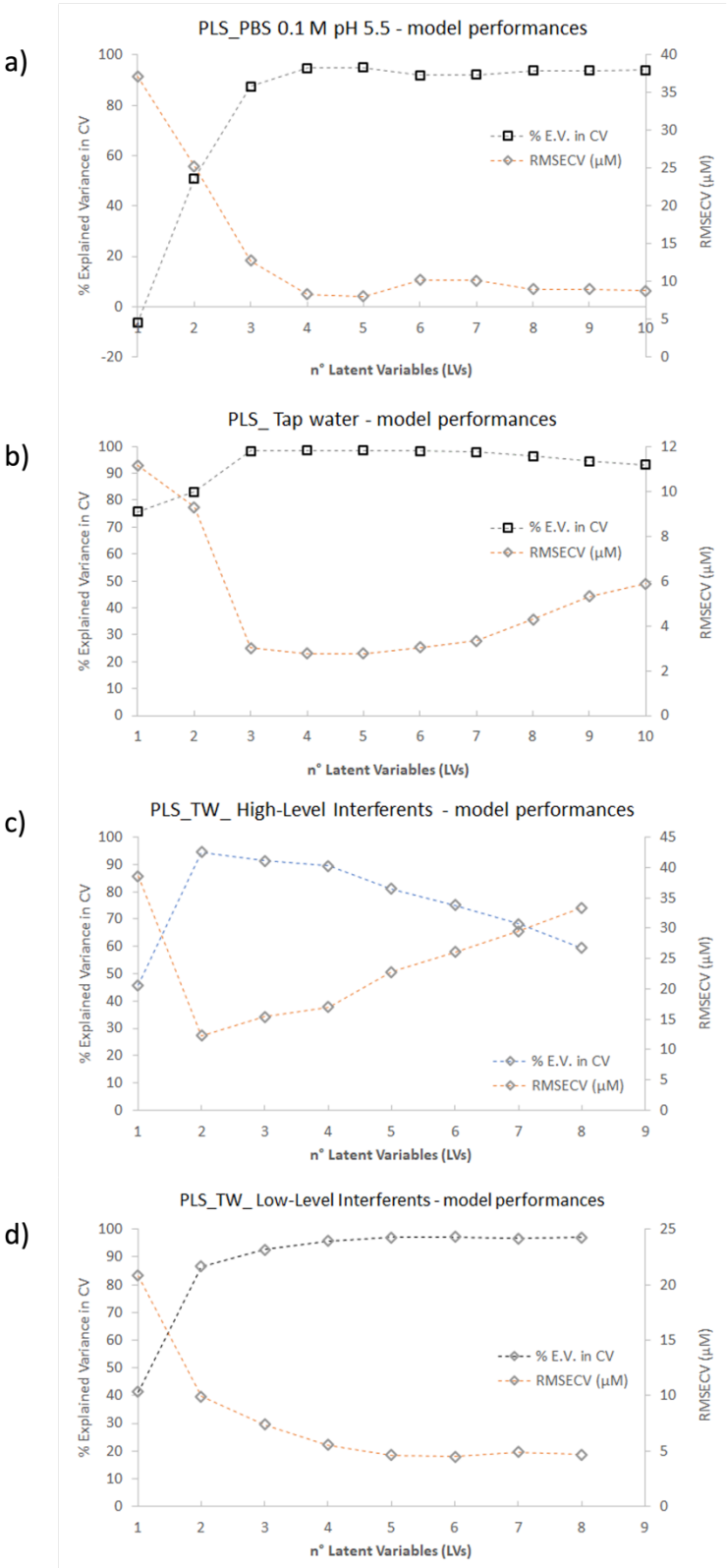

F 6.5- 3. Model performances' graphs for (a) PLS/S-G model MCPA in PBS 0.1 M pH 5.5; (b) PLS/S-G model MCPA in tap water; (c) PLS/S-G model MCPA in tab water spiked with high-level interferents; (d) PLS/S-G model MCPA in tab water spiked with low-level interferents. The red arrow indicates the number of latent variables selected to build the PLS model.